UNIVERSITY OF CALIFORNIA SAN DIEGO

Ocean Dynamics of Greenland's Glacial Fjords at Subannual to Seasonal Timescales

A dissertation submitted in partial satisfaction of the
requirements for the degree Doctor of Philosophy

in

Oceanography

by

Robert M. Sanchez

Committee in charge:

Professor Fiammetta Straneo, Chair
Professor Helen A. Fricker
Professor Sarah N. Giddings
Professor Jennifer A. MacKinnon
Professor Keiko K. Nomura

2023

The Dissertation of Robert M. Sanchez is approved, and it is acceptable in quality and form for publication on microfilm and electronically.

University of California San Diego

2023

EPIGRAPH

"I care about lots of things, " said Slartibartfast, his voice trembling partly with annoyance, but partly also with uncertainty.

"Such as?"

"Well," said the old man, "life, the Universe. Everything, really. Fjords."

Douglas Adams, Life, The Universe and Everything

TABLE OF CONTENTS

LIST OF FIGURES

LIST OF TABLES

ACKNOWLEDGEMENTS

I would like to acknowledge and thank my advisor Fiamma Straneo for all the support, guidance and mentorship she has provided me during my Ph.D. Fiamma is a kind and insightful scientist who has shaped my thinking, read countless drafts, and supported my scientific endeavors. It has been a pleasure getting to work together.

Thank you to my committee members: Helen Fricker, Sarah Giddings, Jen Mackinnon, and Keiko Nomura. Your wisdom and thoughts were always appreciated, and I always felt supported under your guidance.

Next, I would like to acknowledge all my group members, Jamie, Monica, Aurora, Alex, Matt, Marta, Margaret, Izi, Tiago, Donald, as well as the MESOM basement club Susheel, Maya, Chloe, and honorary group members Morven and Theresa. I will miss getting coffee in the lab and being able to talk about science and life, and I'm so glad many of us were able to spend time together at sea. Thank you to my office mate, Margaret, for your friendship, support, and many, many helpful scientific conversations. Thank you to Donald for teaching me MITgcm, talking box models and fostering a life-long love of cricket. Also, thanks to both Helen and Fiamma for promoting a positive and inclusive group environment.

Last, I would like to thank my family and friends. This dissertation would not have been possible without all of your support. Thank you to my parents, Marci, Ryan, Carson and Jordan for your love and encouragement. Thank you to the 2017 PO cohort - Alice, Annie, Channing, Emma, Lauren, and Noel for all the laughs, commiseration, advice, and love. Thank you to the pickleball crew for keeping me distracted during these crazy years. Special thank you to Emma whose support was immeasurable.

Chapter 2, in full, is a reprint of the material as it appears in Journal of Atmospheric and Oceanic Technology, 2021. Sanchez, R. , Straneo, F. , Andres, M. , (2021), Using Acoustic Travel Time to Monitor the Heat Variability of Glacial Fjords., *Journal of Atmospheric and Oceanic Technology*, 38, 1535-1550, 10.1175/JTECH-D-20-0176.1. ©American Meteorolgical Society. Used with permission. The dissertation author was the primary investigator and author

of this paper.

Chapter 3, in full, is a reprint of the material that has been accepted in *Journal of Physical Oceanography*, Sanchez, R., Slater, D., Straneo, F. , (2023) Delayed Freshwater Export from a Greenland tidewater glacial fjord. American Meteorolgical Society, 2023. Used with permission. The dissertation author was the primary investigator and author of this paper.

Chapter 4, in part, is currently being prepared for submission for publication of the material. Sanchez, R. , Straneo F., Hughes, K., Barbour, P. , Shroyer, E. , Mechanisms controlling the seasonal variability of Sermilik Fjord. The dissertation author was the primary investigator and author of this material.

VITA

2017	Bachelor of Science in Geophysics, California Institute of Technology
2019	Master of Science in Oceanography, University of California San Diego
2023	Doctor of Philosophy in Oceanography, University of California San Diego

PUBLICATIONS

Sanchez, R., Straneo, F., Hughes, K., Shroyer, E., Barbour, P., (2023) "Mechanisms controlling the seasonal variability of Sermilik Fjord" (in prep).

Sanchez, R., Slater, D., Straneo, F., (2023) "Delayed Freshwater Export from a Greenland tidewater glacial fjord"*Journal of Physical Oceanography* (Accepted)

Sanchez, R., Straneo, F., Andres, M., (2021) "Using Acoustic Travel Time to Monitor the Heat Variability of Glacial Fjords" *Journal of Atmospheric and Oceanic Technology, 38* 1535-1550. doi:10,1175/JTECH-D-20-0176.1

ABSTRACT OF THE DISSERTATION

Ocean Dynamics of Greenland's Glacial Fjords at Subannual to Seasonal Timescales

by

Robert M. Sanchez

Doctor of Philosophy in Oceanography

University of California San Diego, 2023

Professor Fiammetta Straneo, Chair

Mass loss of the Greenland Ice Sheet is expected to accelerate in the 21st century in response to both a warming atmosphere and ocean, with consequences for sea level rise, polar ecosystems and potentially the global overturning circulation. Glacial fjords connect Greenland's marine-terminating glaciers with the continental shelf, and fjord circulation plays a critical role in modulating the import of heat from the ocean and the export of freshwater from the ice sheet. Understanding fjord dynamics is crucial to predicting the cryosphere and ocean response to a changing climate. However, representing glacial fjord dynamics in climate models is an ongoing challenge because fjord circulation is complex and sensitive to glacial forcing that is poorly understood. Additionally, there are limited observations available for constraining models and

theory. This dissertation aims to improve our understanding of fjord dynamics, focusing on key aspects (heat variability, freshwater residence time, and fjord exchange) which need to be included in glacial fjord parameterizations.

We use three approaches combining novel observations, idealized, modeling and numerical simulations to investigate the dynamics of fjord circulation at different spatial scales. First, we investigate the heat content variability in the fjord using acoustic travel time (Chapter 2). We demonstrate that acoustic travel time can be used to model fjord stratification during winter months and monitor heat content variability at synoptic and seasonal timescales. Secondly, we use a combination of *in situ* observations and an idealized box model to evaluate freshwater residence time in a west Greenland Fjord (Chapter 3). We find that meltwater from the ice sheet is mixed downward across multiple layers near the glacier terminus resulting in freshwater storage and a delay in freshwater export from the fjord. Finally we analyze a multi-year realistically forced numerical simulation of Sermilik Fjord in southeast Greenland and identify the impact of shelf and glacial forcing on fjord exchange (Chapter 4). We show that the glacial-driven circulation is more efficient at renewing the fjord and that the sign of the exchange flow is related to the along-shelf wind stress. This dissertation strengthens our understanding of the fundamental connections between oceans and glaciers, and will lead to improved representation of ice-ocean interactions in climate models.

Chapter 1

Introduction

Glacial fjords serve as conduits between a retreating ice sheet and a warming ocean. Mass loss from the Greenland Ice Sheet is predicted to accelerate during the 21st century, contributing to sea level rise (Bamber et al., 2019; Goelzer et al., 2020). Between 2013 and 2017, the melting of the ice sheet contributed 0.61 ± 0.08 mm/yr to sea level rise and has a total sea level rise potential of 7.4 m (Smith et al., 2020; Shepherd et al., 2020). This mass loss has been attributed to both higher atmospheric temperatures and increased ocean forcing at the margins of marine-terminating glaciers (Straneo et al., 2011; Straneo and Heimbach, 2013; Cowton et al., 2018; Slater and Straneo, 2022). Fjord circulation regulates ocean forcing by transporting ocean heat to glacier termini, driving submarine melting of glaciers and ice mélange and replenishing the reservoir of available heat (Chauché et al., 2014; Mortensen et al., 2011; Holland et al., 2008). However, the sparseness of observations in a dynamic and complicated environment limit our understanding of near-ice heat variability and its connection to fjord circulation (Straneo and Cenedese, 2015). Understanding the drivers of fjord heat variability is essential for accurately representing ocean forcing of glaciers in climate models.

As the Greenland Ice Sheet melts, freshwater is discharged through fjords before reaching the global ocean. The increasing export of freshwater has consequences on ocean ecosystems, regional circulation, salinity, and potentially large-scale deep convection (Böning et al., 2016; Frajka-Williams et al., 2016; Arrigo et al., 2017; Oksman et al., 2022; Thornalley et al., 2018;

Hendry et al., 2021). At the same time, freshwater can modify fjord dynamics by initiating circulation and enhancing mixing through buoyant convection, potentially feeding back on submarine melting (Carroll et al., 2015; Bendtsen et al., 2021; Zhao et al., 2022a). In order to predict the impact of the Greenland Ice Sheet on oceans and ecosystems, we need to determine how fjord dynamics alters freshwater export both spatially and temporally.

The controls on the ice-ocean system occur across a range of scales from the subpolar gyre in the North Atlantic to the thin ice-ocean boundary layer where melting occurs. Greenland is located at the confluence of warm and salty subtropical-origin waters coming from the Atlantic ocean and cold and fresh waters coming from the Arctic (Fig. 1.1., Snow et al., 2021; Gelderloos et al., 2017; Le Bras et al., 2021; Sutherland and Pickart, 2008). It is the hydrographic properties (temperature, salinity, relative volume) of these waters which set the boundary conditions for fjords and ultimately on marine-terminating glaciers (Straneo et al., 2012; Gladish et al., 2014a; Mortensen et al., 2018; Schaffer et al., 2020). At the fjord scale (20 - 100 km), dynamics are influenced by both external water mass variability and glacial discharges, including the fact that an injection of buoyant meltwater can spark an overturning circulation within the fjord (Gladish et al., 2014b; Straneo et al., 2011). Close to the glacier terminus (< 5 km), circulation is complex with intense recirculation, vigorous upwelling buoyant plumes, and ambient melting of submerged ice (Slater et al., 2018; Mankoff et al., 2016; Chauché et al., 2014; Jackson et al., 2020). The vast range of scales of glacial fjords make the ice-ocean system both a difficult and exciting frontier of research.

Study of glacial fjord dynamics is limited by the challenge of maintaining and collecting measurements in ice-hazardous and remote locations (Straneo et al., 2019). Most observations are biased towards the summer when the fjords are more accessible. Additionally, moorings are in constant danger of coming into contact with icebergs which can be hundreds of meters deep (Straneo et al., 2016). The heads of fjords are typically congested with a thick mélange preventing measurements near the terminus. To deepen our knowledge of fjord dynamics, we need to leverage the capabilities of innovative observation techniques and develop realistic models

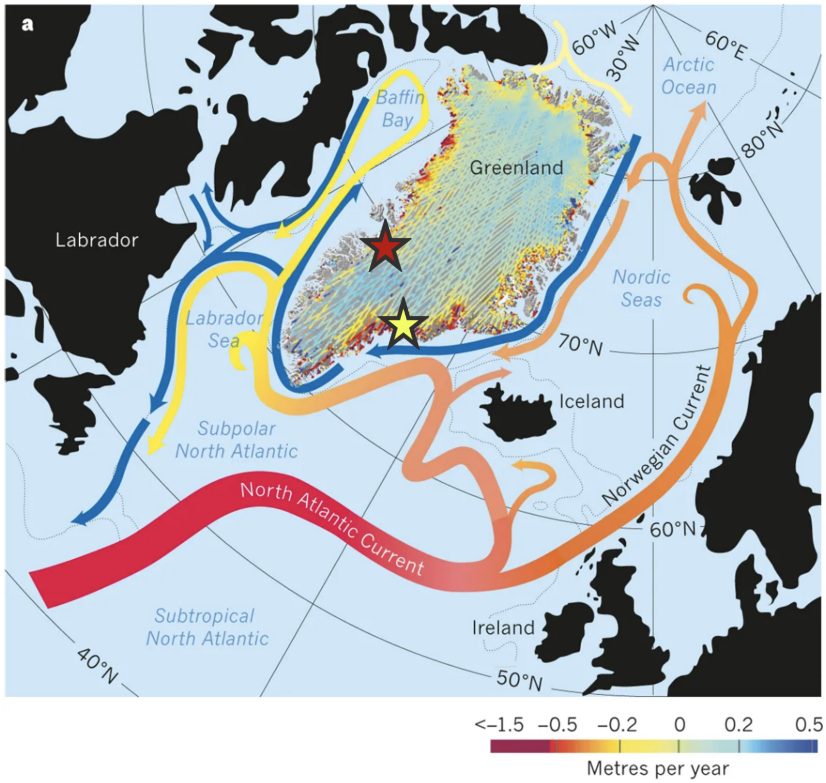

Figure 1.1. Adapted regional map from Straneo and Heimbach (2013). The yellow star is Sermilik Fjord, the site of Chapters 2 and 4. The red star is Saqqarleq, the site of Chapter 3.

validated by data.

In Chapter Two, we investigate the relationship between acoustic travel time and glacial fjord heat content. We use a pressure-sensor-equipped inverted echo sounder (PIES) to measure acoustic travel time and compare the signal against moored temperature and salinity data in Sermilik Fjord (Fig. 1.1). We demonstrate that acoustic travel time can be used to model fjord stratification during winter months and monitor heat content variability at synoptic and seasonal timescales. This work encourages the use of a PIES as part of a long-term monitoring system.

In Chapter Three, we determine freshwater residence time in Saqqarleq (Fig. 1.1). We use a combination of *in situ* observations and an idealized box model to evaluate freshwater (meltwater) storage near the terminus (< 2km). We find that freshwater is mixed vertically resulting in an accumulation of freshwater near the fjord head and a delay in peak freshwater export of a month. Therefore, freshwater residence time in fjords needs to be accounted for in global ocean models.

In Chapter Four, we analyze the fjord-shelf exchange in a multi-year realistically forced numerical simulation of Sermilik Fjord in southeast Greenland. We use the Total Exchange Flow (TEF) framework to identify the impact of shelf and glacial forcing on fjord exchange on seasonal timescales. We show that the glacial-driven circulation is more effective at renewal than the shelf-driven circulation and that the sign of the exchange flow is related to the along-shelf wind stress. These results imply that the shelf-driven circulation sets water-mass variability, but is less involved in the direct transport of heat to the glacier.

These three chapters combine novel observational datasets, idealized modeling and numerical simulations to investigate the dynamics of fjord circulation at different spatial scales (Fig. 1.1). We analyze the inflow of heat at the fjord scale (Ch. 2), the export and accumulation of freshwater close to the terminus (Ch. 3), and the dynamics which control exchange across the whole glacier-fjord-shelf system (Ch. 4). The dissertation works towards a goal of improved representation of ice-ocean interactions in climate models, highlighting key aspects (heat variability, freshwater residence time, and fjord exchange) which need to be included in

parameterizations. Understanding fjord dynamics is crucial to predicting the cryosphere and ocean response to a warming climate.

Chapter 2

Using Acoustic Travel Time to Monitor the Heat Variability of Glacial Fjords

Abstract

Monitoring the heat content variability of glacial fjords is crucial to understanding the effects of oceanic forcing on marine-terminating glaciers. A Pressure-sensor equipped Inverted Echo Sounder (PIES) was deployed mid-fjord in Sermilik Fjord in southeast Greenland from August 2011 to September 2012 alongside a moored array of instruments recording temperature, conductivity and velocity. Historical hydrography is used to quantify the relationship between acoustic travel time and the vertically-averaged heat content, and a new method is developed for filtering acoustic return echoes in an ice-influenced environment. We show that PIES measurements, combined with a knowledge of the fjord's two-layer density structure, can be used to reconstruct the thickness and temperature of the inflowing water. Additionally, we find that fjord-shelf exchange events are identifiable in the travel time record implying the PIES can be used to monitor fjord circulation. Finally, we show that PIES data can be combined with moored temperature records to derive the heat content of the upper layer of the fjord where moored instruments are at great risk of being damaged by transiting icebergs.

2.1 Introduction

Under sustained global warming the Greenland Ice Sheet is predicted to continue losing mass during the 21st century with consequences for sea-level rise (Bamber et al., 2019; Goelzer et al., 2020). Changes in the oceanic heat available for melting are thought to be one of the main drivers of glacial retreat (Holland et al., 2008; Motyka et al., 2011; Straneo and Heimbach, 2013; Khazendar et al., 2019). The amount of heat available for melting, in turn, depends on the hydrographic properties of fjords which connect marine-terminating glaciers with the continental shelf (Straneo et al., 2012). However, our knowledge of the variability of ocean properties in glacial fjords is limited by the challenges of maintaining consistent, multi-year observations (Straneo et al., 2016, 2019). Since ocean circulation models presently cannot resolve fjords, long-term measurements are key to mapping and building an understanding of the physical mechanisms controlling fjord variability.

The melt rate of a glacier is set by heat fluxes across the ice-ocean boundary layer. These heat fluxes are a function of ocean temperatures and velocities near the glacier, and are influenced by both the local release of subglacial discharge and the large-scale fjord circulation (Jenkins, 2011; Slater et al., 2018; Sutherland et al., 2019; Jackson et al., 2020). Thus to diagnose heat content variability and infer melt-rate variability, observations are needed of both fjord water-mass properties and fjord circulation (Straneo et al., 2019). Of primary interest is knowing the heat content of the inflowing water at roughly the grounding line depth of the glacier which induces submarine melting and has been correlated to changes in ice discharge (Holland et al., 2008; Motyka et al., 2011; Luckman et al., 2015; Khazendar et al., 2019). Additionally, measurements are needed of near-ice velocities which ultimately transfer heat across the ice-ocean boundary layer and have recently been shown to significantly affect glacial melt rates (Slater et al., 2019; Sutherland et al., 2019; Jackson et al., 2020). Lastly, far-field monitoring of the large-scale fjord circulation is needed to quantify the variability of the heat transport towards the glacier and renewal within the fjord (Straneo et al., 2011; Jackson et al., 2020). Measurements of these

desired variables are presently limited due to the extreme challenges of working in glacial fjords.

Monitoring Greenland's glacial fjords is difficult because of the high costs of operating in such remote and hazardous environments (Straneo et al., 2019). Ocean measurements have been primarily limited to the summer when weather conditions are less harsh and the fjords more navigable. While moorings have had some success in capturing the temporal variability of fjords (Mortensen et al., 2014; Jackson and Straneo, 2016; Carroll et al., 2018; Boone et al., 2018), their effectiveness is often limited because of icebergs that have deep keels which can extend down hundreds of meters (Straneo et al., 2016). To avoid destruction, the top-most flotation and instruments on a mooring are typically far below the surface or confined to a shallow embayment. Because of the challenges of observing glacial fjords, a diverse set of instruments and measuring techniques are required.

One potential approach for measuring the heat content variability of glacial fjords without succumbing to damage from icebergs is to use bottom-mounted acoustic devices. Bottom-to-surface round trip acoustic travel time is an integrated measurement that depends on the depth and sound speed properties of the water column (Del Grosso, 1974). Since the speed of sound in seawater is primarily a function of temperature, acoustic travel time over a fixed depth is proportional to the integrated heat content of the overlying water (Watts and Rossby, 1977).

In this study, we investigate the potential use of acoustic travel time to monitor fjord properties relating to glacial melt variability, such as heat content, through observations collected in Sermilik Fjord (SF) in East Greenland. Using hydrographic data, we show that seasonal and interannual changes in integrated heat content are associated with a measurable signal in acoustic travel time (Section 2). We provide a description of how to process acoustic travel time data in an ice-influenced environment (Section 3). Next, acoustic travel time data collected in SF with a Pressure-sensor equipped Inverted Echo Sounder (PIES) deployed on the seabed alongside a traditional oceanographic mooring are used to investigate the extent to which PIES measurements can diagnose quantities that are relevant to studies of fjord circulation and fjord variability (Section 4). We show that acoustic travel time can be used to (4a) infer the thickness

and temperature of the deep, warm inflowing water in the winter, (4b) track fjord circulations that are associated with shifts in the pycnocline and (4c) remotely measure the heat content of the top layer of the fjord. We finish with a discussion of potential challenges and benefits of using PIES to monitor glacial fjords (Section 5).

2.2 Regional Setting and Theory

2.2.1 Hydrographic Properties of Sermilik Fjord

We first investigate acoustic travel time using hydrographic data collected in SF in southeast Greenland. The fjord connects Helheim Glacier, the fifth largest outlet glacier of the Greenland Ice Sheet and two smaller glaciers, Midgård and Fernis, to the continental shelf (Fig. 2.1). The Helheim-Sermilik system is one of the most well-studied glacial fjord environments in Greenland with continuous measurements since 2008 (Straneo et al., 2016). The fjord is 550-900 m deep, about 75-100 km long and varies in width from 5-10 km. The fjord, like the adjacent continental shelf, is composed of cold and fresh Polar Water (PW) from the Arctic over relatively warm and salty Atlantic Water (AW) from the Irminger Sea.

Conductivity Temperature and Depth (CTD) profiles were collected throughout SF in the summers of 2011-2017, and eXpendable CTDs (XCTD) were deployed by helicopter in the winter of March 2010 (Table 2.1). In the winter, the fjord's density structure resembles two-layers with cold and fresh PW [Conservative Temperature (Θ) < 0 °C, Absolute Salinity (S_A) < 33.3 g kg^{-1}] above relatively warm and salty AW ($\Theta > 3$ °C, $S_A > 34.7$ g kg^{-1}) (Fig. 2.2a-b) (Straneo et al., 2010). The two water masses can be characterized as weakly stratified "layers" separated by a sharp pycnocline centered around 200 m depth. In the summer, the fjord stratification and temperature structure is more complex due to the presence of a third water mass, a mixture of meltwater and ocean water called glacially modified water (GMW, Fig. 2.2a-b) (Beaird et al., 2018). In SF, GMW appears as a relatively warm and salty intrusion in the upper 250 m due to the entrainment and upwelling of deep AW by buoyant freshwater released at depth

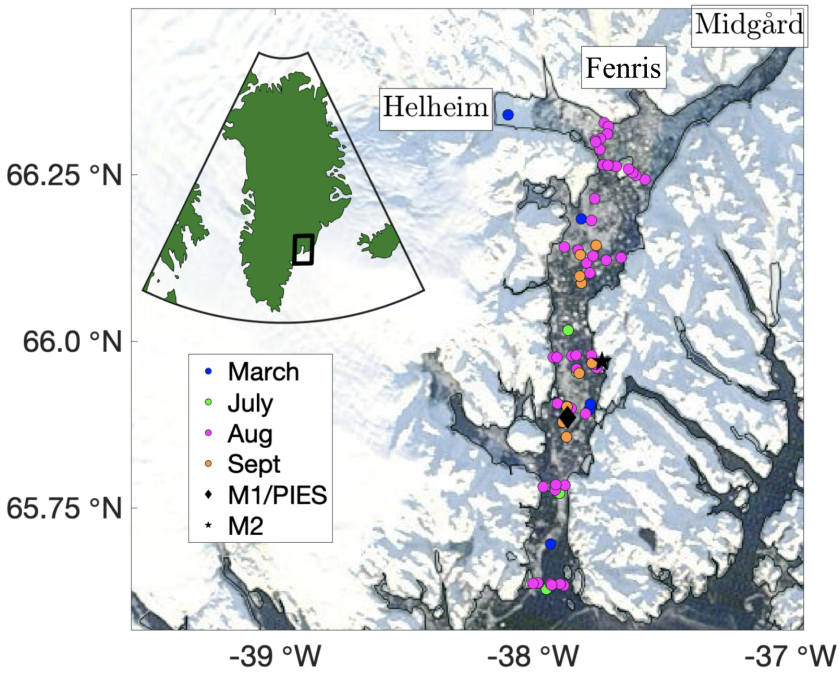

Figure 2.1. A map of Sermilik Fjord which shows the locations of all the CTD profiles collected as well as the locations of the moorings and PIES. The inset shows the fjords location with respect to the Greenland continent. The glaciers locations of Helheim, Fenris, and Midgård are also labeled.

Table 2.1. Details of XCTD and CTD collection dates and previously published data.

Instrument	Data Collection Time	Previously Published
XCTD	March 2010	Straneo et al. (2011)
CTD	August 2011, September 2012, August 2013	Jackson and Straneo (2016)
CTD	August 2015	Beaird et al. (2018); Cape et al. (2019)
CTD	July 2017	unpublished

(Straneo et al., 2010, 2011). However above 50 m, GMW appears as a relatively fresh anomaly due to the increased concentration of freshwater towards the surface (Straneo et al., 2011; Beaird et al., 2018). The casts taken during the summers show that both inflowing AW and exported GMW temperatures can vary by over 1 °C interannually. The sound speed derived from the mean hydrographic profiles generally increases with depth and resembles the temperature profiles (Fig. 2.2c).

2.2.2 Relationship between Travel Time and Heat Content

Travel time (τ) is expressed by:

$$\tau = 2 \int_{-H}^{\eta_s} \frac{1}{c(z)} dz, \tag{2.1}$$

where H is the seafloor depth (m), η_s is the sea surface height (m), $c(z)$ is the speed of sound (m s^{-1}), and the 2 arises because τ is a round-trip travel time. Since sound speed is approximately proportional to temperature, from (1) we expect acoustic travel time to be approximately proportional to integrated heat content (Watts and Rossby, 1977). However, glacial fjords have large vertical and horizontal density gradients due to significant freshwater input that can potentially affect c and therefore τ. Thus, we first test our hypothesis that τ is proportional to integrated heat content in glacial fjords by using the hydrographic profiles (Table 2.1).

The CTD casts were primarily taken during the summer months (July, August, September),

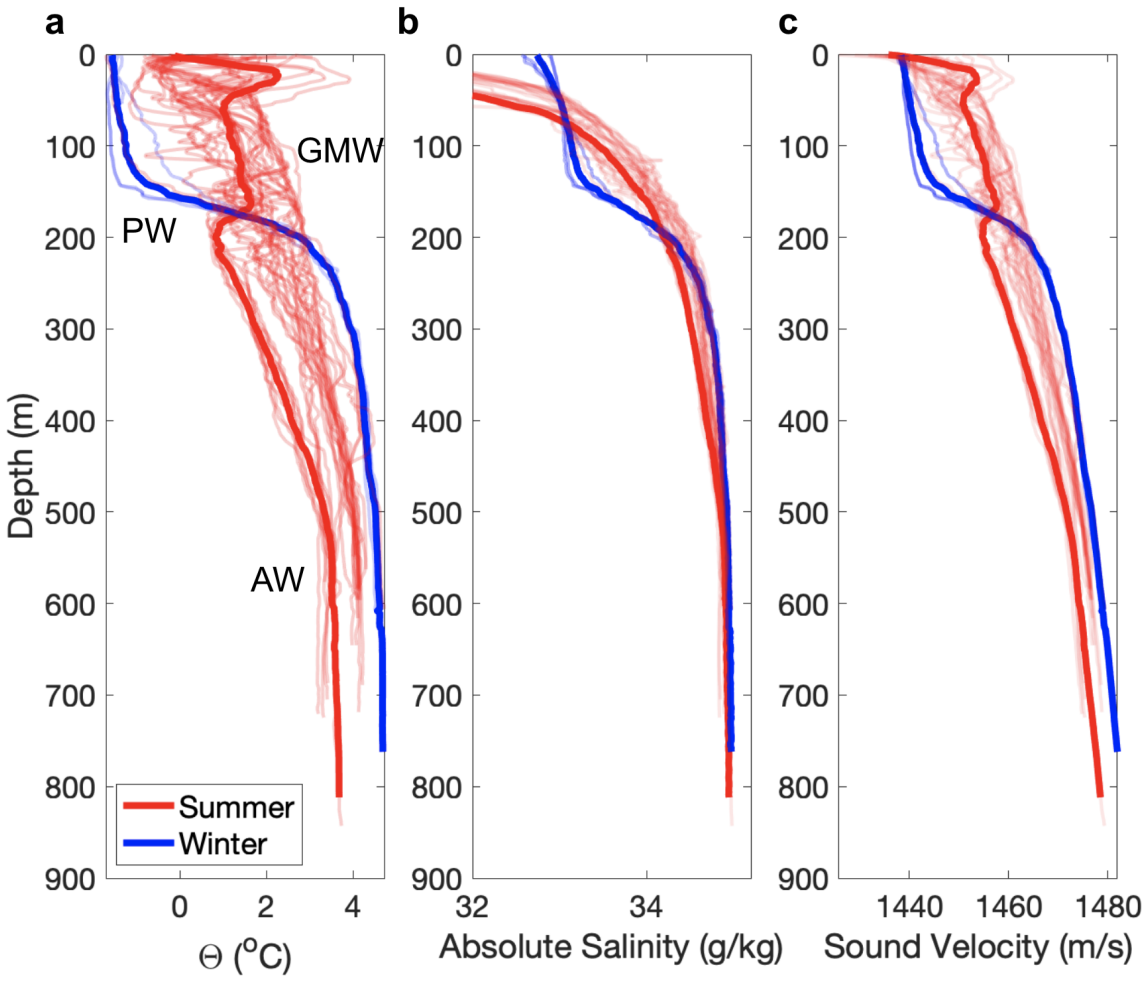

Figure 2.2. CTD profiles collected in Sermilik Fjord from 2010 -2017. In red (blue) are those profiles collected in summer (winter). The bold blue is from March 2010 and the bold red is September 2012 (when the PIES was recovered). a) Conservative Temperature, b) Absolute salinity, c) Sound Velocity.

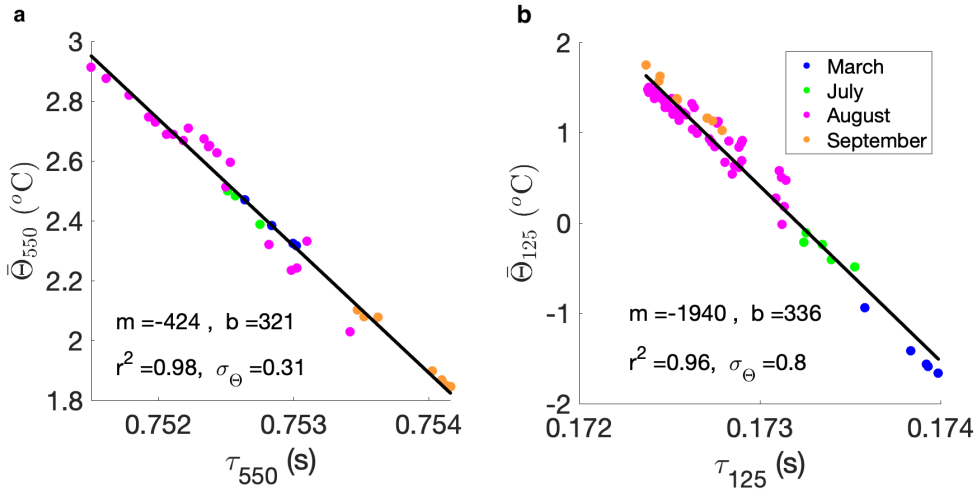

Figure 2.3. a) Travel time calculated from the surface down to 550 m against the average conservative temperature over the same depth range. Colors indicate month. b) Same but down to 125 m.

and XCTD casts were collected during a rare winter survey (March 2010). The temporal coverage, in addition to the spatial variability within the fjord (Fig. 2.1), provides a useful range of property distribution that allows us to test the relationship between travel time and water column temperature. From each CTD/XCTD profile, we derive the sound speed profile (Roquet et al., 2015) and subsequently integrate it to produce τ according to (1). Variations in the calculated travel time are then compared to the integrated heat content, here estimated by the the vertically-averaged conservative temperature ($\overline{\Theta}$) for each cast (Fig. 2.3a and 2.3b). We find that there exists a strong linear relationship between τ and $\overline{\Theta}$ over both 125 m (r^2 = 0.96) and 550 m (r^2 = 0.98).

Since SF, like most glacial fjords, experiences significant salinity gradients both spatially and temporally, we examine the impact of salinity on our interpretation of travel time by estimating how $\overline{\Theta}$ -predicted from τ- would differ if a mean salinity profile was used in place of the observed salinity. We find that τ has an average error of 0.14 milliseconds (ms) if calculated using a mean salinity profile from all CTD casts (hereafter denoted with a subscript μ) in place of the actual salinity profile. Using a linear regression to compare the predicted $\overline{\Theta}$ and $\overline{\Theta}_\mu$ (r^2=0.97, var_Θ=0.1

$°C^2$), we can deduce that salinity variability would introduce an error in $\overline{\Theta}$ of up to 0.06 °C. This value is smaller than the typical seasonal and summer interannual variability in $\overline{\Theta}$ (0.35° C, 0.31°C), but is of similar magnitude to the observed spatial variability within a given summer of 0.07 °C . Therefore we conclude that the impact of salinity of travel time is limited and that the interannual and seasonal travel time variability in SF is largely attributable to variability in temperature.

2.2.3 Interpreting Acoustic Travel Time

Variability in τ is driven by the properties and relative distribution of water masses which influence $\overline{\Theta}$. For example, an increase in τ could be the result of an increased thickness of the cold PW layer, or could be the result of the decrease in temperature within a given layer. With a basic understanding of glacial fjord circulation one can link τ variability with the variability of physically meaningful quantities. Here we summarize basic concepts of fjord circulation and subsequently use them for the interpretation of τ.

Measurements and models have shown that, in the summer, the circulation is driven in large part by the release of subglacial runoff (or subglacial discharge; Straneo et al. 2011; Sciascia et al. 2013a; Carroll et al. 2015; Slater et al. 2018) - atmosphere-driven melting at the surface of the ice-sheet released into the fjord at depth. This injection of fresh, buoyant water drives an upwelling plume that entrains ambient waters including submarine meltwater from the glacier. The resulting circulation is similar to an estuarine exchange flow with an inflowing lower layer of oceanic water and an outflowing upper layer of GMW (Motyka et al., 2003).

In the winter, SF is dominated by a fluctuating baroclinic circulation, called the shelf-driven circulation (Jackson et al., 2014; Harden et al., 2014; Sutherland et al., 2014b; Jackson and Straneo, 2016). This circulation is typically driven by downwelling-favorable along-shore winds, northeasterlies, which depress the pycnocline on the shelf and drive an inflow into the upper-layer of the fjord. Eventually the fjord adjusts, the pycnocline relaxes and the velocity reverses. Since this circulation mode varies the height of the pycnocline, it can produce an identifiable signal in

acoustic travel time.

We use past studies of SF to estimate the impact on travel time that we can expect from the dominant drivers of heat variability: the shelf-driven circulation and the variability of inflowing AW. While the shelf-driven circulation and AW variability can affect heat content through changes in both layer thickness and layer properties, we simulate the shelf-driven circulation through changes to layer thickness only and AW variability through changes to layer temperature only. The shelf-driven circulation is associated with pycnocline fluctuations that are about 50 m (Jackson and Straneo, 2016; Jackson et al., 2018). Using temperature profiles collected from CTDs, we estimate a vertical displacement of the pycnocline by 50 m would produce a change of τ equivalent to 1.4 ms (Sup. Fig. 1). Similarly, we account for the impact of AW temperature variability on τ by decreasing the AW layer temperature in a CTD cast by 0.1 °C - the average standard deviation of temperature on synoptic (4-10 day) timescales. Decreasing the AW temperature by 0.1 °C produces a change in τ of 0.3 ms. On interannual timescales however, the inflowing AW temperature can vary by as much as 1 °C (Straneo et al., 2016). Decreasing the AW temperature by 1 °C produces a change in τ of 1.6 ms which is roughly equivalent to the impact of pycnocline fluctuations. Therefore, inflowing AW variability produces a variability in τ comparable to the shelf-driven circulation over much longer timescales.

2.3 Data and Processing

The PIES measures τ by releasing a 12 kHz acoustic ping and recording the echo from the sea surface. It sends a burst of 4 pings every 10 minutes and records the first 4 echoes from each burst for a total of 24 echoes an hour. To prevent nearby reflectors from dominating the signal, for example overlying floats, the PIES incorporates a ”lockout time” and only listens for returns after a set amount of time has elapsed. The ”lockout time” however, does not guarantee that the remaining echoes are from the surface. Other strong reflectors such as icebergs, sediments, and small organisms (e.g., Watts et al. 2006) can also lead to an early echo.

When icebergs pass over a PIES field of "vision", they affect the travel time magnitude enabling an estimation of iceberg draft and speed (Andres et al., 2015; FitzMaurice et al., 2016). Additionally, the presence of sea ice can act as a rigid cap and reduce observed travel time variability (Andres et al. (2015), Sup. Fig. 4) Here, we filter out the ice-influenced signals and instead focus on times when the echo is from the sea surface and the travel time is informative of ocean heat content. Therefore, the first step in PIES processing is to remove those echoes that are from reflectors within the water column. In this case, we chose to remove echoes that were 0.007 s (approximately 10 m) less than the median travel time, $\tau = 1.1628$s (Sup. Fig. 3.) This cutoff value is generous enough to ensure that all potential surface data are retained while also removing those echoes that are obviously not from the sea surface. Among the discarded echoes are those used by Andres et al. (2015) to track icebergs.

After the initial filtering of the PIES returns, the remaining pings (n ¡ 24) are averaged to produce a single hourly travel time (τ_{hr}). In traditional PIES environments, sea surface scatter is the dominant source of noise, and the remaining pings produce an hourly distribution that is skewed towards late returns (Li et al., 2009). In general, if a distribution is positively (negatively) skewed it has a tail extending to the right (left) of the distribution. Under conventional PIES processing, the quartile method is used to generate an appropriate average of τ_{hr} (Kennelly et al., 2007). In the quartile method, pings are sorted by τ and the average of the first $n/6$ values past the first quartile are used to determine τ_{hr}. For example, if all pings made it past the first filter, then $n = 24$ and the average of the sixth through ninth quickest return echoes would determine τ_{hr}.

We found that in a glacial fjord, the return distribution of echoes was not consistently skewed. The presence of sea ice and smaller icebergs can influence the return signal and produce a bias towards early echoes (left skewed) rather than the late echoes typically seen in the open, ice-free ocean. Therefore, we modified the traditional quartile method to account for potential early echoes. First the skewness, or third-central moment, of the hourly distribution was calculated. If the skewness of the hourly distribution was greater than 0.5, the original quartile

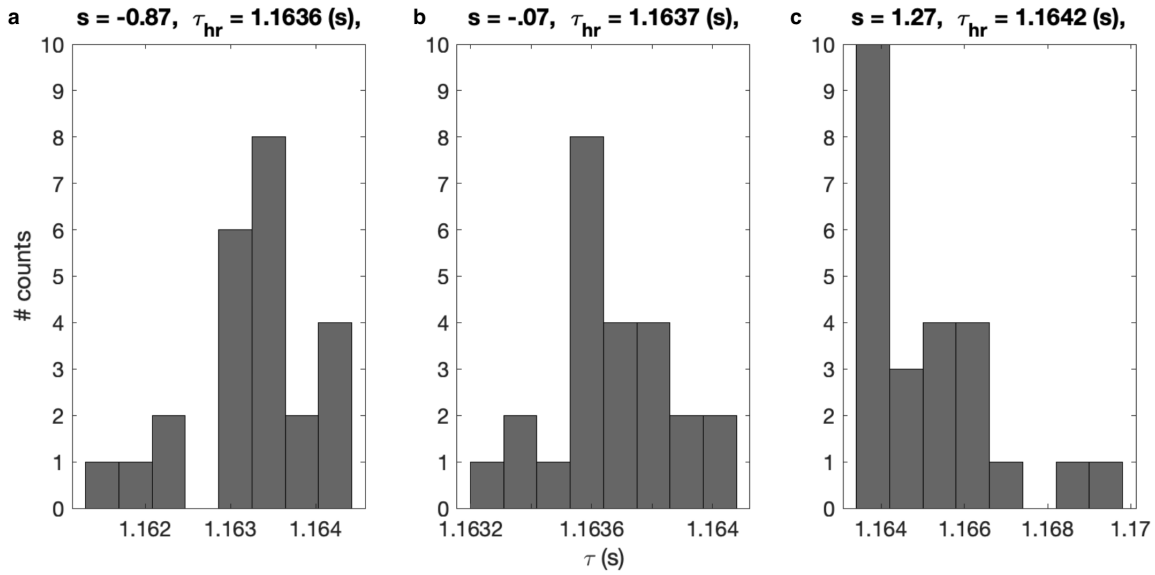

Figure 2.4. Examples of the distribution of acoustic echoes received in an hour with the skewness (s) and averaged τ_{hr}. a) A negatively skewed hourly distribution. b) A weakly skewed hourly distribution. c) A positively skewed hourly distribution (typical of the open ocean).

method was used (Fig. 2.4c). If the skewness was between -0.5 and 0.5, then the average of the $n/6$ values surrounding the median were used to determine τ_{hr} (Fig. 2.4b). If the skewness was less than -0.5, the average of the first $n/6$ values prior to the third quartile value was used to determine τ_{hr} (Fig. 2.4a).To ensure a large enough sample size to compute the skewness, hourly distributions with $n < 16$ were discarded. Roughly 20% of the τ_{hr} were removed because they did not meet this criterion. Gaps in the time series were filled through linear interpolation. Any large spikes in the data, such as those greater than 3 standard deviations from their nearest neighbor, were removed. Lastly, the tidal fluctuations from the τ_{hr} signal were removed using harmonic analysis (Pawlowicz et al., 2002). A flow-chart of the method for processing the PIES is given in Figure 2.5.

The PIES also includes a pressure sensor which can be used to identify changes in the path length of the acoustic ping. After removing the atmospheric pressure (10.1325 dbar), the pressure record shows a mean bottom pressure of 862.55 dbar and tidal amplitudes of ±1.8 m during spring tides and ±0.5 m during neap tides (Andres et al., 2015). While the induced tidal

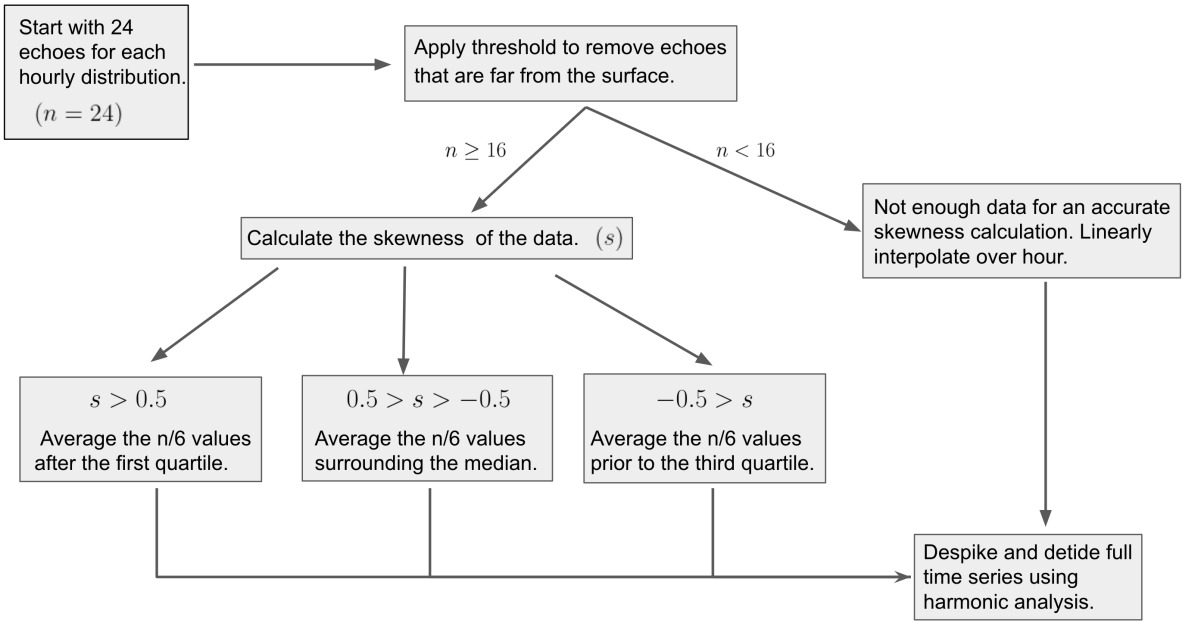

Figure 2.5. A flow-chart of the methodology used to process the PIES hourly return echoes.

velocities in the fjord are weak, the tides still contribute significant enough change in the water column depth to be seen in the travel time record due to their effect on the path length traveled by the acoustic pings. The pressure record was detided, and the residual pressure variations had an effect on travel time of about 10^{-4} s, an order of magnitude smaller than changes due to the water column heat content. Additional changes to the path length can occur through internal waves which have a small expression in the sea surface, but these have a comparatively small effect and can be smoothed though low-pass filtering (Li et al., 2009). The pressure record is used here to get an accurate reading of the depth of the PIES and estimate the magnitude of travel time variations associated with tides but is not used otherwise.

The PIES was deployed alongside a mooring (M1, Fig. 2.1) equipped with CTDs and thermistors so that the travel time calculated from the directly measured hydrographic properties using the sound speed equation of Del Grosso (1974) could be compared with the PIES-measured acoustic travel time (Table 2.2, also Jackson et al. 2014; Jackson and Straneo 2016). The surface-most instrument on M1 was set to 246 m to limit damage from icebergs. A second set

of shallower moorings (M2) was deployed in an embayment on the eastern side of the fjord with CTDs at 125 m and 261 m. Like Jackson and Straneo (2016), we assume the cross-fjord differences between M1 and M2 are small and treat the moorings as if they are in the same location. This assumption is supported by CTD surveys which reveal small lateral variability in water properties compared to the depth and time variability documented by the moorings. Additionally, comparisons of CTDs deployed around 250 m display a small difference (~0.3 °C) compared to the instrument's overall temporal variability (0-5 °C). At 852 m depth, a CTD was mounted externally on the PIES and agreed with a calibrated PIES internal temperature sensor to within 0.01 °C (Meinen et al., 2020). All vertical gaps in the mooring data were filled with linear interpolation. However, due to bio-fouling the conductivity data at the bottom were unusable and salinity was extrapolated to the seabed using conductivity measured at 657 m and the salinity gradient from deep CTD casts. Lastly, the mooring M1 was equipped with an upward-facing Acoustic Doppler Current Profiler (ADCP; Table 2.2) that was analyzed in Jackson et al. (2014) and is used in this paper to provide a reference velocity (Section 4.b).

2.4 Results

2.4.1 Estimating the thickness and temperature of inflowing AW in the winter

Here we develop a model that relates variations in τ to simultaneous variations in the depth of the pycnocline, building on the results of Jackson and Straneo (2016) who showed that the fjord can be described as a two-layer system in the winter and that pycnocline displacement dominates the heat content variability within the fjord. A two-layer model is appropriate for SF in the winter because submarine melt is reduced and the PW and AW layers each remain weakly stratified. Additionally, since only two water masses dominate the fjord, the thermocline is at approximately the same depth as the halocline and the average temperature of the fjord can be estimated solely by knowing the depth of the pycnocline (Jackson and Straneo, 2016).

Table 2.2. Details of Mooring Instrument setup. Platform location is specified in the map on Figure 2.

Platform	Instrument	Measurement	Sampling Period (min)	Depth (m)
M1	RBR XR-420 CTD	conductivity, temperature, pressure	30,30,15	246,657
	SBE37 MicroCAT CTD	conductivity, temperature, pressure	7.5	396, 541
	Onset HOBO Tidbit v2	temperature	30	276, 296, 316 336,356
	75kHz RDI Teledyne Workhorse Long-Ranger ADCP	velocity	120	396-30 (10 m bins)
M2	SBE37 MicroCAT CTD	conductivity, temperature, pressure	7.5	125,261
P1	Pressure Inverted Echo Sounder	acoustic travel time, temperature, pressure	60, 7.5, 7.5	852
	SBE37 MicroCAT CTD	conductivity, temperature, pressure	7.5, 7.5, 7.5	852

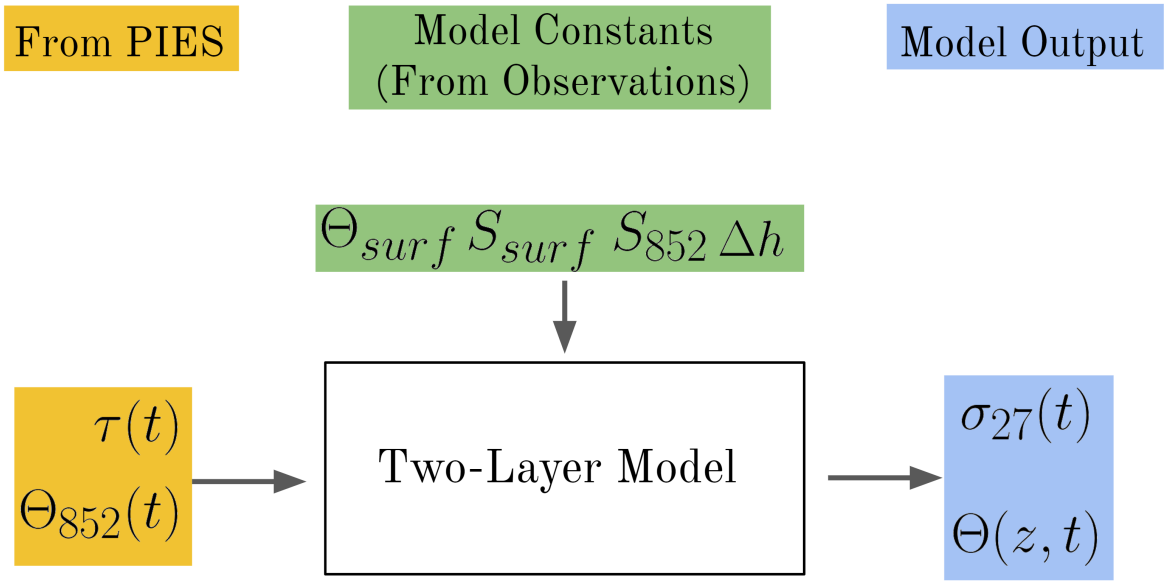

Figure 2.6. Schematic showing how the PIES travel time data can be used to determine the temperature and thickness of the inflowing AW. The model takes as its input from the PIES: travel time (τ) and bottom temperature (Θ_{bot}). It gives as output the depth of the pycnocline (z_{pyc}) and estimated two-layer temperature (Θ_{2LM}). The model is tuned to Sermilik Fjord using constants derived from the XCTD observations: surface temperature (Θ_{surf}), surface salinity (S_{surf}), bottom salinity (S_{bot}) and pycnocline thickness (Δh) and is detailed in Appendix A. The depth of the pycnocline is the depth of σ_{27}.

Details of the two-layer model (2LM) are given in the appendix (Appendix A), but in short, the model assumes a two-layer structure for temperature and salinity and shifts the pycnocline depth to match the observed τ. The model takes as its input travel time $\tau(t)$ and bottom temperature $\Theta_{bot}(t)$ and gives as its output the vertical structure of temperature $\Theta_{2LM}(z,t)$ and pycnocline depth $z_{pyc}(t)$ (Fig. 2.6).

A comparison of the model and mooring observation record is given in Figure 2.7 and visually the two appear similar during the time period (winter) when we expect the two-layer model to be valid. During this window, the root-mean square deviation (RMSD) between temperature measurements at 550 m and 852 m is 0.21 ° C, compared to the overall standard deviations of 0.48 ° C and 0.41 ° C, respectively, showing that the typical vertical temperature

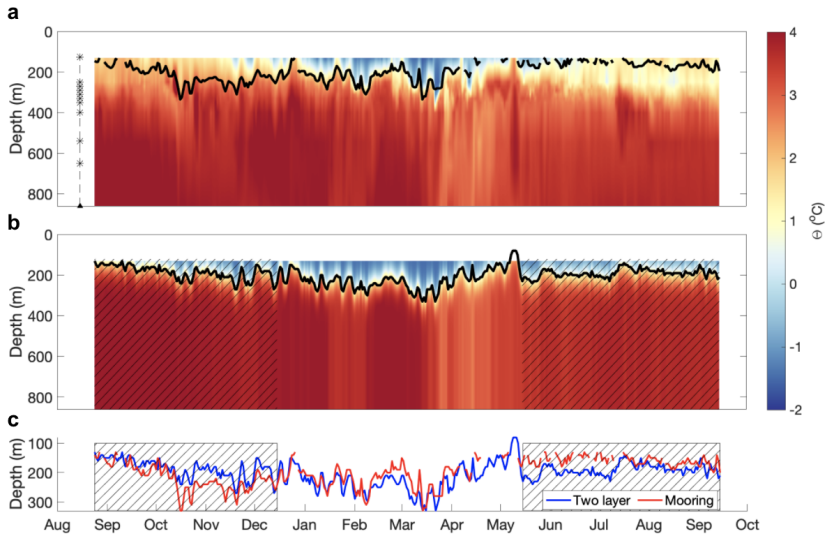

Figure 2.7. a) Conservative Temperature vs Depth from mooring data (Aug 2011 to Oct 2012) with the location of the instruments noted and the isopycnal σ_{27} = 1027 kg m^{-3} shown in black. Note the shallowest instrument is located at 125 m. The tick marks on the horizontal axes of this and all subsequent time series denote the beginning of the month. b) Conservative Temperature vs Depth (m) created from the two-layer model of the fjord. Areas outside of the winter months are hatched and the visualization is limited to 125 m for easy comparison with the moored data. c) Comparison of pycnocline depth represented by the isopycnal σ_{27} as derived from observations and from the model. Note that the mooring record is limited to 125 m, so it is impossible for it to capture the shallowest excursions of the pycnocline such as the peak in May.

difference is smaller than the variability. Therefore, in this fjord which lacks a shallow sill, we can use a bottom temperature sensor as a proxy for the temperature of the whole inflowing layer.

Quantitatively, we define the 2LM to be valid if it can predict the core AW temperature, the pycnocline depth and the ocean heat content within a level of error less than the observed variability. Here we define error as being the RMSD between the observed and 2LM estimated variable. We first consider the core AW temperature, which we define as the mean AW temperature between 450-650 m, we find that the 2LM estimate is correlated with observed core from the mooring AW temperature (r^2 = 0.68, var_{AW} = 0.14 °C^2) with an error of 0.27 °C compared to the observed standard deviation of 0.37 °C. The correlation is improved by smoothing the data to monthly (>30 day) timescales through the use of a low-pass filter. On monthly timescales, we find a strong correlation (r^2 = 0.78, var_{AW} =0.13 °C^2) and the error is reduced to 0.23 °C

which is smaller than both the observed monthly standard deviation of 0.36 °C and previously published estimates of the AW interannual variability of 1 °C (Straneo et al., 2016). Thus, the 2LM is successfully able to estimate the temperature of the core of the inflowing AW to within about 20% of the observed interannual variability.

In addition to AW temperature, the 2LM predicts the depth of the pycnocline. The pycnocline, defined here as the isopycnal σ = 1027 kg m^{-3} is shown in black in the top panels of Fig. 2.7 and roughly tracks the interface between cold and warm waters in both the model and observations. This pycnocline is further examined in Figure 2.7c, which compares the pycnocline depth from the mooring and the 2LM over the entire PIES record. The 2LM pycnocline is at a similar depth as the mooring pycnocline (r^2 = 0.61,var$_{pyc}$= 1680 m^2) and only diverges in the spring when the stratification starts to reflect the arrival of GMW. The error between the 2LM pycnocline and the mooring pycnocline during the winter is 34 m which is smaller than the observed pycnocline standard deviation of 41 m. On monthly timescales, the 2LM estimate is improved (r^2 =0.77, var$_{pyc}$ = 978 m^2) and the error is reduced to 25 m which is substantially smaller than both the observed monthly standard deviation of 35.5 m and the seasonal pycnocline depth range of about 200 m.

We can take the τ-derived 2LM output (temperature and pycnocline depth) to calculate the ocean heat content (OHC) of the AW layer. OHC is calculated with

$$\mathrm{OHC_{AW}} = \rho c_p \int_{852}^{z_{pyc}} \Theta - \Theta_0 \, \mathrm{dz}, \tag{2.2}$$

where ρ is density, c_p is the specific heat capacity, Θ_0 is the reference temperature, 852 is the depth of the PIES and z_{pyc} is the depth of the pycnocline. We set $\Theta_0 = -2.6$ °C, the freezing point of seawater for an absolute salinity of 35 g kg^{-1}. OHC, a function of both temperature and thickness, provides an estimate of the energy available for melting and is a variable that can be used to link heat from the North Atlantic with glacial retreat. OHC derived using τ and the 2LM is shown alongside the mooring-based calculation in Figure 2.8. The OHC calculated from the

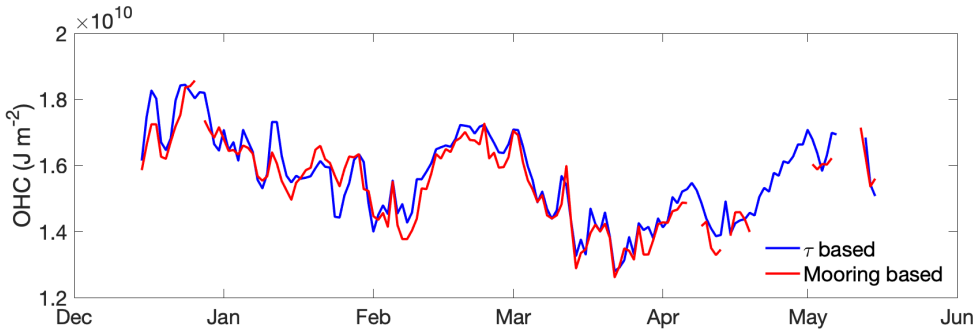

Figure 2.8. OHC content of the AW layer, defined here as from 852 m to z_{pyc}, calculated from both the mooring data and τ.

moorings and 2LM are highly correlated (r^2 = 0.82, var_{OHC} = 1.7×10^{14} J^2 m^{-4}), and we find the 2LM can predict OHC (approximately 1.54×10^{10} J m^{-2}) with an error of 3% which is smaller than the observed standard deviation of 8% and seasonal range of 34%. The success of the 2LM in estimating OHC - a combination of pycnocline depth and AW temperature - demonstrates that the PIES can provide sufficiently accurate (on monthly timescales) long-term monitoring of fjord heat content during the winter, a time of year that is both challenging and expensive to collect *in situ* measurements.

2.4.2 Monitoring the shelf-driven circulation

The shelf-driven circulation in SF is responsible for rapidly transporting heat from the shelf towards the glacier and is the dominant mode of circulation outside of the summer (Straneo et al., 2010; Jackson and Straneo, 2016; Fraser and Inall, 2018). Monitoring of the circulation requires having temperature, salinity and depth recorders in place to track the movement of the pycnocline induced by shelf-fjord exchange. However, as shown with the two-layer model, the position of the pycnocline is associated with a variability in travel time. In this section we examine the PIES's ability to monitor the synoptic variability of heat content associated with the shelf-driven circulation (Harden et al., 2014; Jackson et al., 2014).

First, we demonstrate that the PIES can observe a series of shelf-driven exchange events using those identified in Jackson et al. (2014). That study used this moored data including

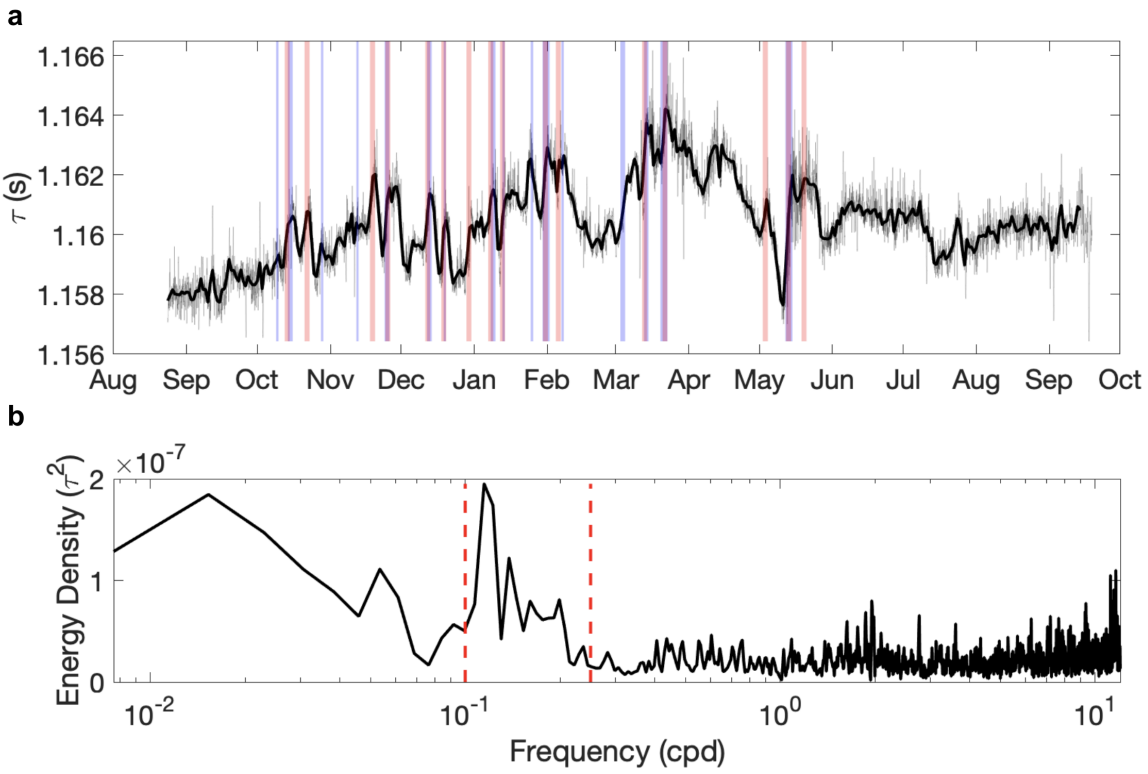

Figure 2.9. a) Travel time record from the PIES with the 16 largest shelf-driven exchange events from Jackson et al. (2014) overlaid in blue. The shelf-driven exchange events defined using τ are overlain in red (see text for detail), with overlapping events in purple. b) Variance Preserving Power Spectrum of the Acoustic Travel Time Time series in (a) with frequency given in cycles per day (cpd) and the 4 to 10 day period represented by the red-dashed lines.

velocity data (M1/M2 Table 2.2) to identify the 16 strongest shelf-driven pulses through peaks in upper-layer volume flux. The upper layer was defined as being above the isopycnal σ_{27} = 1027 kg m^{-3}. An overlay of the upper-layer flux events are shown plotted on top of the travel-time record in blue and purple (Fig. 2.9a). The events coincide with sharp increases in travel time, and indicate that the shelf-fjord exchange is recorded by the PIES. This hypothesis is further supported by a power spectrum of τ (Fig. 2.9b) which shows the dominant variability in travel time occurs on the timescales of the shelf-driven circulation (4-10 days).

We define the PIES's ability to monitor the shelf-driven circulation a success if through the use of τ it can predict maximum pycnocline height and peak velocity with a prediction error and uncertainty less than the observed uncertainty. Uncertainty is defined here as the standard

error. Significant variability exists from event to event and so we produce composites of all the events to reduce the error in the analysis. However, the RMSD calculated from all the individual events is also presented.

We start with two time series: τ_{hr} and depth of the pycnocline calculated from the moored record (z_{pyc}). The time series are band-pass filtered to keep signals between 26 hours and 30 days. This filtered version of τ_{hr} we define as τ_f. Composites are generated by averaging around the peak volume flux events identified from Jackson et. al 2014 (Fig. 2.9a, blue and purple). At the peak volume flux, the composite has increased about 1.5 ms from 50 hours earlier, equivalent to a depth change of about 50 m (Fig. 2.10). The increase in τ_f is due to a thickening of the PW layer as the pulse moves into the fjord. The thicker PW layer results in a colder average temperature and a slower travel time. Around 4 days after the event, τ_f returns to normal, but the events often follow one another resulting in a forcing frequency between 4-10 days. After fitting a linear regression between τ_f and z_{pyc} (not shown), we can estimate the magnitude of the pycnocline fluctuation from τ_f (dashed line, Fig. 2.10). The predicted maximum pycnocline height has a prediction error of 3.9 ± 6 m which is smaller than the composite z_{pyc} uncertainty of 8 m (Fig. 2.10 red shading). Examining the shape of the composite, there is a notable lag of about 34 hrs between the second peak in τ_f and the peak volume flux (t=0). We find the second peak is anti-correlated with pycnocline temperature (r^2 = 0.6, $var_{pyc-\Theta}$ = 0.02 °C^2, Sup. Fig. 5) and is potentially linked to the arrival of new waters from the shelf. However, we do not find a consistent phasing for this second peak and it has a large standard deviation of 17 hrs. We conclude that τ_f has a broader peak in response to shelf-forcing than pycnocline depth because it is responding to both changes in layer thickness and water properties. Next we evaluate the relationship between z_{pyc} and the pycnocline height predicted by τ_f for the individual events. The RMSD calculated from the individual events is 28 m which is substantially higher than the composite error but is comparable to the observed standard deviation of maximum pycnocline amplitude of 31 m. This mismatch highlights the ability of the composite to provide a clearer picture of the relationship between τ_f and z_{pyc}. In short, τ can be used to estimate the average

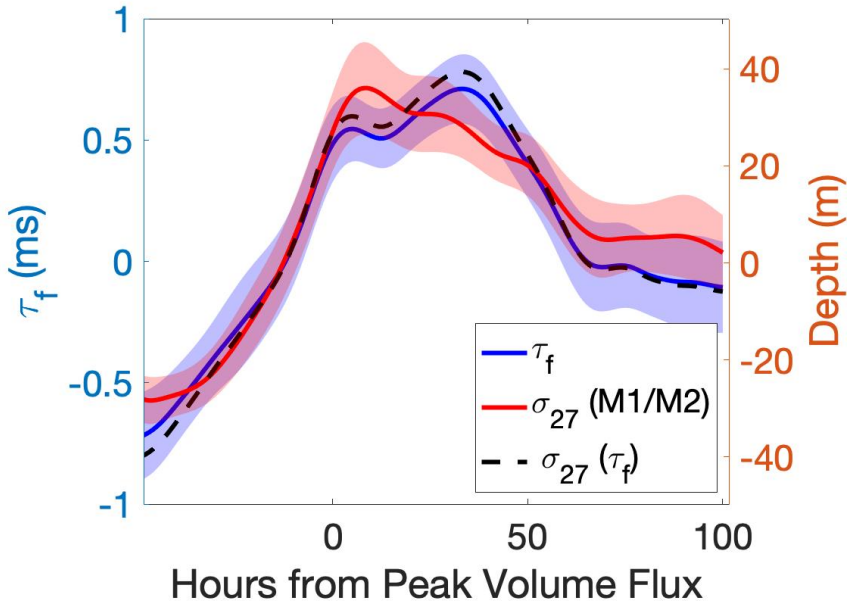

Figure 2.10. Composites of τ_f (blue, left axis), isopycnal σ_{27} (red solid, right axis), and isopycnal σ_{27} predicted from τ_f (dashed, right axis) centered around peak volume flux (Figure 9a blue shading). Note that isopycnal depth is flipped upside down so that it can be easily compared with travel time. All composites are of data that have been 26-hr low-pass filtered with the 30 day low-pass filter background removed. The uncertainty is the standard error of the composite.

magnitude of pycnocline fluctuations associated with the shelf-driven exchange with a error of 50% of the observed standard error.

Knowing the magnitude of the pycnocline fluctuations, we can also make an estimate of the shelf-induced velocity within the fjord. Recent work has shown that the pulses associated with the shelf-driven circulation can be described as a combination of standing and Kelvin waves (Jackson et al., 2018). Specifically, the average velocity of the upper layer of the fjord can be estimated from Equation 29 of Jackson et al. (2018), with details of the calculation provided in Appendix C. Using the estimated pycnocline depth from the PIES, the equation predicts a peak velocity and standard error of 0.41 ± 0.03 m s^{-1}. For comparison, the recorded peak velocity from an ADCP in the upper layer is 0.43 ± 0.05 m s^{-1}. However, the RMSD of predicting the peak velocity from individual events is 0.22 m s^{-1} which is slightly larger than the observed standard deviation of peak velocity of 0.18 m s^{-1}.Therefore the PIES appear better suited to

monitor the average peak velocity from shelf-driven events rather the velocity of individual events.

We can combine the composite approach with the 2LM to estimate the average heat flux associated with the shelf-driven circulation. First we calculate the upper-layer OHC using the 2LM output and a modified form of Equation 2 and then subtract a low-pass (30 day) background signal - the same approach used to generate the τ_f composites. After averaging across the 10 shelf-driven events that occurred between Dec-May and multiplying by fjord width (7.5 km) and predicted average peak velocity (0.41 ± 0.03 m s^{-1}), we calculate an average heat flux of $7.0 \pm 1.8 \times 10^{11}$ W for each shelf-driven exchange. The uncertainty in the heat flux estimate includes both the standard error and the propagated uncertainties from the peak velocity and OHC estimates. To put this heat flux into context, Jackson et al. 2016 calculated a heat budget of Sermilik Fjord and estimated that the average winter heat flux associated with the storage term was $0.3 \pm 7.5 \times 10^{10}$ W. Therefore the shelf-driven events potentially bring a heat flux an order of magnitude higher than the background storage rate and can substantially increase the heat content of the fjord.

We have demonstrated that the shelf-driven circulation excites a response in travel time that can be measured and used by the PIES. Through the use of composites the variability in the τ_f signal can be reduced and sufficiently accurate predictions can be made of average maximum pycnocline amplitude and average peak velocity. However, for effective long-term monitoring the PIES needs to be able to demonstrate the ability to measure these events without the use of an ADCP. Therefore we develop our own criteria for finding shelf-exchange events and define events as a peak in τ_f that is greater than 0.95 ms. The events identified through τ_f are plotted alongside the Jackson et al. 2014 events in red, with events identified by both criteria in purple. Our definition of events coincide for the majority of pulses and primarily mismatches when the peak volume flux is not associated with a large pycnocline fluctuation and thus a peak in τ_f (Fig. 2.9a, blue). These new events can be averaged to produce a composite of τ_f that is centered on 34 hrs prior to the peak in τ_f to account for the previously discussed phase shift between τ_f and

peak volume flux. A new estimate of maximum pycnocline amplitude derived from peaks in τ_f had a composite prediction error of 3.7 ± 5.6 m which is similar to the error 3.9 ± 6 m which was found using the actual shelf-driven exchange events. The precision of detection could likely be improved by correlating along-shore wind stress with peaks in tau (Jackson et al. 2014), but our demonstration was focused on what monitoring could achieve with the use of a PIES alone. We conclude that through appropriate averaging a PIES achieves our criteria for successfully monitoring the frequency, magnitude and peak velocity of shelf-driven exchange events.

2.4.3 Measuring the heat content of the top layer

Converting τ to τ_{top}

Moored instruments in glacial fjords often have a limited vertical range because of the potential damage from icebergs. For example, in this mooring data set, the shallowest CTD was deployed at 125 m which is below the bulk of outflowing GMW (Beaird et al., 2018). Here, we show how PIES can be utilized, in combination with subsurface moorings, to measure the portion of water column that cannot be sampled by moored instrumentation. We define this unsampled region, which spans 0 -125 m, as the top layer, and it should not be confused with the area above the pycnocline which was referred to earlier as the upper layer.

Given a subsurface property record from a mooring and a full-depth τ record, we combine these to derive the travel time of the top layer. In this case

$$\tau_{top} = \tau - \tau_{Mooring}, \tag{2.3}$$

where τ_{top} is the travel time from 0-125 m, τ is the PIES recorded travel time (0-852 m), and $\tau_{Mooring}$ is the travel time calculated from sound speed (1) using the moored instruments (125-852 m).

As a check that the residual τ_{top} is within expected values, τ_{top} was compared against travel times of the upper 125 m calculated from CTDs. The mean 125 m travel time calculated

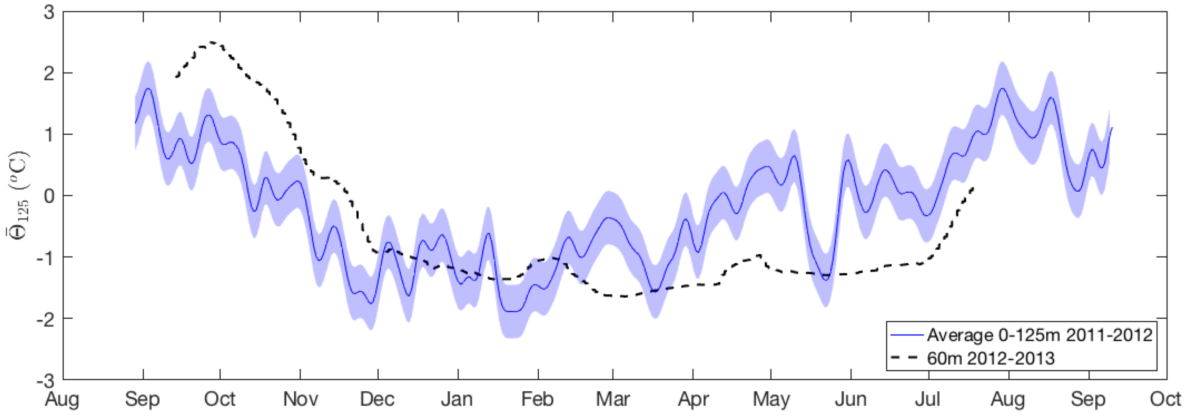

Figure 2.11. The average temperature of the upper 125 m, generated from a residual travel time with a 10-day low-pass filter and uncertainty given in lighter shading. The large drop in May is one of the events identified in Figure 9 and is due to a piteraq. For comparison, the dashed line is conservative temperature recorded at 60 m from September 2012 to August 2013 (see Jackson and Straneo 2016)

for the summer (1 July through 30 September) was $\tau_{topS} = 0.1727 \pm 0.0004$ s and for the winter (1 January through 1 April) was $\tau_{topW} = 0.1738 \pm 0.0005$ s. The average travel time calculated from the CTDs over these time periods was $\tau_{CTDS} = 0.1727 \pm 0.0003$ s for the summer and $\tau_{CTDW} = 0.1739 \pm 0.0002$ s for the winter. Given an uncertainty estimate of 0.0004s (Appendix B), this supports that the residual τ_{top} is a valid representation of the travel time of the upper 125 m.

Since travel time and mean temperature are proportional (Section 2), we can use the relationship

$$\overline{\Theta}_{top} = A\tau_{top} + B, \tag{2.4}$$

to calculate the mean temperature of the upper 125m ($\overline{\Theta}_{top}$) where the constants A and B are determined from a linear fit of hydrography (Fig. 2.3b). The average temperature of the upper 125 m generated with τ_{top} is shown in Figure 2.11. The linear fit occasionally produced values below freezing. Therefore, we cap the average temperature at the freezing point, $T_f = -1.9$ °C, calculated using a pressure of 125 dbar and an absolute salinity of 33.1 g/kg.

The time series was smoothed using a 10-day low-pass filter and shows the general

progression of the average temperature from warmer in the summer to colder in the winter. Starting in late March, the time series shows a general warming trend, which based on pycnocline depth (Figure 2.7), is associated with a thickening of the AW layer. While there is no contemporaneous temperature data available to compare against the residual calculation, a CTD recorded temperature at 60 m from September 2012 to August 2013 (see Jackson and Straneo 2016). The 30-day low-pass filtered 60 m conservative temperature is shown compared to the 125 m average temperature in Figure 2.11. While there are obvious differences between the two signals arising from interannual variability and the fact that the τ-based signal is an average temperature over 125 m while the observed signal is the temperature at just 60 m, they exhibit a comparable magnitude (4 °C) and both show falling temperatures from Oct-Dec and rising temperatures in July. While this comparison cannot be used to validate the τ_{125} approach it is reassuring that the seasonal signals are qualitatively similar.

Identification of extreme temperature events

Katabatic winds, or piteraqs, are common in southeast Greenland and are capable of influencing fjord properties and inducing an exchange flow similar to along-shore winds (Oltmanns et al., 2015; Spall et al., 2017). However, the influence of piteraqs on fjord properties is still poorly understood because the effects are primarily felt in the surface layer of the fjord. The strong down-fjord winds depress the pycnocline and therefore are associated with a signal in τ. Here we demonstrate that with the PIES remotely measuring the top-layer heat content, we can observe the impact of extreme events, such as piteraqs, on fjord temperatures.

A piteraq occurred in SF in May 2012, and is associated with a large temperature drop in $\overline{\Theta}_{top}$ (Fig. 2.11) and a shelf-driven exchange event in the τ record (Fig. 2.9). Focusing in on the event which appears to start on May 9th, the average temperature of the upper 125 m drops by nearly 2 degrees to hover around the freezing point (Fig. 2.12a). Satellite imagery from NASA MODIS shows the fjord initially with low ice cover (Fig. 2.12b), then abruptly covered with sea ice (Fig. 2.12c-e), then the ice flushed out of the fjord (Fig. 2.12f). We are confident the signal is

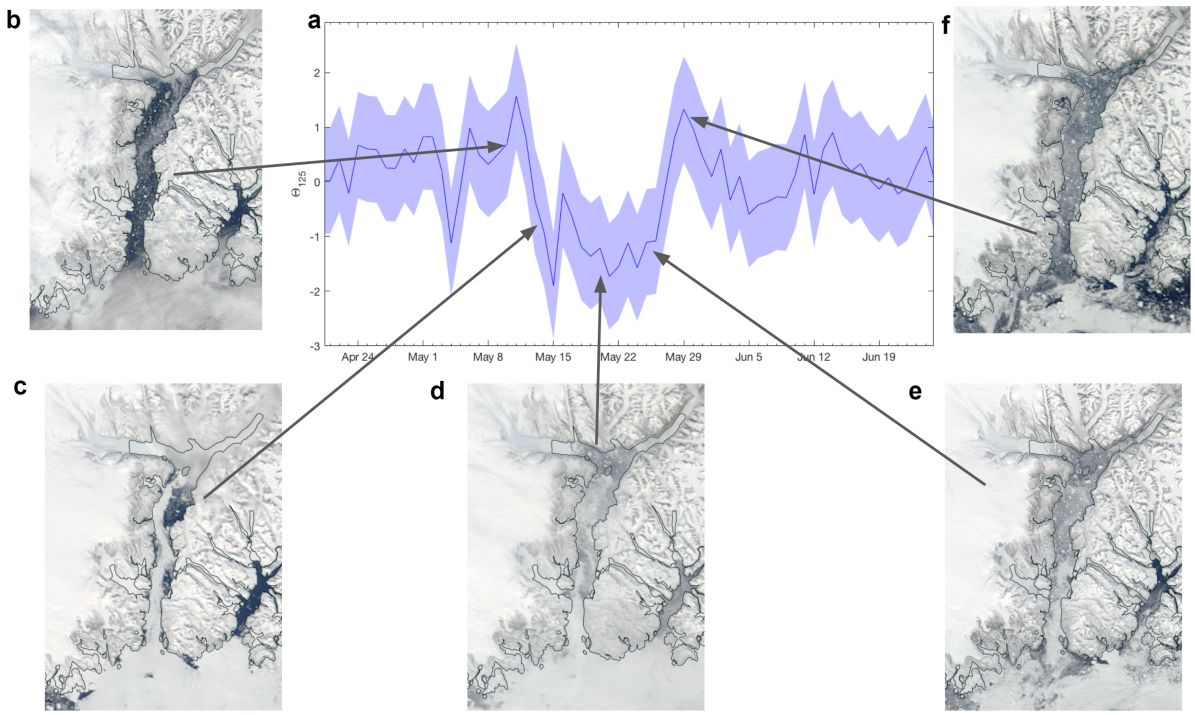

Figure 2.12. a) Zoom in on the piteraq event and the corresponding drop in average temperature in the upper 125 m of the fjord. b-f) MODIS images showing the sea ice coverage of the fjord from the days of May 10,13,20,26,29 2012.

a result of changing temperature rather than contamination by sea ice because ice influence would result in a shorter observed travel time and therefore an increase in temperature. However, further investigation of the piteraq is outside the scope of this paper and a PIES-based piteraq analysis would also need to incorporate local wind data to differentiate shelf-driven events from piteraqs.

2.5 Discussion

2.5.1 Estimating the thickness of AW in the summer

The two-layer model demonstrates that with background knowledge of fjord stratification, travel time can be used to effectively monitor the thickness and properties of inflowing AW in the winter. However, estimating the thickness of the AW layer in the summer is significantly more difficult due to the release of subglacial runoff and the formation of GMW. GMW is composed primarily (88%, Beaird et al. 2018) of entrained and upwelled AW, and appears as a warm, salty

intrusion in the upper-layer of the fjord. Therefore the total-water column heat content is a function of both the thickness of the AW layer and the GMW concentration in the summer.

A simple model to predict the vertical temperature structure in the summer has proved elusive. As the GMW reaches its neutral buoyancy it can mix and increase fjord stratification breaking down the two-layer system. The neutral buoyancy depth of GMW is a function of subglacial runoff flux, fjord stratification and AW temperature (Carroll et al., 2016; Slater et al., 2016; De Andrés et al., 2020), making prediction from τ alone with the present data nearly impossible. Future work with PIES and the development of theory will be necessary before τ can measure both the extent of thermal forcing in the summer and the export of GMW. For now, these competing signals limit the PIES to measuring only the bottom temperature during the summer.

2.5.2 Determining the bounds for the two-layer model

We believe that the two-layer stratification breaks down with the arrival of significant amounts of subglacial discharge in the summer and this can be observed in Figure 11 as the temperature rises in July. However, the transition between summer and winter and how long GMW resides in the fjord in the fall is an open question and the topic of current research. With travel time alone, it is difficult to distinguish if warm water observed in the fall is a remnant of GMW or a seasonal intrusion of warm water originating from the shelf. However, the few CTD casts collected in winter (March) near the location of the PIES show only a weak signal of melting indicating that fjord properties are likely being more influenced by the shelf stratification than the glacier at this time of year. Additionally, the shelf-driven baroclinic circulation is clearly active by October (Jackson and Straneo, 2016) enabling rapid communication between the shelf and the fjord and potentially aiding in the flushing of GMW out of the fjord. Jackson et al. (2014) found that the average volume exchanged with each shelf-driven event was equivalent to 50% of the total upper-layer volume. Therefore, it might be that case that the fjord becomes "two-layer" when the adjacent shelf is two-layer rather than when all the GMW has been removed from the fjord. For the purposes of monitoring the heat content of fjords we have chosen to define the

winter when the two-layer model is successful (December through May) and emphasize the usefulness in the overlapping of PIES and moored data for over a year so that this window can be determined for each individual fjord system.

2.5.3 Deployment Considerations

A PIES can be deployed in glacial fjords that get covered in sea ice. While sea ice results in a reduced variability of travel time pings due to the reduction of sea surface scatter (see Andres et al. 2015) we can still extract a coherent travel time signal in the presence of sea ice since it is a strong reflector at the sea surface. For example, SF was covered in landfast ice for about two weeks from February 26, 2012 to March 10 2012, but we do not have a gap in our travel time series. Our method of averaging hourly travel time is designed specifically to account for the potential changes to travel time due to the presence of sea ice. Sea ice with a thickness of 1 m would potentially decrease travel time by .7 ms (comparable to a thermocline shift of 27 m), but this effect is offset by the cooling of ocean temperatures during sea ice formation (Sup. Fig. 4).

Careful consideration should be given to the location of PIES deployment within glacial fjords. A significant challenge of operating a PIES around ice is extracting signal from areas with semi-continuous iceberg coverage as the majority of pings will be off of icebergs rather than the surface. Specifically, we think that regions that have a high concentration of ice coverage with heterogeneous and deep drafts (deeper than several meters), such as a near-terminus melange, can prevent the PIES from recording a surface measurement. While this might be addressed by limiting the PIES listening range (the "lockout time") to the expected travel time of echoes coming from the surface, it is possible that the echoes would never come in a large enough signal to detect. In SF, we found this to be the case for a PIES deployed about 30 km from the terminus. However, the PIES located around 70 km from the terminus had enough pings bounce off of the surface to produce a reliable travel time signal.

The PIES's effectiveness is also influenced by the choice of lockout time. In our second campaign of data collection we shortened the lockout time to be able to record more information

about the depth of icebergs passing over the PIES. While this change improved the suitability of the record for iceberg detection, it limited the number of echo returns recorded from the sea surface since only the earliest echoes are recorded and we were not able to interpret the surface travel time signal. Thus, there are clear trade-offs when deciding between using the PIES to monitor icebergs or fjord heat variability.

When deploying the PIES in a glacial fjord, it is recommended that for the first year the PIES is deployed alongside a traditional mooring. The PIES can be utilized best when the basic dynamics of the studied fjord are understood and having a mooring present will enable an interpretation of temperature variability on τ. The PIES can then be used for long-term (5 years) monitoring of the fjord and prediction of heat content based on empirical relationships calculated from the first-year data.

2.5.4 Applicability to other glacial fjords

We have presented a case study on the use of acoustic travel time for a single glacial fjord, but the results and techniques are also applicable to some of Greenland's other fjords. While varying in size, Greenland's fjords share common features such as the presence of PW and AW, and a buoyancy-driven circulation in the summer (e.g. Mortensen et al. 2014; Gladish et al. 2014b; Lindeman et al. 2020). Consequently, in the winter when melt rates are low, the fjords are likely to match the stratification on the shelf with cold PW overlaying warm AW (Straneo et al., 2012). Thus, the two-layer model is likely applicable to other fjord systems and could be changed to solve for parameters such as pycnocline thickness or upper-layer temperature. Even the failure of the model can provide insight into the dynamics and stratification of the fjord as it does in the case of SF in the summer. PIES would not be appropriate for glacial fjords that produce continuous melange that extends out to the fjord mouth such as Ilulissat Icefjord, but PIES can work under sea ice or be deployed in the deep tributaries of major glacial fjords. Besides SF, examples of locations for potential PIES deployment include Nuup Kangerlua (Godthåbsfjord), Ikerasak Fjord (Store), Karrat Fjord (Rink) and Kangerdlugssuaq Fjord.

2.6 Conclusion

Understanding the heat variability of fjords is crucial to representing the forcing they apply to glaciers. However, glacial fjords are a challenging environment to observe due to the presence of icebergs and sea ice. We present the use of PIES in a glacial fjord to track heat content variability and monitor fjord circulation. While additional steps need to be taken to ensure the acoustic signal is not contaminated by ice, we have shown that PIES can be used in a glacial setting to measure vertically integrated heat content of the full water column. While the PIES should be combined with other platforms such as CTDs and moorings to make full use of their capabilities, they can also serve alone to recreate the vertical properties of the fjord in the winter. A single PIES can capture large wind events in SF, and without the use of an ADCP infer when pulses entered into the fjord. We envision PIES playing a role in an integrated system of monitoring glacial fjords due to their low-cost, reliability, and long-term measuring capability.

2.7 Acknowledgments

We would like to acknowledge Jamie Holte, Isabella Le Bras, and Margaret Lindeman for helpful discussion and suggestions. Dave Sutherland and Will Ostrom were crucial to the deployment and recovery of the PIES. We also acknowledge the support of the crew of the M/V Viking, Greenland, in carrying out the fieldwork. FS and MA acknowledge funding from the Kerr Family Foundation and the Grossman Family Foundation through the Woods Hole Oceanographic Institution. MA is supported by a grant from the National Science Foundation Office of Polar Programs (1332911). FS and RS acknowledge support from NSF OCE-1657601 and from the Heising-Simons Foundation. We also thank Michael Wood and two anonymous reviewers who substantially helped improve the manuscript.

Data are available through the NSF Arctic Data Center at the following DOIs: (PIES) doi:10.18739/A2RJ6S; (Bottom Moored CTD August 2011-September 2012) doi: 10.18739/ A23X83M74, (CTD profiles March 2010) doi: 10.18739/ A2M03XZ2K, (CTD profiles August

2011) doi: 10.18739/ A2QN5ZC52, (CTD profiles September 2012) doi: 10.18739/ A2VD6P58Q, (CTD profiles August 2013) doi: 10.18739/ A2057CT39, (CTD profiles August 2017) doi: 10.18739/ A2NG4GS8C. CTD data collected in 2015 were made available in the previously published work (Beaird et al., 2018). The remaining mooring data is available through the NOAA National Centers for Environmental Information (NCEI) using NCEI Accession numbers 0126772 and 0127325 .

Chapter 2, in full, is a reprint of the material as it appears in Journal of Atmospheric and Oceanic Technology, 2021. Sanchez, R. , F. Straneo, and M. Andres (2021), Using Acoustic Travel Time to Monitor the Heat Variability of Glacial Fjords., *Journal of Atmospheric and Oceanic Technology*, 38, 1535-1550, 10.1175/JTECH-D-20-0176.1. The dissertation author was the primary investigator and author of this paper.

2.8 Appendix A: Two-Layer Model of Sermilik Fjord

The two-layer model (2LM) assumes the vertical temperature profile of the fjord can be described by the equation

$$T_{2LM}(z) = A\tanh\left(\frac{z - z_{pyc}}{\Delta h}\right) + B, \tag{2.5}$$

where z_{pyc} represents the depth of the pycnocline, Δh the thickness of the pycnocline, with A and B chosen so that the profile asymptotes to the boundary conditions of surface temperature (T_{surf}) and bottom temperature (T_{bot}). Specifically,

$$A = \frac{T_{bot} - T_{surf}}{2}, \tag{2.6}$$

$$B = A + T_{surf}. \tag{2.7}$$

Salinity is described by a similar equation and an assumption is made that temperature and salinity are tightly correlated and therefore sharing the same z_{pyc} and Δh.

The model assumes a constant Δh, T_{surf}, S_{surf}. While the mooring observations indicate the depth of the pycnocline can fluctuate over a 100m range, the relative thickness of the interface remains constant until the arrival of GMW in the summer. Surface fluxes drive variation in T_{surf} and S_{surf}, but based on the winter survey the surface layer does not penetrate deep ($\sim$ 15 m), and solar insolation is generally weak in the winter justifying the constant T_{surf} and S_{surf}. Based on the XCTD casts, the constants were determined to be Δh = 70 m, T_{surf} = -1.5 °C and S_{surf} = 32.8 g/kg. The model was not sensitive to the choice of Δh, T_{surf}, or S_{surf}. However, the isopycnal chosen to represent the pycnocline is sensitive to the choice of surface salinity, and S_{surf} = 32.8 g/kg was found to best match the observations and is representative of PW surface salinity from the March 2010 survey. Since the winter casts we used to determine S_{surf}, and σ_{pyc} were collected in 2010 and the 2LM is evaluated on data from 2012-2013, this suggests the constants have some time invariance over multiple years. However, there might be decadal trends in surface salinity that the 2LM cannot account for and the constants may need to be periodically adjusted. T_{bot} was taken from the PIES, and S_{bot} was assumed a constant 34.75 g/kg. By taking T_{bot} from the PIES, the 2LM is able to adjust to background changes in the temperature of the AW layer. S_{bot} has a minor effect on τ (Sec. 2.b) , but could be improved by incorporating the salinity value from the CTD attached to the PIES. The model solves for z_{pyc} by generating a travel time from the 2LM (τ_{2LM}) and minimizing the difference between τ_{2LM} and the observed τ_{852}.

2.9 Appendix B: Error and Uncertainty

The uncertainty in the value of the τ_{hr}, derived from the spread of the return echoes, was estimated using the standard error approach. The standard error of the mean is given by

$$\delta = \frac{\sigma}{\sqrt{N}}, \tag{2.8}$$

where σ is the standard deviation and N is the number of observations. δ_{hr} was found to vary from .01 to .4 ms, and so .4 ms was used in error propagation. The standard error was reduced to .1 ms by taking a daily mean of τ_{hr} and assuming an average of 19.2 (80%, Sec. 3) valid hourly samples in a day.

The uncertainty in the conversion of the mooring profile into a pseudo-travel time was first estimated by computing a standard error of the daily mean for each of the instruments (see Table 2.2). Additional error (δ_{Loc}) was introduced by combining two mooring profiles in different locations. This error was estimated by computing the difference and standard deviation of two instruments both located around 250 m on M1 and M2. δ_{Loc} was added to the 125 m instrument standard error to account for its different location.

A Monte Carlo method was used to estimate the total uncertainty in the mooring generated pseudo-travel time. First, travel time was calculated for 23 CTD casts. For each of the casts another travel time was calculated using only the depths where instruments were located and with Guassian noise equal to each instrument's standard error added. The uncertainty was estimated to be δ_{hr} = .4 ms by taking the standard deviation of the difference between the actual and noisy travel times.

The uncertainty in the conversion of travel time to heat content was estimated by adding the root mean square deviation ($RMSD$) of the linear fit to the propagated uncertainty of travel time. In other words, if

$$\hat{\Theta} = A\tau + B, \tag{2.9}$$

is the equation of the linear fit, then uncertainty exists due to both the linear fit and the uncertainty of τ. Defining this uncertainty as $\delta_\Theta = RMSD + A\delta_\tau$, where A is slope of the linear fit, the potential uncertainty is estimated as δ_Θ = .82 °C. After a 10-day low-pass filter the uncertainty was reduced to .39 °C.

2.10 Appendix C: Calculating Velocity from Pycnocline Depth

The average velocity of the upper layer of the fjord can be estimated from Equation 29 of Jackson et al. (2018):

$$\overline{v} = \Delta\sigma e^{-W/R_d} \underbrace{\frac{c_1}{h_1}\frac{\cos[\omega/c_1(L-y)]}{\cos(\omega L/c_1)}}_{\text{standing wave}} + \Delta\sigma(1-e^{-W/R_d}) \underbrace{2\frac{c_1}{h_1}\frac{R_d}{W}(1-e^{-W/R_d})\sin[\omega/c_1(L+W/2-y)]}_{\text{Kelvin wave}} \tag{2.10}$$

where the first term is the contribution from the standing wave and the second term is the contribution from the Kelvin wave. Here $\Delta\sigma$ is the range of pycnocline fluctuation calculated from τ_f, W is the fjord width, R_d is the deformation radius, c_1 is the baroclinic wave speed, h_1 is the depth of the upper layer, ω is the forcing frequency, L is the fjord length and y is the location of the mooring. The Kelvin number

$$Ke = \frac{W}{R_d},$$

can be used to scale the influence of rotation. As described by Jackson et al. (2018), interfacial waves in narrow fjords with a small Ke can be described using the 2D standing wave model. While interfacial waves in a wide fjord with a large Ke propagate as Kelvin waves. Like many of Greenland's fjords, SF has a Ke that is $O(1)$ and experiences both of these wave phenomena (Jackson et al., 2018). To estimate velocity using C1, we use τ_f to predict $\Delta\sigma$, and appropriate values for SF for the remaining constants (Table 2.3).

2.11 Supporting Information

Displacement Tests

To evaluate the impact of forcing variability on travel time, we took CTD casts from

Table 2.3. Parameters used in the wave velocity equation (C1) to estimate velocity within the fjord. All values were derived or calculated from data within this paper, and are consistent with the values used in Jackson et al. (2018).

Model Constant	Sermilik Fjord Value
W: fjord width	7.5 km
R_d : deformation radius	7.5 km
c_1 : 1st baroclinic wave speed	1.1 m s^{-1}
h_1: depth of the upper layer	200 m
$1/\omega$: forcing period	6 days
L: fjord length	90 km
y: mooring distance from mouth	30 km

Sermilik Fjord and perturbed them to replicate the impact of a pycnocline fluctuation or Atlantic Water (AW) temperature variability. To replicate the shelf-driven circulation, the pycnocline was shifted by 50 m which is equivalent to the observed pycnocline variability brought from along shore winds (Jackson et al. 2014, 2018). A comparison of the original and displaced temperature profile can be seen in the supplemental Figure 2.13. A similar test was performed on the CTD profiles with the temperature of the lower AW layer shifted by 0.1 and 1 degrees to represent synoptic and interannual variability respectively. The 1 degree version of these tests is shown in the supplemental Figure 2.14. The values reported in the main text come from the winter perturbations which are slightly higher than the values from the summer perturbations (1.5 ms in the summer vs 1.6 ms in the winter).

Travel Time Echoes

In Section 3 of the main text we describe the procedure for averaging hourly return echoes in an ice-influenced environment. The main difference between traditional (ice-free, open ocean) hourly averaging is the need to account for both late and early echoes. The supplemental Figure 2.15 top panel shows all of the return echoes recorded by the PIES with the expected sea surface height in red. The vast majority of echoes are near the sea surface but show the spread of possible travel times recorded by the PIES.

Impact of Sea Ice on Travel Time

Here, we briefly discuss the impact of sea ice on travel time.

Influence on variability: Previously published work by Andres et al. (2015) has shown that sea ice results in a significant reduction in the variability of travel time and identified the period of February 26 2012 through March 10, 2012 as having sea ice present. When sea ice is overhead of the PIES the standard deviation of the detided hourly travel time is significantly reduced from 1.6 ms to 0.95 ms (95%, $p < 0.01$). This reduction in variability is visibly evident in both the raw travel time echoes (Figure 2.15) and when looking at the detided hourly travel time (Figure 2.16 in red). Therefore we suggest looking at a time series of the variability of τ to diagnose the presence of a large concentration of sea ice.

Influence on magnitude: The presence of sea ice over a PIES could result in two outcomes: a reduction in travel time associated with the draft of sea ice changing the path length of an acoustic ping or an increase in travel time associated with the cold water necessary for sea ice formation. Figure S4 shows travel time increasing in the presence of sea ice suggesting that the decreasing heat content has a greater impact on travel time than a reduction in path length. However, we can calculate the impact of ice draft on travel time path length by assuming a sound speed of 1465 m/s and a potential range of ice thickness from 15 cm to 1 m. We estimate the quick growth of fast ice would result in a thin draft ($\sim$ 15 cm) but reported estimates of multi-month maximum seasonal thickness of fast ice in a Svalbard Fjord were as high as 1 m (Gerland and Hall, 2006) so we use these thicknesses as our references for estimating the impact of sea ice on travel time path length. Using these estimates, we calculate a potential decrease in travel time of .1 ms, and 0.7 ms for 15 cm and 1 m ice thickness respectively. These travel time impacts are equivalent to a thermocline shift of 1 m and 27 m, but occuring on a slower timescale than the shelf-driven circulation. Therefore knowledge of local sea ice growth will be helpful in determining if the PIES can be used for long-term monitoring, but the PIES can still accurately measure heat content in glacial fjords with sea ice less than 1 m thick.

Temperature Composite In the main text, we found that the composites of τ_f had a secondary

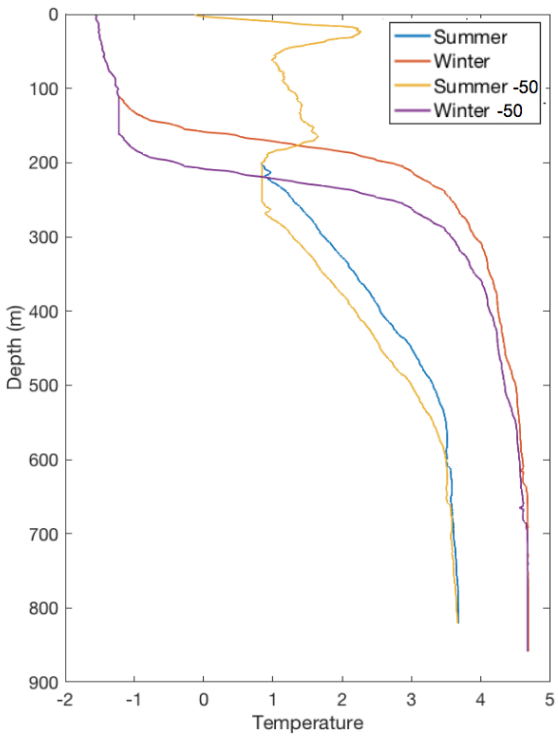

Figure 2.13. Profiles used in displacement analysis. The unperturbed winter profile is in red and the winter profile with a 50 m lower pycnocline is in purple. Same for the summer profiles with the undisturbed profile in yellow and the higher pycnocline in blue. *Temperature is units degree C*.

peak about 34 hours behind the peak volume flux (and the peak in pycnocline displacement). To investigate this phasing, we used the observed pycnocline displacement to predict τ_f - the opposite of the calculation done in the main text- and subtracted this τ_{pyc} from τ_f to produce a residual τ_f which presumably has had the effect of pycnocline heaving removed. We show this compared to composites of the filtered (26-hour low-pass with 30-day low-pass removed) temperature of the pycnocline on Figure 2.17. Visually the two composites appear anti-correlated and we calculate an $r^2 = 0.6$.

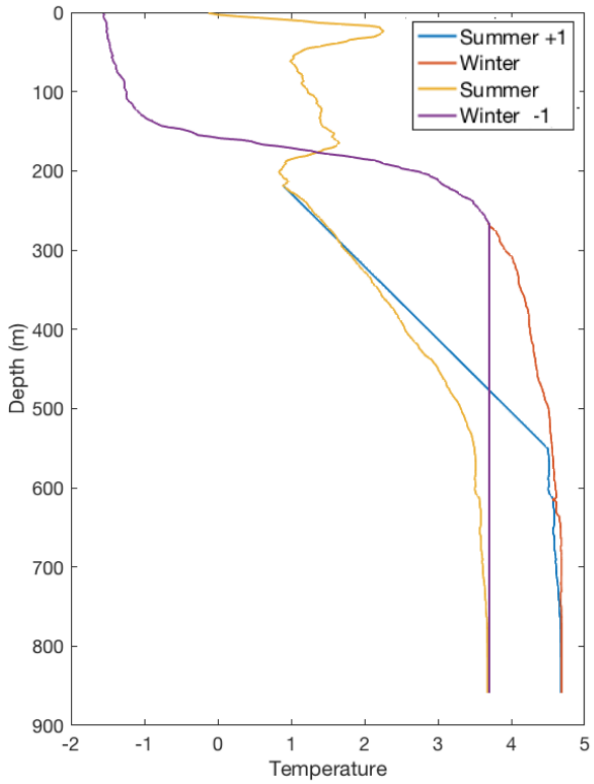

Figure 2.14. Additional profiles with displacement based on temperature profiles. Since the summer profile starts with a cooler AW temperature it was perturbed to be warm and the winter profile was perturbed to be cold. *Temperature is units degree C*

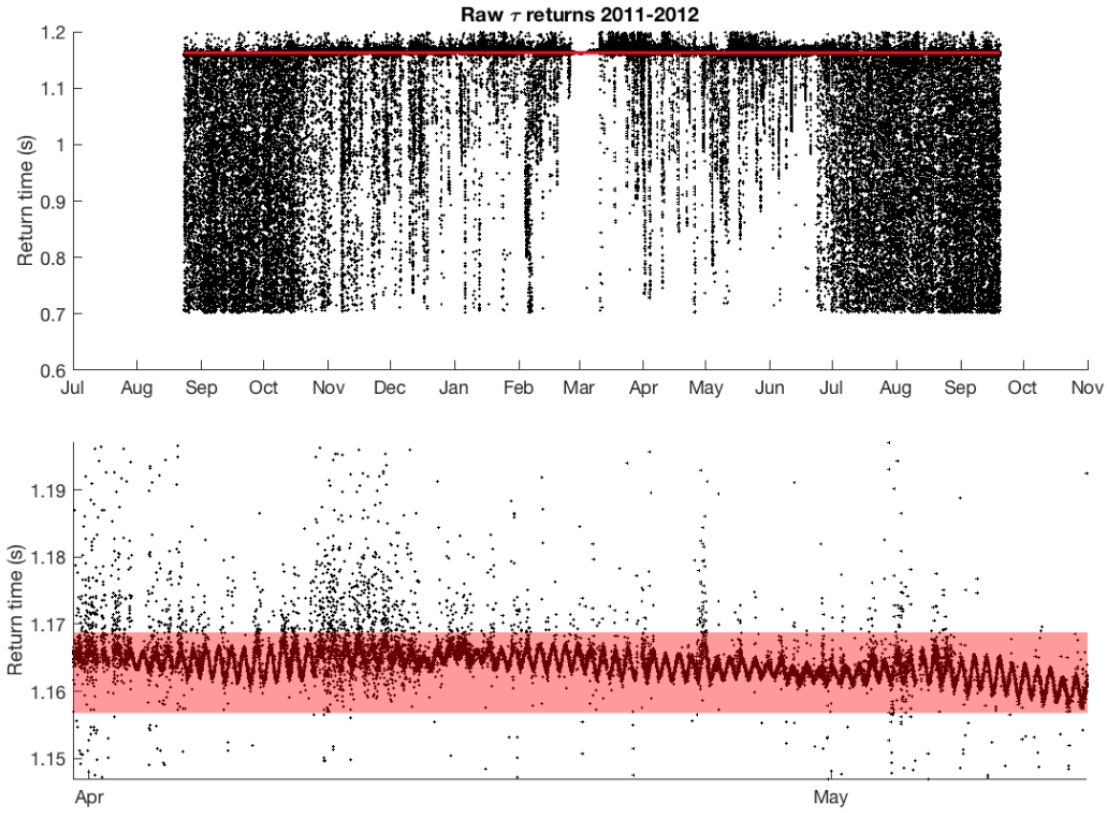

Figure 2.15. Top) raw data of travel time echoes with a red line denoting the expected travel time of a ping off the surface. Bottom) a close up of the raw returns showing the median filter used with the travel time data in red.

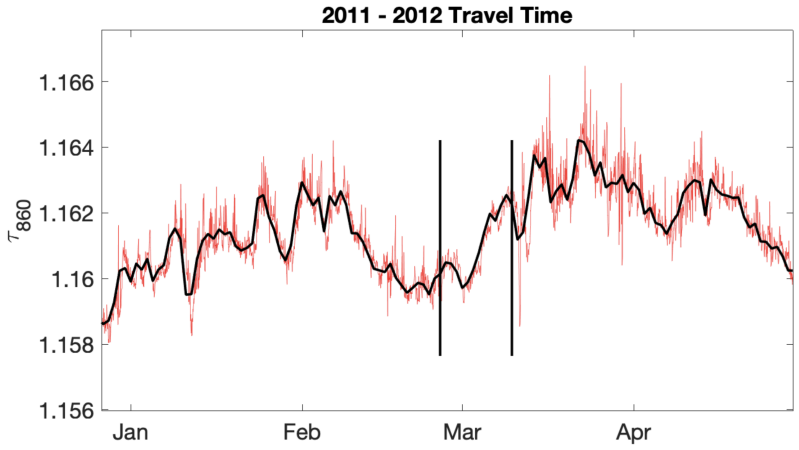

Figure 2.16. Travel Time zoomed in on the period Jan. - April 2012. The red signal is the detided hourly data and the black signal is the daily average. The two black vertical lines on Feb. 26 2012 and Mar. 10 2012 bookend the period when the fjord was covered in fast ice.

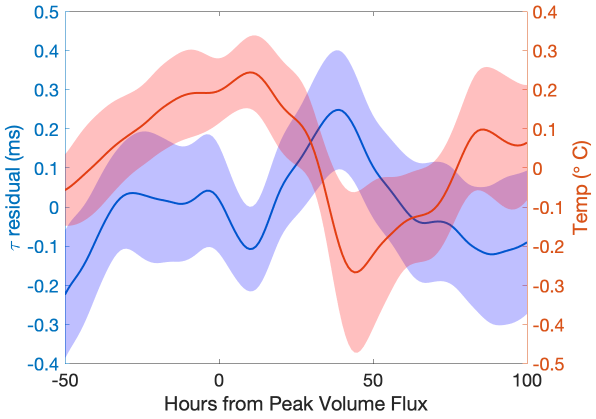

Figure 2.17. Composites of residual τ_f ($\tau_f - \tau_{pyc}$) and pycnocline temperature from the Jackson et al. (2014) shelf-driven exchange events. The shading indicates the range of the standard error.

Chapter 3

Delayed Freshwater Export from a Greenland tidewater glacial fjord

Abstract

Freshwater from the Greenland Ice Sheet is routed to the ocean through narrow fjords along the coastline where it impacts ecosystems both within the fjord and on the continental shelf, regional circulation, and potentially the global overturning circulation. However, the timing of freshwater export is sensitive to the residence time of waters within glacial fjords. Here, we present evidence of seasonal freshwater storage in a tidewater glacial fjord using hydrographic and velocity data collected over 10 days during the summers of 2012 and 2013 in Saqqarleq (SQ), a mid-size fjord in West Greenland. The data revealed a rapid freshening trend of -0.05 ± 0.01 g/kg/day and -0.04 ± 0.01 g/kg/day, in 2012 and 2013, respectively, within the intermediate layer of the fjord (15–100 m) less than 2.5 km from the glacier terminus. The freshening trend is driven, in part, by the downward mixing of outflowing glacially-modified water near the surface and increasingly stratifies the fjord from the surface downwards over the summer melt season. We construct a box model which recreates the first-order dynamics of the fjord and describes freshwater storage as a balance between friction and density-driven exchange outside the fjord. The model can be used to diagnose the timescale for this balance to be reached, and for SQ we find a month lag between subglacial meltwater discharge and net freshwater export. These results indicate a fjord-induced delay in freshwater export to the ocean that should be represented in

large-scale models seeking to understand the impact of Greenland freshwater on the regional climate system.

3.1 Introduction

Mass loss from the Greenland Ice Sheet is predicted to accelerate during the 21st century, further contributing to sea level rise and with downstream consequences on ocean circulation and ecosystems (Bamber et al., 2019; Goelzer et al., 2020; Böning et al., 2016; Frajka-Williams et al., 2016; Arrigo et al., 2017; Oksman et al., 2022). Freshwater fluxes from the ice sheet are discharged in the form of both solid and liquid forms contributing cumulatively 7700 ± 460 km^3 and 8400 ± 1680 km^3 of freshwater respectively, from 2000–2016 (Bamber et al., 2018). The freshwater and its dissolved and particulate chemical content are released into long and narrow fjords before being routed onto the continental shelves where they can affect regional circulation, salinity, biogeochemistry and potentially large-scale deep convection, although recent evidence suggests Greenland's freshwater might remain close to the coast (Straneo and Cenedese, 2015; Böning et al., 2016; Frajka-Williams et al., 2016; Thornalley et al., 2018; Hendry et al., 2021; Le Bras et al., 2021). The freshwater from glaciers also impacts regional ecosystems through both the direct injection of nutrients and the upwelling of ambient deep nutrients leading to highly productive fjords and fisheries (Cape et al., 2019; Meire et al., 2016a,b, 2017; Hopwood et al., 2020) that are, therefore, sensitive to future changes in freshwater fluxes (Hopwood et al., 2018; Oliver et al., 2020). The impact of freshwater will vary depending on how, when and where it mixes with seawater. This mixing is in turn affected by fjord circulation and stratification (Mortensen et al., 2011, 2020). Therefore, determining how fjord dynamics alter the distribution and export of freshwater is crucial to understanding the impact of the Greenland Ice Sheet on the ocean and ecosystems.

The liquid component of freshwater enters fjords in three forms: (i) through direct melting of ice by the ocean (submarine meltwater; SMW), (ii) meltwater from the ice sheet surface that

has drained to the ice sheet base and enters the fjord from beneath a glacier (subglacial meltwater discharge; SGD), and (iii) meltwater from the ice sheet surface that has not drained to the base and enters the fjord at the surface (meltwater runoff). Since it is expected that the majority of surface meltwater does drain to the ice sheet base in this system, and since this study excludes the surface layers of the fjord, we here make no further mention of meltwater runoff. SMW fluxes are sensitive to ocean heat and released at various depths along the face of the terminus. Additionally, SMW is produced by melting icebergs as they transit through the fjord. Meltwater drained as SGD is buoyant and produces turbulent plumes which entrain ambient water and drive a strong overturning circulation within the fjord (Straneo and Cenedese, 2015; Carroll et al., 2017). This overturning circulation, along with tidal flows and shelf-forced fluctuations, drives horizontal and vertical mixing within the fjord and determines the exchange of freshwater with the shelf (Zhao et al., 2021). However, the transport and outflow depth of the SGD plume is sensitive to fjord stratification, resulting in a complex feedback between fjord circulation and freshwater content (De Andrés et al., 2020).

Glacial fjords are often described as being in one of two states, a winter state with decreased stratification and a shelf-influenced circulation, and a summer state with increased stratification and a strong plume-driven circulation (Jackson and Straneo, 2016; Gladish et al., 2014b; Mortensen et al., 2014). These dramatic differences in circulation and stratification can lead to a seasonal description of glacial fjords that overlooks the dynamic evolution of fjords within a season. Additionally, the challenges of obtaining measurements in ice-congested fjords often limit field campaigns to short-duration summer surveys (Stevens et al., 2016; Beaird et al., 2015, 2017; Cape et al., 2019; Motyka et al., 2011; Wood et al., 2018; Moon et al., 2018; Inall et al., 2014; Bendtsen et al., 2015, 2021; Muilwijk et al., 2022). While these surveys provide invaluable snapshots of heat, nutrient, and meltwater fluxes, it is often assumed that the data are representative of the whole summer and some heat budgets explicitly assume the fjord is in a "steady state" or use a single summer average (Inall et al., 2014; Jackson and Straneo, 2016).

However, a limited number of observations have shown significant subseasonal variability

of hydrographic properties in fjords (Stuart-Lee et al., 2021; Carroll et al., 2018; Mortensen et al., 2014, 2013, 2018; Meire et al., 2016b; Mernild et al., 2015). For example, Mortensen et al. (2011, 2014, 2018) show that Godthåbsfjord freshens and the isopycnals deepen throughout the summer, suggesting that fjord processes modulate the timing and vertical distribution of freshwater export. This is in contrast to the approach of large-scale ocean models, which often input freshwater from glacial freshwater at the surface and assume the transit time of meltwater through fjords is negligible (Arrigo et al., 2017; Dukhovskoy et al., 2019). To further understand the subseasonal evolution of glacial fjords and their impact on freshwater export, we use a dataset of high-frequency hydrographic and velocity observations collected over 10 days during each of the summers of 2012 and 2013 in Saqqarleq (previously known as Sarqardleq Fjord), a mid-size fjord in west Greenland associated with Saqqarliup Sermia glacier. The data revealed a rapid freshening trend of 0.05 g/kg/day and 0.04 g/kg/day, in 2012 and 2013 respectively, within the intermediate layer of the fjord less than 2.5 km from the glacier. These freshening trends were of similar magnitude despite the fact that 2012 was a year of record surface melt and 2013 was an average melt year. The freshening indicates that SMW and SGD from the glacier is stored within the fjord leading to a transformation of fjord waters and a delay in the net export of freshwater. A box model is developed to elucidate the storage and release dynamics of the glacial fjord. The box model is formulated for Saqqarleq, but is generic and can be applied to other systems. Our results suggest that Greenland's glacial fjords are nonsteady and respond rapidly to the input of ice sheet meltwater. The freshwater storage results in a lag of peak freshwater export from the glacier to the ocean that needs to be accounted for in any regional or global ocean model that does not resolve fjords and fjord processes.

3.2 Setting, Data and Methods

3.2.1 Setting and Background

We investigate changes within Saqqarleq (SQ), a mid-sized glacial fjord in west Greenland associated with the glacier Saqqarliup Sermia, during a period of sustained SGD. SQ is the southern arm of the Ilulissat Isfjord system which connects Sermeq Kujalleq (commonly referred to as Jakobshavn Isbrae) with Disko Bay (Fig. 3.1a). SQ has a broad sill (S1) about 500 m from the grounding line isolating the glacier from the deepest SQ waters. This sill varies in depth from 50 m at its southwest end to 100 m at its deepest point. The fjord varies in width from about 6 km at the head of the fjord, to 2.2 km in the main channel of the fjord before it connects to Tasiusaq (TQ) and then Ilulissat Isfjord. SQ and TQ are separated by an 80 m deep sill (S2) that is 16 km downfjord of Saqqarliup Sermia, and TQ is separated from Ilulissat Isfjord by a 125 m deep sill (S3). The sill between TQ and Ilulissat prevents the deeper relatively warm basin waters of Ilulissat from reaching SQ.

SQ lacks a thick ice mélange, unlike major glacial fjords such as Ilulissat Isfjord and Sermilik, which enables measurements to be made within 200 m of the terminus and makes SQ ideal for field studies of ice-ocean interactions (Stevens et al., 2016; Mankoff et al., 2016; Slater et al., 2018; Wagner et al., 2019; De Andrés et al., 2020). SGD enters the fjord from below the glacier at two locations, a primary plume located 2.3 km along the terminus from the southwest corner and a secondary plume 4.5 km along the terminus [Fig. 3.1c, (Stevens et al., 2016)]. The secondary plume is associated with substantially weaker SGD resulting in a deeper neutral buoyancy depth (Stevens et al., 2016; De Andrés et al., 2020). A remote-control kayak equipped with a depth-varying CTD sampled within the surface expression of the primary plume in 2013, finding that the plume was composed of 90% entrained ambient water, 10% SGD and less than 0.1% SMW (Mankoff et al., 2016). Along-fjord transects of temperature and velocity revealed that after surfacing, the plume submerged and flowed out as a subsurface jet (Mankoff et al., 2016). A high-resolution simulation of SQ, constrained with observations from 2013, found that

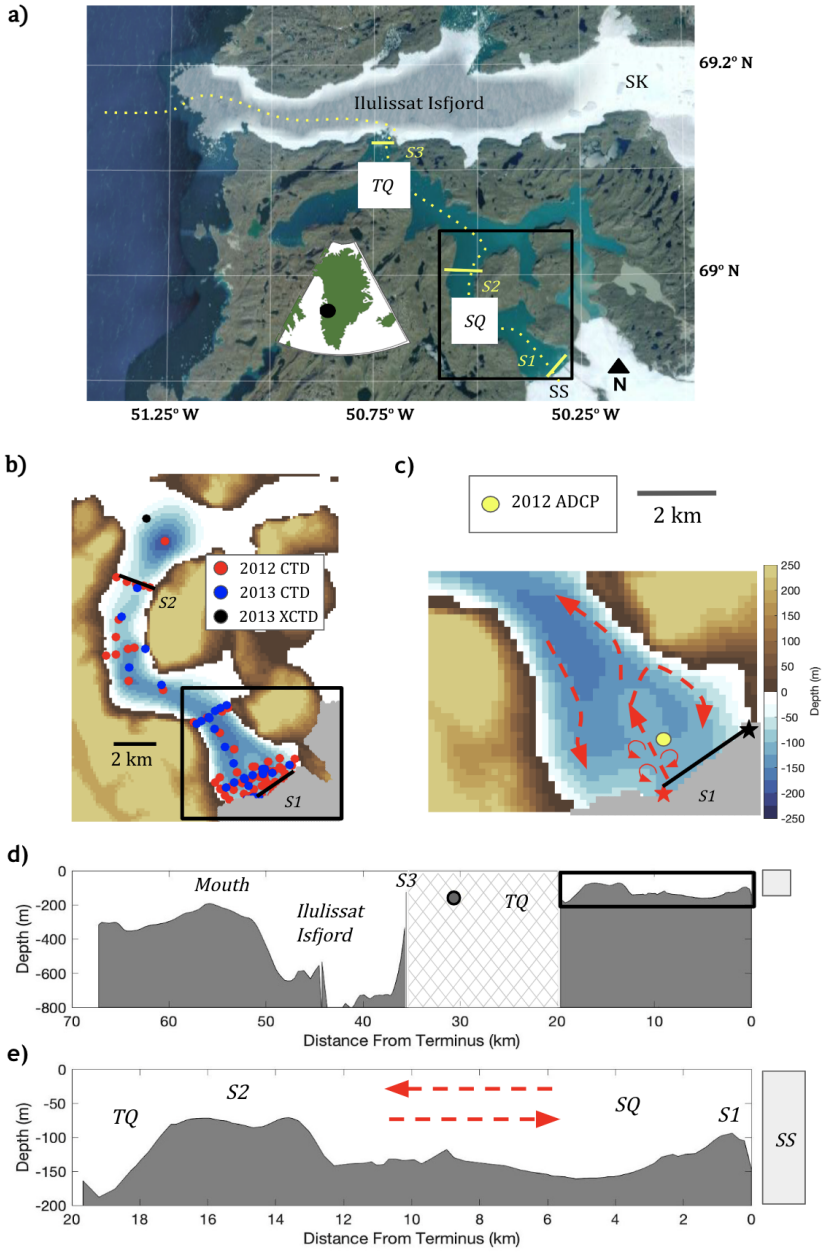

Figure 3.1. a) A regional map of Saqqarleq (SQ), Tasiusaq (TQ) and Ilulissat Isfjord showing sill locations and nearby glaciers Saqqarliup Sermia (SS) and Sermeq Kujalleq (SK). The inset map shows the location of SQ within the Greenland continent. The yellow dashed line is the bathymetry slice shown in (d) and (e). b) Map of SQ with the locations of CTDs in 2012 (red), 2013 (blue) and a 2013 XCTD (black). c) Near-terminus bathymetry and a schematic of the circulation. Locations of the primary plume (red star) and secondary plume (black star) based on Stevens et al. (2016) and location of moored ADCP (Fig. 3.7). d) Along-track bathymetry profile created using BedMachinev3 (Morlighem et al., 2017a). Cross hatching fills the region where data is unreliable. A circle marks the single depth point available (2013 XCTD). e) A close-up of SQ, with overturning schematic.

the plume-turned-jet impinged on the fjord wall and generated a vigorous terminus-scale wide recirculation generating widespread melting of the glacier terminus [Fig. 3.1c, (Slater et al., 2018)].

Previously, De Andrés et al. (2020) used parts of this dataset to explore differences in the surface emergence of a subglacial plume across two consecutive years, including one in a year with record SGD (2012). They found that greater cumulative SGD was associated with increased fjord stratification which, in turn, exerted a dominant influence on plume height. They did not investigate, however, the physical mechanisms controlling the stratification and the potential impacts this stratification has on the export of freshwater.

3.2.2 Data

Conductivity, Temperature and Depth (CTD) profiles were collected from a small boat in the fjord from 17–27 July in 2012 and 23 July – 1 August 2013 (Fig. 3.1b). The profiles were collected using an RBR XR 620 CTD and averaged into 1 dbar bins. 90 casts were collected in 2012 and 96 casts were collected in 2013. In 2012 (2013), 51 (59) of the casts extended to at least 100 m and only these deeper casts were used in our hydrographic analysis. Additionally in 2013, a Sippican eXpendable CTD (XCTD) was collected just outside the 80 m deep S2 in TQ. The data are presented in Conservative Temperature (Θ or temperature), Absolute Salinity (S or salinity) and Potential Density [ρ or density; (McDougall and Barker, 2011)] with stratification defined using the Brunt-Väisälä frequency

$$N^2 = -\frac{g}{\rho_{ref}}\frac{\mathrm{d}\rho}{\mathrm{d}z}, \tag{3.1}$$

where g is gravitational acceleration and $\rho_{ref} = 1026$ kg/m^3 is a reference density.

An upward-looking moored Teledyne RDI 300 kHz Acoustic Doppler Current Profiler (ADCP) was deployed 1.6 km from the terminus (Fig. 3.1c) and collected velocity data from July 2012 – April 2013. The ADCP was deployed on the seafloor at 114 m and recorded velocity in 4

m bins from 10–106 m, after removing the top two bins for side-lobe effects. The barotropic tide was estimated from a pressure sensor, the Arctic Ocean Inverse Tide Model (Padman and Erofeeva, 2004; Erofeeva and Egbert, 2020) when data was unavailable, and subtracted from the ADCP data (Sup. Fig. 3.13). The estimates of SGD entering the fjord are taken from the Modele Atmospherique Regional [MAR;(Fettweis et al., 2017; Delhasse et al., 2020)] with the dataset provided by Mankoff et al. (2020). We also use salinity values collected from seals as reported in Mernild et al. (2015) and calibrate them against our CTD data (Sup. Fig. 3.14).

3.3 Analysis of Observational Data

3.3.1 Background Hydrography

The hydrography of SQ has been investigated by De Andrés et al. (2020) and Stevens et al. (2016), but a brief description is necessary here to provide context for our analysis. During summer, the fjord can be approximated as a three-layer system with a surface layer approximately 10–15 m deep, an intermediate layer between 15–100 m deep and a homogeneous layer deeper than 100 m (BW, Fig. 3.2). Temperature profiles (Fig. 3.2a), reveal a warm surface layer, presumably from solar heating, and a colder layer extending from 15 m to the bottom. There is little difference in temperature between the second and third layer. Interannual differences between 2012 and 2013 are small with mean temperatures below the surface layer of 0.9 °C and 1 °C respectively. Salinity profiles (Fig. 3.2b), show that the intermediate layer of the fjord is substantially fresher in 2012 (mean salinity 31.9 g/kg) than in 2013 (32.9 g/kg). The interannual differences in salinity are consistent with 2012 being a year of record ice sheet surface melt (Nghiem et al., 2012; Tedesco et al., 2013). Below 100 m in the basin layer, the salinity between the two years are similar. This evidence suggests that S1 blocks the majority of glacial water from reaching the basin layer and that BW is primarily composed of waters unmodified by SS and imported from outside of the fjord, similar to the deep basin waters of some shallow-silled glacial fjords (Hager et al., 2022a). This basin water has characteristics of diluted Baffin Bay

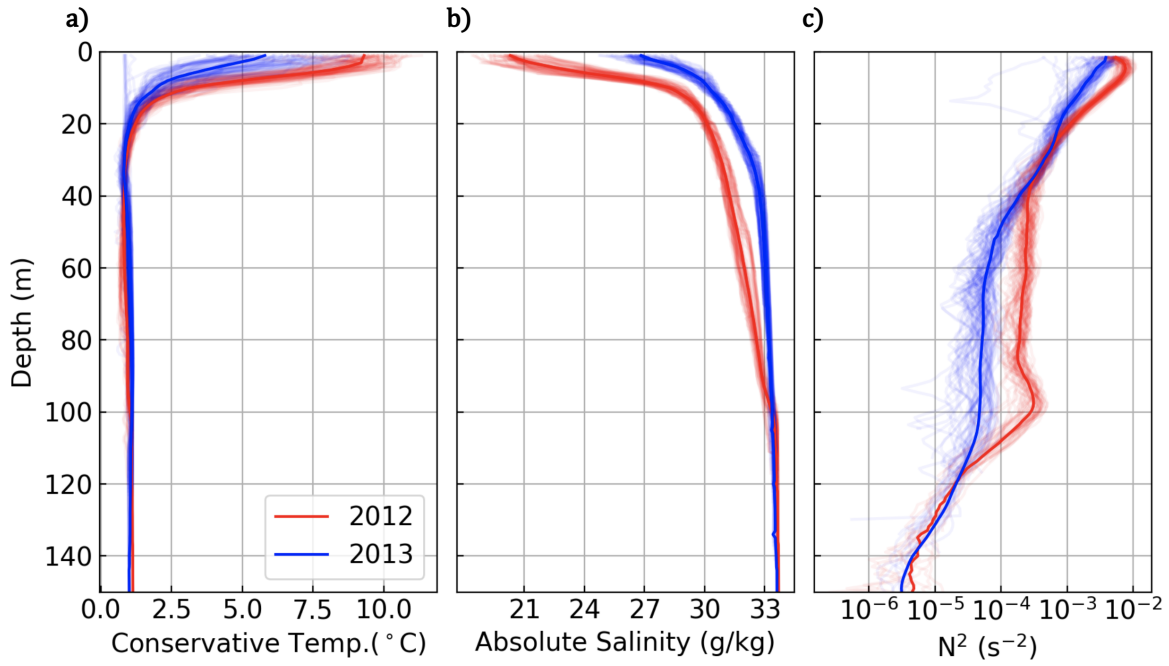

Figure 3.2. a) Conservative Temperature versus depth (red 2012, blue 2013). b) Absolute Salinity. c) Stratification (N^2) over the top 150 m. In all profiles the mean profile is given in bold. The stratification profiles are low-pass filtered over a window of 10 m to remove noise. The x-axis in panel c is logarithmic.

Polar Water, one of the two water masses found in Greenland north of Davis Strait (Gladish et al., 2014b; Stevens et al., 2016; Rysgaard et al., 2020; Mortensen et al., 2022).

The density in SQ is dominated by salinity, and the stratification profiles reveal that decreased salinity above 100 m is associated with increased vertical density gradients (Fig. 3.2). In both years, the stratification exhibits peaks around the surface layer but decreases with depth. Above 40 m, the mean stratification was approximately double in 2012 (2×10^{-3} s^{-2}) compared to 2013 (1×10^{-3} s^{-2}). The mean stratification between 40 to 100 m is about 4 times higher in 2012 (2.7×10^{-4} s^{-2}) compared to 2013 (0.07×10^{-4} s^{-2}). The profiles in 2012 also exhibit a peak in stratification just above the homogeneous layer (100 m) before converging to the 2013 properties reflecting the presence of sill S2.

3.3.2 Continuous Fjord Freshening

We find that SQ gets fresher during the summer field campaign in both years indicating it is not in steady state. We analyze freshwater storage by examining temporal trends in salinity within layers of the fjord. We focus on the intermediate layer (15–100 m depth) because the surface layer shows a high degree of variability, presumably, imparted by processes that are not the focus of this study, such as runoff (meltwater, land and precipitation) and solar insolation (Sup. Fig. 3.16). While these surface processes are important, strong stratification ($N^2 \approx 10^{-2}$ s^{-2}) likely limits their impact at depth in this system. In both 2012 and 2013, the mean salinity over the intermediate layer continuously decreased over the course of each field campaign (Fig. 3.3). The mean salinity also exhibited an along-fjord trend with fresher waters closer to the glacier, but the temporal trend is greater than the longitudinal trend. We can thus rule out that the freshening is due to the advection of freshwater from Ilulissat Isfjord as otherwise the salinity gradient would be reversed. The freshening trend in 2012 is -0.05 ± 0.01 g/kg/day (r^2 = 0.77) and in 2013 is -0.04 ± 0.01 g/kg/day (r^2 = 0.74), with uncertainty defined using a bootstrapping method. This trend is consistent with a moored CTD at 70 m that recorded salinity continuously over this time period (Sup. Fig. 3.15). The CTD data is concentrated near the head of SQ where mixing is likely to be most intense (Bendtsen et al., 2021), and therefore it is unclear how close to the shelf the freshening trend persists. The jet from the glacier outflows at around 20 m depth, but the freshening occurs at all depths (Sup. Fig. 4) suggesting that either the outflowing freshwater is being vertically mixed downwards or strong submarine melting is freshening waters at all depths.

3.3.3 Subglacial Discharge is the Dominant Freshwater Source

Next, we show that the freshening trend is due to an increase in SGD content in the water column. We can visually identify which freshwater source is responsible using a temperature and salinity (TS) diagram with the depths 25 m, 40 m, 80 m and 100 m highlighted in Figure 3.4. The profiles shown are representative of the start, middle and end of the field campaign

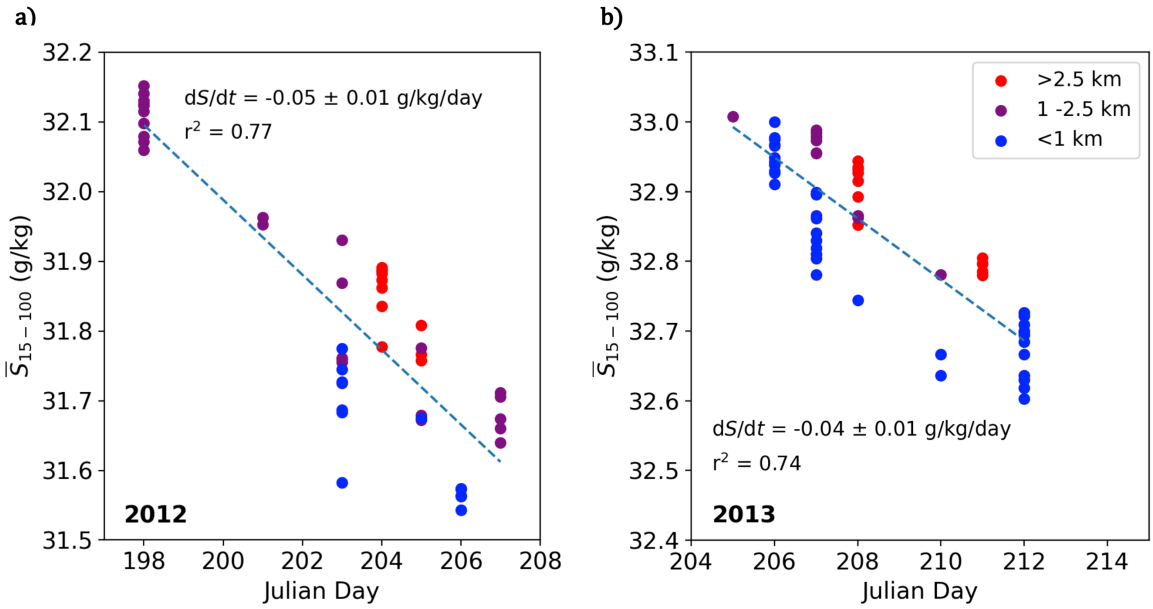

Figure 3.3. a) Mean Absolute Salinity of 2012 CTD profiles from 15–100 m (surface layer to S2 depth) with a best fit trend. Colors indicate distance from terminus. X-axis is the Julian day. b) same but for 2013.

and were all collected from approximately the same distance from the glacier. By looking at the change in temperature associated with freshening we can determine the source of freshwater. For example, we expect freshening driven by SMW to be associated with a substantial cooling of water while freshening due to SGD is associated with a much smaller change in temperature. In 2012, the change in properties at each depth are roughly parallel to the subglacial meltwater discharge-mixing line indicating that the freshening is due to an increase in SGD at depth rather than SMW. However in 2013, only the properties at 25 m appear parallel to the subglacial meltwater discharge-mixing lines while deeper water appears to be on a slope between the subglacial meltwater discharge-mixing line and the submarine melt line. Following the procedure of Mankoff et al. (2016) and Mortensen et al. (2020) (see Supplemental) we use a water-mass analysis to quantify changes in the relative concentration of SGD and SMW (Table 1). The fraction of SGD significantly increased by around 1% in both years ($p < 10^{-4}$ for all cases). Changes in the fraction of SMW were mostly significant ($p < 10^{-4}$ for all cases except 2013 at

Table 3.1. Change in freshwater concentration of SGD and SMW from day 1-10 in 2012 and day 1-8 in 2013.

Depth	2012 ΔSMW	2012 ΔSGD	2013 ΔSMW	2013 ΔSGD
25 m	-0.06 ± 0.03 %	1.5 ± 0.2 %	0.02 ± 0.03 %	1.4 ± 0.3 %
40 m	0.08 ± 0.02 %	1.3 ± 0.1 %	0.11 ± 0.05 %	1.0 ± 0.1 %
80 m	-0.08 ± 0.01 %	1.1 ± 0.1 %	0.06 ± 0.03 %	0.4 ± 0.1 %

25 m), but varied with decreases (2012) or increases (2013) around 0.1 %. In both years the increase in SGD is an order of magnitude higher than changes in SMW. Thus while SMW is present, we conclude that the freshening trend is being driven primarly by the accumulation of SGD. This process must occur from the top down as SGD is exported in the jet which outflows around 20 m depth (Mankoff et al., 2016; Slater et al., 2018).

3.3.4 Interannual Subglacial Meltwater Discharge Differences

Comparison of SGD timeseries from MAR highlights that SGD flux into the fjord was substantially higher in 2012 than in 2013 (Fig. 3.5). In 2012, the SGD flux into the fjord started about 10 days earlier and the mean flux during the period of sustained SGD (DOY 160–215) was 138 m^3/s compared to 111 m^3/s in 2013 (Fig. 3.5a). This increased SGD flux resulted in cumulative freshwater input that was 40% higher in 2012 by the end of summer (Fig. 3.5b). The difference in cumulative SGD grew throughout the summer, such that by the end of the respective field seasons, 0.3 Gt more freshwater had entered in the fjord in 2012 than 2013 (Fig. 3.5c)

3.3.5 Density differences across the outer sill (S2)

Comparison of CTD profiles from inside and outside of SQ shows how the increase in stratification in the inner fjord driven by SGD leads to greater interaction with topography (Fig. 3.6). In 2012, a density difference arose between the fjord interior and exterior near the depth of S2 (80 m), which separates SQ from TQ. Below this sill depth, the outside profile was less stratified and more dense than profiles within the fjord (Fig. 3.6a). This feature is not evident in 2013 (Fig. 3.6b). Note that all profiles have had the linear temporal trend in salinity (Fig. 3.3)

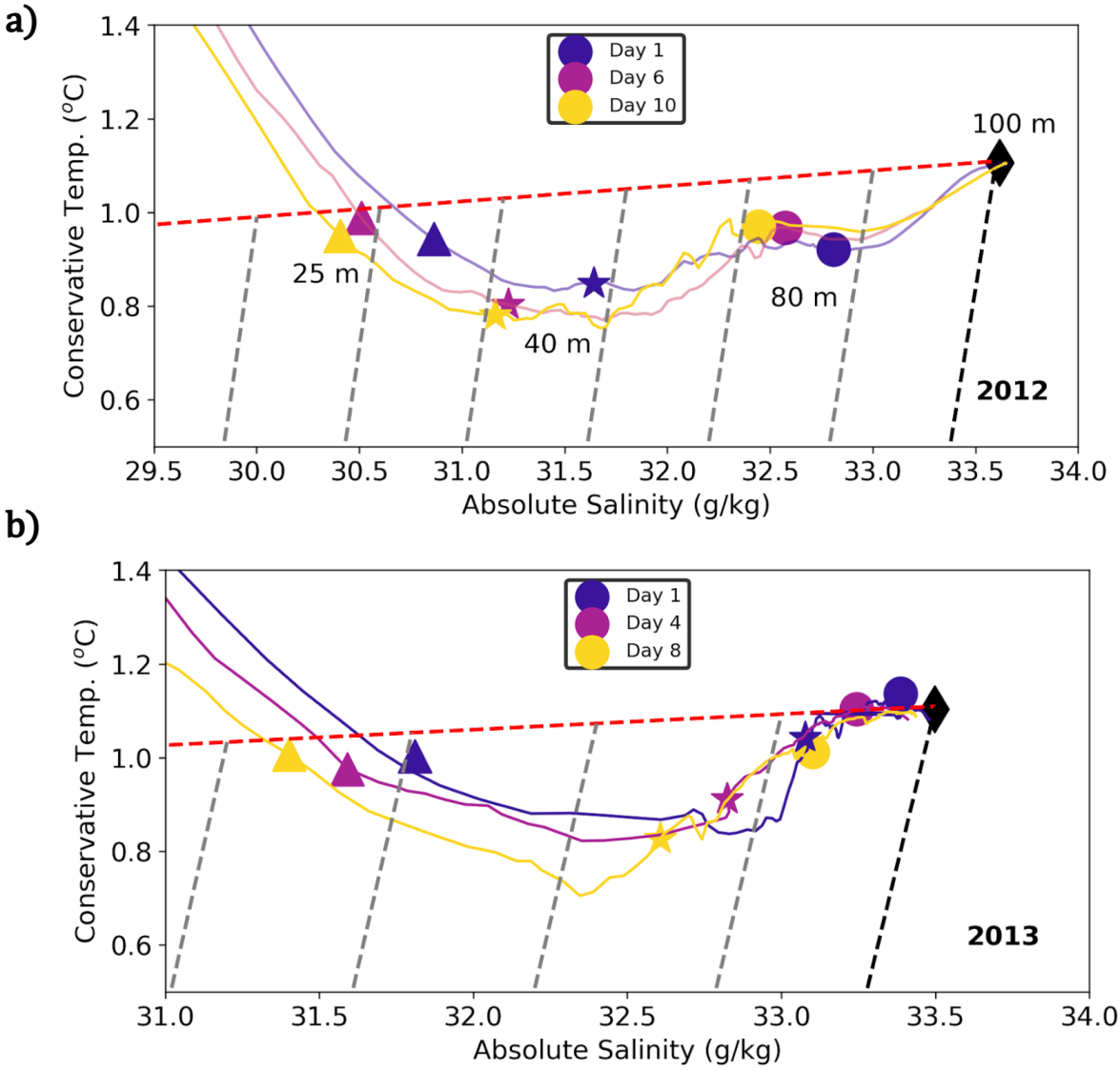

Figure 3.4. a) TS diagram of days 1, 4, and 10 in 2012 with the depths 25 (triangles), 40 (stars), 80 (circles) and 100 m (diamond) highlighted with symbols. b) Same as *a* but for 2013, the final point is from day 8 rather than day 10. On top of the TS diagram, we plot a subglacial meltwater discharge-mixing line (red) which represents the mixing between SGD (S = 0 g/kg, $\Theta = 0\ ^{\circ}C$) and water at 100 m. There are also submarine melt lines (gray lines), or Gade slopes, which represent a hypothetical mixture of BW and SMW (S = 0, Θ = -87 °C)

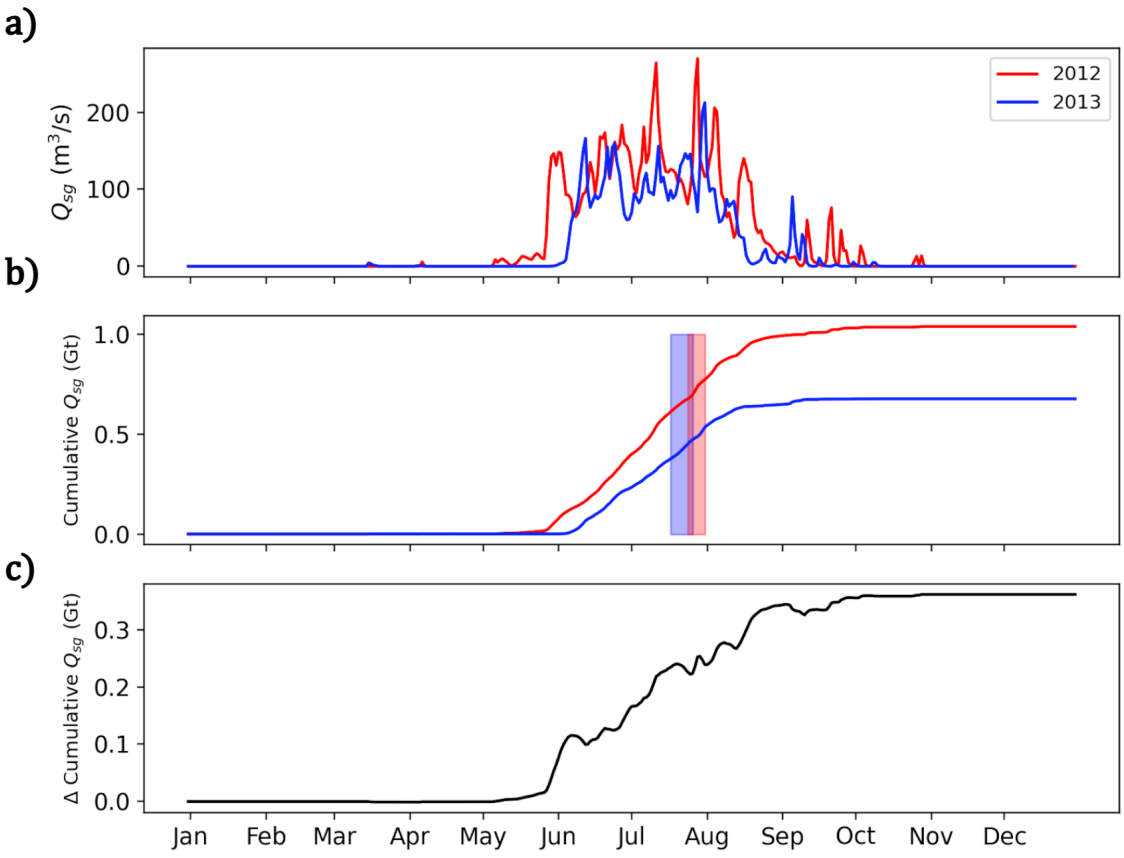

Figure 3.5. a) MAR SGD flux into SQ in 2012 and 2013. b) The cumulative SGD given in units of gigatonnes (Gt). Windows are overlaid during the period of the field campaign in 2012 (red) and 2013 (blue) c) The cumulative difference in SGD between 2012 and 2013.

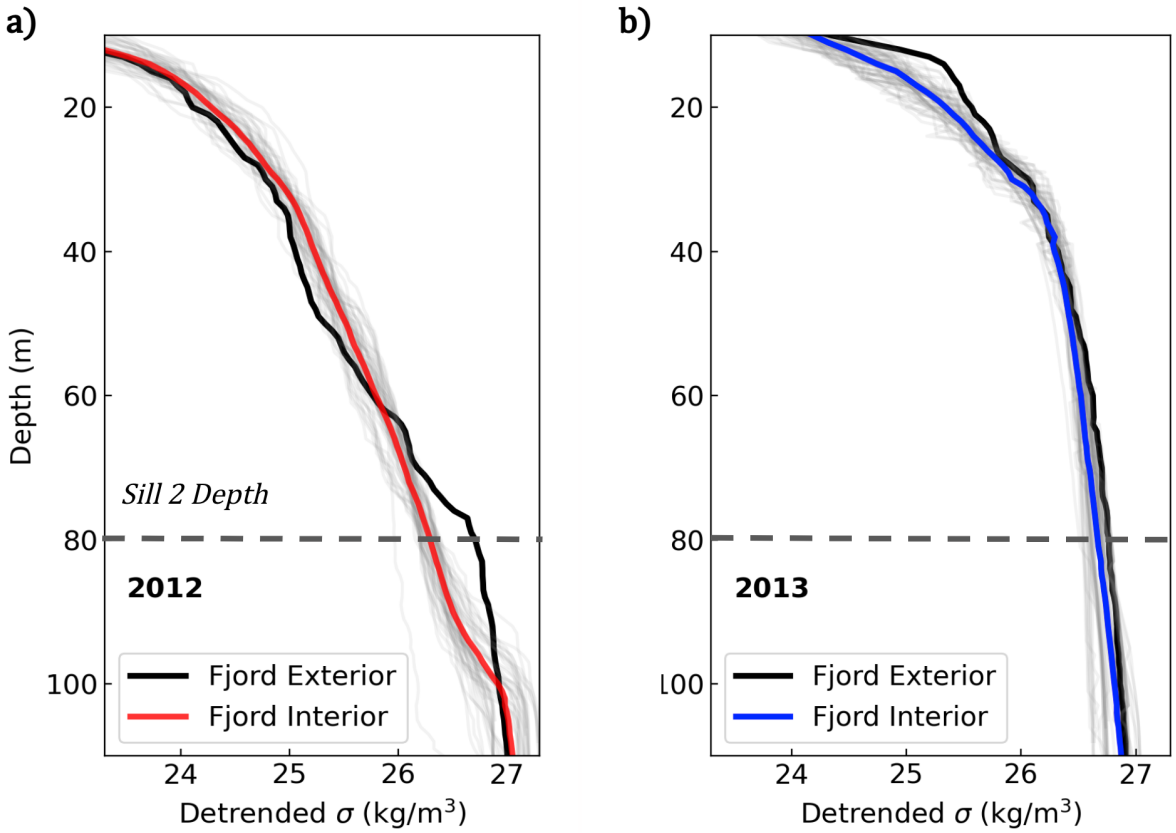

Figure 3.6. a) Detrended potential density anomaly for CTD casts in 2012 where the black cast was taken past S2 in Tasiusaq. The dashed line is the depth of S2. b) Same as *a* but for 2013; note that the black cast was calculated using an XCTD.

removed so that we can compare profiles taken on different days. Only a single cast was available from outside of the fjord in 2012, and only 2 profiles in 2013, however the density is outside the range of variability observed within the fjord, so the feature is less likely to be transient. The density difference which is centered at the sill depth suggests that as freshening progresses within the inner fjord, the sill can block the export of deep, relatively fresh waters. In 2013, when there was no visible difference between interior and exterior casts, the influence of SGD likely did not extend below S2. The density differences at depth between 2012 and 2013 further support the hypothesis that freshwater is being mixed from the surface downward, as the fjord had both a larger SGD flux and a longer time to accumulate freshwater at depth in 2012.

3.3.6 Seasonal Change in Circulation

A moored upward-looking ADCP observed fjord circulation for 9 months starting in July 2012, and the changes in circulation were consistent with a seasonal response to freshwater input (Fig. 3.7). Since the ADCP is located at a single point in an area of recirculation (Fig. 3.1c; Sup. Fig. 3.19), it provides an incomplete description of the full circulation. However, it remains the best data available to characterize the seasonal variation in velocity. Additionally, the depth structure of velocity recorded by the ADCP in July is consistent with the snapshot of overturning recorded by across-fjord transects (Sup. Fig. 3.20–3.24), indicating that the ADCP measurements are correlated with the large-scale fjord circulation. Therefore we separate the ADCP velocity into three phases: the plume-driven overturning circulation during the summer, an adjustment period in September, and a weaker phase of circulation after October (Fig. 3.7a). In July, the outflowing layer was about 30 m thick and centered around 25 m, while the inflowing layer was 40 m thick and centered around the depth of S2, and the basin layer below 100 m had relatively weak velocities (Fig. 3.7c). During this time period, the plume-driven overturning is clear with the upper layer (25 m) flowing straight out towards the mouth and the middle layer (80 m) flowing in towards the glacier (Fig. 3.7b). In late August, the estimated SGD flux dropped below 15 m^3/s (10% of peak; Fig. 3.5) and the upper layer was no longer consistently directed oceanward and there was intermittent flow reversal. In the middle layer however, the flow remained directed towards the glacier, although it was weaker in magnitude and eventually dropped below 0.005 m/s in October. During this transition period in September, the along-fjord velocity can be described as weak, but steady inflow below 20 m (Fig. 3.7c). The rapid change in the upper-layer velocity direction suggests that the plume-driven overturning is quickly shut down after SGD weakens, but that a weaker inflow is still present at depth. This weaker exchange flow could be driven by the density gradient between the fjord and S2 (Fig. 3.6a) that was previously maintained by the plume and recirculation. After October, the lower circulation is weak (< 0.005 m/s) and no longer directed towards the glacier. The time interval between the plume shut down

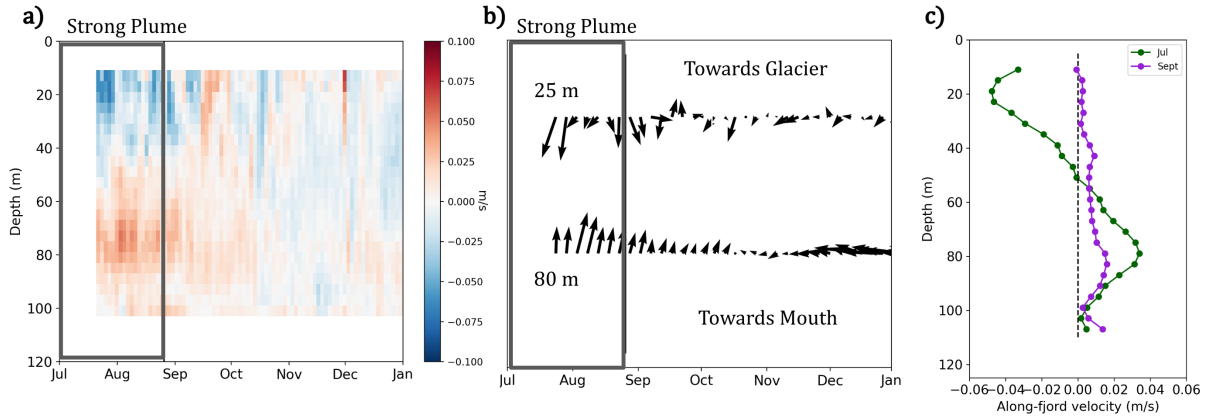

Figure 3.7. a) Time series of (2-day running mean) along-fjord velocity from moored ADCP. Negative velocities are directed out of the fjord. The time period when SGD is substantial (> 10% of peak) is outlined in black. b) Directional plot of the (5-day running mean) along-fjord velocity at the depths 25 m (top) and 80 m (bottom). Arrows pointing directly up show flow towards the glacier. West is to the right and the along-fjord velocity is defined positive at 170 degrees from North at this location. c) Vertical profile of along-fjord velocity averaged over the months of July (green) and September (purple).

(Q_{sg} < 15 m^3/s) and the shift in circulation to weak velocity is approximately 45 days. Although we lack CTD observations in the fall, Mernild et al. (2015) show a rapid salinity increase in SQ coincident with the shift away from the overturning circulation observed by the ADCP in September.

3.4 Box Model of Freshwater Storage and Export

We develop a box model to better understand the seasonal variability of fjord circulation and estimate storage of freshwater. The observations imply that under sustained SGD the fjord freshens (Fig. 3.3) and that freshwater is mixed downward throughout the summer (Fig. 3.6) before eventually being exported in the fall (Fig. 3.7). However, we lack measurements to capture this process continuously and instead rely on observations collected from different years as proxies of different points in the melt season. A box model enables us to explore the dynamics controlling the seasonal cycle and quantify timescales for both freshwater storage and export.

The model is similar in style to previous minimal fjord models in that layer thicknesses

and properties evolve according to parameterized exchange with the SGD plume (Zhao et al., 2021) and the external fjord basin (Tasiusaq, Babson et al., 2006; Gillibrand et al., 2013). The model is kept as simple as possible intending to resolve only the first-order dynamics controlling the salinity of the fjord.

3.4.1 Box Model Setup

Model Layout

We assume the fjord can be described as a three-layer system where the top layer is composed of outflowing glacially-modified water, the middle layer has inflowing water above sill height, and the basin layer has water that is isolated in the deep basin by the sills (Fig. 3.8). These layers roughly correspond to the observed salinity layers (Fig. 3.2), and are meant to represent the overturning circulation within the fjord (Fig. 3.7c). The boxes are forced by a plume at the glacier end and can exchange water in and out of the fjord at the sill 2 (Fig. 3.8). The fjord has a total depth H and surface area A that is constant with depth. The bottom box represents the waters below sill depth at all times, and therefore we set and hold fixed H_3. Since water is entrained into the plume from this layer, this necessitates the inclusion of an overflow term, Q_O, that represents a flux from the middle layer to the bottom layer. The fjord exterior is assumed to be composed of water with an average salinity S_{ext}.

Temperature is dynamically passive since density gradients are dominated by salinity, and because temperature is relatively homogeneous below 15 m we neglect it from the box model. Submarine melting of the glacier is not included as a freshwater source because it is an order of magnitude smaller than the SGD flux (Table 1) and its omission simplifies the model equations. However in fjords that have large concentrations of icebergs such as Ilulissat Isfjord or Sermilik, SMW would have to be included as a freshening term (e.g. Moon et al. 2018, Bearid et al. 2018). Furthermore, inclusion of submarine melting in the box model was found to have little impact on freshwater storage (Sup. Fig. 3.26). We wish to keep the model as simple as possible to understand the effects of the primary freshwater source (SGD) so we neglect the effects of sea

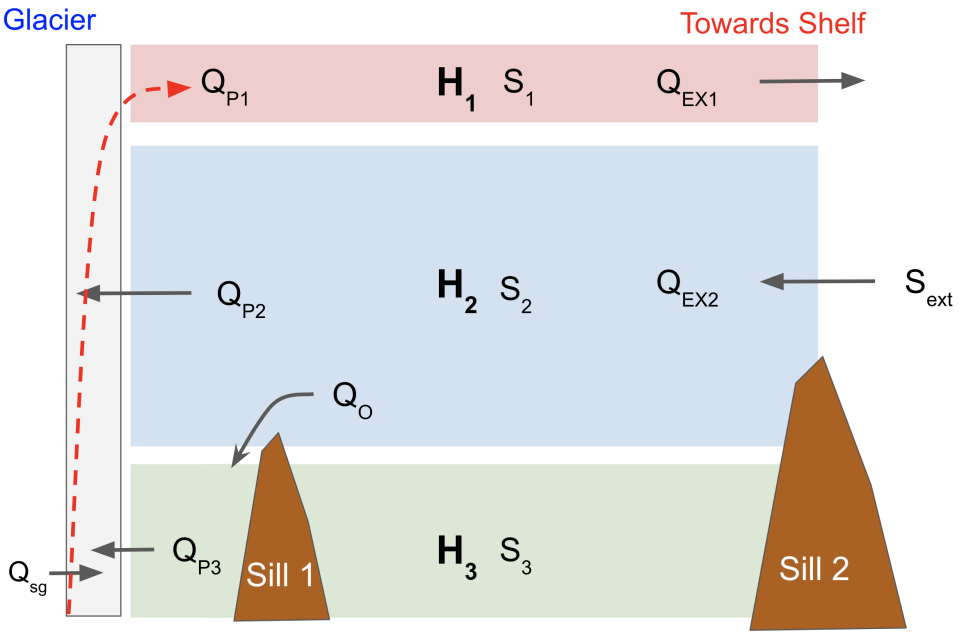

Figure 3.8. Schematic of the box model comprising an outflowing upper layer, and inflowing middle layer and a deep passive layer. Layer thickness and salinity is H_j, and S_j respectively where j denotes the layer. Volume flux exchange occurs at the fjord head due to the plume (red) which entrains from the boxes (Q_{Pj}) and at the outer edge due to fjord-shelf density gradients (Q_{EXj}). Sill 1 limits the depth of H_1 and overflow term Q_O is necessary to keep the basin layer volume constant. Sill 2 sets the height of the outflowing layer.

ice, winds, icebergs and surface forcing. Lastly, the model does not include mixing between layers explicitly, instead mixing is represented through changes in the layer thicknesses which are controlled by the balance between the SGD plume and exchange at the mouth.

Plume to Fjord Exchange

The effect of SGD is represented through a line plume which entrains ambient water as it rises and then outflows into the upper box H_1. Buoyant plume theory (Jenkins, 2011; Straneo and Cenedese, 2015) provides analytical expressions for plume volume fluxes, and the volume of ambient water entrained into the plume from the basin layer is given by

$$Q_{P3} = \alpha^{2/3}(g'_0)^{1/3} w^{2/3} Q_{sg}^{1/3} H_3, \tag{3.2}$$

where α is the entrainment coefficient, $g'_0 = g\beta_S S_3$ is the reduced gravity of the SGD relative to the basin layer, w is the plume width in the across-fjord direction, Q_{sg} is the SGD and H_3 is the thickness of the basin layer. The volume entrained is therefore determined by the initial buoyancy flux ($g'_0 Q_{sg}$) and the height over which the plume rises (H_3). The volume entrained from the middle layer into the plume is similarly given by

$$Q_{P2} = \alpha^{2/3} (g'_{P2})^{1/3} w^{2/3} (Q_{sg} + Q_{P3})^{1/3} H_2, \tag{3.3}$$

where $g'_{P2} = g\beta_S (S_2 - S_{P2})$ is the reduced gravity of the plume relative to the middle box and the volume flux of the plume entering the middle box has grown to include the entrained water Q_{P3}. The volume flux from the plume into the upper box is then equal to

$$Q_{P1} = Q_{sg} + Q_{P3} + Q_{P2}. \tag{3.4}$$

We also require expressions for the salinity of the plume as it rises. The salinity of the plume as it enters the middle box is

$$S_{P2} = \frac{Q_{P3} S_3}{Q_{P3} + Q_{sg}}, \tag{3.5}$$

and the salinity of the plume as it enters box 1 is

$$S_{P1} = \frac{Q_{P3} S_3 + Q_{P2} S_2}{Q_{P3} + Q_{sg} + Q_{P2}}. \tag{3.6}$$

External Fjord Exchange

The volume flux exchange out of the fjord could be parameterized in a number of ways depending on whether the flow is externally-forced (e.g., hydraulic control, wind forcing), or internally-forced, as is typical for estuarine circulation (Sutherland et al., 2014b; Zhao et al., 2018, 2021). Zhao et al. (2021) provides scalings for estimating the volume flux at the sill using

the density gradient across the sill for hydraulically controlled or relatively wide (geostrophic transport) fjords. Hydraulic control occurs when the Froude number $Fr = U/c$, a ratio of the advective speed U over baroclinic wave speed c, is greater than 1 at constrictions or sills. Ship-mounted ADCP velocity transects (Fig. S8–S12) show that although $Fr > 1$ close to the glacier within the jet, $Fr < 1$ at the sill so we do not believe hydraulic control to be occurring. We also found the predicted hydraulic control transport (12000 m^3/s) to overestimate transport from a ship-mounted ADCP transect (Sup. Fig. 3.25 (1900–6700 m^3/s, Sup. Table 3.4). The importance of geostrophic flow in estuaries can be quantified through the Kelvin number ($Ke = W/L_d$), a ratio of the fjord width over the deformation radius $L_d = c/f$, where c is again the baroclinic wave speed and f is the Coriolis frequency (Carroll et al., 2017; Jackson et al., 2018). In SF, Ke is around 1 in the channel (2 km width) and $Ke > 1$ in the wide basin (5 km width). Therefore, rotational effects are important in the wide basin, but flow within the channel is a combination of vertical and horizontal shear (Valle-Levinson, 2008). The predicted geostrophic transport (2600–3600 m^3/s) was similar to an estimate of the gravitational (estuarine) transport (2200 m^3/s), lending support for both approaches. We note that these two theories are not necessarily incompatible with one another. Ultimately, we choose to go with a gravitational parameterization since the primary density gradient we are interested in is produced close to the terminus, rather than across the sill. Therefore we set the exchange flow using a gravitational (estuarine) circulation

$$Q_{EX1} = W U_g \frac{H_s}{2}, \tag{3.7}$$

where W is the width of the fjord in the channel, U_g is a scalar velocity for the gravitational circulation and $H_s/2$ is half the sill depth and a scale height associated with the gravitational circulation to turn it into a volume flux. Note that we are solving for the volume flux and not for the layer velocity, since U_g is a scalar velocity not the velocity in a specific layer. In this way, a thin layer should be physically associated with a concentrated flux (faster velocity) and a larger layer should be associated with a diffuse flux (slower velocity).

While gravitational circulation is often dominant in shallower estuaries, we believe it is still appropriate for some glacial fjords despite their relatively large depths due to the vigorous mixing occurring within the plume system, along sidewalls or at sills. An estimate for the strength of the gravitational circulation can be derived assuming a balance between the baroclinic pressure gradient and friction (Geyer and MacCready, 2014)

$$U_g = \frac{g\beta_S H_{12}\bar{S}_x}{r}, \tag{3.8}$$

where $\bar{S}$ is the vertically-averaged salinity over the first two layers, the subscript x denotes an along-fjord gradient and $1/r$ is a frictional time scale. Equation 3.8 is a modified gravitational circulation where the classical mixing time scale H^2/K_m has been replaced by a frictional time scale $1/r$ due to uncertainty in the source of mixing. The average along-fjord salinity gradient can be rewritten:

$$\begin{aligned} \bar{S}_x &= \frac{1}{L}\left(S_{ext} - \bar{S}\right), \\ &= \frac{1}{L}\left(S_{ext} + \frac{H_1}{H_{12}}(S_2 - S_1) - S_2\right). \end{aligned} \tag{3.9}$$

where L is the along-fjord length scale, which we have chosen to be the distance from the glacier to the shelf.

Combining equations 3.7, 3.8, and 3.9 gives:

$$\begin{aligned} Q_{EX1} &= \frac{g\beta_S H_{12} H_s W}{2Lr}\left(S_{ext} + \frac{H_1}{H_{12}}(S_2 - S_1) - S_2\right), \\ &= \frac{\Gamma_{EX}}{r}\Delta\bar{S}. \end{aligned} \tag{3.10}$$

with the salinity gradient ($\Delta\bar{S}$), friction (r) and fjord geometry (Γ_{EX}) controlling exchange with the out of the fjord. The inflowing exchange flow term is defined overall from conservation of

volume within the fjord to be

$$Q_{EX2} = Q_{EX1} + Q_{sg} + Q_O. \tag{3.11}$$

Conservation Equations

Using the Boussinesq approximation, we neglect variations in density and approximate mass conservation with volume conservation. The conservation of volume for each of the boxes is given by the equations

$$A\frac{\mathrm{d}H_1}{\mathrm{d}t} = Q_{P1} - Q_{EX1}, \tag{3.12}$$

$$A\frac{\mathrm{d}H_2}{\mathrm{d}t} = -Q_{P2} + Q_{EX2}, \tag{3.13}$$

$$A\frac{\mathrm{d}H_3}{\mathrm{d}t} = -Q_{P3} + Q_O = 0, \tag{3.14}$$

where the choice $Q_O = Q_{P3}$ ensures the thickness of the deep box does not change. After substituting the volume conservation equations (3.12,3.13,3.14) into salinity conservation equations we arrive at the simplified salinity equations:

$$AH_1\frac{\mathrm{d}S_1}{\mathrm{d}t} = Q_{P1}(S_{P1} - S_1), \tag{3.15}$$

$$AH_2\frac{\mathrm{d}S_2}{\mathrm{d}t} = Q_{EX2}(S_{ext} - S_2), \tag{3.16}$$

$$AH_3\frac{\mathrm{d}S_3}{\mathrm{d}t} = Q_O(S_{ext} - S_3). \tag{3.17}$$

Initial Conditions and Forcing

The model is initially set up to resemble SQ in the spring before the melt season. We initially set $S_{ext} = S_1 = S_2 = S_3 = 33.57$ g/kg such that at the start of the melt season the box model

is constant in salinity. In the absence of submarine melting, and provided that S_{ext} is also constant in time (an assumption we make for these simple simulations), we then have $S_2 = S_3 = S_{ext}$ throughout the simulation. This choice simplifies the vertically averaged salinity to be

$$\bar{S} = S_{ext} - \frac{H_1}{H_{12}}(S_{ext} - S_1). \tag{3.18}$$

While this model includes a constant external salinity and constant friction coefficient, versions of the model with time-varying constants gave qualitatively similar results (Sup. Fig. 3.28). The layer thicknesses are initially set to $H_1 = 2$ m, $H_2 = 98$ m, and $H_3 = 50$ m, which is the height of sill S1. A minimum thickness of 2 m is required for the top two layers to keep the model stable and ensure that the model always has all three layers present. The box model geometry is chosen to be as close as possible to SQ with $A = 6.26 \times 10^7$ m^2, $W = 2$ km, $H_s/2 = 40$ m and $L = 60$ km. For the plume parameters, $\alpha = 0.13$, $w = 90$ m, and $\beta_S = 0.75 \times 10^{-3}$ kg/g (Jackson et al., 2017). The friction coefficient $r = 0.0012$ 1/s was chosen because it produced the best model fit with the observations. It is hard to compare this friction coefficient with observations, however comparison against a close analog, the diffusivity mixing time scale H_{12}^2/K_m, suggest the value of the coefficient is high (see Supplemental). The relatively high friction may be seen as compensating for the lack of recirculation in the box model.

The model is forced with SGD taken from the regional climate model MAR (Fig. 3.5; Mankoff et al. (2020)) and we assume a 15% uncertainty (Mankoff et al., 2020). The model is solved by stepping through the conservation equations with a Backwards Implicit Euler scheme using a 0.1 day timestep. The model is run from day 70 to day 365 in each of 2012 and 2013.

3.4.2 Model Results

We start with the box model's seasonal evolution and then compare the predicted salinity and salinity trends with observations. As SGD enters the fjord, the exchange out of the fjord is initially weak and so the top layer thickens (Fig. 3.9a). H_1 thickens earlier in 2012 than 2013

since SGD enters the fjord earlier, but both reach a maximum thickness of about 70 m. The salinity in the upper layer decreases (Fig. 3.9b) as freshwater is not sufficiently exported. The freshening of the upper layer starts earlier in 2012, but both years reach a minimum in salinity near day 218. As Q_{sg} weakens at the end of summer then the average salinity in the plume grows (Eq. 3.6) and S_1 starts to level off. Since the reduction in Q_{sg} occurs at a similar time in 2012 and 2013, salinity minimums in S_1 occur at similar times in both years.

As the upper layer gets thicker, the plume has less distance to rise and so less volume is entrained by the plume, decreasing Q_{P1} (Fig. 3.9c). At the same time, the changes in H_1 and S_1 increase the density gradient between the fjord and external fjord basin resulting in a higher exchange flow Q_{EX1}. H_1 increases until the exchange flow is greater than the inflow from the plume. Ultimately however, Q_{EX1} overtakes Q_{P1} only when Q_{sg} decreases and the plume shuts down. Since the crossing point is tied to Q_{sg}, it also occurs at a similar time in both years.

When Q_{EX1} overtakes Q_{P1} the fjord starts to net export the freshwater that was stored during the melt season Fig. 3.9c. We can estimate a timescale for this export as the time taken to exchange all water in the upper layer if the exchange is maintained at its maximum value:

$$\tau_{export} = \frac{AH_1(t_{min})}{Q_{EX1}(t_{min})}, \tag{3.19}$$

where t_{min} is the time when the salinity is minimized and Q_{sg} starts to fall off. In 2012 and 2013, τ_{export} = 48 and 57 days, respectively, which is similar to the 45 day adjustment timescale estimated from changes in the baroclinic circulation in 2012 (Fig. 3.7).

The box model results compare reasonably well with the $\bar{S}$ measurements from CTD casts collected in 2012 and 2013, with a mean square error (MSE) of 0.61 g/kg that is reduced after taking into account the uncertainty in Q_{sg} (Fig. 3.10a). The model also predicts an increase in vertically averaged salinity after the plume shuts off that is consistent with the seal observations from Mernild et al. (2015). The modeled magnitude of salinity trend early in the season matches the magnitude of the observations, but suggest that the magnitude of $\mathrm{d}\bar{S}/\mathrm{d}t$ (Fig. 3.10b) decreases

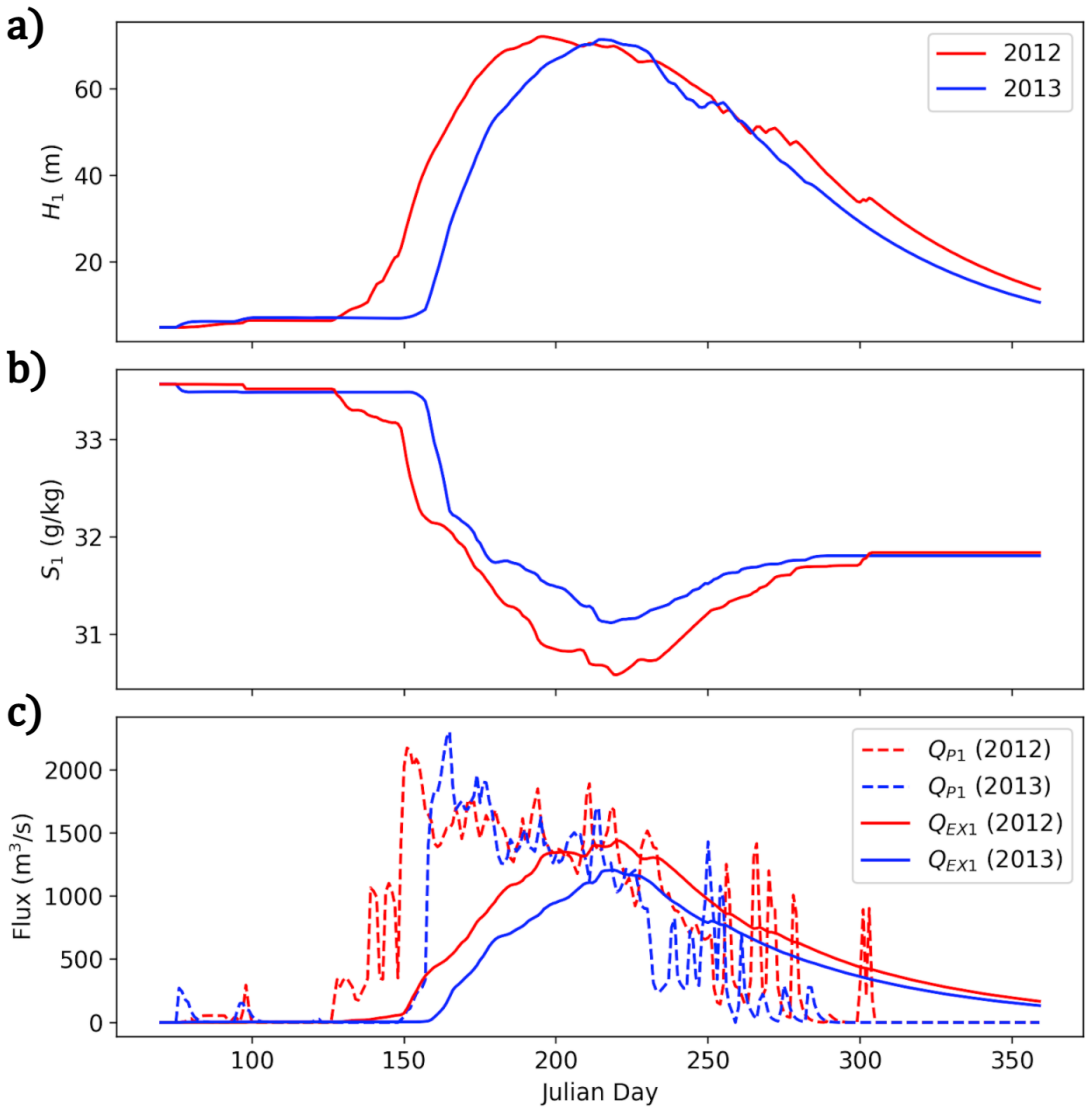

Figure 3.9. a) Box model H_1 for 2012 (red) and 2013 (blue) as a function of Julian day. b) same as a, but for S_1. c) Volume fluxes in and out of the top box with dashed lines for the plume fluxes in and solid lines for exchange flow fluxes out.

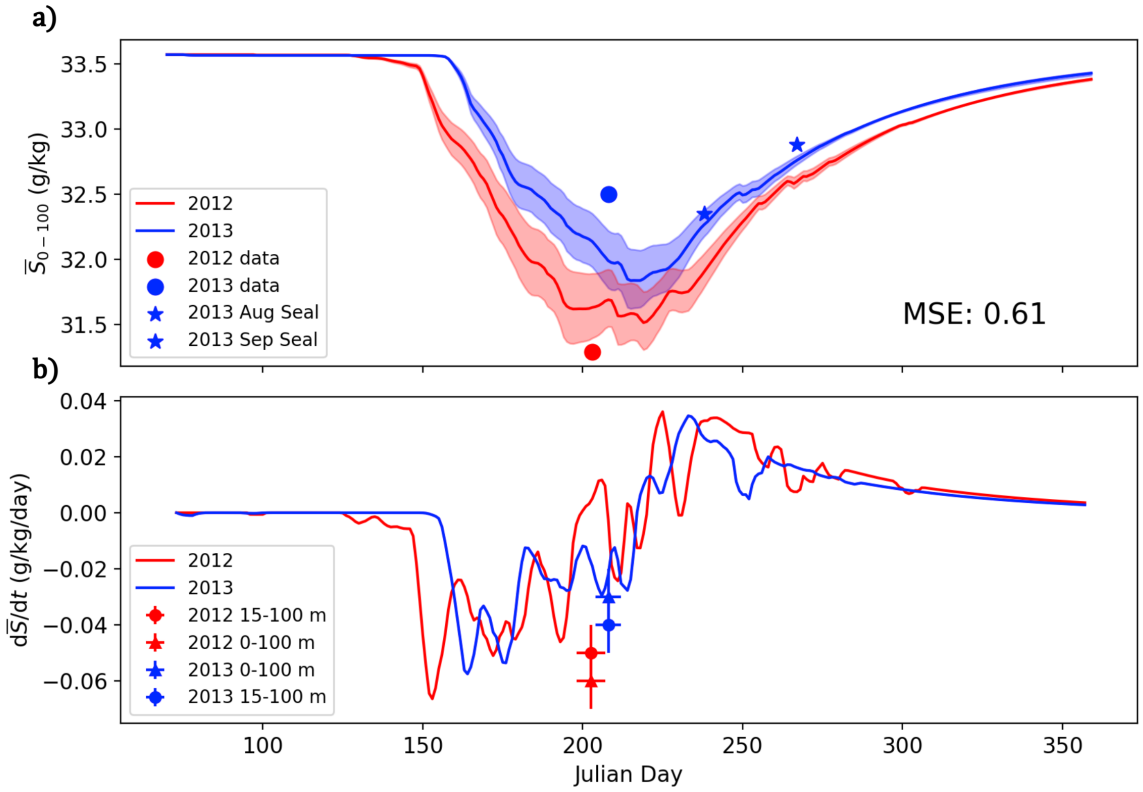

Figure 3.10. a) Comparison of the observed vertically averaged salinity ($\bar{S}$) from 0 to 100 m from both the field campaigns and Mernild et al. (2015) seal data against the box model vertically averaged salinity. The shading represents the uncertainty due to SGD flux. b) The derivative of $\bar{S}$ from the box model compared against the observed salinity trends (Fig. 3.3). The circles are the salinity trend from 15–100 m (Fig. 3.3) while the triangles are the observed trend from 0–100 m. The horizontal error bars represent the length of the field campaign and vertical error bars represent the uncertainty in the salinity trend. Note the box model does not contain any surface forcing.

over summer. Taken as whole, the comparisons against observations suggest the box model does a reasonable job of capturing the observed salinity properties given the model's simplicity. Potentially, the model needs a greater sensitivity to Q_{sg}, since $\bar{S}$ is underestimated in 2012 and overestimated in 2013.

3.4.3 Freshwater Export

The combined mean salinity of a layer H_{fw} of pure freshwater and a layer $H_{12} - H_{fw}$ of water with salinity S_{ext} is

$$\bar{S}_{fw} = \frac{H_{fw}S_{fw} + (H_{12} - H_{fw})S_{ext}}{H_{12}}, \tag{3.20}$$

and therefore we could define the pure freshwater volume in the fjord by $V_{fw} = AH_{fw}$, assuming that there is no freshwater below the inner sill. The mean salinity in Eq. 3.20 is equivalent to $\bar{S}$ (Eq. 3.18) and so the net freshwater accumulation or export can be be expressed as

$$\frac{\mathrm{d}V_{fw}}{\mathrm{d}t} = A\frac{\mathrm{d}H_{fw}}{\mathrm{d}t} = -H_{12}A\frac{\mathrm{d}\bar{S}}{\mathrm{d}t}\frac{1}{S_{ext}}, \tag{3.21}$$

after rearranging Eq. 3.20 and taking the derivative. Additionally, since we know the freshwater fluxes into the fjord (Q_{sg}) we can solve for the freshwater flux out of the fjord Q_{fw} through the relation

$$Q_{fw} = Q_{sg} - \frac{\mathrm{d}V_{fw}}{\mathrm{d}t}. \tag{3.22}$$

As seen in the box model salinity, the fjord begins to accumulate freshwater once Q_{sg} is non-zero in early summer (Fig. 3.11a), because the exchange out of the fjord is insufficient to balance the plume fluxes (Fig. 3.9c, 3.11b). Freshwater continues to accumulate until it reaches a maximum at 0.3–0.4 Gt around day 218 in both 2012 and 2013. Beyond this, Q_{sg} decreases and the export of freshwater between fjord basins exceeds freshwater input, so that the freshwater volume in the fjord decays exponentially through the fall (Fig. 3.11a,b). The peak of Q_{fw} is smaller than the peak magnitude of Q_{sg} because the freshwater flux is distributed over a longer time period. In both years, the peak freshwater fluxes from the fjord are offset from SGD input by about a month (Fig. 3.11b). The ratio of freshwater stored, $R = 1 - Q_{fw}/Q_{sg}$, shows a roughly linear decrease in freshwater storage with most freshwater stored early in the season, and most

exported late in the season (Fig. 3.11c).

3.4.4 Scaling for freshwater storage

We can generalize the results of the box model to other fjord systems by examining the factors controlling the boundary volume fluxes which set the fjord freshwater content. First, we scale the salinity gradient as

$$\overline{S}_x = \frac{V_{fw}}{V_f + V_{fw}} \frac{S_0}{L_S}, \tag{3.23}$$

where V_{fw} is the volume of freshwater inside the fjord, $V_f = HLW$ is the volume of the fjord, S_0 is a reference salinity and L_S is the length scale of the salinity gradient, which is not necessarily the same as the length scale of the fjord. Noting that $V_f \gg V_{fw}$, we end up with a scaling for the exchange flow from Eq. 10 as

$$Q_{ex} = C_{out} \times \frac{H_s V_{fw}}{2 L L_S r}, \tag{3.24}$$

where C_{out}=$g\beta_S S_0$ includes all the constants which vary little from fjord to fjord.

Similarly the plume flux can be approximated from Eq. 2 as

$$Q_p = C_{in} \times Q_{sg}^{1/3} H^* + Q_{sg} + Q_{smw}, \tag{3.25}$$

where $C_{in} = \alpha^{2/3} g'^{1/3} w^{2/3}$ is a constant, $H^* = H_{gl} - H_s/2$ is the height the plume rises before it enters the top box, and Q_{smw} is the submarine meltwater contribution. Noting that Q_{smw} and Q_{sg} are much smaller than the first term (e.g. Mankoff et al., 2016), the ratio of export to storage can be written as

$$R_{stor} = \frac{C_{out} V_{fw} \delta}{C_{in} Q_{sg}^{1/3} L L_S r}, \tag{3.26}$$

where δ is the height of the outflowing layer ($H_s/2$) over the height of the rising plume (H^*); analogous to the height of the sill over the height of the grounding line. If the grounding line is the same depth as the sill then δ=1, while realistic examples are δ=0.18 for Ilulissat Isfjord (IL), 0.36 for Saqqarleq (SQ) and 0.73 for Sermilik (SM). From Eq. 26 it is clear that δ is an

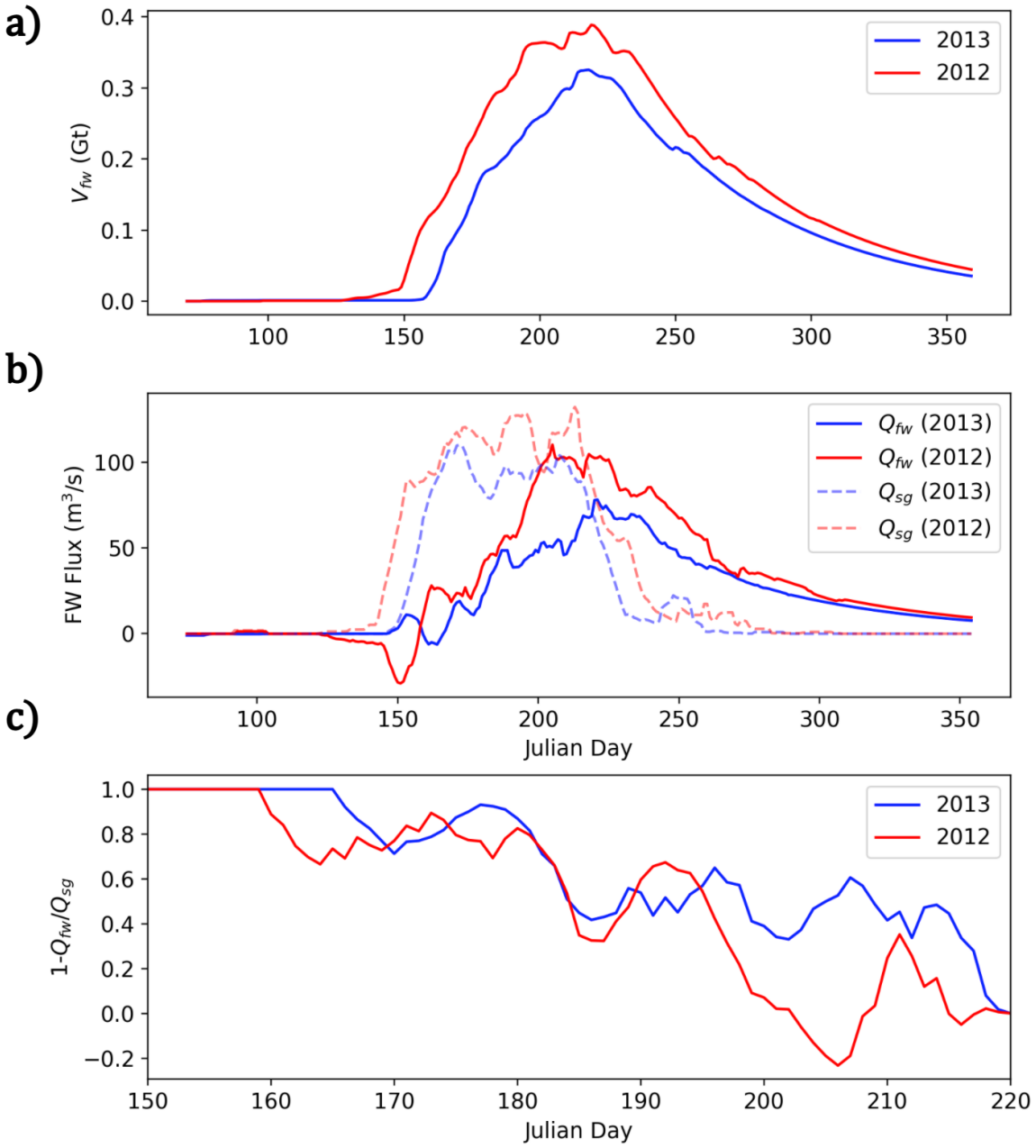

Figure 3.11. a) The volume of freshwater (V_{fw}) stored in the box model for 2012 (red) and 2013 (blue) as a function of Julian day. b) Freshwater export (Q_{fw}) from Eq. 3.22 and SGD (Q_{sg}) in the box model. The a 10-day running mean has been applied to smooth the signal. c) The fraction of SGD that was stored in the fjord during the time period when the plume was active.

important parameter controlling freshwater residence time, consistent with Carroll et al. (2017). Additionally, increasing the length of the fjord and the density gradient length scale reduce the exchange flow strength, although for larger systems this increase in storage is likely compensated by a larger total freshwater content (V_{fw}) which increases the density gradient. If friction is dominated by bottom dissipation, then r will be smaller in deeper fjords, but if r is primarily determined by sidewall dissipation or mixing near the plume it might take a similar value from system to system.

We can evaluate how V_{fw} compares across fjord systems under steady state. Initially, the stored freshwater will start out small and all glacial fjords should be in a position where $R_{stor} < 1$. However as V_{fw} increases, a steady state regime will be reached when $R_{stor} = 1$. Using representative values (Table 3.2): we set $R_{stor} = 1$ and get a V_{fw} of 1.9, 0.20, and 2.5 (10^9 m^3) for SM, SQ and IL, respectively, indicating IL will store the most freshwater before exchange is efficient at removing it. However, as a proportion of fjord volume these are 0.004, 0.03, and 0.008 for SM, SQ, and IL which indicates we should expect the greatest changes in mean salinity to occur in SQ. Based on Eq. 3.26, we see that SQ might be uniquely placed to observe large freshening because it is relatively small and has a moderate sill height compared to grounding line depth. For other systems, such as SM, the combination of a deep sill and large fjord volume may limit the observed freshening. With a known rate of freshwater input (eg, Q_{smw} or Q_{sg}), this threshold V_{fw} could be turned into a residence time. However, these results are based on the assumption that fjord circulation can be described as a gravitational circulation. The exchange of other glacial fjord systems might be primarily wind-driven, geostrophic or hydraulically controlled (e.g. Jackson et al., 2014; Schaffer et al., 2020; Zhao et al., 2021) and so care should be taken in choice of the exchange flow parameterization. Lastly, for systems with significant iceberg cover, we expect iceberg melt to significantly impact the freshwater budget such that it should be accounted for in the box model Moon et al. (2018); Davison et al. (2020).

Table 3.2. Table of values used in the exchange flow scaling for three fjord systems. Q_{sg} is the average SGD in July in 2012 and 2013 (Mankoff et al., 2020). For Sermilik and Ilulissat we assume $L = L_s$ because these systems connect directly with the shelf.

Fjord	Q_{sg}	L	L_s	V_f	$\delta = H_s/2H^*$
Sermilik	1350 m^3/s	90 km	90 km	5×10^{11} m^3	0.73
Saqqarleq	125 m^3/s	16 km	60 km	7×10^9 m^3	0.36
Ilulissat	1750 m^3/s	50 km	50 km	3×10^{11} m^3	0.18

3.5 Discussion

3.5.1 Mechanisms driving freshwater storage

We observe that the mean salinity of SQ decreases during the melt season due to the net accumulation of freshwater. We propose that this process occurs primarily through vertical mixing of SGD. Initially, the density-driven exchange out of the fjord is insufficient at removing freshwater stored near the head, but as the fjord freshens, the exchange flow increases until either the plume shuts off or the fjord reaches steady state. In this section, we discuss these steps in more detail and discuss the possible physical processes contributing to freshwater storage.

The hydrographic observations indicate that the region close to the glacier (< 6 km from the terminus) was accumulating freshwater during the field seasons (Fig. 3.3) and that the freshening occurred from the surface downward. While submarine melting of glaciers, especially in larger fjords, provides a freshening source at depth, we identify SGD as the primary freshwater being stored. This finding is consistent with independent estimates of freshwater flux into the fjord as Wagner et al. (2019) estimated a combined calving and SMW flux of 0.5 Gt/yr during summer compared to our MAR-estimated SGD flux of 3.5–4.4 Gt/yr during summer.

Using our box model we explored the balance between plume-driven freshwater storage and density-driven freshwater export between fjord basins. Early in the melt season, the exchange out of the fjord is weak and freshwater from the jet is mixed vertically (Fig. 3.12a). This process

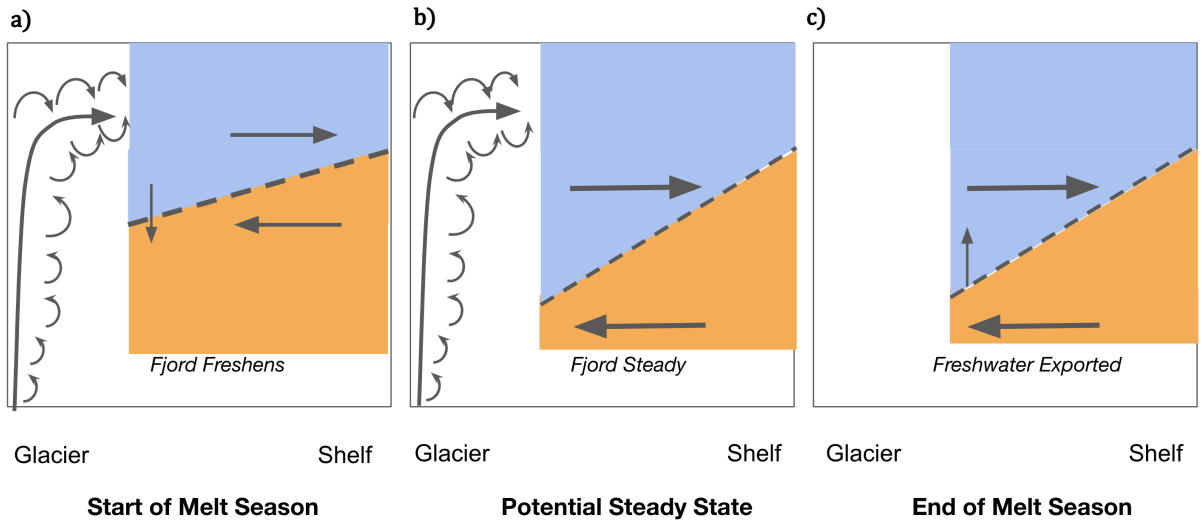

Figure 3.12. Schematic of the freshwater storage process. The first panel represents the start of the melt season with mixing near the head of the fjord deepening the pycnocline and relatively weak exchange flow. The middle panel represents a potential steady state that could be reached during the melt season between exchange and mixing within the fjord. The third panel represents the end of the melt season or when mixing tied to the buoyancy-driven circulation weakens and exchange is strong.

deepens the pycnocline within the fjord, akin to H_1 increasing in the model, and is consistent with observed stratification and density profiles of the fjord (Figs. 3.2, 3.6). As the pycnocline deepens, the along-fjord density gradient between the fjord and the shelf increases until a crossing point is reached between the tendency for storage and export (Fig. 3.12b). After the plume shuts down, freshwater is no longer accumulated and the fjord adjusts through exchange with the external fjord basin over the next 45 days (Fig. 3.12c). In reality, the along-fjord density gradient is non-linear in space with the majority of the isopycnal gradients occurring close to the glacier (Mankoff et al., 2016), and mixing in the rest of the fjord likely relatively weak, but not negligible (Bendtsen et al., 2021).

In our box model, the mixing of freshwater between layers is not represented explicitly and instead is included in the exchange parameterization through the frictional time scale $1/r$. Although the friction appears physically consistent with shear-driven mixing from the jet (see Supplemental), other possible sources of mixing which could be represented include dissipation

along the walls of the fjord or in the lee of a sill. These mixing processes are common in non-glacial fjords (Klymak and Gregg, 2004; Staalstrøm et al., 2015) and along sinuous submarine canyons (Wain et al., 2013), and will be intensified in the presence of recirculation. Additionally, small scale mixing from the submarine melting of ice outside of the plume would enhance the background diffusivity, and future field campaigns should be designed to estimate the energy budgets of these systems.

The parameterization could further be improved by representing recirculation which likely acts to increase the residence time of freshwater in the fjord. Recirculation gyres driven by plumes are found in both observations and models to exist near termini in fjord (Carroll et al., 2017; Slater et al., 2018; Zhao et al., 2021) and large scale recirculations in glacial fjords are connected to glacial melt-rates and overturning strength (Zhao et al., 2022a). The strong recirculation cell in SQ can potentially contribute to freshwater storage by redirecting SGD away from the export and back into the plume. Although only a snapshot, ADCP transects across the fjord indicate the volume flux in the recirculation gyre was substantially higher than in the main channel and approximately 50% of the main outflow was redirected back towards the plume in 2013.

We propose the stratification of the fjord increased during the summer, in part due to vertical mixing of freshwater. Glacial fjord plumes are energetic and turbulent (Podolskiy et al., 2021), and shear-driven mixing from buoyant jets can take freshwater at the surface (or within the plume itself) and mix it down below the primary export depth. Recently Bendtsen et al. (2021) found that turbulent mixing rates close to the terminus of Store Gletscher were 100 times higher than mixing rates in the rest of the fjord. Additionally, De Andrés et al. (2020) showed that in 2012 the hydrographic properties of the plume-turned-jet were significantly diluted within a few hundred meters of the terminus indicating that there was additional entrainment and mixing by the jet outflow. Velocity transects across SQ (Sup. Figs. 3.20–3.24), show that the Froude is greater than 1 in the core of the outflowing jet indicating that the jet was an inertial-driven flow susceptible to strong shear-driven mixing.

Freshwater storage has also been observed in a glacial fjord in LeConte, Alaska due to the outflow plume impinging on the sill and being redirected back towards the glacier (Hager et al., 2022a). In that study, a reflux coefficient (Cokelet and Stewart, 1985; MacCready et al., 2021) is calculated which quantifies the amount of export that is mixed vertically back towards the glacier. In a more generic box model than the one we have presented, a reflux coefficient that is a function of Q_{sg} could be added to the fjord-exchange parameterization. Tidal flow over the sill is responsible for the intense mixing which leads to the observed freshwater storage in Godthåbsfjord (Mortensen et al., 2011, 2014). Another potential source of mixing includes internal waves which can be generated by the plume when it impinges on the pycnocline or from tidal flow over the sill (Ezhova et al., 2016, 2017; Mortensen et al., 2014; Stuart-Lee et al., 2021). Therefore, sills and regions close to the terminus are likely mixing "hot spots" that are elevated by SGD plumes and buoyancy-driven circulation (Bendtsen et al., 2021). Lastly, the interior stratification of the fjord could increase due to the compression of isopycnals with no significant interior mixing taking place. In this scenario, the isopycnal layer corresponding to the neutral buoyancy depth of the plume thickens and the isopycnals below and on top of the neutral buoyancy depth get closer together. However, if this was the dominant mechanism of observed freshening, then the profiles would overlap in TS space in contrast to our observations, which indicate mixing with SGD and SMW (Fig. 3.4).

3.5.2 Delayed Freshwater Export

In ocean circulation models that include Greenland Ice Sheet freshwater forcing, the effects of freshwater storage within glacial fjords should be included as the potential lag can be significant. The lag in peak freshwater export, or freshwater residence time, determined from the box model in SQ is about a month. Our estimated timescale of stored freshwater export is faster than in nearby Ameralik fjord (Stuart-Lee et al., 2021) and Godthåbsfjord (Mortensen et al., 2018), but these glacial fjords have strong tidal mixing and are primarily renewed by dense coastal overflows in the winter. However, our timescale of stored freshwater export is similar to

the timescale of destratification that occurs in the fall in LeConte, Alaska (Hager et al., 2022a).

It is clear that the lag in freshwater export will be determined by the relationship between exchange at the mouth Q_{ex} and the volume flux from the plume Q_p as our scaling showed (Eq. 3.26). In a system where Q_{ex} is primarily driven by shelf-forcing (e.g. along-shore winds, eddies, coastal trapped waves) then Q_{ex} will be independent of Q_p and freshwater storage will be set by whether the shelf forcing acts to enhance or reverse the buoyancy-driven flow (Giddings and MacCready, 2017). If however, Q_{ex} is driven by buoyancy forcing from the glacier, then its value at the mouth will be sensitive to the amount of reflux or recirculation which occurs within the fjord both of which can act to increase freshwater storage. These volume fluxes will also be influenced by fjord geometry. For example, fjords that are narrow and have shallow sills will limit Q_{ex} resulting in a larger delay of freshwater export (Zhao et al., 2021). Given the sensitivity of fjord-shelf exchange to a number of parameters (e.g. tides, winds, iceberg presence, fjord geometry), continental-wide estimates of freshwater export delay will need to be informed by observations of both hydrography and bathymetry from within a large number of Greenland's glacial fjords (Straneo et al., 2019).

3.5.3 Applicability to other fjord systems

Due to several factors such as fjord size and the presence of a single oceanic water mass, it is easier to detect freshwater storage in SQ than in other glacial fjords. As shown with Eq. 3.26, the volumes of larger glacial fjords such as Sermilik or Ilulissat Icefjord reduce the magnitude of observable salinity trends despite greater freshwater fluxes. However, Stuart-Lee et al. (2021) observed freshwater storage and delayed export occuring in Ameralik, a land-terminating glacial fjord in West Greenland. In that study they attributed the freshwater storage to intense tidal mixing at the sill which drew down freshwater from the surface and increased fjord stratification during the summer and into the fall. This process could also be occurring in SQ and future work should aim to quantify the contribution of tidal mixing at the sill versus mixing induced by the plume/jet. We attribute the mixing primarily to physical processes linked with the jet because we

observe freshening first near the terminus and then at S2. However, the two mixing processes are likely working together to increase the fraction of freshwater that is stored.

The processes that led to rapid freshening in SQ, including turbulent plumes and glacier-wide recirculation, will be active in all of Greenland's major glacial fjords since they are driven by SGD. Making equivalent observations to those in SQ at large glacier-fjord systems is extremely challenging due to mobile and thick ice mélange, but the downsloping isopycnals observed near the heads of some glacial fjords (Gladish et al., 2014b; Jackson and Straneo, 2016; Beaird et al., 2015) could be evidence of a vigorous near-terminous circulation. Experiments with additional endmembers, such as noble gases or oxygen, which can be used as meltwater tracers, are needed to confirm the late departure of freshwater in other systems (Beaird et al., 2015, 2017, 2018).

3.6 Conclusion

Glacial fjord circulation and properties are often described as bi-modal with plume-driven circulation and strong stratification in the summer and a shelf-driven circulation and weak stratification in the winter. This viewpoint overlooks the potentially significant subseasonal variability within fjords and the potential for transient storage of ice sheet freshwater. We find evidence that during the summer, freshwater is stored within Saqqarleq, a mid-sized glacial fjord in west Greenland, resulting in non-steady mean salinity during the melt season. Specifically, observations of salinity collected in SQ show a freshening trend of 0.05 g/kg/day and 0.04 g/kg/day in 2012 and 2013 respectively . The observations suggest that vertical mixing of SGD increases stratification and freshwater content within the fjord when the plume is active. We developed a box model that is forced by SGD at its glacial boundary and a density-driven exchange with at its sill boundary. Competition between these boundary conditions determines whether freshwater is being stored or removed from the fjord. The box model indicates that glacial fjords with intense mixing are inefficient at removing freshwater, resulting in a lag of 25–30 days between the peak SGD entering the fjord and the freshwater export from the fjord.

Future work should aim to identify this process in larger glacial fjords and quantify the interior mixing that redistributes freshwater. Our results provide evidence that fjords modulate the timing and magnitude of ice sheet freshwater entering the wider ocean; processes that should be represented in large-scale climate models if we are to better predict the impact of ice sheet meltwater on the ocean.

3.7 Acknowledgments

We would like to acknowledge Margaret Lindeman for helpful discussion and suggestions. We acknowledge Clark Richards, Rebecca Jackson, Sarah Das, Jeff Pietro and others for help in collection of the data. RS and FS acknowledge funding from the NSF. DAS acknowledges support from NERC Independent Research Fellowship NE/T011920/1.

Data for 2013 is available through the NSF Arctic Data Center at the following DOIs: 2013 Ship-based ADCP measurements (doi:10.18739/A2P843W9W); 2013 CTD profiles (doi:10.18739/A2B853H78); moored ADCP (doi:10.18739/A2G73753N); pressure data (doi:10.18739/A2M03XZ70). The 2012 Ship-based ADCP and CTD measurements are available through the NOAA National Centers for Environmental Information (NCEI) using NCEI Accession Number 0210572. The subglacial meltwater discharge data is available from Mankoff et al. (2020). Python notebooks to run the box model are available upon request.

Chapter 3, in full, is a repreint of the material that has been accepted in *Journal of Physical Oceanography*, 2023, Sanchez, R., Slater, D., Straneo, F. , American Meteorolgical Society, 2023. Used with permission. The dissertation author was the primary investigator and author of this paper.

3.8 Supporting Information

Detiding Velocity

In order to remove tides from the moored ADCP and velocity transects we need to

calculate tidal amplitudes (η). In 2012, a pressure sensor directly recorded tidal amplitudes (Fig. 3.13a) over a two week period. The sensor was in approximately 1.5 m of water. In 2013 and for the moored ADCP, the pressure sensor was not available and so the tides were estimated using output from the Arctic Tide Inverse Model (Padman and Erofeeva, 2004; Erofeeva and Egbert, 2020). The model compares remarkably well with the tidal variations observed at the pressure sensor (Sup. Fig. 3.13). The barotropic tide was therefore removed from the velocity transects and moored ADCP using the relationship

$$U_{tide} = \frac{\mathrm{d}\eta}{\mathrm{d}t}\frac{A_b}{A_c}, \tag{3.27}$$

where A_b is the surface area upstream of the measurement, A_c is the cross-sectional area of the fjord at the measurement, and $\mathrm{d}\eta/\mathrm{d}t$ is the derivative of the sea surface height. The estimated barotropic tide at the location of the moored ADCP is not very large (Sup. Fig. 3.13b) compared to other velocity signals (Fig. 7 main text). However, the barotopic velocity at S2 is predicted to be 0.025 m/s. The phasing of the baroclinic tidal velocity is more difficult to estimate and is thus not removed, but at the ADCP this velocity is within the range 0.05- 0.1 m/s.

Calibrating Mernild et al. (2015) data

We infer seal data from Mernild et al. (2015) to extend our observations into the fall. The data was extracted from Mernild et al. (2015) figures and the data is compared to the results of the box model. We calibrate the seal data against the absolute salinity measured by our field campaigns (Fig. 3.14). Despite the large interannual differences in our salinity profiles above 100 m, we note that the salinity difference below 100 m was only 0.1 g/kg. We adjust the seal data by applying a depth uniform offset of 0.55 g/kg so that the bottom value is in line with those measured by our CTD profiles.

Determining the Freshwater Contributions

We determine the contributions to freshening of waters in the fjord using a water mass analysis. Multiple freshwater sources (SGD and SMW) can potentially drive salinity variability.

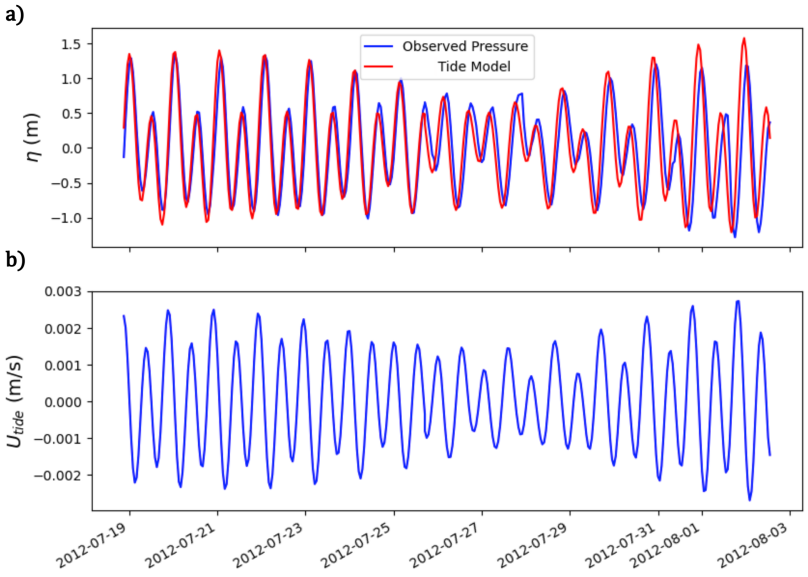

Figure 3.13. a) Comparison of sea-surface height in SF from a pressure sensor and the output from the Arctic Tide Inverse Model. b) Resulting estimate of barotropic velocity at the moored ADCP location.

At each depth, we calculate the observed change that is attributable to SGD versus SMW using a mixing model with temperature and salinity as constraints. This type of water mass analysis is possible if we assume the fjord is originally composed of only a single water mass. Additionally, we are only analyzing data collected below 25 m, which is below the surface layer and potential surface forcing. We follow the procedure of Mankoff et al. (2016) and Mortensen et al. (2020) which uses three conservation equations for temperature (Θ), salinity (S) and volume

$$f^i_{SGD}\Theta_{SGD} + f^i_{SMW}\Theta_{SMW} + f^i_{DW}\Theta_{DW} = \Theta^i_{Obs}, \tag{3.28}$$

$$f^i_{SGD}S_{SGD} + f^i_{SMW}S_{SMW} + f^i_{DW}S_{DW} = S^i_{Obs}, \tag{3.29}$$

$$f^i_{SGD} + f^i_{SMW} + f^i_{DW} = 1, \tag{3.30}$$

to solve for the fraction (f^i) of three water masses [SGD, SMW, and deep water (DW)] at

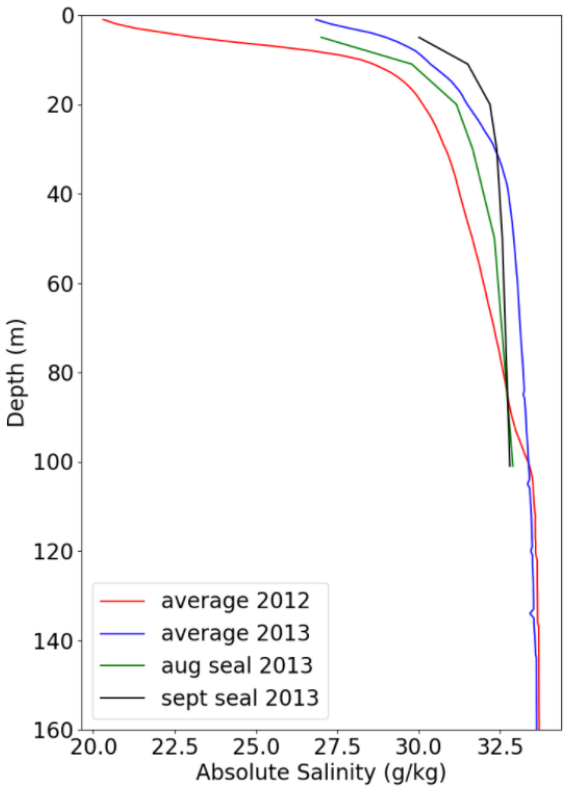

Figure 3.14. Average salinity profiles taken from the field campaign in 2012 and 2013 alongside seal profiles taken from Mernild et al. (2015) that were an average over August and September.

each of the depths i = 25 m, 40 m, and 80 m. DW refers to the homogenous layer below 100 m depth. Θ^i_{Obs}, S^i_{Obs}, Θ_{DW} and S_{DW} come from the observed temperatures and salinities, and SGD is assumed to be freshwater at the freezing point $\Theta_{SGD} = 0$ °C and $S_{SGD} = 0$ g/kg. SMW is represented as a water mass with 0 salinity and an effective temperature of -87 °C, accounting for the latent energy required to melt ice Gade (1979).

After solving for the fractions, we compare the concentration of SGD and SMW between the beginning and end of the field campaign (Days 1-10 in 2012 and 1-8 in 2013). The total uncertainties are calculated by assuming that the uncertainties in Θ^i_{Obs}, S^i_{Obs}, Θ_{DW}, and S_{DW} are equivalent to the standard error of the observations and solving for the fractions using repeated random sampling. Water-mass analysis involving plumes can be sensitive to the choice of ambient endmember (i.e. DW) however, we reduce this sensitivity by analyzing the change in the concentration of the water mass, not the absolute concentration values. Therefore we avoid statements such as "the SGD increased from 5% to 6%" and instead would report "the concentration of SGD increased by 1%". Looking at the change in concentration also acknowledges that the ambient water which participates in melting or plume entrainment likely already contains some amount of glacial freshwater.

Moored Time Series

In 2013, a MicroCAT SBE-37 SM was deployed at 70 m at approximately the same location as the ADCP in 2012 (Fig. 3.19). This was the only salinity measurement on the mooring that was not at the surface. It records a freshening rate of -0.0237 g/kg/day which is near the observed depth average (15-100 m) salinity trend of -0.04 g/kg/day. (Fig. 3.15). The moored time series shows that the trend was consistent and not intermittent.

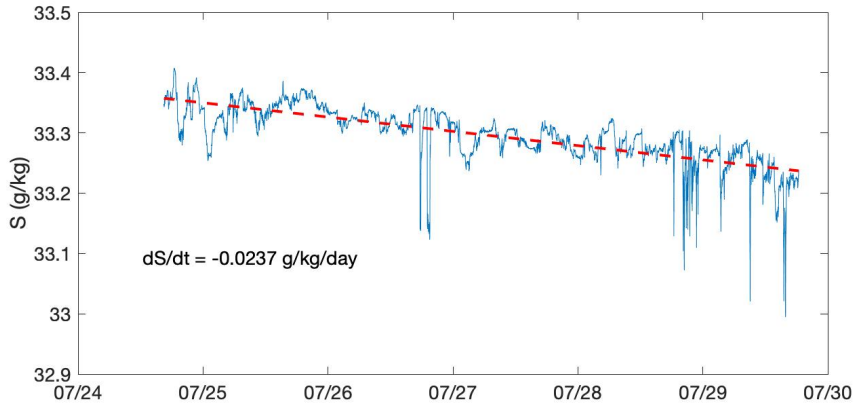

Figure 3.15. Time series of Salinity at 70 m in 2013. The red dashed line is the best fit.

Surface Salinity Trends

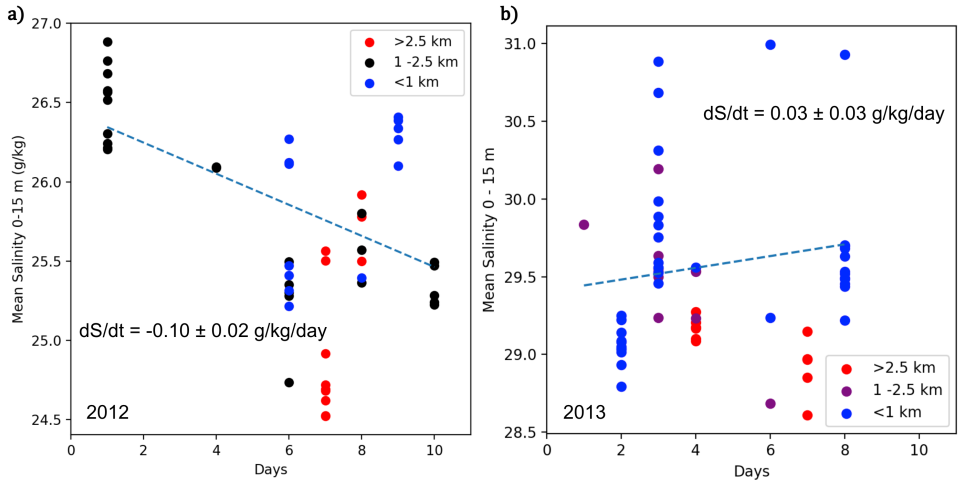

Figure 3.16. a) Mean Absolute Salinity of 2012 CTD profiles from 0 m - 15 m (surface layer) with a best fit trend. Colors indicate distance from terminus. X-axis is the day of the field campaign. b) same but for 2013.

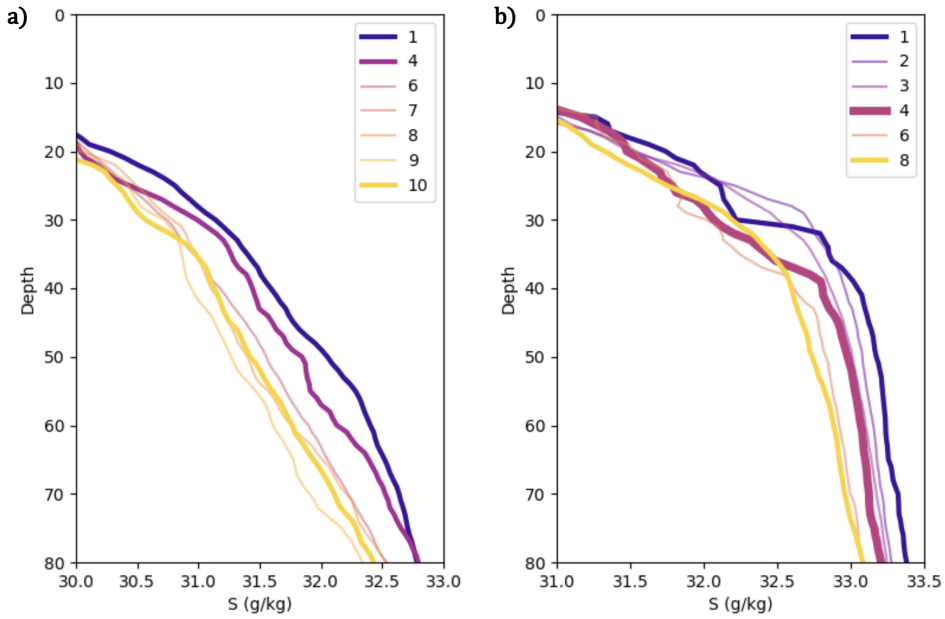

Figure 3.17. a) Daily average salinity profiles in 2012, b) same but for 2013.

Salinity Profiles over time

Figure 3.17 shows the vertical profiles of daily average salinity to accompany Figure 3.4. The profiles are colored by day and show that freshening is occurring at all depths and is not just limited to the surface, although the magnitude of freshening is reduced at depth.

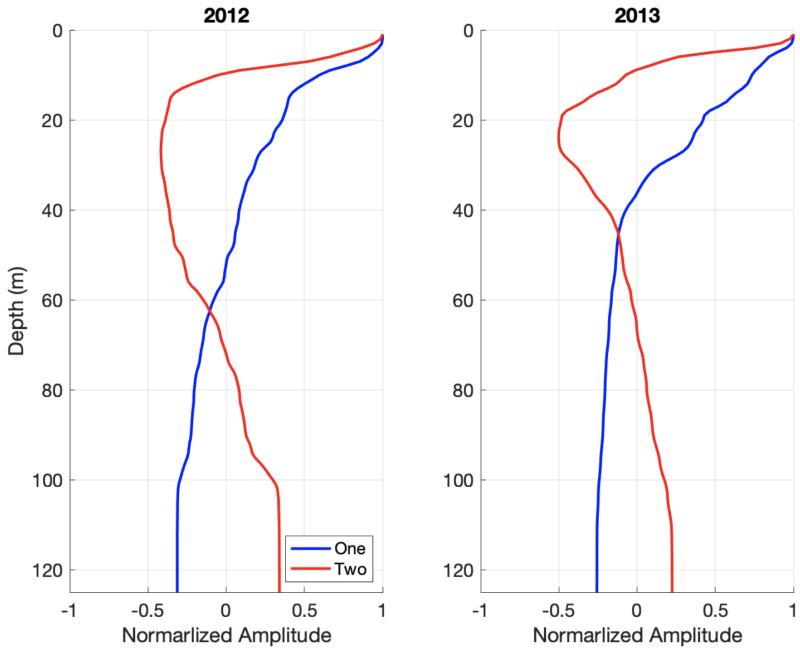

Figure 3.18. Horizontal Normal modes for 2012 and 2013. The mode-one mode was used in the calculation of the zero crossing.

Horizontal Normal Modes

The horizontal normal modes were calculated from the average density profiles within in the fjord in 2012 and 2013 (Fig. 3.18). The modes show the zero-crossing at the depth of 55 m in 2012 and 35 m in 2013. For the calculation of the baroclinic wave speed $c = \sqrt{g'h}$, the reduced gravity g' was calculated from the average density difference in the layers and $h = h_1 h_2/(h_1 + h_2)$ was the effective height.

ADCP and Froude Number Transects

The stratification of the fjord increased during the summer due to vertical mixing of freshwater with the energy to do this potentially supplied by the jet. One method of analyzing the strength of the jet, and thus its ability to mix, is to calculate the Froude number ($Fr = U/c$), a ratio of the advective speed U over baroclinic wave speed c. If $Fr > 1$, then the momentum of the jet exceeds the buoyancy of the jet. When this process occurs in a river plume (analogous to a subglacial discharge jet) the flow becomes unstable and can produce strong shear-driven mixing (Hetland, 2005; Horner-Devine et al., 2015).

Here, Fr was calculated using coincident ADCP and CTD transects across the fjord. The mode-1 baroclinic wave speed is defined as $c = \sqrt{g' h_{eff}}$ where

$$g' = g\frac{\rho_2 - \rho_1}{\rho_2}, \tag{3.31}$$

is the reduced gravity and

$$h_{eff} = \frac{h_1 h_2}{h_1 + h_2}, \tag{3.32}$$

is the effective depth with ρ_1,ρ_2 and h_1, h_2 being the average layer density and layer thickness of the top and bottom layers respectively. We define the interface between layers 1 and 2 to be the zero crossing of the horizontal velocity structure of the mode-1 wave (3.18; Hughes et al. (2018)) rather than using the surface layer depth (10-15 m) since the overturning circulation is deeper than just the surface. Using this formulation, we calculate h_1 in 2012 (2013) to be 55 m (35 m) and c to be 0.3 m/s (0.2 m/s).

ADCP transects in 2012 and 2013 were taken from the main channel at 6 km from the terminus (C) and within the basin at 2 km downfjord (B). In 2013, a transect was also taken close to the jet at 0.5 km downfjord (J) (Fig. 3.19).

In Figures 3.20-3.24 the velocity transects are displayed alongside the Froude number ($Fr = U/c$) with areas where the Froude number is greater than 1 outlined in black. The Froude

Table 3.3. Average critical Froude number of the jet as a function of distance from the terminus.

Year	500 m	2 km	6 km
2012	N/A	1.2	< 1
2013	1.84	1.55	1.1

number of the jet is calculated as the average over regions where $Fr > 1$ and reported in Table 3.3 in the Supplemental. In both years, Fr of the jet is greatest in the wide basin close to the glacier and decreased down-fjord until it fell below 1 in the main channel of the fjord. In 2013 however, an ADCP transect was not taken far enough away from the terminus to identify where Fr fell below 1. The transects confirm that in both years the area of recirculation that was close to the glacier (< 6 km from terminus) was an area of intense inertial-driven flow susceptible to strong shear-driven mixing.

We note that many of Greenland's fjords have a Kelvin number ($Ke = W/L_d$) $\sim O(1)$ Jackson et al. (2018). Increasing the stratification of fjords increases the deformation radius, potentially turning dynamically "wide" fjords into dynamically "narrow" fjords which experience the effects of rotation less and are more vertically sheared. This occurred to some extent in SF in 2012, which had a deformation radius of 3 km compared to 1.4 km in 2013. The fjord channel is 2 km wide and so Ke < 1 in 2012 but Ke > 1 in 2013. Although neither Ke was substantially far from 1, within the channel we observed a boundary current in 2013 but not in 2012 (Fig. 3.21 vs Fig. 3.24).

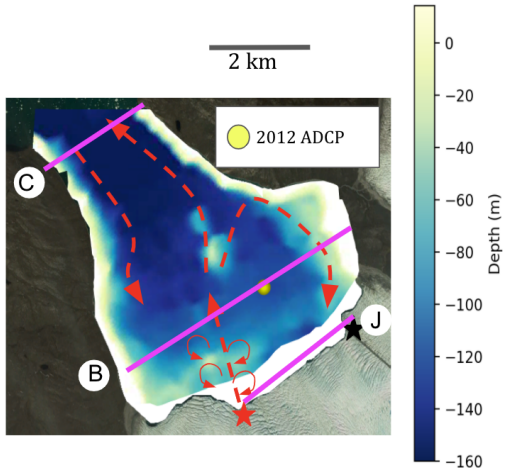

Figure 3.19. Map of the basin of Saqqarleq with the locations of the velocity transects given in magenta. The locations of the transects are the channel (C), the basin (B), and the jet (J). More context for this figure is discussed in the main text Figure 1.

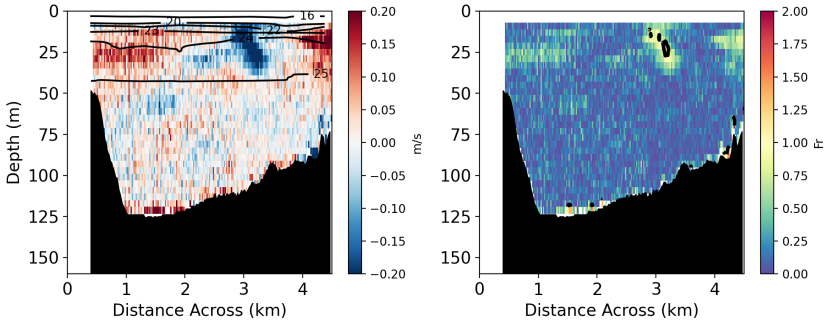

Figure 3.20. Left: Velocity transect in 2012 on line B. The jet is visible around 3 km. Potential Density contours are given in black. For all plots, viewer is facing the glacier so that East is to the left and negative velocities (blue) indicate flow away from the glacier. Right: The Froude number plot with the black contour surrounding the region where $Fr > 1$.

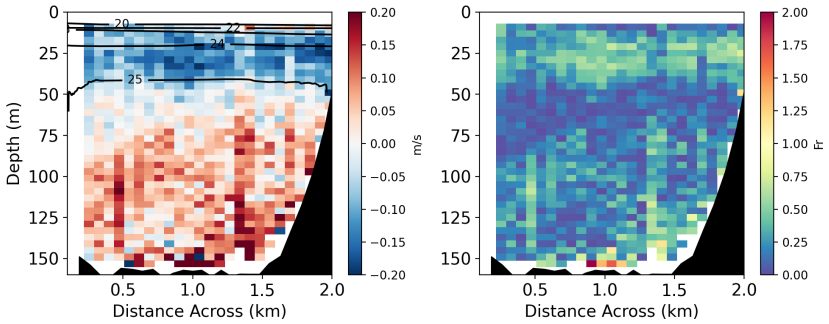

Figure 3.21. Left: Velocity transect in 2012 on line C. The jet is no longer visible distinct from the outflow. Right: The Froude number plot, there are no critical values in the outflow.

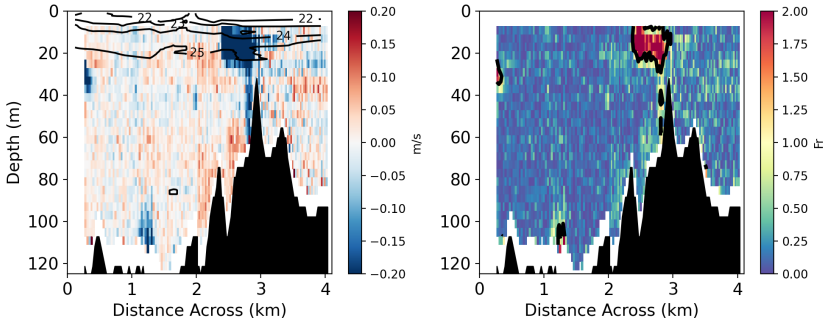

Figure 3.22. Left: Velocity transect in 2013 on line J. The jet is visible around 2.5 km. Right: The Froude number plot.

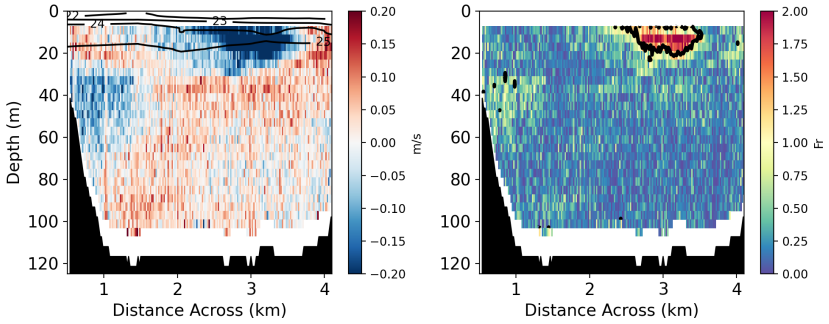

Figure 3.23. Left: Velocity transect in 2013 on line B. The jet is visible around 2.75 km. Right: The Froude number plot.

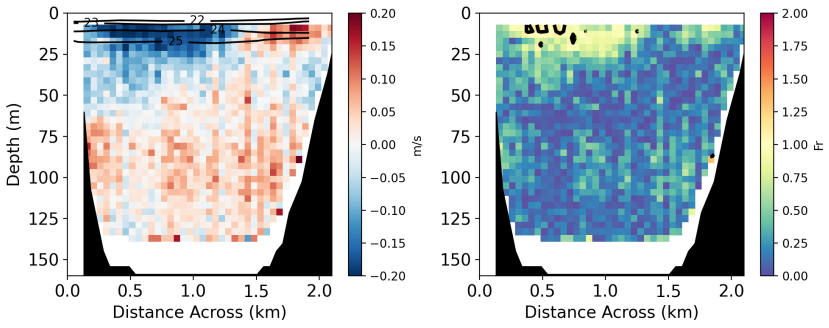

Figure 3.24. Left: Velocity transect in 2013 on line C. A boundary current is outflowing on the left (compare to Figure S7). Right: The Froude number plot.

Transport Estimates In the main text, we discuss possible parameterizations for the exchange flow out of the fjord in the box model. Here, we test the suitablity of using 2-D hydraulic control (Eq. 3.33), 3-D hydraulic control (Eq. 3.34), geostrophic transport (Eq. 3.35) and gravitational circulation (Eq. 3.36). Hydraulic control can occur at narrow constrictions or sills and for a two-layer system, hydraulic theory predicts the outgoing transport to be (Farmer and Freeland, 1983; Sutherland et al., 2014b):

$$Q_{2HC} = \left[\frac{Q_{FW}\beta_S g S_2}{W}\right]^{1/3} \frac{W H_S}{2}, \tag{3.33}$$

where in our model the parameters take values Q_{FW} = 125 m^3/s for the freshwater flux, β_S = 0.75 $\times 10^{-3}$ kg/g, S_2 = 32.5 g/kg, W = 2 km is the fjord width, and H_S = 80 m is the height of the sill. When rotation is important, hydraulic theory changes to Zhao et al. (2021):

$$Q_{3HC} = W\sqrt{g'}\left[\frac{2}{3}\left(H_S - h_1 - \frac{f^2 W^2}{8g'}\right)\right]^{3/2}, \tag{3.34}$$

where $f = 1.36 \times 10^{-4}$ 1/s and h_1 is the depth of the top layer (Eq. **??**). We also include a scaling for geostrophic transport derived using the quasigeostrophic approximation Zhao et al. (2021):

$$Q_{QG} = f L_d^2 [\Delta h_1], \tag{3.35}$$

where Δh_1 is the isopycnal gradient across the sill and L_d is the deformation radius (3 km in 2012, 1.4 km in 2013). Eq. 3.35 assumes that for dynamically-wide fjords the along-fjord pressure head at the sill is similar to the across-fjord pressure head within the fjord. Due to limited observations, we don't use the isopycnal gradient across the sill, but instead use the isopycnal gradient across the fjord channel to calculate Δh_1 (Sup. Fig. 3.21 and 3.24). In 2012 and 2013, h_1 is 3 m and 10 m respectively. Lastly, the gravitational scaling used in the main text is:

$$Q_{GC} = \frac{W H_S g \beta_S H_{12} \overline{S}_x}{2r}, \tag{3.36}$$

where $\overline{S}_x = 2 \times 10^{-5}$ g/kg/m, $H_{12} = 100$ m, and $r = 0.0012$ 1/s.

We compare these 4 estimates to volume transport at the sill calculated from a ship-based ADCP (Fig. 3.25). Unfortunately, this section was taken during the peak ebb tide and while it is not particularly representative of the mean flow, it provides bounds on potential transports. All the volume fluxes are presented in Table 2 in the Supplemental. The gravity-driven circulation and geostrophic transport are both similar to the observed transport while the hydraulic control estimates are much higher.

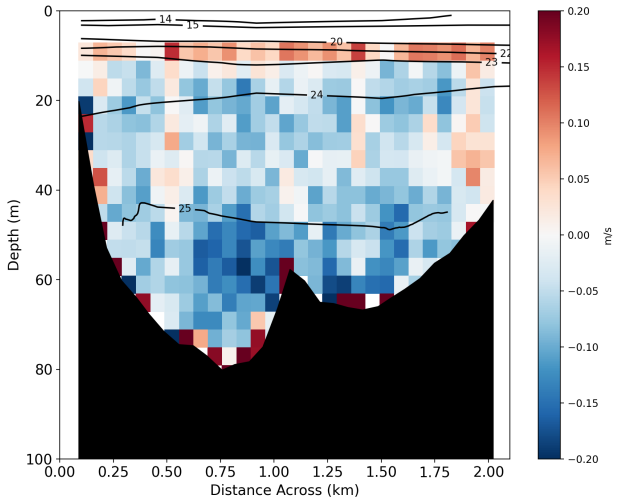

Figure 3.25. Left: Velocity transect in 2012 at Sill 2 (see main text for map). The transect was taken during peak ebb. Positive velocities are flowing towards the glacier and negative out.

Table 3.4. Transport estimates from scaling and ADCP. The range for Q_{QG} comes from differences between 2012 and 2013. Q_{in80} is the incoming volume transport down to 80 m. Q_{out80} is the outgoing volume transport (amplified by the ebb tide). Q_{out55} is the outgoing volume transport down to 55 m, the expected mean flow zero crossing.

Method	Transport (m^3/s)
Q_{2HC}	20000
Q_{3HC}	12000
Q_{QG}	2600 - 3600
Q_{GC}	2200
Q_{in80}	1900
Q_{out80}	6700
Q_{out55}	4300

Box Model Submarine Melting

For the box model presented in the main text we do not include the effects of submarine melting, since the observations indicate that in SQ, the freshwater contribution of ocean-driven melting of the glacier or icebergs is an order of magnitude smaller than SGD. However, recent modeling suggests submarine melting could have a significant impact on the overturning circulation within some fjords (Davison et al., 2020; Zhao et al., 2022a). Therefore, we also run a version of the box model with this freshwater source included and compare it to the main results for the run with 2012 SGD. SMW can be added through the inclusion of a melt volume flux into each layer

$$Q_{mw} = M(z) W_{gl} H_i, \tag{3.37}$$

where W_{gl}= 5 km is the width of the glacier, and $M(z)$ is a melt rate that varies with depth due to thermal forcing like

$$\begin{cases} M = 320 \text{ m/yr} & \text{for } z \leq 10 \text{ m} \\ M = 120 \text{ m/yr} & \text{for } z > 10 \text{ m}. \end{cases} \tag{3.38}$$

with melt rates estimated from Slater et al. (2018). The melt rates are expected to be enhanced in

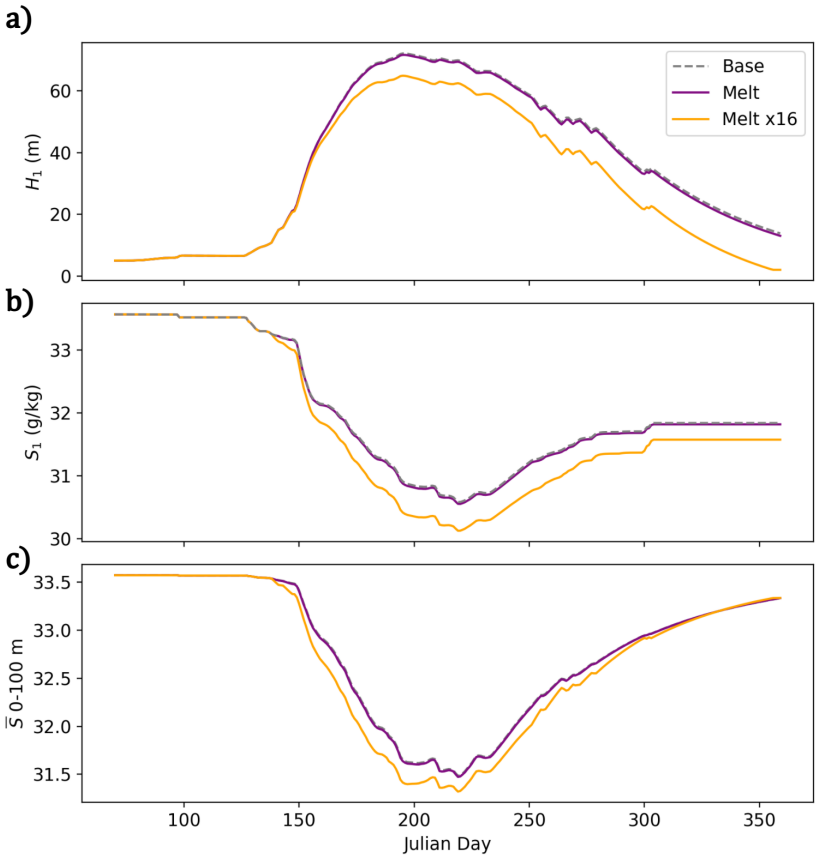

Figure 3.26. a) Height of the upper layer in the box model for the 2012 base case (dashed), the Slater et al. (2018) melt rates (purple) and the maximum possible melt rates (orange) from Wagner et al. (2019). b) The salinity of the upper layer box. c) The average salinity of the upper and middle boxes.

the presence of a strong background circulation and thus this term is only active when $Q_{sg} > 0$. Wagner et al. (2019) suggests these values are likely an underestimate, therefore, we also include a run with the maximum possible melt rate (approximately $16 \times M(z)$) if all of the ice loss at the terminus was due to submarine melting and none due to calving. The second run can be considered an upper bound for the effects of submarine melting.

The inclusion of the modeled melt rates results in negligible difference compared to the base case in upper layer height, salinity or vertically averaged salinity (Fig. 3.26). The case with high submarine melting does deviate a little from the base case and allows us to explore the effects of including the additional freshwater source. Under the high melt run, the height of the

upper layer is smaller than in the base case (Fig. 3.26a), and the salinity in the upper layer is decreased (Fig. 3.26b). In this case, the additional freshwater from submarine melting increases the density-driven exchange flow with the shelf and the height of the upper layer does not deepen as much. Overall, the mean salinity in the fjord is fresher under the high melt run than in the base case due to the additional freshwater flux from the glacier (Fig. 3.26c). The difference in $\bar{S}_{0-100}$ between the base case and the high melt case is 0.25 g/kg which is smaller than the difference in $\bar{S}_{0-100}$ between 2012 and 2013 which is 0.35-0.5 g/kg.

Time-varying Parameters

Two of the box model variables are held constant: the friction coefficient, r, and the external salinity S_{ext}. However, we might expect both of these variables to change in time due to a changing density of the coastal current and a variability in the velocity which drives mixing. Here, we show the results of sensitivity tests when using a time-varying salinity and friction coefficient.

We lack observations from immediately outside SQ to estimate the time-varying external salinity, however Mortensen et al. (2022) includes measurements of the time-varying salinity on the shelf adjacent to Godthåbsfjord. Godthåbsfjord is about 650 km south of Disko Bay, but currents flow north and so this water can be considered upstream of SQ. However, we note that the recirculation of Baffin Bay waters is also able to alter shelf properties in Disko Bay near Saqqarleq. With this caveat in mind, we use the Mortensen et al. (2022) Figure 6 salinity time series as a guideline for the climatology of Disko Bay. Based on this climatology, we generate an idealized time-varying S_{ext} with a similar magnitude and shape as the Mortensen et al. (2022) observations (Sup. Fig. 3.27).

We also test a version of the box model with a time-varying friction coefficient r. The dissipation in the fjord is likely related to the velocity of fjord circulation which is forced by subglacial discharge. Therefore, in the time-varying r case we scale friction according to subglacial discharge as

$$r = \begin{cases} \frac{r_0}{3} + \frac{2}{3}\frac{Q_{sg}}{100} r_0 & 0 \leq Q_{sg} \leq 100 \text{ m}^3/\text{s}, \\ r_0 & 100 \text{ m}^3/\text{s} \leq Q_{sg}, \end{cases} \tag{3.39}$$

where $r_0 = 1.2 \times 10^{-3}$ 1/s is the value in the constant friction case. This form of a time-varying r is motivated by assuming r is proportional to velocity U, that U in turn scales with subglacial discharge (Jackson et al., 2022a; Zhao et al., 2022a) and that our moored ADCP measured

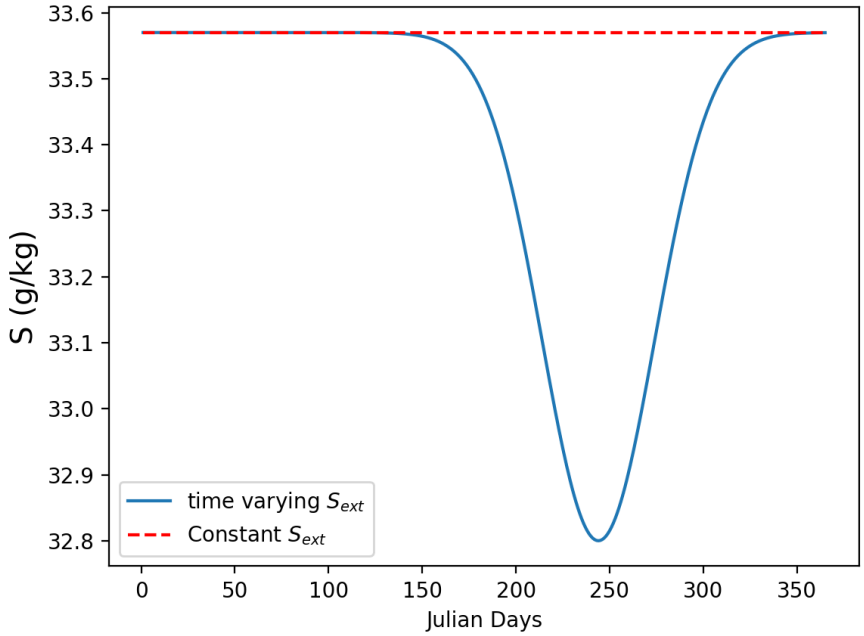

Figure 3.27. External salinity boundary conditions for the box model, showing the constant external salinity used in the main text (dashed red) and an idealized time-varying external salinity tested here (solid blue).

velocities from 0.06 m/s in July (when $Q_{sg} > 100$ m^3/s) to 0.02 m/s in October (when Q_{sg} was much reduced).

The results of our time-varying experiments are shown in Sup. Fig. 3.28. The time-varying external salinity (dashed) results in a weaker density gradient with the shelf in late summer and therefore a more delayed and defuse export of freshwater from the fjord. However, the time-varying friction (dotted) results in a rapid exchange (Sup. Fig. 3.28b) that is enhanced once subglacial discharge (and friction) weakens and this model setup has the shortest residence time. The version of the model with both parameters varying in time (dash-dot) has a similar response to the constant run (solid). All the runs have a qualitatively similar response, especially given the uncertainty in subglacial discharge forcing (Fig. 10). Since the constant run and the time-varying run with both parameters active behave similarly, we use the simple constant S_{ext} and r in the main text.

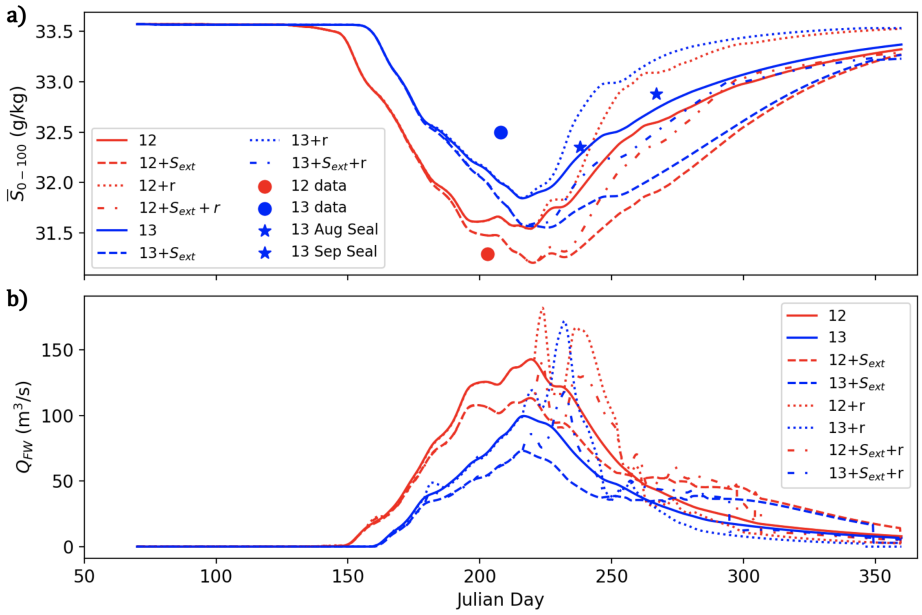

Figure 3.28. a) The vertically-salinity for the fjord as simulated in the box model against observations (see Main text Fig. 10 for more details). The solid lines represent the main text box model set up. The dashed lines are runs with a time-varying external salinity, the dotted lines are runs with a time-varying friction coefficient, and the dash-dotted lines have both terms varying. b) The freshwater fluxes from the model (see Main Text Section 4c)

Choice of friction

In the box model, friction is represented in the parameterization of shelf exchange through the frictional timescale $1/r$. In general, it is expected that friction (and mixing) should be intensified near bottom boundaries, channel contractions and expansions, and in the lee of sills and therefore r should be scaled by one or more of these processes (Pritchard, 1956; Hansen and Rattray, 1965; Stigebrandt, 1999). Our model is based on gravitational circulation with r replacing the usual friction term $H^2/48K_m$. For the proceeding discussion, we focus on the effective diffusivity K_m since it is more commonly associated with gravitational circulation and estimated by observations (e.g., Bendtsen et al., 2021).

Geyer and MacCready (2014) suggest using a mixing length approach where $K_m = u_* L_{turb}$ with u_* a friction velocity and L_{turb} the turbulent mixing length scale. The friction velocity is related to drag and tidal speed (U_{tide}), and the turbulent length scale can be the height of the boundary layer or related to the width of the fjord (Banas et al., 2004; Sutherland et al., 2014b). Since fjords are deep and not well-mixed, the bottom boundary layer is generally small (on the order of meters), but can still be significant. However, in other fjords internal mixing or mixing generated at sills has been a larger source of turbulence (Klymak and Gregg, 2004; Stigebrandt and Aure, 1989). In SQ, a scaling for diffusivity based on boundary layer height is $K_m = C_d^{1/2} U_{tide} H_{bound}$ where $C_d = 1 \times 10^{-3}$ is the drag coefficient and H_{bound} is the height of the boundary layer at the sill estimated to be 1-5 m. U_{tide} is estimated from both the pressure sensor (Sup. Fig. 3.13) and from the ADCP to be 0.05 to 0.1 m/s. These constants gives a K_m estimate in the range of 0.001-0.01 m^2/s in the boundary-layer near the sill.

Another option is to scale K_m according to breaking internal waves generated at the sill which transfer energy against buoyancy forces (Stigebrandt and Aure, 1989). In this scaling, the

incoming internal wave flux is given by

$$E = \rho_{ref}(H_{top}U_{top}^2 + H_{bot}U_{bot}^2)Wc, \tag{3.40}$$

where ρ_{ref} is the reference density, c is the baroclinic wave speed, H_{top} (H_{bot}) is the top (bottom) thickness of the internal wave, and U_{top} (U_{bot}) is top (bottom) velocity with $U_{top}H_{top} = U_{bot}H_{bot}$. The work against buoyancy forces is given by

$$B = \rho_{ref}K_m N^2 A H_{12}, \tag{3.41}$$

where the last two terms represent an estimate of the volume over which the mixing occurs. Stigebrandt and Aure (1989) suggest that about 5% of the incoming internal wave flux goes into dissipation in fjords. After some algebra and combining Eq. 3.40 and 3.41 we arrive at another expression for a diffusivity

$$K_m = 0.05 \times \frac{2H_{top}U_{top}(1 + \frac{H_{top}}{H_{bot}})Wc}{N^2 A H_{12}}, \tag{3.42}$$

where K_m clearly varies with stratification N^2 both directly and through changing the interface depth. Using the range of interface depths (Sup. Fig. 3.18), velocities (0.05-0.1 m/s) and stratification (main text Fig. 3) observed in SQ we estimate $K_m = 5 \times 10^{-6}$ to 5×10^{-5} m^2/s with the largest variability coming from choice of stratification. If the internal wave velocities are higher than we expect, a greater percentage is converted to dissipation or the stratification is significantly weaker (such as at the beginning of the melt season or below 100 m), K_M would be an order of magnitude higher.

Additionally, we could parameterize the diffusivity in relation to the shear-driven mixing from the jet. The entrainment velocity normal to the jet is given by

$$w_e = 0.05 U_{jet} Ri_b^{-0.75}, \tag{3.43}$$

where $Ri_b = g\beta(S_{jet} - S_0)H_{jet}/U_{jet}^2$, is the bulk Richardson number, that is, the balance between buoyancy jump and shear across the jet (Princevac et al., 2005; Gillibrand et al., 2013). S_{jet}, U_{jet} are the salinity and velocity of the jet respectively, S_0 is the salinity at $U = 0$ below the jet and H_{jet} is the distance from the center of the jet to the depth where $U = 0$. To turn the entrainment velocity into a diffusivity we multiply it by the scale height of the jet such that

$$K_m = w_e H_{jet}, \tag{3.44}$$

and using appropriate values from our ADCP transects ($H_{jet} \approx 15$ m), we end up with a range of $K_m = 0.25$ - 0.34 m^2/s. However, this value of diffusivity is likely only relevant near the jet and an overestimate in other parts of the fjord.

Ultimately, within the box model we impose a value of $K_m = 0.25$ m^2/s equivalent to $r = 0.0012$ 1/s since it produces the best fit with the observations. This value is close to the estimate made from jet-driven mixing, but is higher than the estimate produced from internal waves and boundary layer dissipation. In addition, sidewall dissipation in the near-terminus circulation where velocities are intense, while not evaluated here, might play an underappreciated role in fjord-scale mixing. These methods are simple attempts at scaling the diffusivity and future work should aim to quantify the different processes contributing to mixing.

Chapter 4

Mechanisms controlling the seasonal variability of Sermilik Fjord

Abstract

Glacial fjords connect the Greenland Ice Sheet (GrIS) with the continental shelf, and fjord dynamics are responsible for the import of oceanic heat to the GrIS and the export of ice sheet meltwater to the ocean. The fjord exchange of heat and salt at the fjord mouth, along with vertical mixing within the fjord, modifies properties including ocean heat content and stratification, and ultimately sets the boundary conditions for ice-ocean interactions. However, uncovering the physical mechanisms controlling exchange is difficult due to limited observations and the numerous interactions between traditional and glacial drivers of fjord circulation. Here, we use a high-resolution, realistically-forced numerical simulation of Sermilik Fjord in southeast Greenland to differentiate between the exchange flow driven by shelf variability and that driven by subglacial discharge. Comparison with observations shows that the model reproduces the relevant dynamics. We use the Total Exchange Flow (TEF) framework to analyze the seasonal changes in the exchange flow of the fjord. We find that the seasonality of the winds drives seasonal reversals in the exchange flow, that the exchange flow is primarily plume-driven during the summer, and that the plume-driven circulation is more effective at renewal than the shelf-driven circulation. Understanding the response of fjord-shelf exchange to external forcing is a critical step towards improved representation of ice-ocean interactions.

*The model was developed and run by Emily Shroyer, Kenneth Hughes and Phil Barbour. Robert Sanchez performed the primary data analysis.

4.1 Introduction

Glacial fjords connect the Greenland Ice Sheet (GrIS) with the continental shelf, and fjord dynamics are responsible for the import of oceanic heat to the GrIS and the export of ice sheet meltwater to the ocean. The fjord exchange of heat and salt at the fjord mouth, along with vertical mixing within the fjord, modifies properties including ocean heat content and stratification, and ultimately sets the boundary conditions for ice-ocean interactions (Straneo and Cenedese, 2015; Holland et al., 2008; Straneo et al., 2011; Shroyer et al., 2017; Mortensen et al., 2018; Hager et al., 2022b). Understanding fjord exchange is therefore crucial to predicting the impact of the ocean on marine-terminating glaciers and the consequences of exported freshwater on regional circulation and ecosystems (Hopwood et al., 2020; Straneo and Heimbach, 2013; Rysgaard et al., 2003).

Numerous external drivers influence glacial fjord exchange on hourly to seasonal timescales. Traditional drivers of fjord exchange include tides (Washam et al., 2020; Mortensen et al., 2011), winds (Moffat, 2014), surface runoff (Stuart-Lee et al., 2021), and internal waves (Inall et al., 2015), while glacial drivers include terminus and iceberg melt (Davison et al., 2020), and subglacial discharge (Carroll et al., 2015) (see for Reviews: Straneo and Cenedese, 2015; Inall and Gillibrand, 2010; Cottier et al., 2010; Farmer and Freeland, 1983). However, untangling the individual role of these drivers is challenging because many of the effects are cumulative and difficult to isolate with limited observations (Straneo et al., 2019). In this study, we will focus on differences between glacial forcing and shelf forcing (e.g., winds, external water-mass variability), as these are the two dominant forcing mechanisms in southeast Greenland (Jackson et al., 2014; Jackson and Straneo, 2016).

Glacial fjords undergo substantial seasonal variability in forcing that further complicates

diagnosing drivers of fjord circulation (Mortensen et al., 2014; Jackson and Straneo, 2016; Hager et al., 2022b). Glacial forcing from submarine melting and ice sheet meltwater runoff is strongest in summer, but shelf-forcing seasonality is dependent on factors such as sea ice, boundary currents and wind forcing which can vary regionally (Carroll et al., 2018; Gelderloos et al., 2017; Gladish et al., 2014a). Observations are biased towards the summer and away from ice-congested areas, limiting comparisons between glacial-driven circulation and shelf-driven circulation. Consequently, we lack a deep understanding of the relative role of the shelf-driven circulation vs. plume-driven circulation in setting fjord properties seasonally, and how these circulation modes vary along fjord.

Models of glacial fjords have been a useful tool in isolating different forcing mechanisms and overcoming data limitations. Very high-resolution (5 – 100 m) models have brought insight into the dynamics of subglacial discharge plumes (e.g., Xu et al., 2012; Sciascia et al., 2013b; Kimura et al., 2014; Carroll et al., 2015; Ezhova et al., 2017) and led to plume representation into larger fjord models (Cowton et al., 2015a; Jenkins, 2011). Fjord-scale models have allowed for an assessment of the impact of along-fjord winds, along-shore winds and shelf forcing on fjord dynamics (Spall et al., 2017; Jackson et al., 2018; Fraser and Inall, 2018; Zhao et al., 2021), of iceberg melt on water mass transformation (Davison et al., 2020; Kajanto et al., 2022), of sea ice retreat on fjord circulation (Shroyer et al., 2017), and of fjord geometry, including ice mélange, on fjord renewal (Gladish et al., 2014b; Carroll et al., 2017; Hager et al., 2022b; Zhao et al., 2021; Hughes, 2022). While these models have significantly improved our understanding of glacial fjord processes, they are usually run on idealized bathymetry or with idealized forcing limiting any comparison with observations.

We use a high-resolution, realistic numerical simulation of Sermilik Fjord, in southeast Greenland, forced by ERA5 winds and ASTE boundary conditions, to differentiate between the exchange flow driven by the variability of the shelf and that driven by subglacial discharge. Comparison with observations shows that the model reproduces the relevant dynamics over multiple years and through seasonal transitions. We find that the seasonality of the along-shore

winds drives seasonal reversals in the exchange flow, that the exchange flow is primarily plume-driven during the summer, and that the plume-driven circulation is more effective at renewal than the shelf-driven circulation. Understanding the response of fjord-shelf exchange to external forcing is a critical step towards improved representation of ice-ocean interactions in climate models.

4.2 Setting and background

4.2.1 Sermilik Fjord

Sermilik Fjord (SF) is part of a large glacial fjord system in southeast Greenland (Fig. 4.1). The fjord varies in width from 5 – 10 km, is 550 – 900 m deep, and is about 80 km long before branching into Helheim Fjord, Fenris Fjord, and Midgaard Fjord going from west to east (Fig. 4.1). Each of these fjords, in turn, connects to their namesake outlet tidewater glacier. A leading hypothesis for recent glacial retreat is that the increased presence of relatively warm water at depth, coupled with vigorous circulation initiated by increasing ice sheet runoff, has increased the submarine melting of marine-terminating glaciers (Straneo et al., 2011; Holland et al., 2008; Wood et al., 2018, 2021; Khazendar et al., 2019; Slater and Straneo, 2022; Jackson et al., 2022b). Midgaard Glacier has retreated the most of the three glaciers over the past 40 years (Mouginot et al., 2019), but Helheim Glacier is currently one of the largest outlet glaciers in Greenland (Mankoff et al., 2020; Enderlin et al., 2014). Helheim saw a rapid acceleration in the 2000s (Howat et al., 2005; Luckman et al., 2006) and is expected to retreat rapidly again after a period of relative stability (Williams et al., 2021).

The relative volumes of water masses within the fjord set the heat available for melting. During the winter, SF is composed of two water masses: cold and fresh Polar Water (PW) of Arctic origin and a deep, relatively warm and salty water of Atlantic origin (AW) (Sup. Fig. 4.19). SF has a deep sill (500 m) allowing significant water column exchange with the shelf. As a result, the water masses in the fjord broadly match those found on the adjacent shelf and are

steered into SF through Sermilik Trough (ST), a deep trough that cuts across the shelf before turning parallel to the fjord mouth (Fig 4.1). The water properties within the trough are a mixture of waters from the East Greenland Coastal Current (EGCC) and the Irminger Sea, and therefore fjord properties are dependent on the relative volumes of PW and AW on the shelf (Snow et al., 2021; Harden et al., 2014). During the summer, the water masses within the fjord become more challenging to identify due to the the arrival of Warm Polar Water (WPW) from the shelf and the introduction of multiple types of freshwater from the glacier. WPW is a relatively warm and fresh water mass formed from surface warming of PW and is most prominent near the mouths of fjords. Within the fjord, submarine meltwater is formed through direct melting of submerged ice (icebergs and glacier terminus) and cools the water locally. Lastly, subglacial discharge is freshwater injected into the fjord at the glacier terminus. This discharge comes from ice sheet surface meltwater that is routed to the bed of the glacier and enters the fjord at depth. Subglacial discharge generates a turbulent buoyant plume which drives an overturning circulation, upwells warm and salty AW into shallower depths and enhances submarine melting (Carroll et al., 2015; Beaird et al., 2018; Jackson et al., 2022b; Slater et al., 2022; Slater and Straneo, 2022).

4.2.2 Background on fjord-shelf exchange

Shelf-driven circulation

In SF, along-shore and along-fjord winds dominate exchange between the fjord and shelf (Straneo et al., 2010; Jackson et al., 2014). Shelf winds run southwest and parallel to the coast resulting in downwelling conditions that generate large pycnocline displacements. These pycnocline displacements create a density gradient within the fjord initiating baroclinic circulation with shallow inflow and deep outflow (Klinck et al., 1981; Aure et al., 1996; Jackson et al., 2014). As the pycnocline relaxes, the circulation reverses. Wind-driven pycnocline displacements have generated observable pulses within Sermilik Fjord and are associated with large heat and salt fluxes (Straneo et al., 2010; Jackson et al., 2014). The fjord heat content is dominated by pycnocline fluctuations which change the relative abundances of AW and PW and

obscure the influence of glacial forcing (Jackson and Straneo, 2016; Sanchez et al., 2021).

Both Fraser et al. (2018) and Jackson et al. (2018) have identified coastal-trapped waves as the primary mechanism through which the wind-driven forcing is communicated to southeast glacial fjords, and coastal-trapped waves have been observed in other dynamically-wide Arctic Fjords (Inall et al., 2015). The coastal-trapped waves can generate a Stokes Drift that enhances the background circulation and increases the mean heat transport towards the glacier (Fraser and Inall, 2018; Fraser et al., 2018; Inall et al., 2015). However, in recent modeling studies by Gelderloos et al. (2021, 2022), the authors concluded that the majority of coastal-trapped waves observed in southeast Greenland were not generated by local winds, but rather were generated further upstream. Models have also disagreed on the extent to which the waves dissipate within fjords and contribute to mixing. Further observational studies are needed to clarify the generation and impact of coastal-trapped waves in southeast Greenland.

Local winds also play an important role in forcing SF (Oltmanns et al., 2015). Downslope, katabatic winds can flow down the fjord with hurricane intensity (Oltmanns et al., 2015). Modeling studies suggest these winds produce a similar baroclinic response in the fjord to shelf barrier winds (Spall et al., 2017; Carroll et al., 2017; Zhao et al., 2021). The response of fjord circulation to along-fjord winds is also dependent on fjord width, and along-fjord winds can generate Ekman transport in sufficiently wide fjords (Carroll et al., 2017). However, the connectivity between along-shore and along-fjord winds and their impact on fjord circulation is still poorly understood.

Other drivers of fjord-shelf exchange include tides and eddy fluxes. Tides are a strong source of mixing in shallow-silled west Greenland Fjords, but are generally weak for deep fjords such as SF (Mortensen et al., 2011; Stuart-Lee et al., 2021). Eddies are an important driver of heat and freshwater fluxes across the Greenland shelfbreak (Pacini et al., 2021), can be found at the mouths of fjords and within troughs (Fraser and Inall, 2018; Sutherland et al., 2014a; Zhao et al., 2022b), and depending on the strength of eddy activity may propagate into the fjord and enhance mixing and melting (Zhao et al., 2021, 2022b). However, diagnosing eddy contributions

to exchange is outside the scope of this study and we instead focus on the impact of winds and coastal-trapped waves.

Buoyancy-driven circulation

During the summer, injected subglacial discharge rises as a buoyant plume and drives an overturning circulation within the fjord. Depending on fjord width, the outflowing buoyant jet can set up a horizontal recirculation which enhances background melting (Slater et al., 2018; Jackson et al., 2020; Zhao et al., 2022a,b). Additionally, modeling studies have shown that melting icebergs can enhance background circulation by up to 10% (Davison et al., 2020; Kajanto et al., 2022). The outflowing volume flux is primarily composed of ambient water entrained into the plume (Mankoff et al., 2016) and the plume is therefore a significant source of water mass transformation. While plumes have the potential to renew deep basin waters efficiently, modeling studies have shown that the height of the grounding line over the height of the sill is a critical factor in limiting the rate of renewal within glacial fjords (Carroll et al., 2017; Zhao et al., 2021). Thus, the influence of the plume-driven circulation on fjord-shelf exchange is a function of both subglacial discharge flux and fjord geometry.

4.3 Methods

4.3.1 Model setup*

We ran nearly three-year simulations (Mar. 2015–2017) of a regional model of Sermilik Fjord and its adjacent shelf (Fig. 4.1) using the MITgcm (Marshall et al., 1997; Adcroft et al., 2004). Horizontally, the domain is 360×640 cells that are 280×280 m. There are 32 vertical levels with 10 m resolution in the top 200 m increasing to 100 m at the seafloor at 950 m. Seafloor bathymetry is based on BedMachine v3 (Morlighem et al., 2017b).

Vertical mixing in the model uses the K profile parameterization (Large et al., 1994) with a background viscosity of 10^{-4} m^2 s^{-1} and diffusivities for temperature and salinity of 10^{-5} m^2 s^{-1}. Horizontal viscosity uses harmonic diffusion together with a Smagorinsky scheme (defined in

the MITgcm as viscAhGrid = 0.01, viscAhGridMax = 1, and viscC2smag = 3). Advection of temperature and salinity uses a third-order flux limiter scheme. The quadratic bottom drag coefficient is 2×10^{-3}. The standard time step is 60 s and reduced to 30 s as needed for some months. Output snapshots are saved every three hours.

Sea ice is not included, so ocean temperatures can drop below the freezing point during winter.

No Glacier Run

By default, winds, surface air temperature, specific humidity and downwelling short- and long-wave radiation come from the ERA5 reanalysis (Hersbach et al., 2020). At the ocean boundaries, temperature, salinity, and velocity come from the Arctic Subpolar Gyre State Estimate 'ASTE' (Nguyen et al., 2021). On each of the three boundaries on the shelf, there are sponges that are 20 grid cells wide in which T, S, u, and v are relaxed to the boundary conditions with time scales of 3 hours on the outer edges and 30 hours on the inner edges. Initial model fields also come from ASTE. The ASTE fields are updated daily and interpolated onto each time step. This run is referred to as the No Glacier (NG) run.

With Glacier Run

A subglacial discharge plume and glacier was added to the default set-up in the With Glacier (WG) run. Cold, fresh water was input at the three glaciers at the north end of SF (those named in Fig. 4.1). This water originates as suface melt, and peaks in summer. It makes its way through to the base of the ice sheet and enters the ocean at depth at the grounding line to become a buoyant, turbulent plume. The plume dynamics are parameterized following Cowton et al. (2015b). Discharge values come from regional climate simulations compiled by Slater et al. (2020). A constant discharge is used for each month. Subglacial discharge is applied to all months and varies interannualy. Peak discharge in the summer at each glacier is 300–600 $\mathrm{m^3\ s^{-1}}$. Discharge in the winter is 5–20 $\mathrm{m^3\ s^{-1}}$.

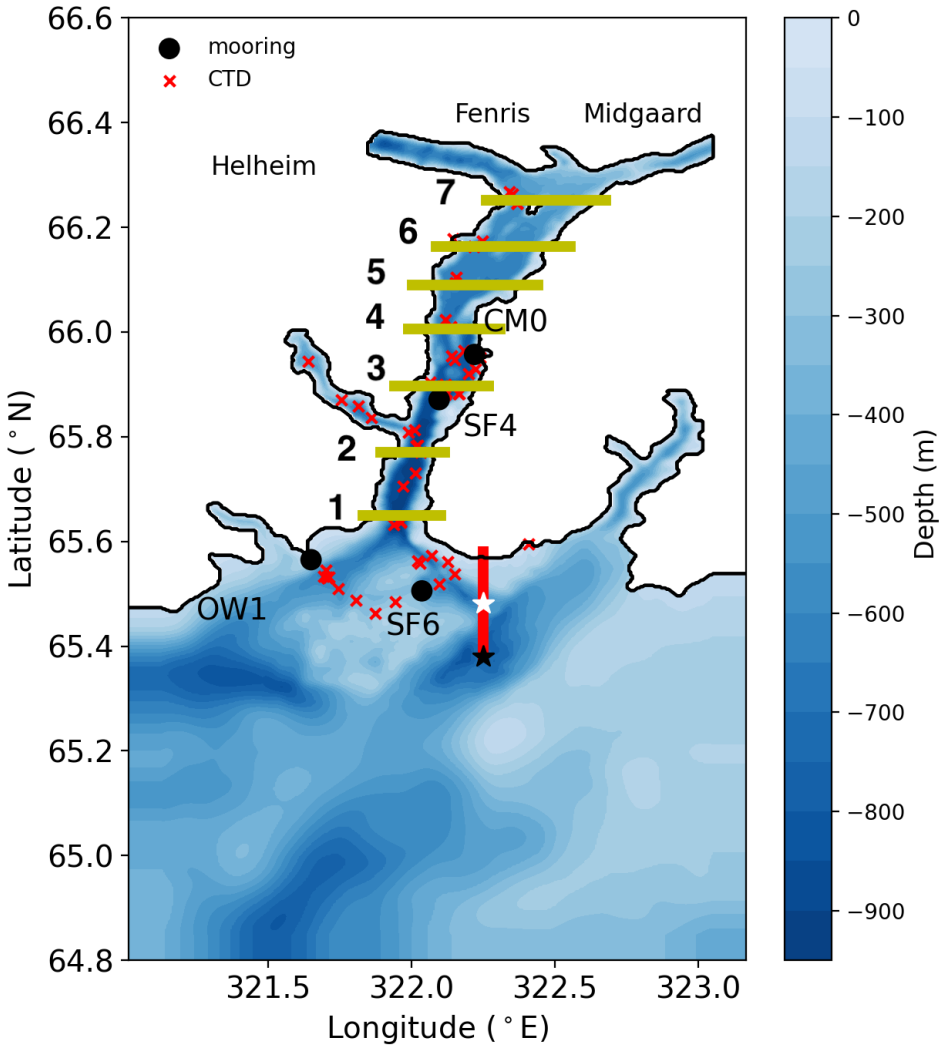

Figure 4.1. Model domain and bathymetry. In yellow are the gates used for the calculation of TEF fluxes in Sermilik Fjord. The red line is the coastal section used for the shelf seasonality analysis. The locations of observations used in the model comparison are given in black circles (moorings) and red crosses (CTD). The glacier names are given at the top. The black star is the location used for the shelf wind analysis and the white star is within Sermilik Trough (ST).

No Glacier High-Resolution Run

We also run a version of the model that uses a higher-resolution wind product and no glacier (NG-HR). The global ERA5 product is insufficient to resolve atmospheric dynamics that require higher spatial and temporal resolution within and around SF. Therefore, a nested atmospheric simulation using Polar WRF (Hines and Bromwich, 2008) was run such that the region encompassing the fjord has 2-km grid spacing. The outer domain with 18-km spacing encompassed all of Greenland and was initialized and forced at its boundaries with the ERA5 product. Further, this high-resolution model was re-initialized every 3.5 days to avoid drift from actual conditions with consecutive simulations blended with a 12-hour overlap period to avoid sudden shifts.

4.3.2 Observational data

The model runs presented in this paper are some of the first multi-year simulations of a Greenland glacial fjord with realistic atmospheric and oceanic forcing. Validation and comparison of the model against observations is limited to a select number of moorings, although these moorings span different regions of the fjord-shelf system (Fig. 4.1). We compare the model to three moored Conductivity, Temperature and Depth (CTD) instruments (Table 4.1) from August 2015 to July 2017 located on the shelf at 350 m and in the fjord at 60 m and 400 m (Fig. 4.1). We also compare the model output to moored Acoustic Doppler Current Profiler (ADCP) velocity data collected in the fjord and on the shelf (Table 4.1). We compare the model output to 64 ship-based CTD profiles collected during summer surveys in 2015 and 2017. Lastly, we also include 4 winter XCTD profiles from March 2010 for additional context.

We evaluate the model using the Wilmott Skill Score (WS, Willmott, 1982) defined as

$$WS = 1 - \frac{\frac{1}{N}\sum_{i=1}^{i=N}(m_i - o_i)^2}{\frac{1}{N}\sum_{i=1}^{i=N}(|m_i - \overline{o}| + |o_i - \overline{o}|)^2} = 1 - \frac{MSE}{\frac{1}{N}\sum_{i=1}^{i=N}(|m_i - \overline{o}| + |o_i - \overline{o}|)^2}, \tag{4.1}$$

where m_i is a model value, o_i is the observation value, the overbar denotes an average, MSE is

Table 4.1. Observation Information: the name, the instrument type, depth of instrument, time period of deployment, sampling period and variables recorded. CM0, SF4, and SF6 moored instruments located at a single location. Θ is Conservative Temperature, S is absolute salinity, P is pressure, V is velocity.

Label	Instrument	Depth	Actiive Time	Sample Resolution	Variables
CM0	SBE 37 MicroCAT	60 m	August 2015 – July 2017	15 min	Θ,S,P
SF4	SBE 37 MicroCAT	400 m	August 2015 – July 2017	15 min	Θ,S,P
SF6	SBE 37 MicroCAT	350 m	August 2015 – July 2017	15 min	Θ,S,P
SF4 ADCP	75 kHz RDI Teledyne Workhorse Long-Ranger ADCP (Upward Facing)	381 – 41 m (10 m bins)	August 2015 – July 2017	30 min	V
OW1 ADCP	75 kHz RDI Teledyne Workhorse Long-Ranger ADCP (Upward Facing)	143 – 18 m (5 m bins)	August 2015 – July 2017	30 min	V
CTD 2015	SBE 25plus MicroCAT	Full Depth	August 2015	1 m	Θ,S,P
CTD 2017	SBE 25plus MicroCAT	Full Depth	July 2017	1 m	Θ,S,P

the mean square error and there are N paired model and observation points. The WS provides a metric for comparison across different model parameters, such as temperature and salinity, and is a commonly used tool when evaluating realistically forced models (e.g., Liu et al., 2009; Elias et al., 2012; Giddings et al., 2014; Kärnä et al., 2015). A model score WS=1 indicates complete agreement between the model and observations and WS=0 indicates complete disagreement.

We also use the correlation coefficient (r) to diagnose the covariance between two variables. The correlation coefficient is

$$r = \frac{\frac{1}{N-1}\sum_{i=1}^{i=N}(m_i - \overline{m})(o_i - \overline{o})}{\sigma_m \sigma_o}, \tag{4.2}$$

where σ_x is the standard deviation of x. The statistical significance of the correlation coefficient is calculated using the effective degrees of freedom defined as the e-folding scale of the autocovariance of the observations (Emery and Thomson, 2001; Lindeman et al., 2020).

4.3.3 Total Exchange Flow

The transport of heat, salt, nutrients and other tracers within the fjord is set by the exchange flow. In traditional estuaries, the exchange flow describes the sub-tidal mean circulation, typically with inflowing salty water at depth and outflowing fresher water near the surface (MacCready and Geyer, 2010). A key aspect of the classic exchange flow is that the circulation is set up by river input and mixing, and drives a volume flux out of the estuary many times greater than the initial freshwater volume flux. Applying the exchange flow concept to glacial fjords, we might expect wind-driven synoptic variability (3-10 days) to play the role of tides (high-frequency oceanic variability) and for glacial freshwater to play the role of river input (buoyancy) in setting up a sub-annual (low-frequency) exchange flow (Jackson and Straneo, 2016). Using the exchange flow framework, we can then analyze the role of shelf and glacial forcing in setting fjord properties.

We evaluate bulk properties of the model exchange flow such as incoming/outgoing volume flux Q_{in}, Q_{out}, incoming/outgoing Salinity S_{in}, S_{out}, and incoming/outgoing Temperature Θ_{in},

Θ_{out} using the Total Exchange Flow (TEF) framework (MacCready, 2011; MacCready et al., 2018; Burchard et al., 2018; Lorenz et al., 2019). TEF allows a calculation of exchange flow properties consistent with the Knudsen relation in salinity space (Burchard et al., 2018). In traditional TEF, averages are calculated in salinity coordinates rather than spatial coordinates allowing both tidal and subtidal fluxes to contribute to the exchange flow. For SF, temperature gradients are non-negligible and partially compensate salinity, therefore, we use density coordinates rather than salinity coordinates to evaluate the changes in volume, salinity and heat transport (Lorenz et al., 2020). Using the notation of Lorenz et al. (2020), the TEF transport (Q^c_ρ) of a tracer c in density coordinates is

$$Q^c_\rho = \left\langle \int_{A(\rho)} cu \mathrm{d}A \right\rangle, \tag{4.3}$$

where $A(\rho)$ is the area of a cross section with densities greater then ρ, u is the velocity normal to the cross section defined to be positive inwards, and $\langle\rangle$ denotes temporal averaging. For example if $c = 1$, then Eq. 4.3 calculates the net volume transport with $Q_\rho(0) = Q_{BT}$, the total barotropic flux, and $Q_\rho(\rho_{max}) = 0$. We sort the data into 1000 discrete potential density bins and we find the TEF fluxes are not sensitive to further increase in bin numbers. The model does not include tides and the dominant variability is synoptic, so we use a 30-day rolling mean in place of a tidal filter, to average over the wind variability (Jackson and Straneo, 2016). Similar to tides, we expect the fjord response to wind forcing to be osciliatory, and therefore the TEF framework can capture subsynoptic fluxes that are lost when using an Eulerian framework. The derivative of Eq. 4.3 gives a tracer flux

$$q^c_\rho(\rho) = -\frac{\partial Q^c_\rho(\rho)}{\partial \rho}, \tag{4.4}$$

as a function of density class. To get the total incoming (outgoing) tracer flux we then integrate Eq. 4.4 over the portions that are inflowing (outflowing). We use the dividing salinities method (Lorenz et al., 2019) which identifies the extremum in Q^c_ρ as the dividing density class ρ_{div} to define inflowing and outflowing regions. The bulk tracer values are $c_{in} = Q^c_{in}/Q_{in}$ and $c_{out} = Q^c_{out}/Q_{out}$ where c can be salinty S, Potential Temperature Θ or Potential Density ρ.

(Note, that values of ρ reported are potential density anomaly, ρ - 1000 kg/m^3, for convenience). Additional details for calculating TEF from a numerical model are given in Lorenz et al. (2019). All TEF ouput is calculated here using the pyTEF library (Lorenz et al., 2020). We calculate TEF values on 7 transects along SF fjord (Fig. 4.1). For the time series of TEF transport, we show the transport at the 3rd line (SF Line 3).

4.3.4 Analytical model of shelf-driven circulation

Analytical models will enable us to diagnose the drivers of the exchange flow and attribute specific dynamics for observed transport. In this study, we utilize the framework for shelf-driven circulation introduced by Jackson et al. (2018, J18). J18 used an idealized model to explore the response of fjords to shelf forcing as a function of fjord adjustment time and the Kelvin number. The fjord adjustment timescale is given by $\omega L/c_i$, where ω is the forcing frequency, c_i is the baroclinic wave speed, and L is the length of the fjord. The adjustment timescale for SF is 1-2 days and is not substantially shorter than the forcing frequency of 3-10 days and so density fluctuations take some time to propagate into the fjord. The Kelvin number, $Ke = W/L_d$, is the ratio of the fjord width W over the deformation radius $L_d = c_i/f$ where f is the Coriolis frequency. Ke is used to diagnose the relative importance of rotation to fjord dynamics, and SF has a $Ke \sim O(1)$. Therefore, SF lies in a parameter regime in which both rotation and traditional 2-dimensional dynamics are important. J18 described the shelf forcing as a combination of a 2-dimensional standing wave and a 3-dimensional Kelvin wave. The theory was found to compare favorably with observations of pycnocline fluctuations and velocity in Sermilik Fjord (Jackson et al., 2018; Sanchez et al., 2021). The volume flux in a single layer associated with shelf forcing and coastal waves is given by

$$Q_{cw} = \mathrm{e}^{-Ke} W c_i \frac{\sin\big(k(L-y)\big)}{\cos(kL)} \eta_M + (1-\mathrm{e}^{-Ke})^2 \frac{2c_i W}{Ke} \sin\big(k(L+W/2-y)\big)\eta_M, \tag{4.5}$$

where η_M is the amplitude of the density fluctuation at the mouth, y is the distance from the mouth, and $k = \omega/c_i$ is the wavenumber. Eq. 4.5 is a modified form of Eq. 29 from J18 where the first term is the standing wave contribution and the second term in the combination of the outgoing and incoming Kelvin wave. In our analysis, we will be examining changes in fjord-shelf exchange over monthly timescales, but the primary wind forcing occurs between 3 to 10 days (Appendix A) and so we use a 60-day high-pass filter to remove seasonal variability. We define density fluctuations as

$$\eta_M = \frac{\overline{\rho^{hp}}}{\overline{\rho_z}}, \tag{4.6}$$

where $\overline{\rho^{hp}}$ is the 60-day high-pass filtered section-averaged potential density at the mouth of the fjord, and $\overline{\rho_z}$ is the annual section-averaged vertical density gradient at the mouth. Plugging η_M into Eq. 4.5 calculates the volume flux in a given layer. If we treat the fjord as two layers than we assume this flux is balanced by an opposite flux in the other layer. Therefore, the incoming flux will switch between the top and bottom layers as the pycnocline fluctuates, and so the total incoming flux can be written as $Q^*_{sh} = |Q_{cw}|$, where the star indicates this is an analytical model. Lastly, we apply a 30-day rolling average to smooth out synoptic scale fluctuations in Q^*_{in}.

4.3.5 Analytical model for plume-driven circulation

Plume dynamics can be approximated using buoyant plume theory (Morton et al., 1956) which describes the evolution of buoyancy for a rising plume. As the plume rises it entrains ambient water and is diluted reducing its overall buoyancy. For an unstratified fjord, the volume flux of an outflowing plume is given by (Cowton et al., 2015a; Morton et al., 1956; Straneo and Cenedese, 2015; Zhao et al., 2022a)

$$Q^*_p = c_\epsilon B^{1/3} (Z)^{5/3}, \tag{4.7}$$

where $c_\epsilon = (6/5)(9/5)^{1/3}\pi^{1/3}\epsilon^{4/3}$ is the entrainment factor for a half cone plume with $\epsilon = 0.13$, $B = g'_0 Q_{sg}$ as the initial buoyancy flux, and Z as the height over which the plume rises. The

buoyancy flux is composed of the initial reduced gravity $g'_0 = g(\rho - \rho_W)/\rho$ between the ambient density ρ and freshwater ρ_w, and subglacial discharge Q_{sg}. For the deeper part of the fjord, uniform density is a reasonable approximation, however in shallower water, stratification plays an important role in limiting the plume rise height (De Andrés et al., 2020). The height a plume rises under constant stratification is given by (Turner, 1973; Hunt and Kaye, 2005; Slater et al., 2016)

$$Z_{nb} = 1.95(N^2)^{-3/8}\left(\frac{B}{2\pi\alpha^2}\right)^{1/4} - \frac{5}{6\alpha}\left(\frac{32\alpha Q_{sg}^2}{5\pi^2 g'_0}\right)^{1/5}, \tag{4.8}$$

where $N^2 = -g\frac{\mathrm{d}\rho}{\mathrm{d}z}$ is the Brunt-Väisälä frequency. We use the neutral buoyancy height Z_{nb} in place of Z in Eq. 4.7 to calculate the predicted plume volume flux Q_p^*. In the absence of additional mixing and circulation within the fjord, Q_p^* would be the outgoing volume flux.

4.4 Results

4.4.1 Model Description

Shelf Circulation and Variability

We start with a brief description of the model circulation and properties to provide context for the exchange analysis. SF is located at the confluence of PW carried in from the coastal current (EGCC) and AW transported along ST (Fig. 4.2a,). This location allows the variability of the large-scale currents feeding into SF to be observed in the model temperature field spatially. Closer to the surface, the EGCC can be seen as a westward flowing current carrying relatively cold water (Fig. 4.2a). The current keeps warmer surface water isolated offshore. The gradient between these two water masses is relatively diffuse indicating lateral mixing over the shelf and trough. At greater depths, relatively warm AW is steered into the fjord along ST, although there are recirculation cells within the trough system (Fig. 4.2b). From a fixed depth perspective, the AW appears to lose heat as it enters the fjord from the trough system, but this does not take into account the along-shelf isopycnal gradient (discussed later this section) which lowers cooler water from above close to the coast. Current velocities along the shelf are much stronger than

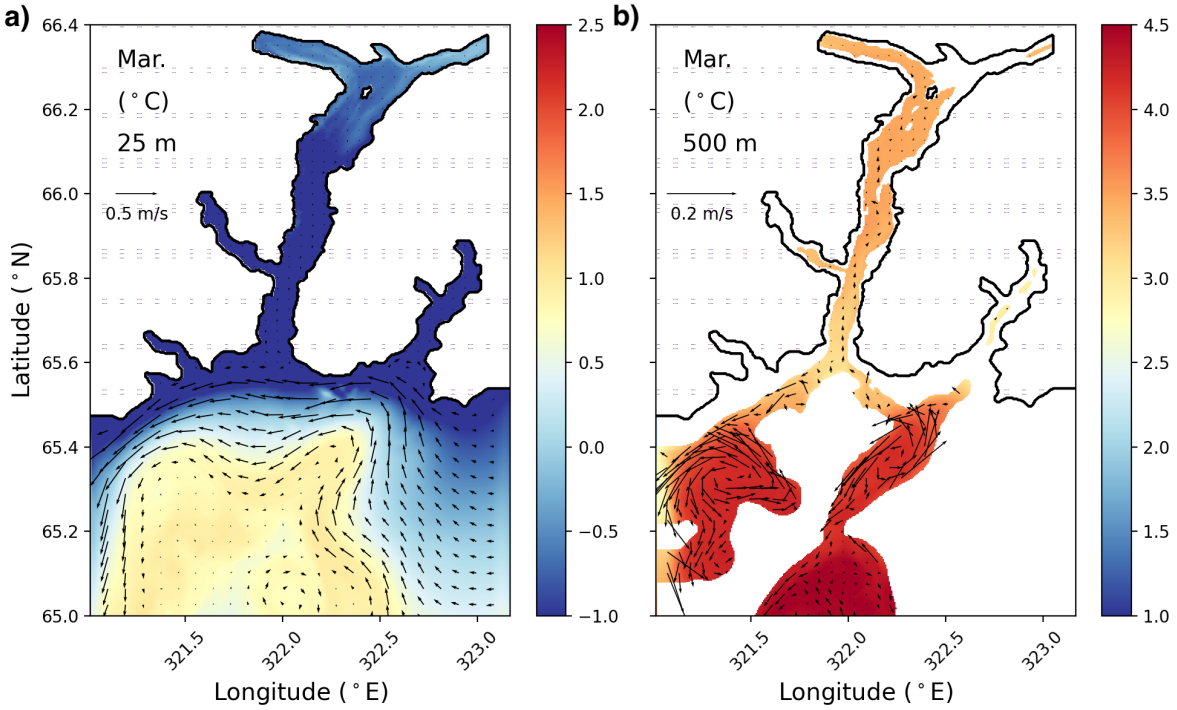

Figure 4.2. (a-b) Average (March 2017) of temperature and velocity from the NG run at 25 m depth and 500 m depth. Note the different colorbars between the two panels.

within the fjord.

The wind stress on the shelf (used in both the NG and WG runs) exhibits a strong seasonality (Fig. 4.3). The along-shore wind stress is oriented primarily to the southwest (Appendix A) resulting in mean downwelling-favorable winds. Individual wind events can be intense along the shelf reaching magnitudes as high as 0.8 N/m^2. A low-pass wind stress, τ_{lp} is calculated using a 60-day rolling mean followed by a 25-day rolling mean to further smooth out any remaining synoptic variability. τ_{lp} shows the winds are strongest from November to May and weakest from June to August (Fig. 4.3a).

The model allows us to explore the full seasonal variability of the shelf upstream (east) of SF (Fig. 4.1, red). Two month averages of temperature in the NG run are highest in the fall (Sep. – Oct.) and coolest in the spring (Mar. – Apr., Fig. 4.4). In September, when the waters on the shelf are warmest, the AW extends all through the water column and onto the shelf (Fig. 4.4e). During the rest of the year, a cold PW cap is present close to the coast, however its lateral

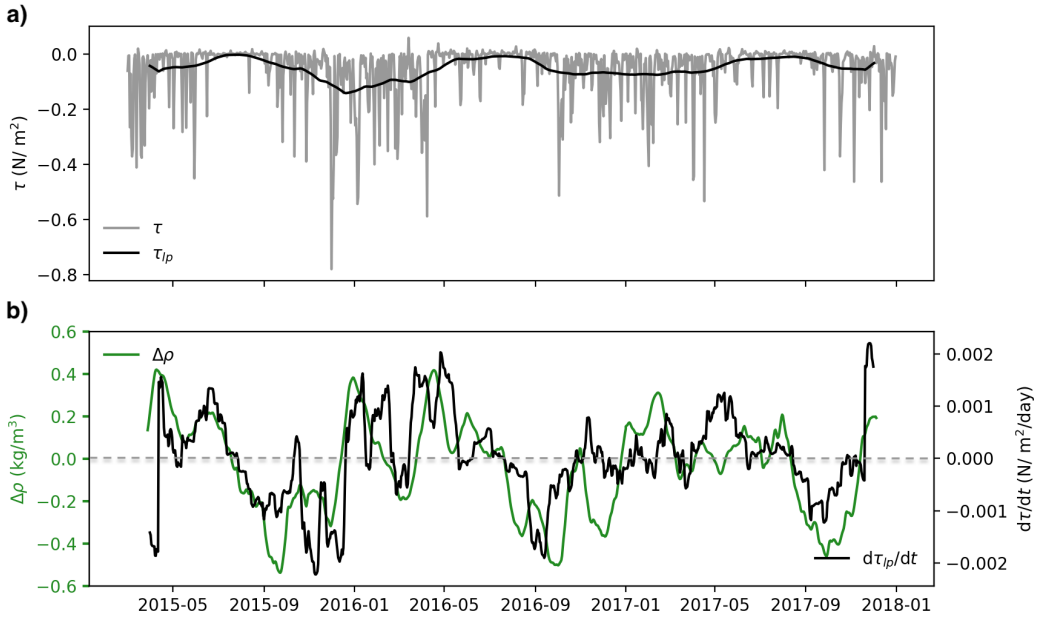

Figure 4.3. a) The daily along-shelf wind stress (gray) and τ_{lp} (black). Negative is towards the southwest (Appendix A). b) In green (left axis) is the difference between the TEF calculated ρ_{in},ρ_{out} at SF line 3. Positive indicates inflow at depth. The right axis (black) is the derivative of the (60-day low-pass) along-shelf wind stress (τ_{lp}).

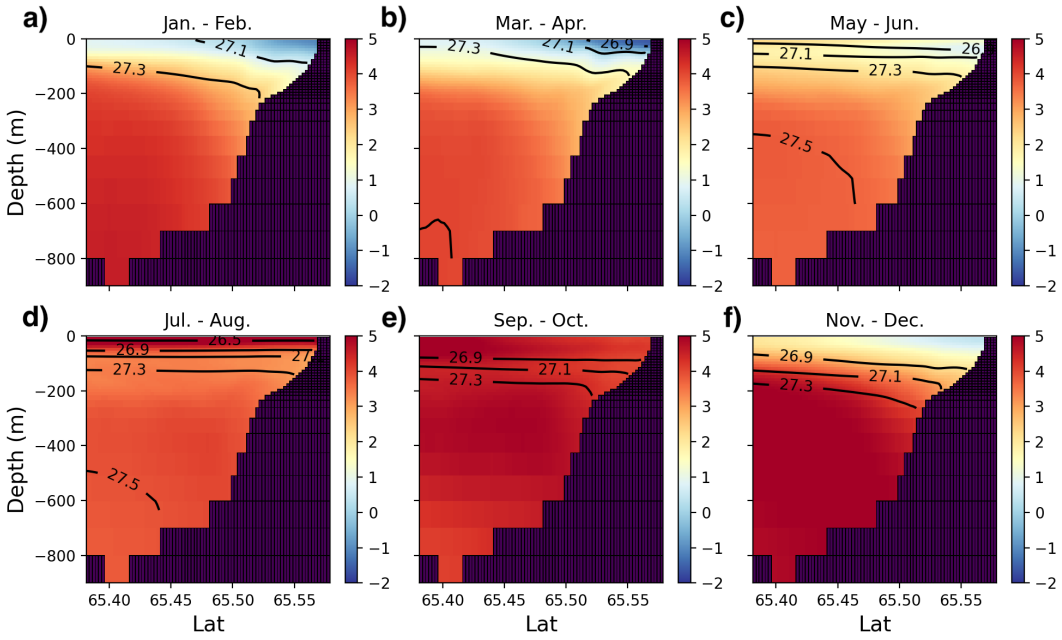

Figure 4.4. Two month averages of coastal section temperature (No Glacier run, see Fig. 4.1 for location). View is facing west with coast on right. Contours are isopycnals of potential density anomaly (26.5, 26.9, 27, 27.3, 27.5). Temperature has units of ° C.

extent appears variable and dependent on the steepness of the isopycnal gradients. The isopycnal gradients are steepest in January and therefore, the ratio of cold PW to warm AW is highest at this time of year. The transect is upstream of the fjord and there is little difference in temperature between the NG and WG run (not shown), and therefore we assume the forcing associated with isopycnal displacement on the shelf is active and equivalent in both runs.

In addition to the seasonal cycle in temperature, the shelf transects show the variability in isopycnal location and gradient (Fig. 4.4). The density gradients across the shelf are strongly correlated with the along-shelf wind stress ($r = 0.78$, $p < 10^{-3}$). Therefore, the isopycnals are compact and relatively flat in the summer months when the winds are weaker. The flat isopycnals above 200 m correspond with the full water column intrusion of warm water onto the shelf. The isopycnals start to steepen in the fall and early winter in response to downwelling-favorable winds (Appendix A). The coastal current is in geostrophic balance, and the coastal current is strongest in the fall and winter when isopycnals are steepest (Fig. 4.5).

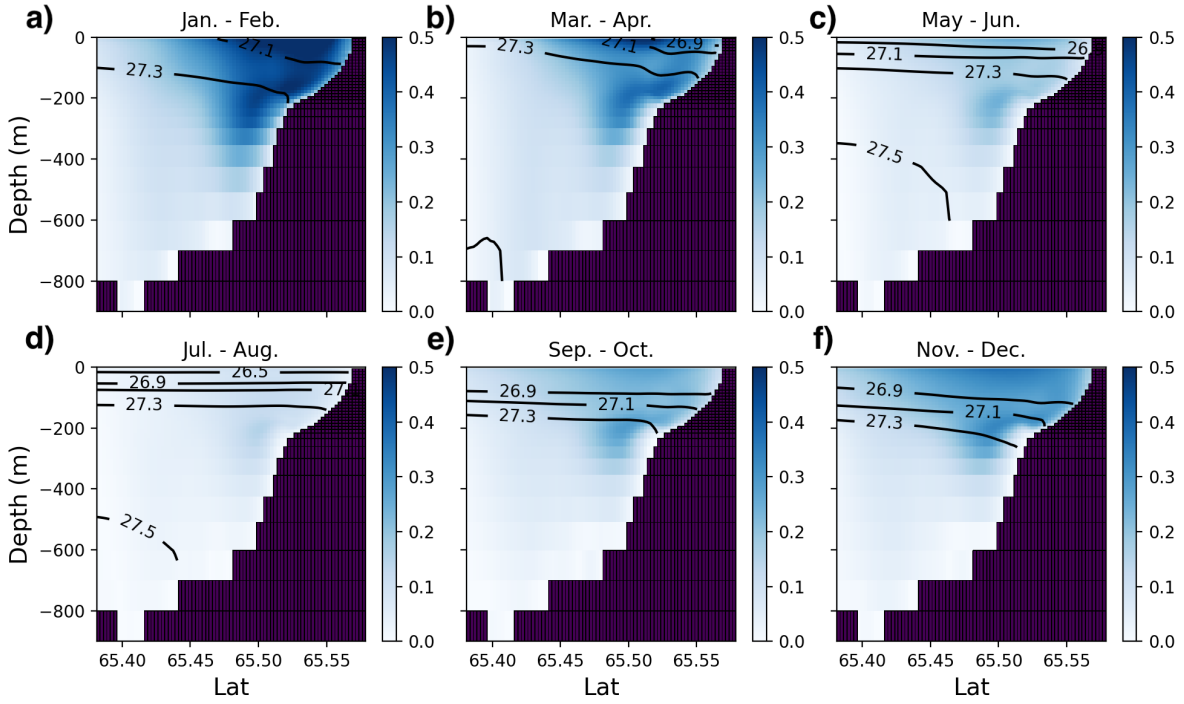

Figure 4.5. Two month averages of coastal section velocity (No Glacier runs). View is facing west with coast on the right. Contours are isopycnals of potential density anomaly (26.5, 26.9, 27, 27.3, 27.5). Velocity is defined positive westward (equatorward) for this figure and has units of m/s.

We also examined the coastal current downstream (west) of the fjord. The NG and WG runs diverge and a relatively fresh wedge can be observed close to the coast in the WG run July through September (Sup. Fig.4.22). However, in these downstream sections we do not observe substantial differences in temperature or current velocity (Sup. Fig. 4.23).

Fjord circulation and properties (No Glacier)

Next, we describe the fjord circulation in the absence of any glacial forcing. The circulation at the mouth is characterized by both vertical and horizontal shear throughout the year (Fig. 4.6a–c). The sign of the horizontal shear changes, but is always present indicating rotation influences fjord dynamics year round. In April, the circulation is closest to 2-dimensional with outflow around 100 m and inflow at depth. By October, the circulation at depth has reversed and is flowing out of the fjord and between 200 m and 500 m the flow is primarily going into fjord.

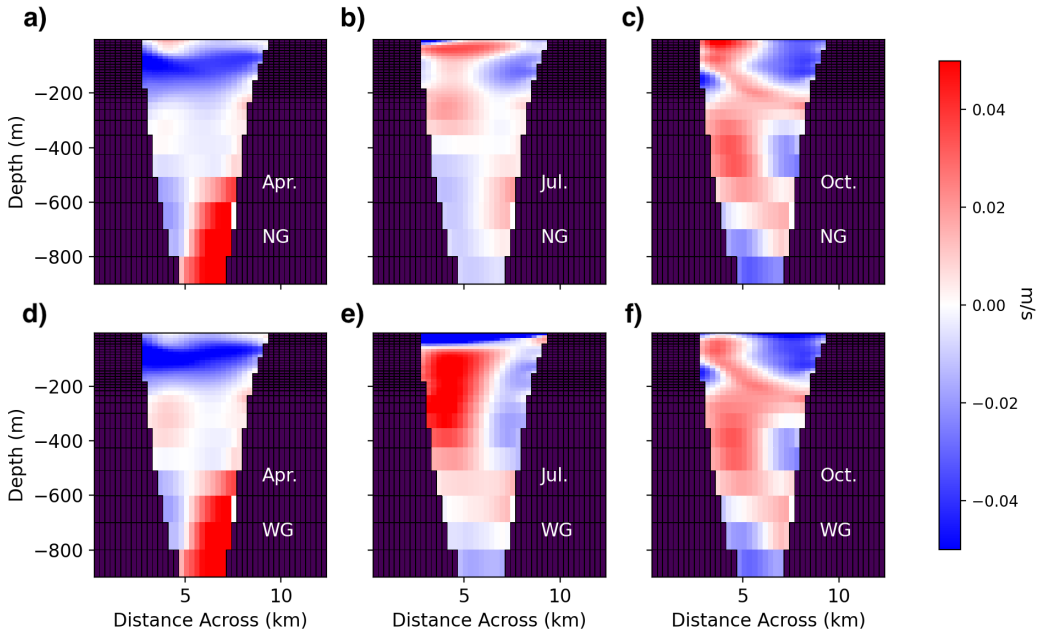

Figure 4.6. a–c) monthly averages of velocity at the mouth of the fjord in April, July and October for the No Glacier run. d–f) in April, July and October for the With Glacier run. Positive velocities are flowing into the fjord.

We also examine the along-fjord variability in temperature and bathymetry in the NG run. SF is deep resulting in little along-fjord variability in temperature and density (Fig. 4.7a–c). Isopycnals lie flat within the fjord and only have a notable slope in the upper 100 m and approaching topography. The fjord depth rises steadily from 900 m at the mouth to 500 m near the branching point (70 km) and increases in depth again as it approaches Helheim glacier (90 km). In summer, an along-fjord gradient in temperature can be seen in the upper 100 m, with warmer water at the fjord mouth and remnant PW at the fjord head.

The seasonal variability of the fjord circulation is visible through a width-averaged overturning streamfunction. The overturning circulation is positive in April with inflow at depth and outflow near the surface (Fig. 4.8a). In July, the circulation is sluggish and slightly negative (Fig. 4.8b). By October, the circulation appears three-layered with at fully reversed circulation at depth and a shallower cell in the upper 250 m (Fig. 4.8c).

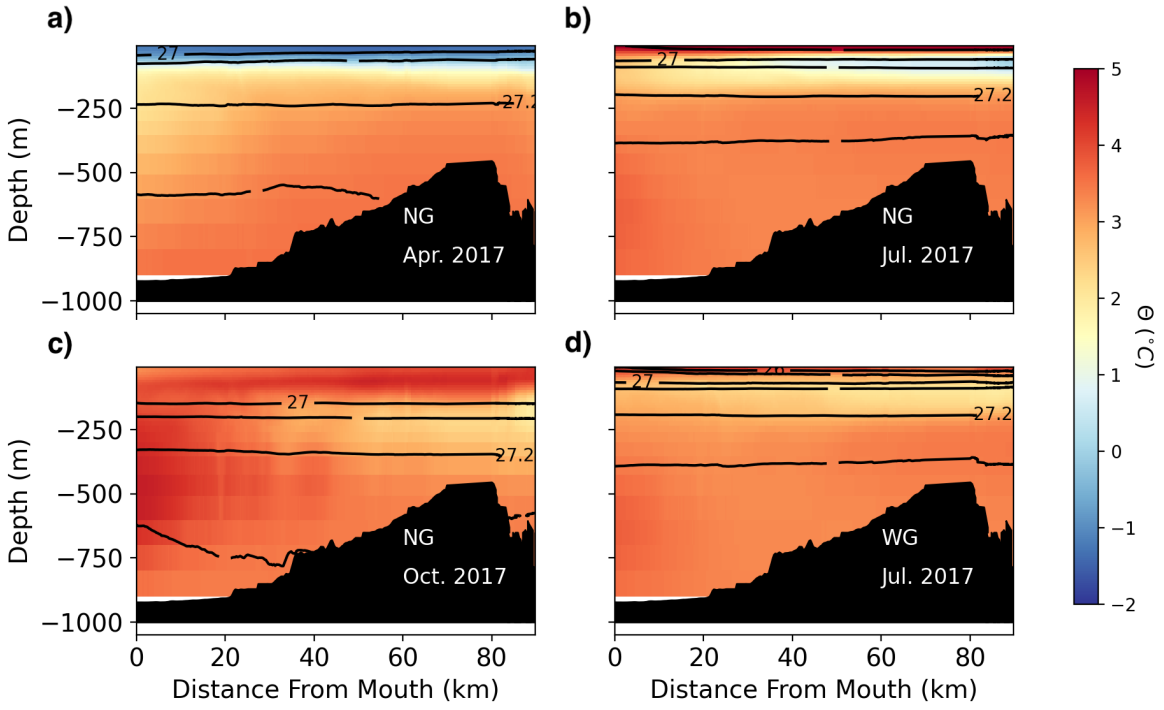

Figure 4.7. Along Fjord width-averaged monthly temperature in April (a) and July (b) and October (c) for the NG run and July (d) for the WG run. The contours are isopycnals of potential density anomaly (26, 27, 27.15, 27.35, 27.45 kg/ m^3).

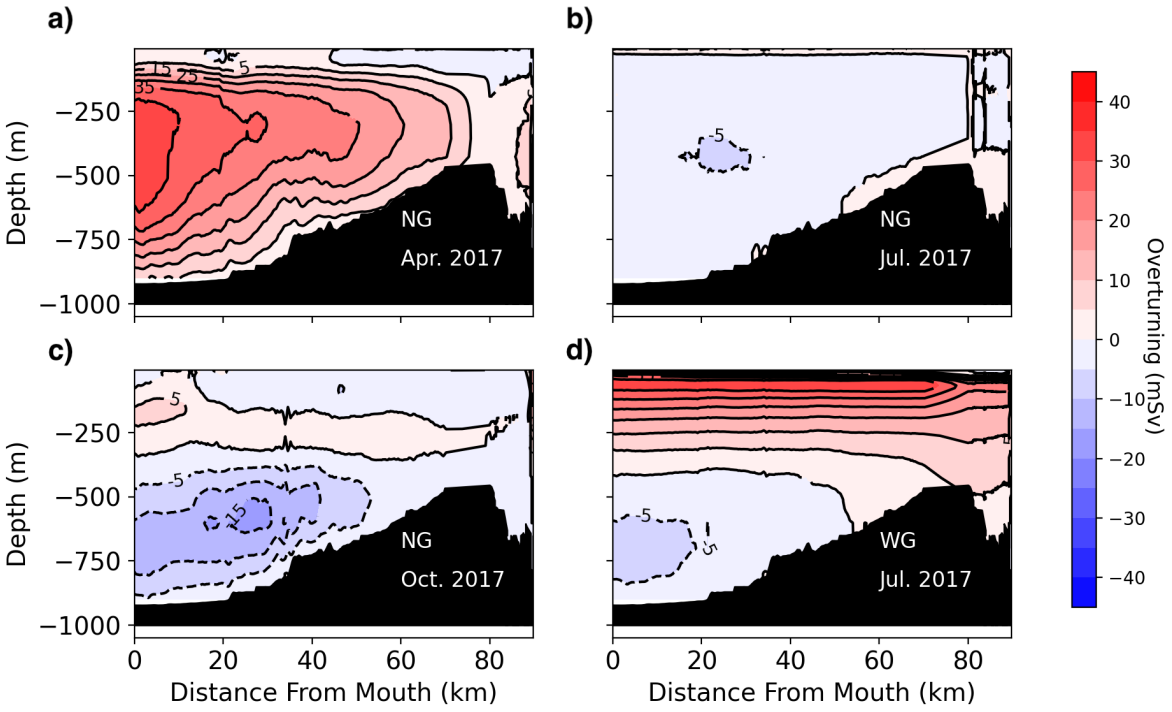

Figure 4.8. Width and monthly-averaged overturning streamfunction over April, July and October (NG), and July (WG) in 2015. Counter-clockwise flow is a positive streamfunction.

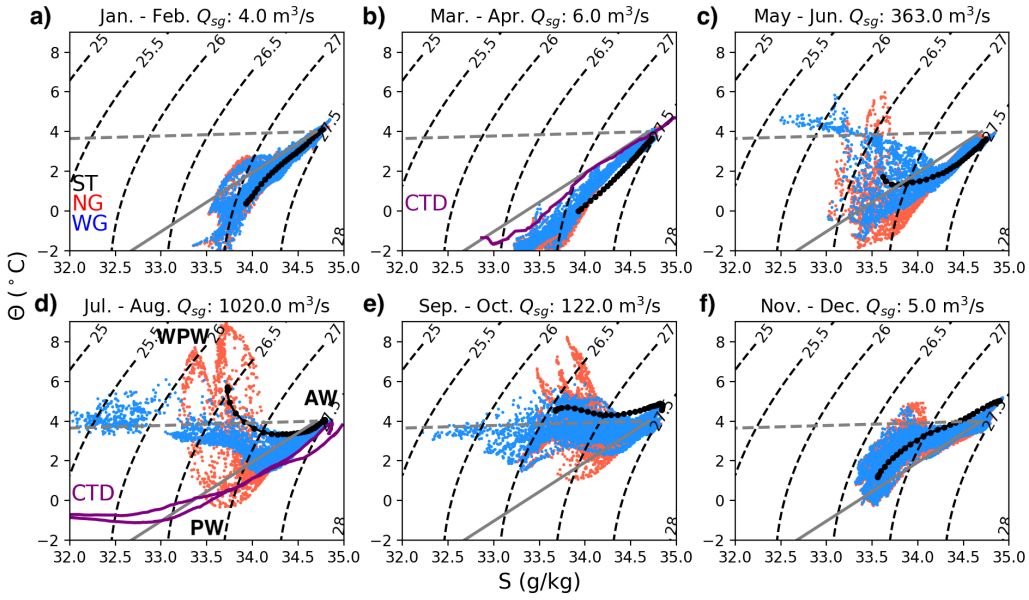

Figure 4.9. Section-averaged TS properties at SF Line 3. Each panel shows the TS properties over a 2-month period with the spread coming from time (daily) and depth. The blue dots are from the WG run and the red dots are from the NG run. The black line is the TS properties in Sermilik Trough (ST). The gray solid line is the melt-mixing line and the gray dashed line is a subglacial discharge mixing line. The contours are potential density anomaly. Q_{sg} is the two-month average subglacial discharge. The average TS from CTD profiles collected in Aug. 2015, Jul. 2017, and Mar. 2010 are in purple. The water mass locations are labeled in panel d.

Lastly, we describe the water properties at SF Line 3 in temperature and salinity (TS) space in the NG run (red, Fig. 4.9). In the the absence of glacial forcing (NG run), the shelf variability is also seen mid-fjord (black, Fig. 4.9). WPW is found seasonally near the surface ($\Theta \approx 8$ °C), PW ($\rho \approx 27.0$ kg/m^3) is found at the temperature minimum, and AW is the saltiest and densest water ($\rho \approx 27.5$ kg/m^3). We see that in the winter months (Jan. – Apr.) the fjord model properties lie in between PW and AW, and the fjord can be described as a two-layer system (Fig. 4.9). As the surface warms, a distinctive "U" shape forms from the three water masses present: WPW, PW and AW. As the surface cools, the system starts adjusting back towards a two-layer system.

Fjord circulation and properties (With Glacier)

The inclusion of glaciers and subglacial discharge plumes alters the fjord circulation and temperature, especially in summer. Revisiting the circulation at the mouth, there is substantial difference between the WG and NG runs in July, with a much stronger outflow near the surface and a defined recirculation in the middle part of the fjord in the WG run (Fig. 4.6d–f). In the NG case, the circulation is on average weaker and is multi-layered. The non-summer months (Apr. and Oct.) show little difference in velocity magnitude and structure between the two model runs. Taken as a whole, the mouth cross-sections demonstrate that the spatial structure of the circulation is complex and highly variable. In this study, we are primarily interested in overturning (vertical shear) and therefore will be analyzing width-integrated exchange flows.

The shallow along-fjord temperature in July in the WG run is substantially warmer than in the NG run (Fig. 4.7d). This difference can be attributed to subglacial discharge entraining ambient AW and bringing it up to shallower depths via the plume. Differences between the WG and NG run in the along-fjord isopycnals in Apr. and Oct. are minimal (not shown) indicating that in the absence of large amounts of subglacial discharge ($> 100^3$/s) the fjord is dominated by the shared wind-driven exchange. The overturning steamfunction in the WG run shows the plume drives strong outflow near the surface (Fig. 4.8d). Below 400 m, the July WG streamfunction is negative similar to the July NG run. The WG run also has stronger circulation near the fjord head which is expected given the subglacial discharge plume.

The TS properties in the WG run reveal the influence of the plume on fjord water properties. The WG run (blue, Fig. 4.9) starts diverging substantially from the NG run in June due to large amounts of subglacial discharge. This divergence follows the subglacial discharge-mixing line, and the end result is a cooler and fresher surface water mass and the ”erasing” of the clear PW signal (temperature minimum). The WG run properties converge back to those of the NG run in October, and therefore we can state that the time period of subglacial discharge influence is June – September. The summer and winter CTD observations are also included for context. They show

that the model surface waters are biased warm during the summer, likely due to a lack of iceberg melt.

4.4.2 Exchange-flow structure

Having described the seasonal variability in circulation in the WG and NG runs, we now evaluate the exchange flow and the influence this has on fjord properties. The volume transport as a function of depth at SF Line 3 for the NG run is shown in Figure 4.10a. We focus on the transport at SF Line 3 as this location is closest to the mooring SF4 and is representative of transport away from mixing processes at the head and the mouth of the fjord. With three years of data, a picture emerges of seasonal volume transport in the fjord with a reversing circulation below 200 m (Fig. 4.10a). The volume transport is filtered through a 30-day rolling mean to remove the first-order synoptic variability associated with the winds. The volume transport is roughly in two layers below 200 m (Fig. 4.10). The circulation is inflowing at depth in the spring and reverses to outflowing during the summer. This circulation is interrupted, especially in the upper 200 m, by the cumulative effects of wind events that are not completely filtered out. The low-frequency transport appears to be dominated by the seasonal cycle indicating the importance of seasonal variability on the shelf-driven circulation. The WG run contains both the plume and shelf forcing, and so we "isolate" the plume-driven circulation by subtracting the WG run from the NG run. The "isolated" plume-driven transport shows a strong seasonal cycle with an increase in outflowing transport during the summer and a compensating inflow between 200 and 500 m (Fig. 4.10b). The coherence of the "isolated" plume-driven transport gives confidence the two forcing mechanisms add together approximately linearly.

Applying TEF to SF line 3 enables us to calculate the seasonal volume transport of the fjord in density space (Fig. 4.11) and allows direct connection with water mass variability. The composite TEF analysis shows that the NG transport is generally concentrated in the most dense layers. During the first half of the year, the deep flow resembles a traditional estuary with inflow at depth and outflow at lighter densities. As seen in depth space (Fig. 4.10), the flow reverses

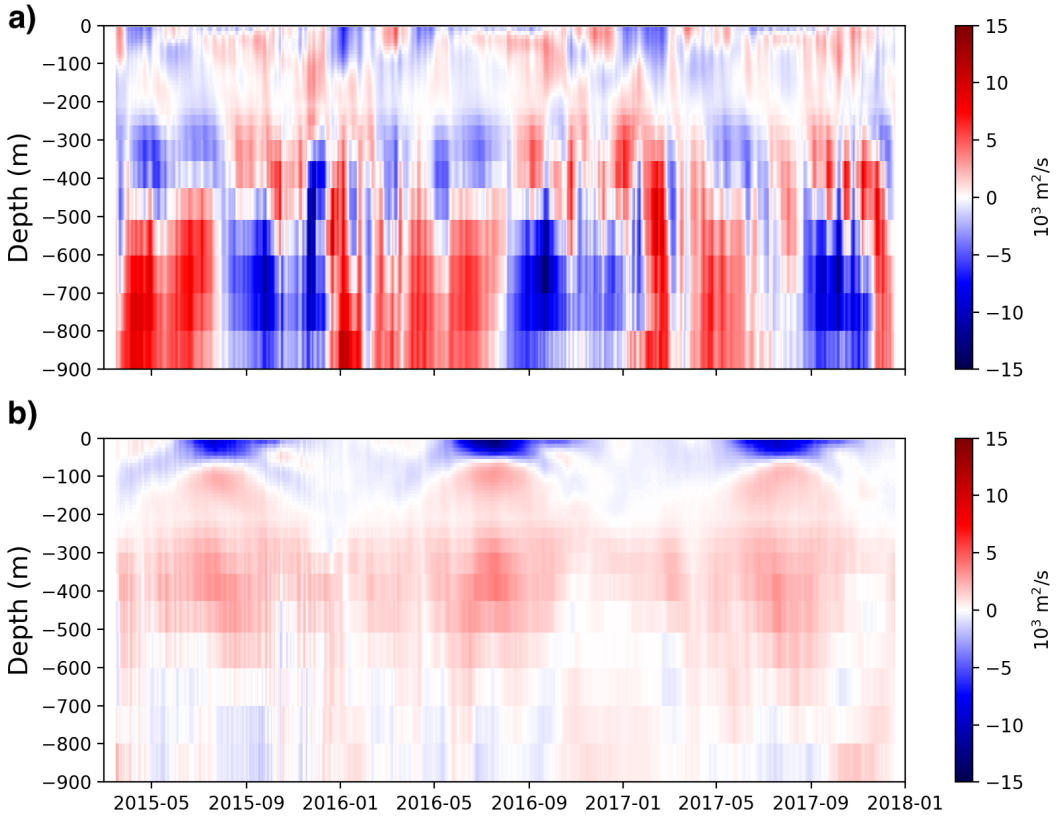

Figure 4.10. a) 30-day rolling mean volume transport in the NG run at SF line 3 as a function of depth and time. Positive transport is into the fjord. b) The difference between the volume transport in the WG run and the NG run at SF line 3.

in the second half of the year. Upon closer inspection, the inflowing density from Jan. – Jun. can be seen to be getting progressively denser filling the fjord with a greater concentration of AW. When the exchange reverses, the outflowing deep water can be seen getting progressively lighter. The WG run stands out in the summer and it overtakes the background NG run (Fig. 4.11). The inclusion of the plume alters the total circulation enough to prevent the deep reversal from occurring until later in the fall. The TEF composite profiles also highlight the multi-layered exchange occurring in SF (Fig. 4.10). In the winter months, there are multiple zero crossings separating the outflowing and inflowing "cores" at 27 kg/m^3 and 27.3 kg/m^3 respectively. The multiple inflows raise questions as to the physical meaning of TEF terms such as S_{in} or S_{out}. With this caution in mind, our analysis of TEF bulk values will assume they are representative of a larger 2-dimensional overturning circulation.

The exchange flow reversal exports a dense water mass associated with AW (Fig. 4.9 and 4.11) and is therefore an important lever in reducing the heat available to melt. We propose that the seasonality of the winds is responsible for the reversal by flattening isopycnals during the spring. The mean state of the winds along the shelf is consistently downwelling favorable, such that a relaxation towards no winds acts effectively as upwelling. The changing slope of isopycnals in Sermilik Trough are qualitatively consistent with this picture (Fig. 4.4).

The relationship between low-frequency wind forcing and the exchange reversal is tested by comparing the time derivative of low-pass along-shelf wind stress (τ_{lp}) and TEF exchange (Fig. 4.3). The exchange flow direction is represented through a 25-day rolling mean of $\Delta\rho = \rho_{in} - \rho_{out}$ in the NG run at SF Line 3. When $\Delta\rho > 0$, the exchange flow is positive with inflow at depth. The derivative of the wind stress is significantly correlated with $\Delta\rho$ ($r = 0.55$, $p < 10^{-3}$) suggesting that wind variability is consistent with the sign of the exchange flow. The seasonal variability of wind stress therefore likely plays an important role in setting the amount of AW in SF with relaxing winds leading to a greater concentration of AW.

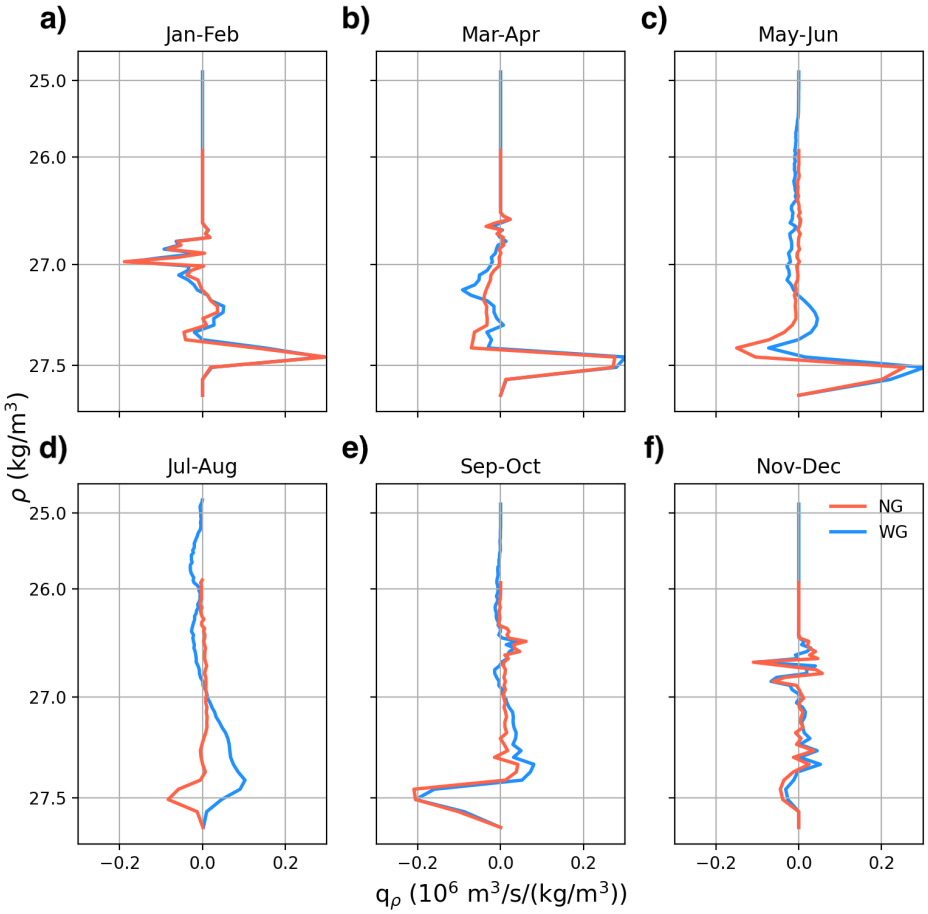

Figure 4.11. The composite TEF analysis at SF Line 3 for the three years of model runs. Each panel is a three-year average over the two months. The x-axis is volume flux per density class. The y-axis is potential density anomaly ρ . Note the y-axis is nonlinear so that greater resolution can be given to the deepest densities. Red is from the NG run, and blue is from the WG run. 100 density bins were for used this figure instead of 1000 for visual smoothness.

4.4.3 Variability of TEF bulk properties

The exchange flow of the fjord can be defined as

$$Q_e = \frac{Q_{in} - Q_{out}}{2}, \tag{4.9}$$

where Q_{in} is the TEF inflowing volume flux and Q_{out} is the outflowing flux with $Q_e \geq 0$ (MacCready et al., 2018). In the NG run, the cycle of the exchange flux is consistent with the seasonal cycle of wind forcing with the greatest flux occurring during the winter months (max 60 mSv) and weak exchange during the summer (max 10 mSv) (Fig. 4.12a). The exchange flux in the WG run diverges from the NG run during the summer and drives a magnitude of exchange that is comparable to the shelf-driven exchange in winter. Since the plume forcing is strongest in the summer when the shelf-driven circulation is weakest, the fjord is able to experience exchange above 30 mSv for the majority of the year.

We decompose the exchange flux into the plume-driven exchange (WG-NG) and shelf-driven exchange (NG) and compare the results against theory (Eq. 4.5 & Eq. 4.7) using values in Table 4.2. The exchange flux predicted by plume theory is strongly correlated with the plume flux in the model ($r = 0.89$, $p < 10^{-3}$) (Fig. 4.12b). The high correlation, suggests that the plume-driven circulation is mostly set by the boundary conditions (plume) and not by additional mixing away from the glacier. The exchange flux predicted by variation in pycnocline depth is correlated with the NG exchange flux ($r = 0.65$, $p < 10^{-3}$, Fig. 4.12c). The theory appears to overestimate the fjord's response to the largest wind events, but otherwise lends confidence that the shelf-driven exchange flux can be described through coastal wave dynamics. The pycnocline variability which is used in Eq. 4.5 is correlated with the along-shelf wind stress ($r = -0.61$, $p < 10^{-3}$) consistent with a wind generation mechanism.

Subglacial discharge drives a large salt exchange and export of freshwater onto the shelf (Fig. 4.12d). The salt exchange is defined as $Q_e \Delta S$ where $\Delta S = S_{in} - S_{out}$. When $\Delta S > 0$, the

Table 4.2. Variables used in Eq. 4.5 and Eq. 4.7.

Symbol	Variable	Value
c_i	baroclinic wave speed	0.75 m/s
L	fjord length	90 km
f	Coriolis Frequency	1.3×10^{-4} /s
W	fjord width	7.5 km
y	distance from mouth	30 km
k	wavenumber	1.4×10^{-5} rad/m
g'_0	reduced gravity	0.0263 m/s^2
$\overline{\rho_z}$	density gradient 0-240 m	-0.004 kg / m^2
$\overline{N^2}$	Summer Stratification 0-240 m	0.008 /s^2

exchange flow is positive with inflowing salty water at depth and the export of fresher water above. The plume is the largest seasonal driver of the salt flux with the WG run salt flux peaking during the summer (Fig. 4.12d). In the absence of subglacial discharge forcing, the salt flux is relatively weak during the summer. The rest of the year the salt flux is variable due to wind forcing but is generally negative in the fall and positive during the winter when the circulation reverses.

The heat exchange is defined as $Q_e \Delta\Theta \rho c_w$ where $\Delta\Theta = \Theta_{in} - \Theta_{out}$ and c_w is the specific heat capacity of seawater. When $\Delta\Theta > 0$, the exchange flow is positive with inflowing warm water at depth and the export of cooler water above. The heat exchange is dominated by the shelf-driven circulation (Fig. 4.12e) and therefore fluctuates between positive and negative depending on wind-strength. The addition of subglacial discharge results in a negative heat exchange in the WG run, that is the fjord is exporting heat, but this flux is small in comparison to the larger fluctuations in the winter.

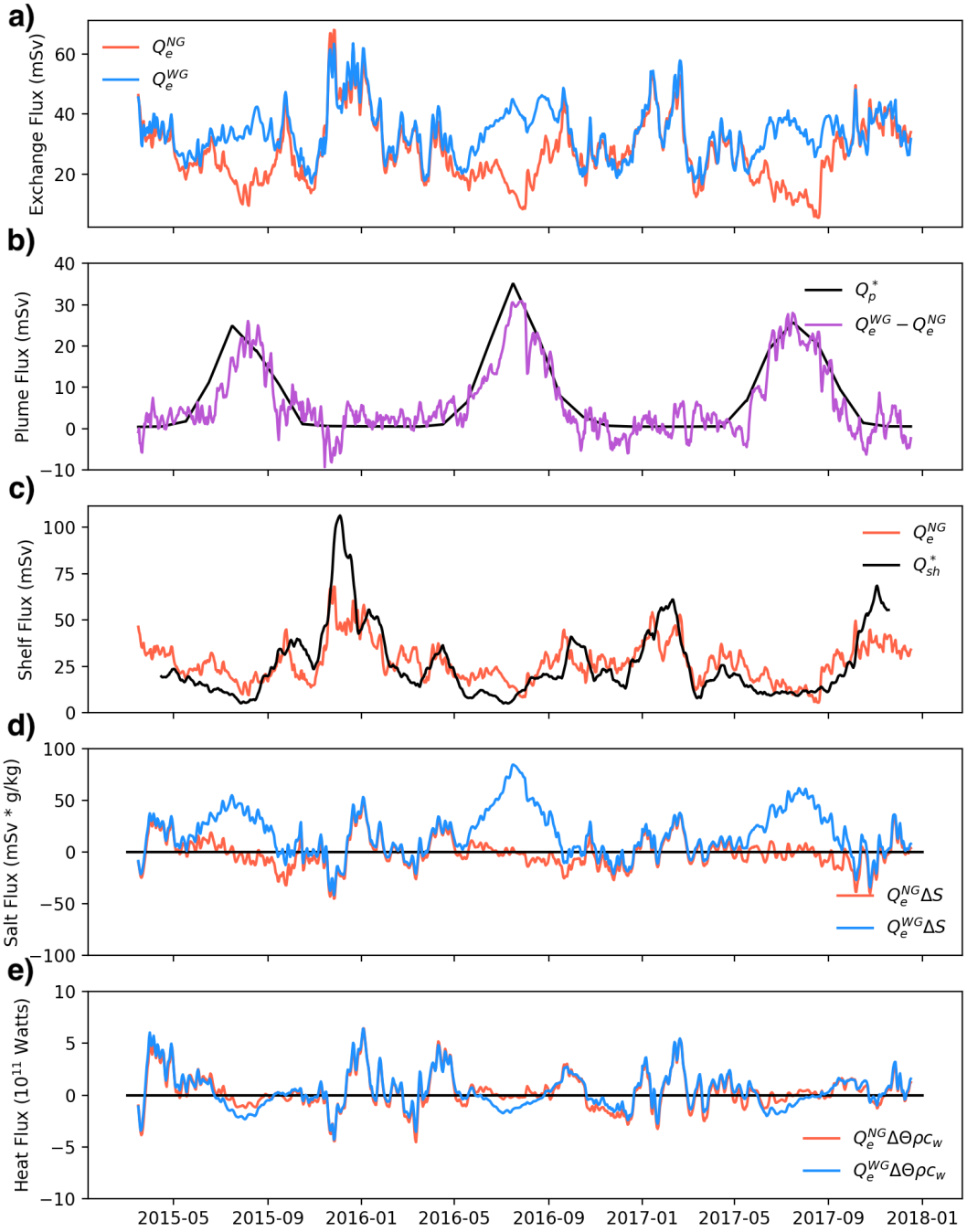

Figure 4.12. a) Exchange flux at SF line 3 in the NG and WG run. Units are in mSv (10^3 m^3/s). b) Plume flux derived from Plume Theory (Q_p^*) and the difference between the WG and NG runs at SF line 3. c) Exchange flux estimated from coastal-trapped waves (J18) and the NG run. d) Salt Flux from the exchange flow. The black line separates positive (incoming salt) from negative salt flux. e) Heat flux from the exchange flow. Positive Heat flux would make the fjord warmer.

In summary, the TEF results and shelf-plume forcing comparison indicate that the timing of subglacial discharge results in a strong exchange flow when the shelf-driven circulation (Q_e^{NG}) is relatively weak. Both the shelf and plume-driven circulation (Q_e^{WG}-Q_e^{NG}) fit our analytical models lending confidence to our understanding of the drivers of the exchange flow. The salt flux in the WG run is relatively steady in the summer, while both the heat and salt flux in the winter are more variable.

4.4.4 Along-Fjord Variability of Q_e

Next, we investigate the relative effectiveness of the shelf-driven circulating vs. plume-driven circulation in flushing waters at different locations in the fjord. As seen in the exchange flow time series (Fig. 4.12), the WG run is dominated by plume-forcing in the summer (Jun. – Aug.) and shelf-forcing outside the summer. The shelf-driven circulation, active in spring (Mar. – May) and autumn (Sep. – Nov.), is most intense at the mouth of the fjord and decays with distance (Fig. 4.13a) consistent with wave dynamics. In contrast, the plume-driven circulation in summer flows down the fjord relatively unchanged resulting in a near constant along-fjord exchange flux consistent with a source of water from the plume. We note that in September in the WG run, downwelling does not propogate all the way to the fjord and is resisted by the late season subglacial discharge with the exchange flow changing sign away from the mouth (Sup. Fig. 4.25). The bulk TEF properties S_{in} and S_{out} are nearly constant along the length of the fjord (Sup. Fig. 4.27) suggesting that vertical mixing is weak in the fjord interior.

The flushing time V/Q_e is defined as the volume upfjord of a section divided by the exchange flux and is a scaling for residence time within the fjord. The flushing time when the shelf-driven circulation dominates (Spring, Autumn) is relatively constant over the first half of the fjord around 180 days before dropping down to 100 days (Fig. 4.13b). The plume-driven circulation flushing time is similar near the mouth of the fjord, but drops linearly towards the head resulting in a flushing time of 50 days closer to Helheim Fjord. The contrasting along-fjord profiles (linear vs. constant) suggests the plume-driven circulation is more effective at renewing

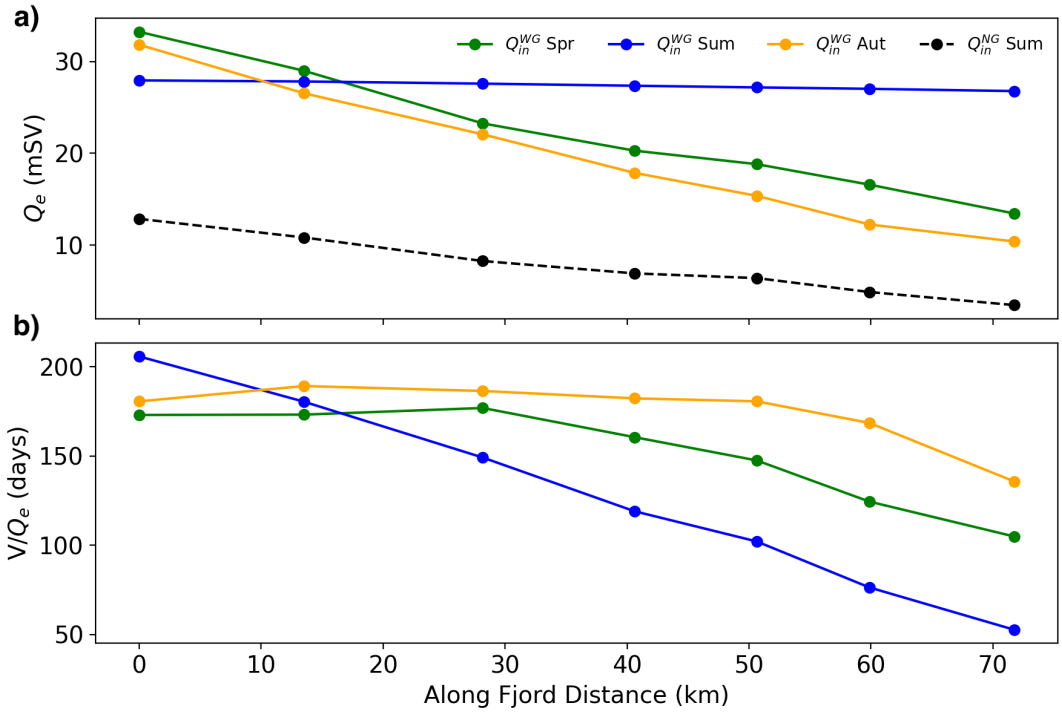

Figure 4.13. a) Along-fjord TEF exchange flux in 2015. Seasons are three month averages. The x-axis is distance from the mouth. The solid lines are from the WG run and the black dashed line is from the NG run during the summer. b) The fjord volume upstream of the mouth divided by the exchange flux. Spr. is Spring (Mar. – May), Sum. is Summer (Jun. – Aug.), Aut. is Autumn (Fall, Sep. — Nov.).

the fjord than the shelf-driven circulation. For a long fjord such as SF, the magnitude of the shelf-driven circulation has been reduced by 66% 70 km upfjord while the plume-driven circulation is, by definition, most intense near the terminus. This flushing time is meant to provide a scaling for residence time within the fjord, and we note other residence time scalings such as the freshwater fraction method produce different residence times, but a qualitatively consistent picture. We also tested for freshwater storage by calculating the lag between subglacial discharge input and peak freshwater export similar to Chapter 3. We did not observe significant freshwater storage with the peak export averaging a two-week delay over the three years which we attribute to the transit time of water (0.1 m/s) across the fjord.

4.4.5 Model and Data Comparison

The analysis of the model runs show that the seasonality of the along-shore winds drive a reversal in the exchange flow, and that the timing of shelf vs. plume forcing results in a relatively high exchange throughout the year. To lend support that the model results are applicable to the real world Sermilik Fjord, we compare the WG model time series to 3 moored CTD instruments. The moored instruments recorded temperature and salinity on the shelf at 350 m and in the fjord at 60 m and 400 m from August 2015 – July 2017. The model appears to do a reasonable job of recreating the seasonal temperature variability in the shallow part of the fjord (Willmott Score, $WS = 0.72$). There is a warm bias in the model PW during the summer that was captured by the CTD profiles (Fig. 4.9), but the model does a better job of capturing the cooler PW temperature in the winter (Fig. 4.14c). The model is less capable of recreating surface salinity ($WS = 0.39$) and misses the large salinity minima which occur in the fall. The deeper moorings, especially the one on the shelf, do a better job of recreating salinity variability and temperature variability capturing both the minima in winter and the maxima in summer. (Table 4.3, Fig. 4.14).

We compare the volume transport from the model with the transport calculated from the ADCP (Sup. Fig. 4.20). Splitting the transport into seasons, the observed transport and standard deviation in the summer months (Jun. – Aug.) is 74 ± 26 mSv (10^3 m^3/s) and non-summer months (Oct. – May) is 26 ± 7.7 mSv. The modeled transport is 33 mSv in summer and 36 mSv in the non-summer; both are within 1.6 standard deviations of the observed transport. Although the model transport appears to be underestimating transport in the summer.

4.4.6 Sensitivity to wind forcing

We found that the primary mechanism driving the shelf-forcing was the seasonal variability of the along-shore winds, in this case from ERA5. A simulation using Polar WRF winds that are high resolution (NG-HR) allows us to test the sensitivity of the results to the choice of atmospheric forcing. The use of a high-resolution wind forcing increases the exchange flow of

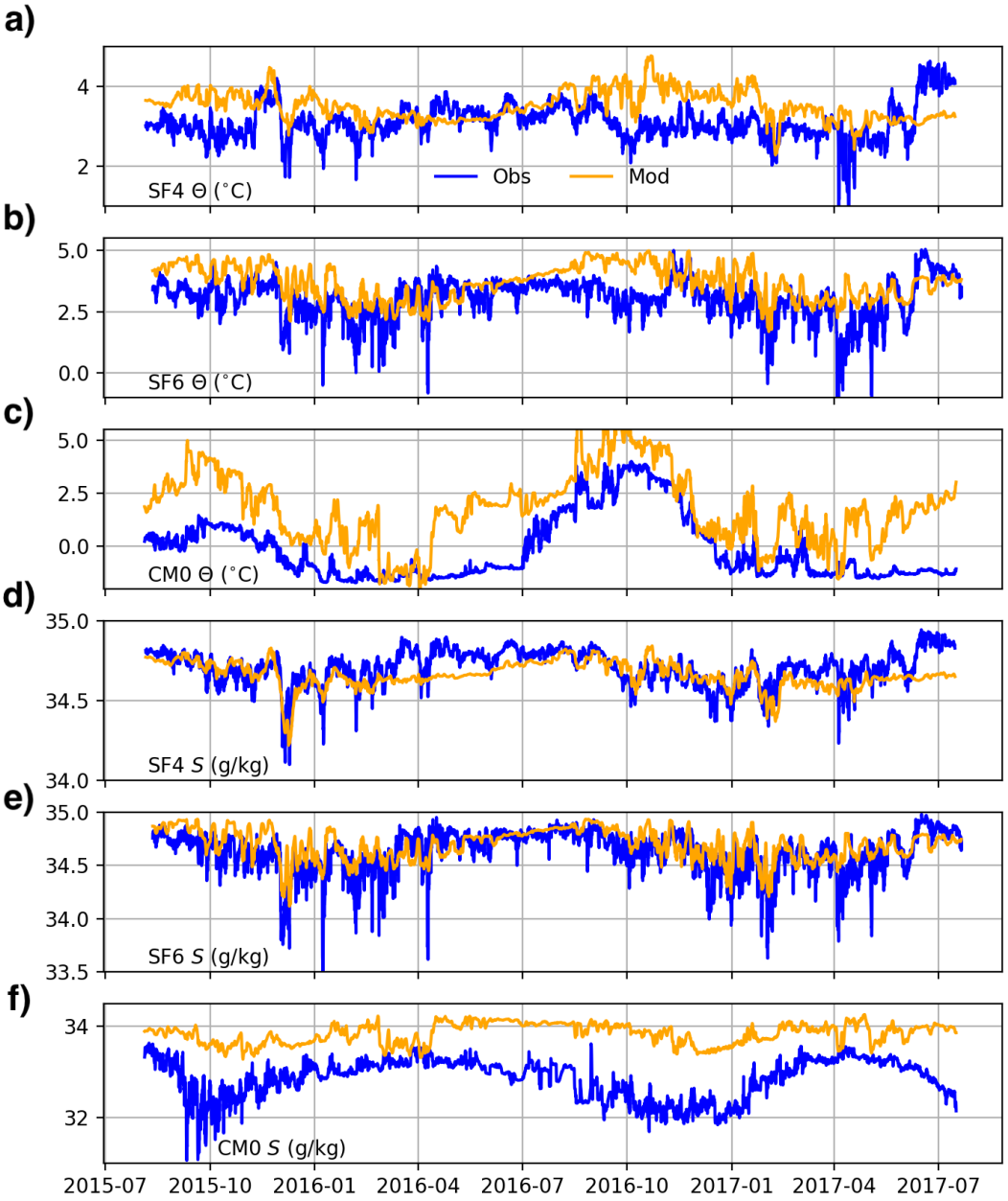

Figure 4.14. Comparisons between the mooring (blue) and model output (orange). a-c) are Conservative Temperature (Θ) at SF4, SF6, and CM0 at 400 m, 350 m, and 60 m respectively. d-f) are Absolute Salinity (S) at SF4, SF6, and CM0.

the fjord (Fig. 4.15c). Only 9 months (March – December 2015) of data are available at the time of analysis, but a direct comparison with the base NG run shows that exchange is doubled on average at SF line 3 although the seasonality is largely the same with a minimum occurring in summer. The NG-HR run results in a more intense exchange due to both the presence of stronger along-shelf winds, but also the ability to resolve along-fjord winds (Appendix A). In density space, we see that although the exchange flow is enhanced, the vertical structure of the flow is similar between the two runs (Fig. 4.15a,b). An exception perhaps, is that the outflow and inflow at lighter densities ($\rho < 27$ kg/m^3) are more developed in the NG-HR run than the NG run . Since surface radiative forcing is the same between models, we attribute this shallower exchange to the effects of direct wind forcing in the fjord. In sum, the large-scale pattern (vertically and temporally) of the exchange flow is similar between the NG and NG-HR run, but the magnitude of exchange is enhanced under the NG-HR run.

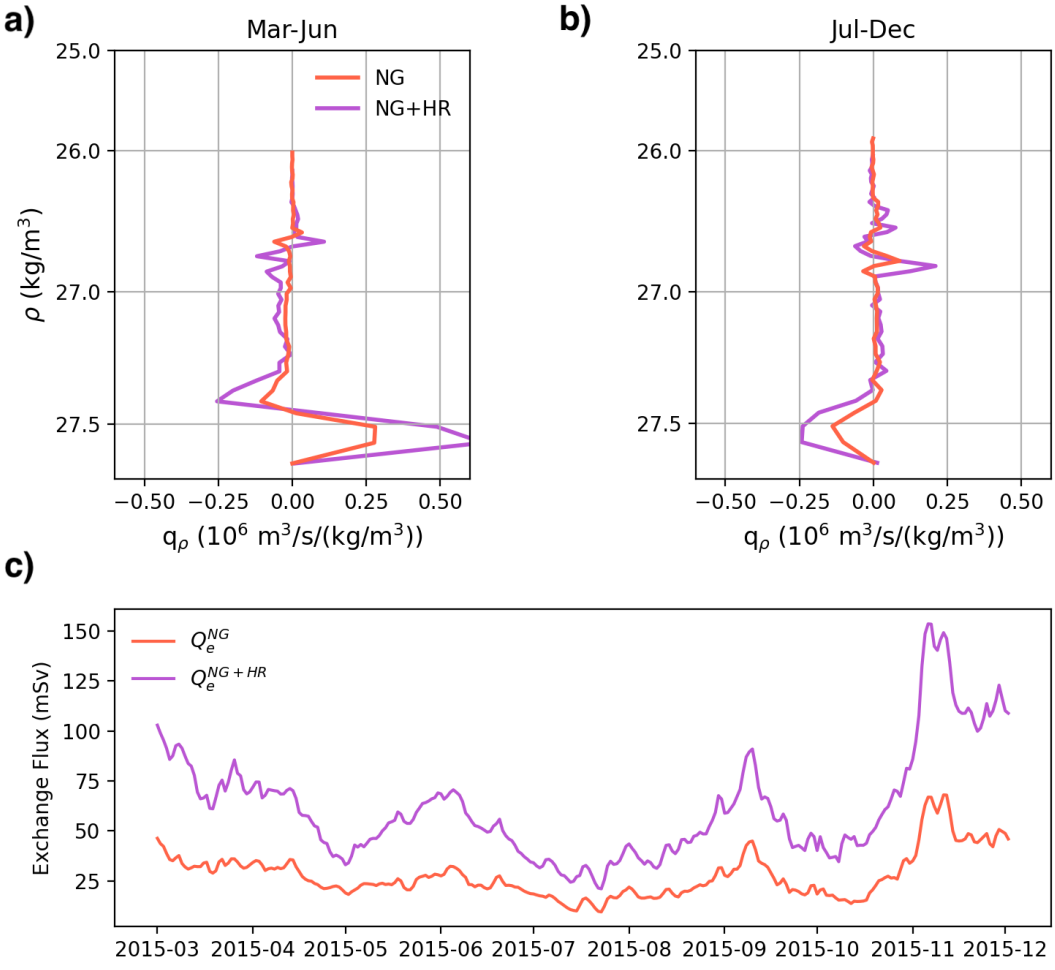

Figure 4.15. a) Mean of the TEF transport per density class from March – June. The x and y axis are repeated from Fig. 4.11. b) Same as a, but over the time period July – December. c) TEF exchange flux from Mar. – Dec. 2015 at SF Line 3.

4.5 Discussion

4.5.1 Model Limitations

Both visually (Fig. 4.14) and quantitatively (Appendix B), the model does a reasonable job of capturing the temperature and salinity variability seen in the observations. The mooring data on the shelf is significantly correlated in both temperature and salinity with the model giving confidence that shelf-forcing is accurately represented. Additionally, the volume transport in the model does not deviate substantially from the estimates of the transport from the observations, although it does underestimate the summer transport (Sup. Fig. 4.20). However, we recognize that the model cannot reproduce the shallower properties such as PW salinity and stratification because it is missing freshwater sources such as icebergs, sea ice and surface runoff. Other models (Davison et al., 2020; Kajanto et al., 2022) and observations (Moon et al., 2018) suggest the freshwater flux from icebergs can increase the strength of circulation and significantly modify (cool and freshen) shallow fjord properties. Recently, Kajanto et al. (2022) showed, for a similar large fjord in west Greenland, that without icebergs the model could not reproduce the observed properties. Therefore, our results are focused on shelf-forcing and plume transport, both of which appear reasonably well represented, and we leave iceberg forcing to be implemented in a future study.

4.5.2 Implications

Coastal current variability

We find the seasonality of the along-shore winds to be a major driver for the direction of the exchange flow, with the exchange flow reversing in summer due to the increasing of across-shelf isopycnals gradients. This process is similar to other exchange flow reversals which occur in mid-latitude non-glacial fjords in the Pacific Northwest. For example in the Salish Sea, river plumes from neighboring estuaries can reverse the exchange flow in downwelling conditions by changing the fjord-shelf density gradients (Giddings and MacCready, 2017). While we have

focused on the impact of winds, clearly changes in the density or volume of the coastal current (EGCC) outside SF could also impact fjord-shelf exchange. Presently, we find the transport of the EGCC in our model to be dominated by winds (Fig. 4.5) and this is consistent with observations of the EGCC further downstream near Cape Farewell (Le Bras et al., 2018). However, the EGCC is fed with freshwater from melting glaciers and sea ice (Le Bras et al., 2021; Foukal et al., 2020; Sutherland and Pickart, 2008), and in a warming climate, buoyancy might play a more important role in setting the current strength and across-shelf isopycnal gradients.

Freshwater export and mixing

The model results shed light on the challenge of accurately representing plume dynamics in fjord-scale models. We found that the along-fjord variability in volume flux (Q_e) was constant along the length of the fjord during the summer WG run (Fig. 4.13) and that the isolated plume-driven circulation (WG - NG) was strongly correlated with plume theory (Fig. 4.12). Therefore, it appears that the plume-driven circulation in the model is entirely set by the subglacial discharge plume parameterization with little mixing down the fjord. These findings are consistent with other modeling studies that use the IcePlume package (e.g., Zhao et al., 2021; Carroll et al., 2017), but are inconsistent with observations which suggest there is additional mixing of freshwater export as it flows down fjord (De Andrés et al., 2020; Muilwijk et al., 2022). Recent observations find that mixing is intensified near glacier termini (Sanchez et al. (2023); Bendtsen et al., 2021), although the physical mechanisms responsible (e.g., waves, ambient melt, turbulent jets) are poorly constrained. The lack of additional mixing and entrainment into the plume as it flows down fjord potentially explains some of the discrepancy between the observed and modeled summer transports. Future work should aim to address this discrepancy either with the inclusion of more realistic ambient melt, a focus on higher resolution simulations or the inclusion of particles to track freshwater.

Warm-water seasonality

Identifying the heat content variability of glacial fjords is essential given the sensitivity of submarine melting to warm water. We found that temperatures in the fjord peaked in the fall when warm water flooded the shelf (Fig. 4.4). In Nuup Kangerlua, warm water peaks in the summer when mixing at the sill can draw down relatively warm surface water (Mortensen et al., 2011). In central west Greenland, warm water fills the fjord in spring due to a combination of upwelling, reduced sea ice, and advection (Carroll et al., 2018). In nearby Kangerdlugssuaq, the temperature peaks in winter due to a seasonal pathway of increased AW reaching the fjord mouth (Gelderloos et al., 2017). While at 79 °N Glacier, the seasonal cycle is secondary to interannual variability in setting fjord temperature properties (Lindeman et al., 2020)! Therefore, it appears that the seasonality of warm water for Greenland fjords depends primarily on external forcing that varies continent wide.

We find that the temperature of the fjord peaks in the fall, while the heat flux appears to peak in spring. The temperature maximum in the fall is likely a result of seasonally-warmed AW advecting into the fjord and is consistent with observations (Sutherland et al., 2013; Harden et al., 2014). In contrast, the heat flux into the fjord peaks in the spring as a result of relaxing isopycnals causing the AW layer to thicken. The heat flux variability suggests the fjord adjusts rapidly to changing shelf conditions. If the fjord adjusted slowly, we would expect the seasonal cycle of heat flux to match the cycle of temperature on the shelf with the largest heat exchange occurring in September. With these mechanisms in mind, we expect "warming" AW to increase the heat in the fall, while a reduction in along-shore winds would increase heat in the spring through a thickening of the AW layer. However, the impact this external heat has on glaciers will depend on iceberg concentration and the fjord transport of heat to the terminus.

Lastly, we point out that the inclusion of substantial submarine melting (e.g. from icebergs) is likely to change the heat flux interpretation during the summer. In the WG run, the heat flux is negative during the summer as a result of upwelled AW and a shallow outflowing

plume (Fig. 4.7d). If the upper-layer was properly cooled, we would observe a positive heat flux. A steady and positive heat flux would be consistent with observations (Jackson and Straneo, 2016). As the streamfunction shows (Fig. 4.8d), the plume-driven circulation drives AW transport all the way towards the glacier, and therefore, increased subglacial discharge should lead to increased AW transport and greater melting of both the terminus and icebergs. Inclusion of melting could then lead to a feedback with an increased buoyancy-driven circulation (Kajanto et al., 2022; Zhao et al., 2022a). To explore this question fully, more realistic melting needs to be included in numerical models.

Relationship between glacial stability and shelf forcing

Warmer ocean and atmospheric temperatures have been linked to increased glacial retreat in east Greenland (Straneo et al., 2011; Cowton et al., 2018). In SF, glacial retreat has also been correlated with the negative phase of the North Atlantic Oscillation (NAO) index (Andresen et al., 2012, 2014), the dominant mode of atmospheric climate variability in the North Atlantic related to pressure differences between Portugal and Iceland. A negative NAO index is associated with increased AW relative to PW, leading to increased heat transport across the shelf (Christoffersen et al., 2011). The positive phase of the NAO index is correlated with glacial stability despite increased low-pressure systems and storms along the east Greenland coast potentially increasing circulation within fjords (Harden et al., 2011; Andresen et al., 2014). Our model is consistent with this correlation, as we find that under reduced winds (and downwelling), shelf isopycnals flatten and the fjord-shelf exchange promotes an increase in AW. Therefore, our results extend into the fjords the dynamical connection between large-scale wind variability and heat transport across the shelf (Christoffersen et al., 2011). We find the seasonality and direction of the along-shore winds play an important role in setting oceanic thermal forcing of the glacier.

4.6 Conclusion

Glacial fjords play an important role in the climate system by exchanging heat and salt between the ice sheet and open ocean. We analyze the output from a three-year simulation of a glacial fjord with realistic forcing and identify the impact of shelf and plume forcing on fjord exchange. In SF, the minimum of the along-shelf wind stress happens to coincide with peak glacial forcing generating two distinct regimes, a shelf-driven circulation in non-summer months with variable heat and salt exchange, and a plume-driven circulation in the summer with a large and steady salt flux. The sign of the exchange flow is related to the seasonality of the along-shelf wind stress and undergoes a seasonal reversal when downwelling winds subside. The plume-driven exchange shows little along-fjord variability and is more effective at renewing tracers than the shelf-driven circulation which peaks at the fjord mouth.

4.7 Acknowledgments

We acknowledge Margaret Lindeman for helpful discussions and suggestions.

Chapter 4, in part, is currently being prepared for submission for publication of the material. Sanchez, R. , Straneo F., Hughes, K., Barbour, P. , Shroyer, E. , Mechanisms controlling the seasonal variability of Sermilik Fjord. The dissertation author was the primary investigator and author of this material.

4.8 Appendix A: Wind Stress Analysis

Along-shore wind stress is the primary driver of fjord circulation outside of the summer. In this appendix, we evaluate the wind stress on the shelf using the wind stress at the southern edge of the coastal transect (Fig. 4.1) and wind stress in the fjord at SF Line 6. We also compare the high-resolution (NG-HR) WRF winds against the base case (NG) ERA5 winds.

The primary direction of winds on the shelf in both the NG and NG-HR runs is to the southwest indicating the wind is downwelling favorable (Fig. 4.16). Windrose plots taken from

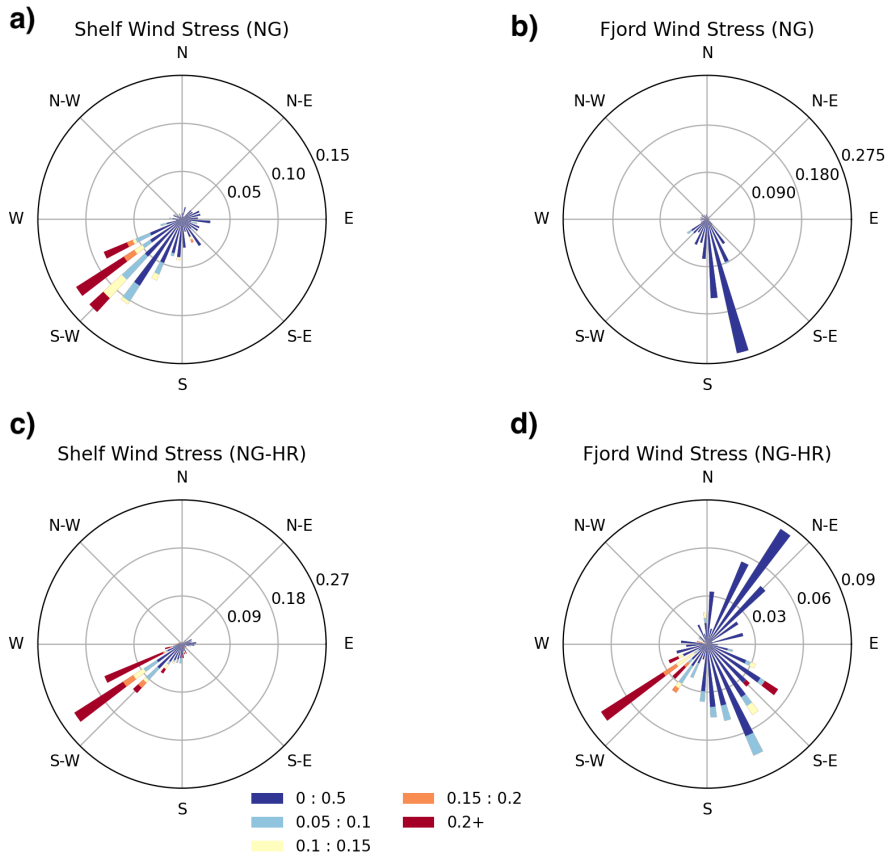

Figure 4.16. Windrose plots for the shelf wind stress NG run (a), fjord wind stress NG run (b), shelf wind stress NG-HR run (c), and fjord wind stress NG-HR run (d). The magnitude of the bar indicates frequency of direction, the color is wind strength. Units are in N/m^2

within the fjord show that down-fjord intense winds are only observed in the NG-HR model. As an example, Figure 4.17. shows a map of wind stress during an intense down-fjord wind event. Only the NG-HR run captures the event, while the NG run generates the wind stress on the shelf.

The spectra of salinity at 150 m at SF Line 5 (Fig. 4.18) has a peak between 3 – 10 days, the frequency range expected for synoptic wind forcing in the observations (Jackson et al., 2018). There doesn't appear to be any major differences in the dominant frequencies between the NG-HR run and the NG run with the exception of slight peak at 1.7 days in the NG-HR run. The HR run has more energy at all frequencies. From this analysis we can determine that the 3 – 10 day timescale expected from observations drives fluctuations in the model as well.

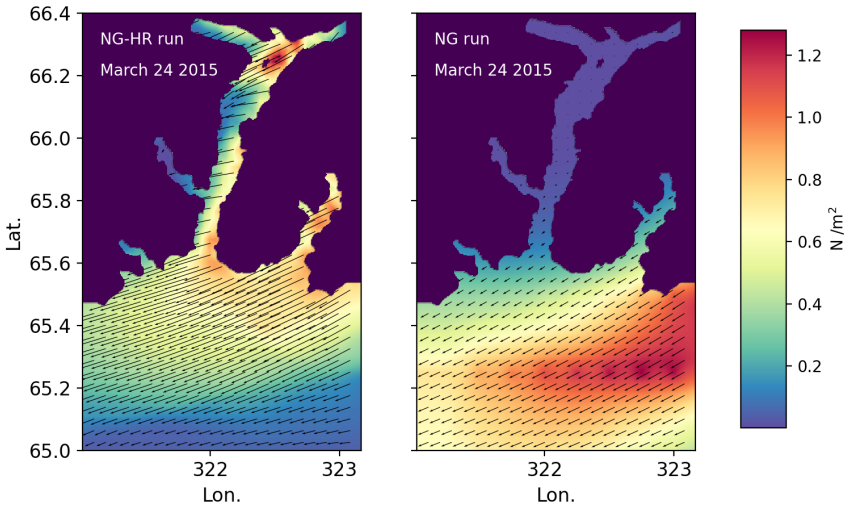

Figure 4.17. a) Example down-fjord wind event in the NG-HR run. Color is wind stress magnitude and the arrow is the direction. b) Same event in the NG run.

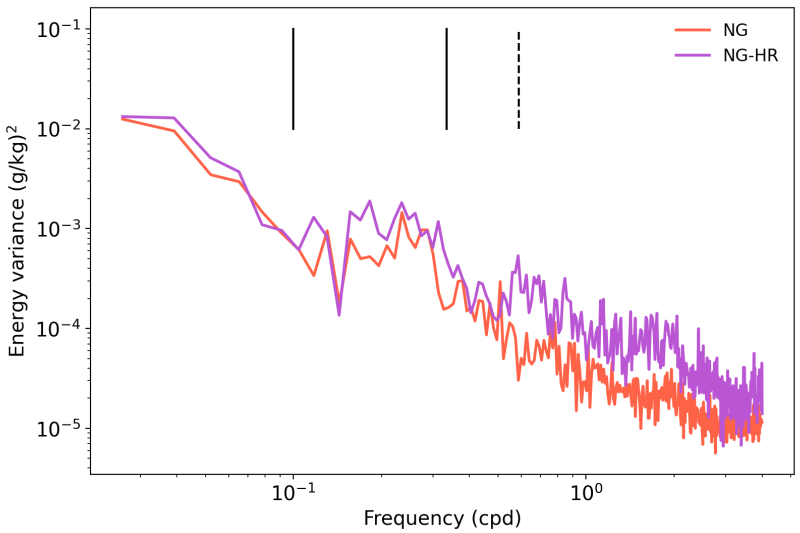

Figure 4.18. Variance Preserving Spectra of salinity at SF Line 5 from 2015. The black lines band the 3 – 10 day period and the dashed line is a period of 1.7 days.

Table 4.3. Statistics and skill scores for the mooring temperature, salinity and velocity time series. The first column is the variable and mooring. Columns 2 – 4 are the Willmott Score (WS), Mean Square Error (MSE) and correlation coefficient (r) for the low-pass filtered time series, and columns 5 – 7 are statistics for the high-pass filtered time series. Significance is denoted with a star.

Variable	WS_{lp}	MSE_{lp}	r_{lp}	WS_{hp}	MSE_{hp}	r_{hp}
CM0 S	0.39	1.1	0.46	0.39	0.04	0.13
CM0 Θ	0.72	4.0	0.89*	0.47	0.35	0.31
SF4 S	0.71	0.01	0.57	0.64	0.04	0.50*
SF4 Θ	0.31	0.37	-0.05	0.45	0.09	0.21
SF6 S	0.77	0.01	0.79*	0.65	0.12	0.48*
SF6 Θ	0.54	0.79	0.57	0.61	0.13	0.41*
OW1 U	0.26	0.02	0.44	0.39	0.02	0.12*

4.9 Appendix B: Willmott Scores for Observations and Model

We evaluate the model using the Wilmott Skill Score (WS, Willmott, 1982). A model score WS=1 indicates complete agreement between the model and observations and WS=0 indicates complete disagreement. We don't calculate WS or r scores for SF4 since the observed transport is an estimate and not directly measured. We isolate seasonal from synoptic forcing by splitting all the data up into two time series: a low-pass time series y_{lp} generated from consecutive 25-day and 30-day rolling means and a high-pass time series $y_{hp} = y - y_{hp}$ generated from removal of the low-pass series from the original data. The effective degrees of freedom are calculated for all compared time-series with the minimum number of degrees used. The highest scores are for the shallow temperature (CM0), and deep salinity (SF4 and SF6). The shelf (SF6) high-pass filtered temperature and salinity also have relatively high WS ($> .6$) indicating the model captures the shelf properties well.

4.10 Supporting Information

Comparison against Profiles

We compare the WG model output to CTD profiles collected in August 2015 and July

2017 and categorize the profiles as shelf (N=24) and fjord (N=48) profiles. When all profiles are averaged together, we see the model (solid, Sup. Fig. 4.19a) does a reasonable job of capturing the observed (dashed, Sup. Fig 4.19a) mean temperature at depth. It also recreates the basic vertical structure of temperature with a warm AW mass at depth, a cold PW mass around 100 m, and a WPW mass near the surface. We also include the average of XCTD profiles taken in March 2010 and compare it to the mean model output at SF4 in March 2016. The winter profiles are from a different year and so a direct comparison is limited, but the model pycnocline appears significantly shallower than in observations and is generally saltier. Unfortunately, in all seasons, the model overestimates the temperature of the PW resulting in a warm bias. Reasons for this bias potentially include the lack of icebergs in the fjord, lack of sea ice along the coast and a warm bias from the ASTE boundary conditions. The model appears to do a reasonable job of capturing the salinity in the fjord at depth, but overestimates the salinity above 300 m resulting in weaker stratification in the model than in reality (Sup. Fig. 4.19b). In both the temperature and salinity fields, the differences between the model and observations are much larger than the differences between the fjord and the shelf.

MSE, WS and r were calculated between the model and the summer CTD profiles for the parameters vertically-averaged salinity ($\overline{S}$), vertically-averaged temperature ($\overline{\Theta}$), vertical salinity difference (55 m – Bottom, ΔS) and vertical temperature difference ($\Delta\Theta$, Table A1). The statistics were also calculated for only the deep portion of the CTD profiles (250 m – Bottom) since this part of the model seemed to perform better. Caution should be exercised when evaluating the statistics of the CTD profiles because the sample size is small, and the profiles within a field campaign are likely not independent from one another. With these caveats in mind, we find the vertically-averaged salinity has the highest WS index, r, and is the only parameter that is statistically significant within both the fjord and shelf. It is clear the upper 250 m of the model need to be improved to more realistically capture the vertical stratification. The inclusion of icebergs and an iceshelf into the model seem to make some progress towards this goal (Kajanto et al., 2022, unpublished iceberg runs), but the ASTE boundary conditions will likely also need

to be improved. For more robust CTD profile and model comparison, data is needed outside of the summer melt season and collected in multiple independent campaigns.

Velocity and volume transport from the model are compared to ADCP data from the middle of fjord (SF4) and the shelf (OW1). At SF4, we break the velocity record into a summer (June 1 – August 31) and winter (October 1 – May 1) time series similar to Jackson and Straneo (2016). The seasonal mean (from two years) along-fjord velocity structure from the observations compares poorly to the model output (Sup. Fig. 4.19c,d) due to the challenges in recreating realistic fjord stratification. During the summer, the model outflow is at the surface while the observations show outlfow centered around 100 m. This mismatch can partly be explained by plume dynamics as the model stratification is much weaker than the observations (Sup. Fig. 4.19b) resulting in a plume that reaches close to the surface rather than finding a deeper neutral buoyancy (De Andrés et al., 2020). The primary inflow which compensates the outflow is therefore also shallower in the model. In the winter, the profiles also have a mismatch that can potentially be explained by fjord stratification. In the observations, the fjord has a sharp pycnocline around 200 m (sup. Fig. 4.19b) while the model lacks this pycnocline. This difference in pycnocline structure and depth results in a concentrated baroclinic flow centered around 200 m in the observations and a diffuse baroclinic flow centered closer to 350 m in the model.

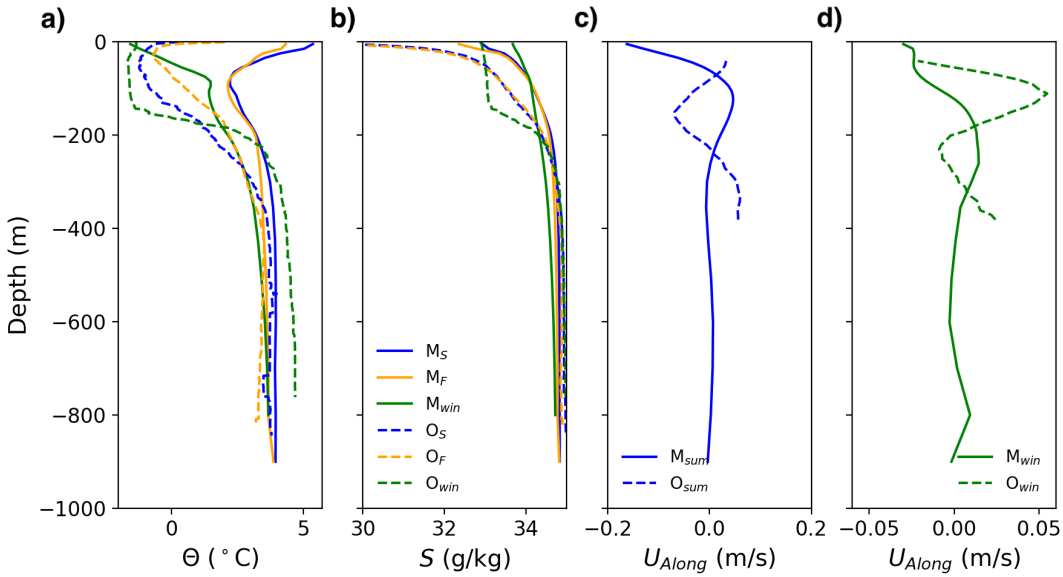

Figure 4.19. a) the spatially-averaged CTD temperature profiles versus depth for both the model (solid) and observations (dashed) in the fjord (yellow, N=48), on the shelf (blue, N=24), and in the winter (green, N=4). b) same but for absolute salinity. c) The average along-fjord velocity at SF4 during the summer (June 1 – August 31). The solid line is the model and the dashed line comes from the SF4 ADCP. d) same as c but for the winter (October 1 – May 1.)

Table 4.4. Statistics and skill scores for the summer CTD data. The first column is the variable and includes the difference in vertically-averaged salinity and temperature ($\Delta\overline{S}, \Delta\overline{\Theta}$), the difference in for depths greater than 250 m ($\Delta\overline{S_d}, \Delta\overline{\Theta_d}$), and the difference between the model and observations for the vertical stratification ($\Delta(\Delta S), \Delta(\Delta\Theta)$. Columns 2 – 4 are the fjord profiles, and columns 5 – 7 are the shelf profiles. Significance is denoted with a star.

Variable	WS_F	MSE_F	r_F	WS_S	MSE_S	r_S
$\Delta\overline{S}$	0.66	0.47	0.98*	0.70	0.52	0.99*
$\Delta\overline{S_d}$	0.55	0.01	0.57*	0.66	0.01	0.62
$\Delta\overline{\Theta}$	0.3	2.1	-0.24	0.40	7.7	0.11
$\Delta\overline{\Theta_d}$	0.1	0.33	-0.51	0.31	0.32	-0.05
$\Delta(\Delta S)$	0.29	0.93	0.15	0.48	0.93	0.77*
$\Delta(\Delta S_d)$	0.47	0.01	0.39	0.52	0.03	0.49
$\Delta(\Delta\Theta)$	0.33	9.63	-0.33	0.37	114	0.27
$\Delta(\Delta\Theta_d)$	0.48	0.29	0.20	0.49	0.7	0.21

ADCP Transport

We estimate volume transport from the ADCP using 3 methods of extrapolation: surface extrapolation using constant shear from the top three bins, surface extrapolation using a constant value, and bottom extrapolation using a linear shear down to zero (Jackson and Straneo, 2016). For each method, the part of the water column not extrapolated is filled with a constant value to ensure no net transport. We multiply this velocity profile by the fjord width and use two different estimates of fjord width resulting in 6 transport estimates that we use to define uncertainty. We apply a 30-day rolling mean to velocities prior to calculating incoming volume transport. The ADCP-derived incoming volume transport is the same magnitude as the modeled transport, but has a larger volume flux during the summer than the model and a smaller flux in the winter (Sup. Fig. 4.20). While the instantaneous velocities in the winter can be much higher than in the summer, averaging removes most of the oscillatory signal resulting in weaker average velocities (Sup. Fig. 4.19).

We also compare the 30-day rolling mean model velocity in the western end of Sermilik Trough with the 30-day rolling mean velocity recorded at OW1 focusing on the depth 120 m where data was cleanest (Sup. Fig. 4.20). The along-shelf modeled velocity was significantly larger than the observed velocity reaching velocities around 0.3 m/s in the model compared to 0.1 m/s by the ADCP. However, both are flowing westward with a mean negative velocity, consistent with the presence of an equatorward coastal current, and both are minimized in the summer when winds and coastal current freshening are weakest.

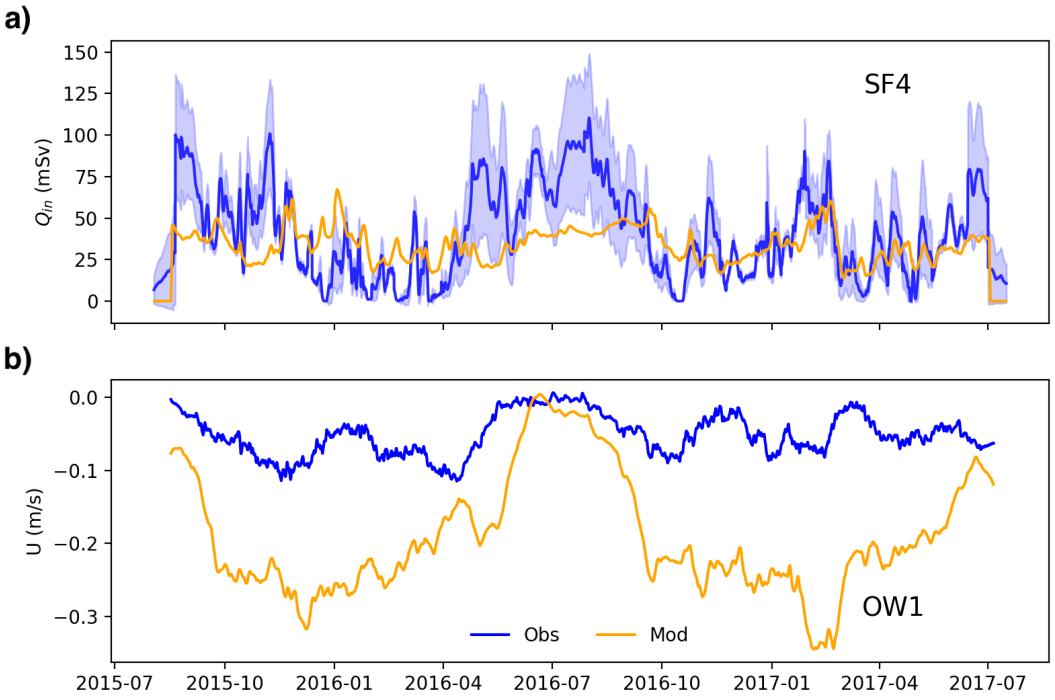

Figure 4.20. a) Time series comparisons between the incoming volume transport calculated from the ADCP at SF4 (blue) and model output (orange). b) The along-shelf velocity averaged over 110 – 130 m from the ADCP at SF6 and the model. All velocities have had a 30-day rolling mean applied.

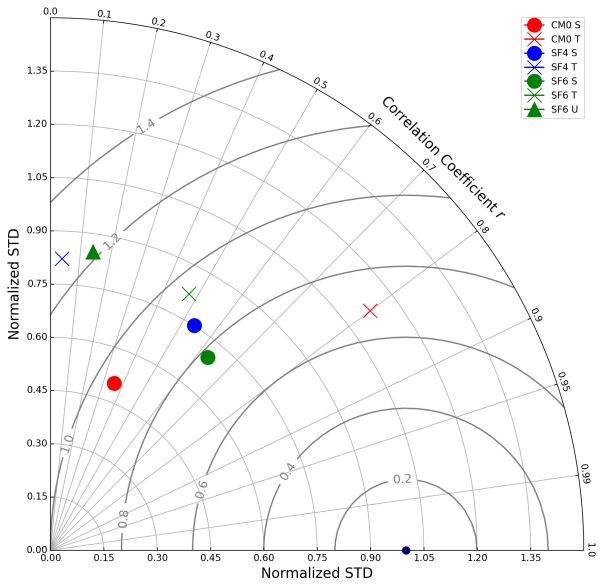

Figure 4.21. A Taylor Diagram comparing the relative skill of the different model parameters. The distance from the origin is the standard deviation normalized by the observed standard deviation. The angle is the correlation coefficient and the RMSE is the distance from the reference point (purple) which represents the perfect model.

Taylor Diagram A Taylor Diagram (Taylor, 2001) allows succinct comparison of statistics (r,MSE σ) between different model variables. The unfiltered time series from the model and observations are plotted on top of a Taylor Diagram in Sup. Figure 4.21. From this diagram, we can see that model variables which perform best are the shallow fjord temperature, followed by deep fjord salinity, and then the shelf variables.

Coastal Series Upstream

Other TEF Time Series

Along Fjord TEF Tracers

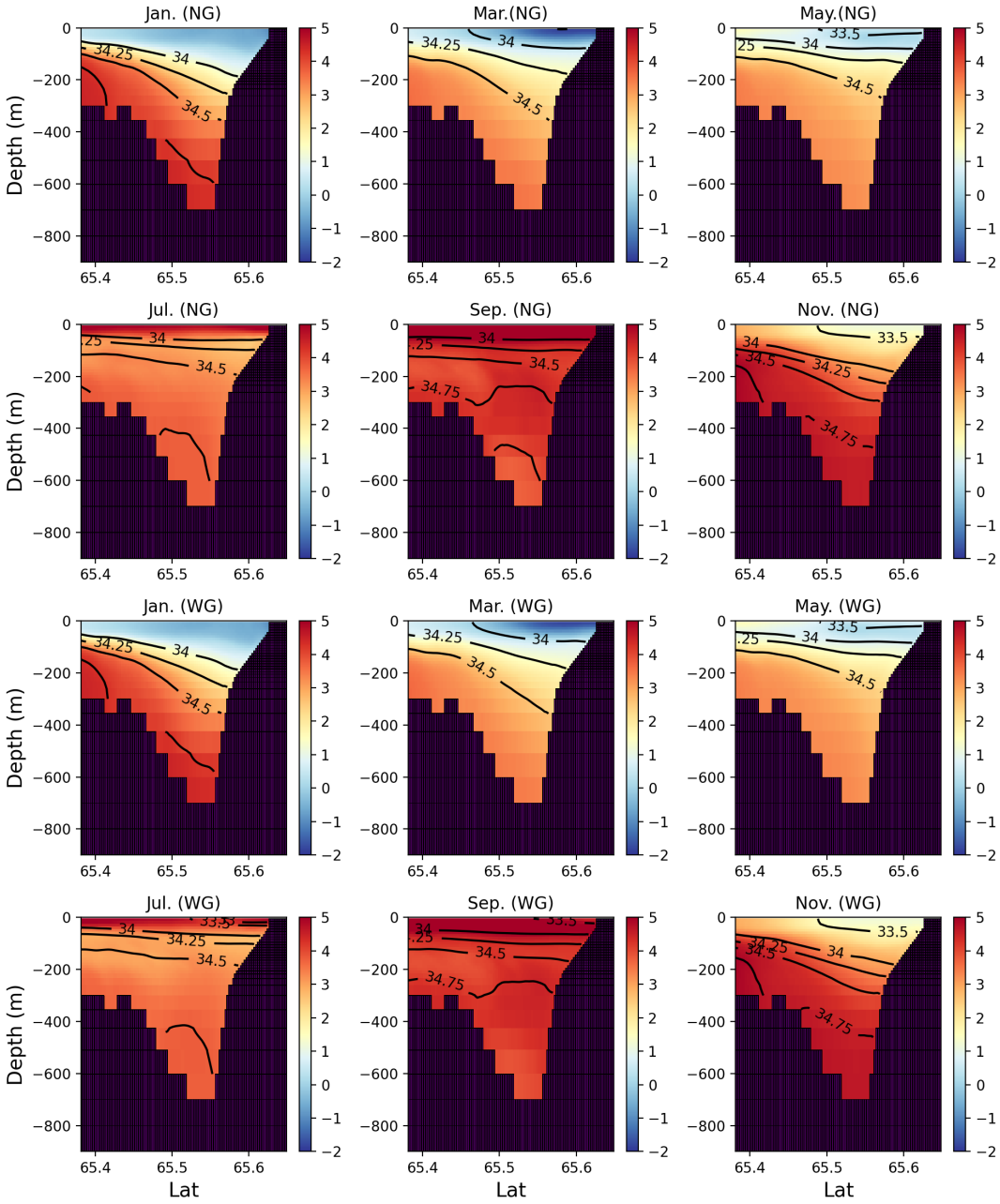

Figure 4.22. Monthly-average shelf temperature transect downstream (west) of the fjord. Contours are isohalines (32,32.5,33,33.5,34,34.25, 34.5,34.75,35) g/kg. The top six panels are from the NG run, the bottom six are from the WG run.

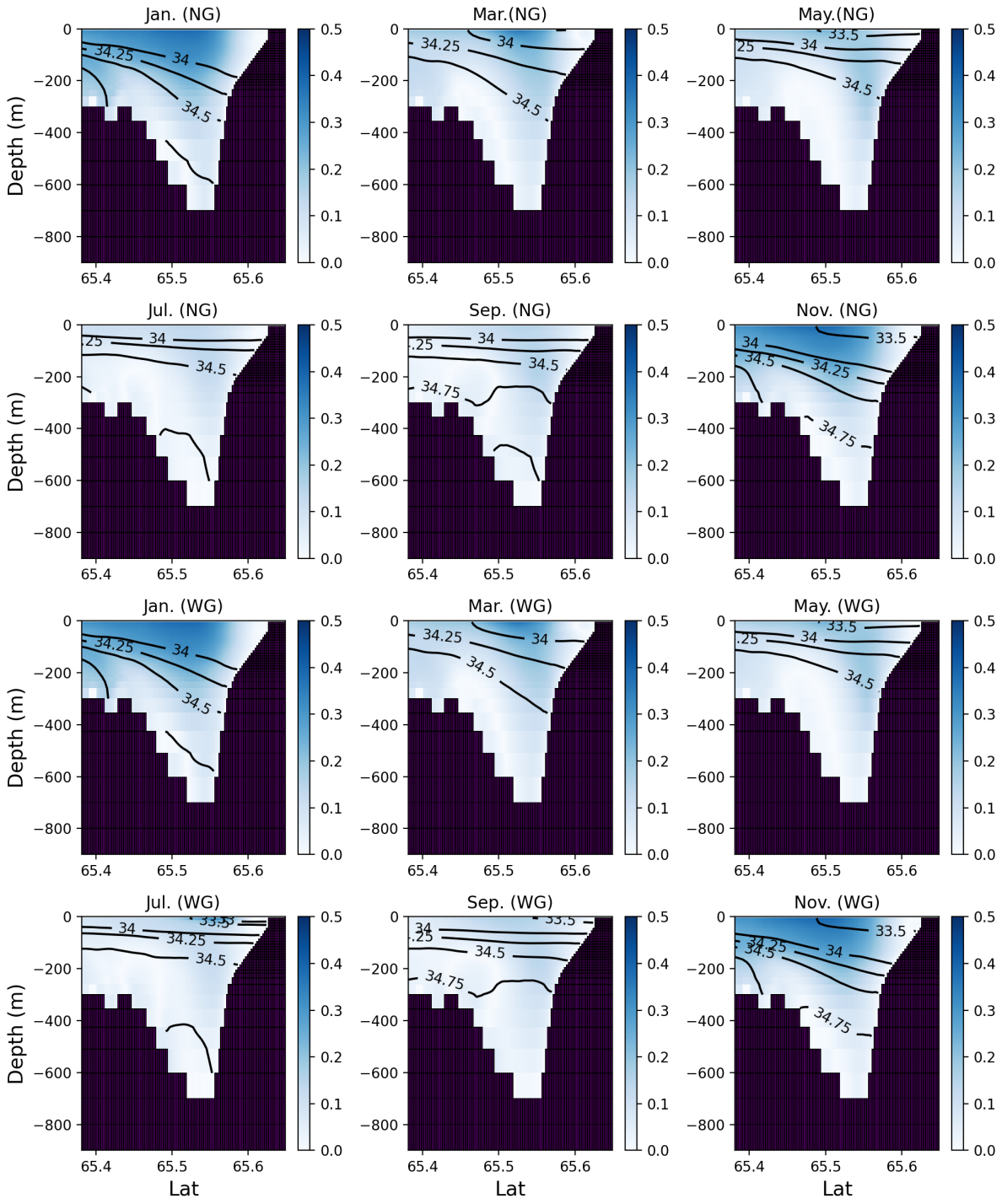

Figure 4.23. Monthly-average shelf velocity transect downstream (west) of the fjord. Positive velocity is oriented west. Contours are isohalines (32,32.5,33,33.5,34,34.25, 34.5,34.75,35) g/kg. The top six panels are from the NG run, the bottom six are from the WG run.

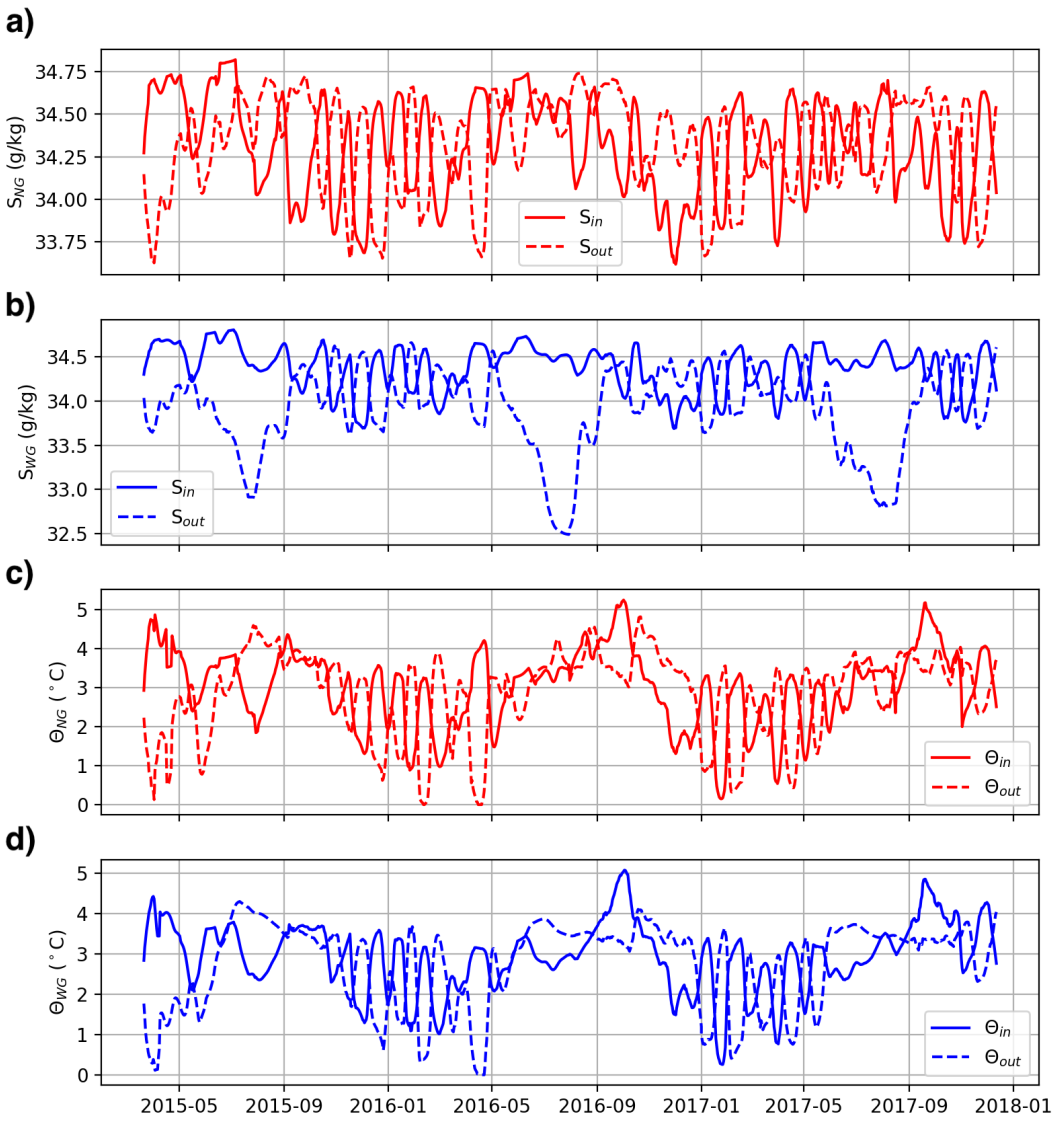

Figure 4.24. Additional Time Series of TEF bulk values.a) The TEF Salinity time series for the NG run. b) The TEF Salinity time series for the WG run. c) The TEF temperature time series for the NG Run. d) The TEF temperature series for the WG run. These values were used in the calculation of ΔS and $\Delta\Theta$ in Fig. 4.12.

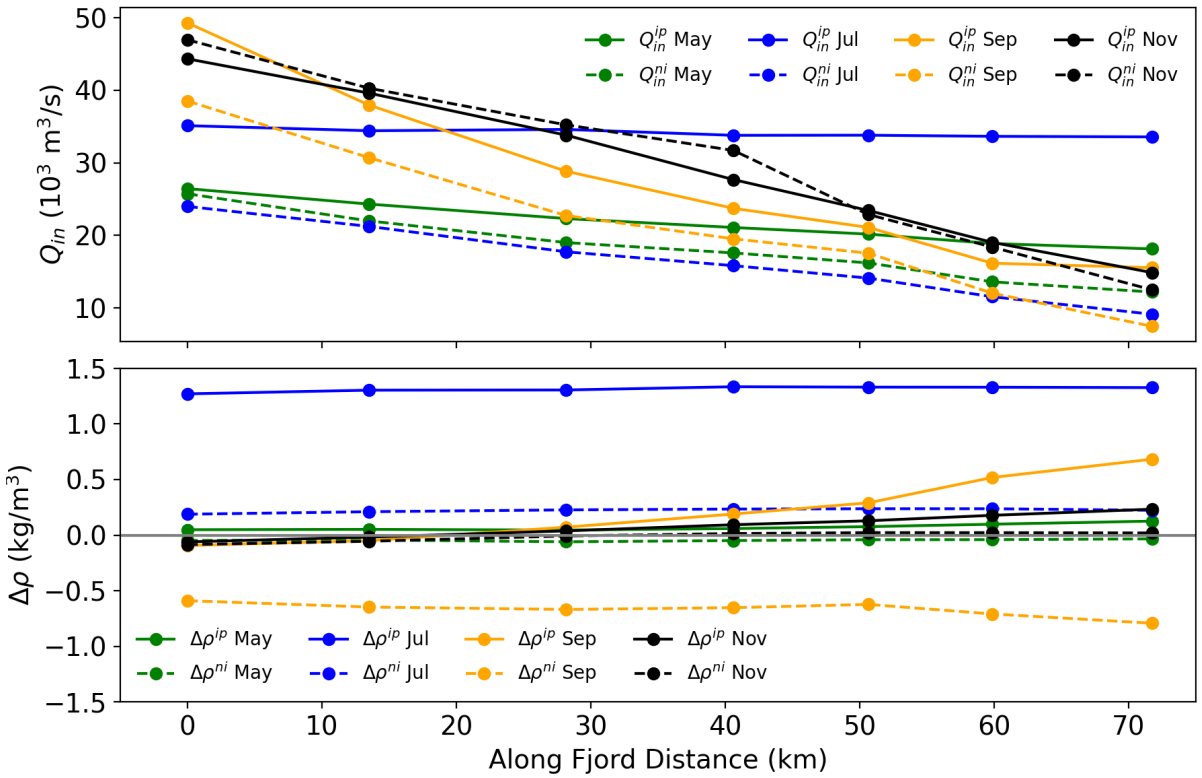

Figure 4.25. Monthly-average TEF along fjord Q_{in} in the WG and NG run. The x-axis is distance from the mouth. The bottom panel is ρ_{in}-ρ_{out}.

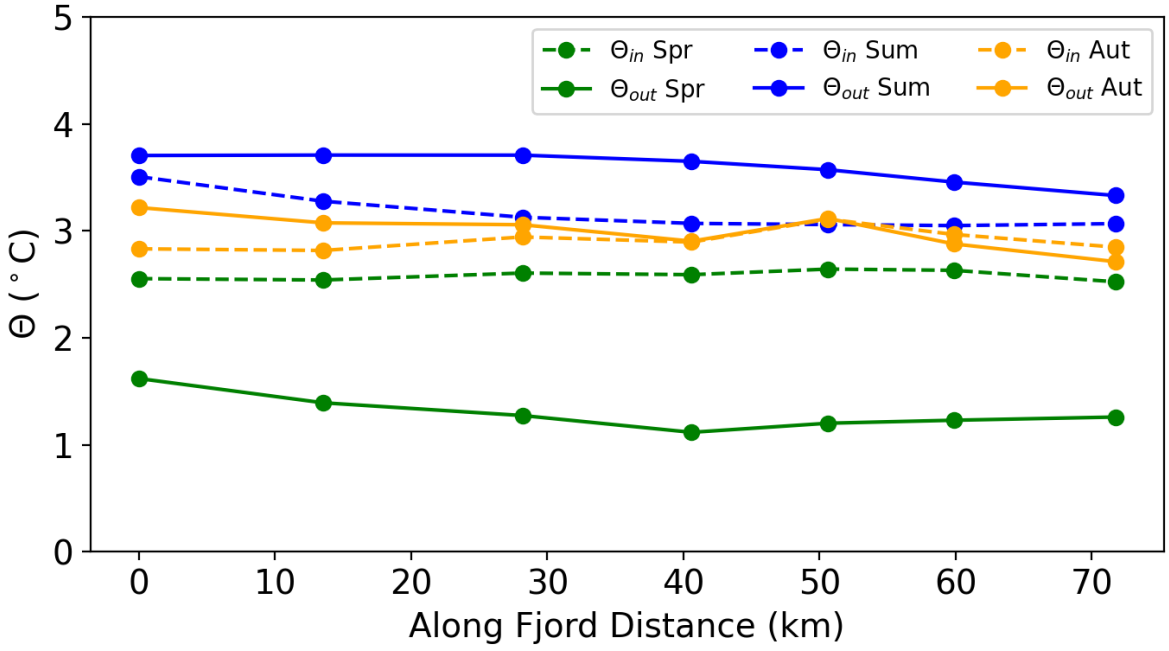

Figure 4.26. TEF along fjord Θ_{in}. Seasons are three month averages. The x-axis is distance from the mouth. Compare to Fig. 4.13.

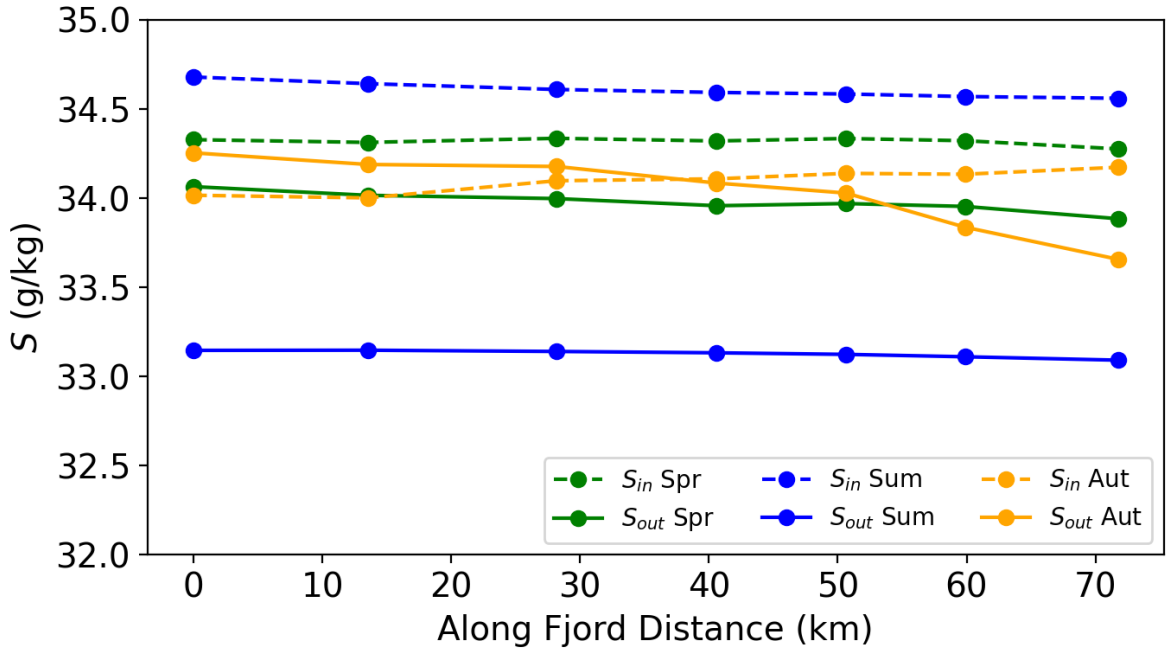

Figure 4.27. TEF along fjord S_{in}. Seasons are three month averages. The x-axis is distance from the mouth. Compare to Fig. 4.13.

Chapter 5

Conclusion

The mass loss of the Greenland Ice Sheet is emblematic of the broader changes to our planet wrought by climate change. As the ice sheet melts, it will contribute to sea level rise affecting communities globally (Bamber et al., 2018; Box et al., 2022). The additional freshwater influx into the ocean has the potential to impact regional and large-scale circulation including deep convection (Böning et al., 2016; Boone et al., 2018; Frajka-Williams et al., 2016; Le Bras et al., 2021). Within fjords, there are likely to be dramatic changes to circulation and water properties affecting local communities that depend on fjord ecological productivity for their livelihoods (Straneo et al., 2022; Hopwood et al., 2020; Meire et al., 2017). Greenland's glacial fjords are therefore important systems worthy of study because they lie at the intersection of ice, oceans and people.

Our knowledge of glacial fjord dynamics has increased considerably over the past decade, but there are still fundamental gaps that need to be addressed. For example, how does ocean forcing translate into glacial melting, and what factors control forcing variability? The remoteness of glacial fjords and the ice-hazardous conditions of fieldwork have severely limited observations. Modeling glacial fjords is also challenging because accurately representing the system requires resolving icebergs, turbulent plumes, and continental shelf coastal dynamics. One way forward is to leverage new observational techniques and accurately distill first-order dynamics into idealized models.

This dissertation combines novel observational datasets, idealized modeling, and numerical simulations to investigate the dynamics of glacial fjords. In Chapter 1, we investigated the relationship between acoustic travel time and fjord heat content. We demonstrated that PIES could be a potential low-cost monitor of fjord heat variability. In Chapter 2, we identified freshwater storage in observations and estimated freshwater residence time using an idealized model. This work can be used as a building block towards more complex models of fjord-shelf interactions. In Chapter 3, we analyzed a multi-year realistically forced simulation of a glacial fjord. We determined the individual role of glacial vs. shelf forcing in driving the exchange flow of Sermilik Fjord.

While these results shed insight on fjord dynamics, they lead to new questions and new avenues of research. Some questions to guide future work include: where is mixing distributed throughout the fjord and which mechanisms drive mixing? Additionally, what role does higher frequency oceanic forcing play close to the glacier? For example, how do coastal-trapped waves interact with mélange? Ideally, we can also apply these dissertation results to interdisciplinary research including the impact of fjord dynamics on the transport of tracers such as nutrients or heavy metals. Lastly, we should extend focus beyond fjords to the continental shelf and explore the dynamics of exported freshwater and its interactions with shelf-trough systems.

Understanding glacial fjord dynamics will lead to improved representation of ice-ocean interactions at the climate scale and better predictability of fjord properties at the local scale. This dissertation is a step towards a stronger understanding of fundamental connections between the ocean and glaciers. However, more observations are needed alongside improved models to continue scientific advancement. Ultimately, these investments will be necessary given the central role of the Greenland Ice Sheet in our changing climate.

References

Adcroft, A., C. Hill, J.-M. Campin, J. Marshall, and P. Heimbach, 2004: Overview of the formulation and numerics of the MIT GCM. *Proceedings of the ECMWF seminar series on Numerical Methods, Recent developments in numerical methods for atmosphere and ocean modelling*, 139–149, 139–149.

Andres, M., A. Silvano, F. Straneo, and D. R. Watts, 2015: Icebergs and Sea Ice detected with Inverted Echo Sounders. *J. Atmos. Oceanic Technol.*, **32**, 1042–1057, https://doi.org/10.1175/JTECH-D-14-00161.1, https://doi.org/10.1175/JTECH-D-14-00161.1.

Andresen, C. S., F. Straneo, M. H. Ribergaard, A. A. Bjørk, T. J. Andersen, A. Kuijpers, N. Nørgaard-Pedersen, K. H. Kjær, F. Schjøth, K. Weckström, and A. P. Ahlstrøm, 2012: Rapid response of Helheim Glacier in Greenland to climate variability over the past century. *Nat. Geosci.*, **5**, 37–41, https://doi.org/10.1038/ngeo1349, https://doi.org/10.1038/ngeo1349.

Andresen, C. S., S. Schmidt, M.-S. Seidenkrantz, F. Straneo, A. Grycel, C. H. Hass, K. Henrik Kjær, N. Nørgaard-Pedersen, L. M. Dyke, J. Olsen, and A. Kuijpers, 2014: A 100-year record of changes in water renewal rate in Sermilik fjord and its influence on calving of Helheim glacier, southeast Greenland. *Continental Shelf Research*, **85**, 21–29, https://doi.org/10.1016/j.csr.2014.05.017, https://doi.org/10.1016/j.csr.2014.05.017.

Arrigo, K. R., G. L. v. Dijken, R. M. Castelao, H. Luo, A. K. Rennermalm, M. Tedesco, T. L. Mote, H. Oliver, and P. L. Yager, 2017: Melting glaciers stimulate large summer phytoplankton blooms in southwest greenland waters. *Geophys. Res. Lett.*, **44**, 6278–6285, https://doi.org/10.1002/2017GL073583, https://doi.org/10.1002/2017GL073583.

Aure, J., J. Molvær, and A. Stigebrandt, 1996: Observations of inshore water exchange forced by a fluctuating offshore density field. *Mar. Pollut. Bull.*, **33 (1)**, 112–119, https://doi.org/10.1016/S0025-326X(97)00005-2, https://doi.org/10.1016/S0025-326X(97)00005-2.

Babson, A. L., M. Kawase, and P. MacCready, 2006: Seasonal and Interannual Variability in the Circulation of Puget Sound, Washington: A Box Model Study. *Atmos.–Ocean*, **44**, 29–45, https://doi.org/10.3137/ao.440103, https://doi.org/10.3137/ao.440103.

Bamber, J. L., M. Oppenheimer, R. E. Kopp, W. P. Aspinall, and R. M. Cooke, 2019: Ice

Sheet Contributions to Future Sea-Level Rise from Structured Expert Judgment. *Proc. Natl. Acad. Sci.*, **116**, 11 195–200, https://doi.org/10.1073/pnas.1817205116, https://doi.org/10.1073/pnas.1817205116.

Bamber, J. L., R. M. Westaway, B. Marzeion, and B. Wouters, 2018: The land ice contribution to sea level during the satellite era. *Environ. Res. Lett.*, **13**, 063 008, https://doi.org/10.1088/1748-9326/aac2f0, https://doi.org/10.1088/1748-9326/aac2f0.

Banas, N. S., B. M. Hickey, P. MacCready, and J. A. Newton, 2004: Dynamics of Willapa Bay, Washington: A Highly Unsteady, Partially Mixed Estuary. *J. Phys. Oceanogr.*, **34**, 2413–2427, https://doi.org/10.1175/JPO2637.1, https://doi.org/10.1175/JPO2637.1.

Beaird, N., F. Straneo, and W. Jenkins, 2015: Spreading of greenland meltwaters in the ocean revealed by noble gases. *Geophys. Res. Lett.*, **42**, 7705–7713, https://doi.org/10.1002/2015GL065003, https://doi.org/10.1002/2015GL065003.

Beaird, N., F. Straneo, and W. Jenkins, 2017: Characteristics of meltwater export from jakobshavn isbræ and ilulissat icefjord. *Ann. of Glaciol.*, **58**, 107–117, https://doi.org/10.1017/aog.2017.19, https://doi.org/10.1017/aog.2017.19.

Beaird, N., F. Straneo, and W. Jenkins, 2018: Export of Strongly Diluted Greenland Meltwater From a Major Glacial Fjord. *Geophys. Res. Lett.*, **45**, 4163–4170, https://doi.org/10.1029/2018GL077000, https://doi.org/10.1029/2018GL077000.

Bendtsen, J., J. Mortensen, K. Lennert, and S. Rysgaard, 2015: Heat sources for glacial ice melt in a west Greenland tidewater outlet glacier fjord: The role of subglacial freshwater discharge. *Geophys. Res. Lett.*, **42**, 4089–4095, https://doi.org/10.1002/2015GL063846, https://doi.org/10.1002/2015GL063846.

Bendtsen, J., S. Rysgaard, D. F. Carlson, L. Meire, and M. K. Sejr, 2021: Vertical Mixing in Stratified Fjords Near Tidewater Outlet Glaciers Along Northwest Greenland. *J. Geophys. Res. Oceans*, **126**, e2020JC016 898, https://doi.org/10.1029/2020JC016898, https://doi.org/10.1029/2020JC016898.

Boone, W., S. Rysgaard, D. F. Carlson, L. Meire, S. Kirillov, J. Mortensen, I. Dmitrenko, L. Vergeynst, and M. K. Sejr, 2018: Coastal Freshening Prevents Fjord Bottom Water Renewal in Northeast Greenland: A Mooring Study From 2003 to 2015. *Geophys. Res. Lett.*, **45**, 2726–2733, https://doi.org/10.1002/2017GL076591, https://doi.org/10.1002/2017GL076591.

Box, J. E., A. Hubbard, D. B. Bahr, W. T. Colgan, X. Fettweis, K. D. Mankoff, A. Wehrlé, B. Noël, M. R. van den Broeke, B. Wouters, A. A. Bjørk, and R. S. Fausto, 2022: Greenland ice sheet climate disequilibrium and committed sea-level rise. *Nat. Clim. Change*, **12**, 808–813, https://doi.org/10.1038/s41558-022-01441-2, https://doi.org/10.1038/s41558-022-01441-2.

Burchard, H., K. Bolding, R. Feistel, U. Gräwe, K. Klingbeil, P. MacCready, V. Mohrholz, L. Umlauf, and E. M. van der Lee, 2018: The Knudsen theorem and the Total Exchange Flow analysis framework applied to the Baltic Sea. *Prog. Oceanogr.*, **165**, 268–286, https://doi.org/10.1016/j.pocean.2018.04.004, https://doi.org/10.1016/j.pocean.2018.04.004.

Böning, C. W., E. Behrens, A. Biastoch, K. Getzlaff, and J. L. Bamber, 2016: Emerging impact of greenland meltwater on deepwater formation in the north atlantic ocean. *Nat. Geosci.*, **9**, 523–527, https://doi.org/10.1038/ngeo2740, https://doi.org/10.1038/ngeo2740.

Cape, M. R., F. Straneo, N. Beaird, R. M. Bundy, and M. A. Charette, 2019: Nutrient release to oceans from buoyancy-driven upwelling at Greenland tidewater glaciers. *Nat. Geosci.*, **12**, 34–39, https://doi.org/10.1038/s41561-018-0268-4, https://doi.org/10.1038/s41561-018-0268-4.

Carroll, D., D. A. Sutherland, E. L. Shroyer, J. D. Nash, G. A. Catania, and L. A. Stearns, 2015: Modeling Turbulent Subglacial Meltwater Plumes: Implications for Fjord-Scale Buoyancy-Driven Circulation. *J. Phys. Oceanogr.*, **45**, 2169–2185, https://doi.org/10.1175/JPO-D-15-0033.1, https://doi.org/10.1175/JPO-D-15-0033.1.

Carroll, D., D. A. Sutherland, E. L. Shroyer, J. D. Nash, G. A. Catania, and L. A. Stearns, 2017: Subglacial discharge-driven renewal of tidewater glacier fjords. *J. Geophys. Res. Oceans*, **122**, 6611–6629, https://doi.org/10.1002/2017JC012962, https://doi.org/10.1002/2017JC012962.

Carroll, D., D. A. Sutherland, B. Hudson, T. Moon, G. A. Catania, E. L. Shroyer, J. D. Nash, T. C. Bartholomaus, D. Felikson, L. A. Stearns, B. P. Y. Noël, and M. R. v. d. Broeke, 2016: The impact of glacier geometry on meltwater plume structure and submarine melt in Greenland fjords. *Geophys. Res. Lett.*, **43**, https://doi.org/10.1002/2016GL070170, https://doi.org/10.1002/2016GL070170.

Carroll, D., D. A. Sutherland, B. Curry, J. D. Nash, E. L. Shroyer, G. A. Catania, L. A. Stearns, J. P. Grist, C. M. Lee, and L. d. Steur, 2018: Subannual and Seasonal Variability of Atlantic-Origin Waters in Two Adjacent West Greenland Fjords. *J. Geophys. Res. Oceans*, **123**, 6670–6687, https://doi.org/10.1029/2018JC014278, https://doi.org/10.1029/2018JC014278.

Chauché, N., A. Hubbard, J.-C. Gascard, J. E. Box, R. Bates, M. Koppes, A. Sole, P. Christoffersen, and H. Patton, 2014: Ice–ocean interaction and calving front morphology at two west Greenland tidewater outlet glaciers. *The Cryosphere*, **8 (4)**, 1457–1468, https://doi.org/https://doi.org/10.5194/tc-8-1457-2014, https://doi.org/https://doi.org/10.5194/tc-8-1457-2014.

Christoffersen, P., R. I. Mugford, K. J. Heywood, I. Joughin, J. A. Dowdeswell, J. P. M. Syvitski, A. Luckman, and T. J. Benham, 2011: Warming of waters in an East Greenland fjord prior to glacier retreat: mechanisms and connection to large-scale atmospheric conditions. *The Cryosphere*, **5 (3)**, 701–714, https://doi.org/https://doi.org/10.5194/tc-5-701-2011, URL https://www.the-cryosphere.net/5/701/2011/, URL https://www.the-cryosphere.net/5/701/2011/.

Cokelet, E. D., and R. J. Stewart, 1985: The exchange of water in fjords: The efflux/reflux theory of advective reaches separated by mixing zones. *J. Geophys. Res. Oceans*, **90**, 7287–7306, https://doi.org/10.1029/JC090iC04p07287, https://doi.org/10.1029/JC090iC04p07287.

Cottier, F. R., F. Nilsen, R. Skogseth, V. Tverberg, J. Skardhamar, and H. Svendsen, 2010: Arctic fjords: a review of the oceanographic environment and dominant physical processes. *Fjord Systems and Archives*, J. A. Howe, W. E. N. Austin, M. Forwick, and M. Paetzel, Eds., Vol. 344, Geol. Soc. Lond., 35–50, https://doi.org/10.1144/SP344.4, https://doi.org/10.1144/SP344.4.

Cowton, T., D. Slater, A. Sole, D. Goldberg, and P. Nienow, 2015a: Modeling the impact of glacial runoff on fjord circulation and submarine melt rate using a new subgrid-scale parameterization for glacial plumes. *J. Geophys. Res. Oceans*, **120 (2)**, 796–812, https://doi.org/10.1002/2014JC010324, https://doi.org/10.1002/2014JC010324.

Cowton, T., D. Slater, A. Sole, D. Goldberg, and P. Nienow, 2015b: Modeling the impact of glacial runoff on fjord circulation and submarine melt rate using a new subgrid-scale parameterization for glacial plumes. *J. Geophys. Res. Oceans*, **120**, 796–812, https://doi.org/10.1002/2014JC010324, https://doi.org/10.1002/2014JC010324.

Cowton, T. R., A. J. Sole, P. W. Nienow, D. A. Slater, and P. Christoffersen, 2018: Linear response of east Greenland's tidewater glaciers to ocean/atmosphere warming. *Proceedings of the National Academy of Sciences*, **115 (31)**, 7907–7912, https://doi.org/10.1073/pnas.1801769115, https://doi.org/10.1073/pnas.1801769115.

Davison, B. J., T. R. Cowton, F. R. Cottier, and A. J. Sole, 2020: Iceberg melting substantially modifies oceanic heat flux towards a major Greenlandic tidewater glacier. *Nat. Commun.*, **11**, 5983, https://doi.org/10.1038/s41467-020-19805-7, https://doi.org/10.1038/s41467-020-19805-7.

De Andrés, E., D. A. Slater, F. Straneo, J. Otero, S. Das, and F. Navarro, 2020: Surface emergence of glacial plumes determined by fjord stratification. *Cryosphere Discuss.*, 1–41, https://doi.org/10.5194/tc-2019-264, https://doi.org/10.5194/tc-2019-264.

Del Grosso, V. A., 1974: New equation for the speed of sound in natural waters (with comparisons to other equations). *J. Acoust. Soc. Am.*, **56**, 1084–1091, https://doi.org/10.1121/1.1903388, https://doi.org/10.1121/1.1903388.

Delhasse, A., C. Kittel, C. Amory, S. Hofer, D. van As, R. S. Fausto, and X. Fettweis, 2020: Brief communication: Evaluation of the near-surface climate in ERA5 over the Greenland Ice Sheet. *Cryosphere*, **14**, 957–965, https://doi.org/10.5194/tc-14-957-2020, https://doi.org/10.5194/tc-14-957-2020.

Dukhovskoy, D., I. Yashayaev, A. Proshutinsky, J. L. Bamber, I. L. Bashmachnikov, E. P. Chassignet, C. M. Lee, and A. J. Tedstone, 2019: Role of greenland freshwater anomaly in the recent freshening of the subpolar north atlantic. *J. Geophys. Res. Oceans*, **124**, 3333–3360,

https://doi.org/10.1029/2018JC014686, https://doi.org/10.1029/2018JC014686.

Elias, E. P. L., G. Gelfenbaum, and A. J. Van der Westhuysen, 2012: Validation of a coupled wave-flow model in a high-energy setting: The mouth of the Columbia River. *Journal of Geophysical Research: Oceans*, **117 (C9)**, https://doi.org/10.1029/2012JC008105, https://doi.org/10.1029/2012JC008105.

Emery, W. J., and R. E. Thomson, 2001: *Data Analysis Methods in Physical Oceanography (Revised Second Edition)*. Revised second edition ed., Elsevier Science, Amsterdam, https://doi.org/https://doi.org/10.1016/B978-044450756-3/50007-1, https://doi.org/https://doi.org/10.1016/B978-044450756-3/50007-1.

Enderlin, E. M., I. M. Howat, S. Jeong, M.-J. Noh, J. H. v. Angelen, and M. R. v. d. Broeke, 2014: An improved mass budget for the Greenland ice sheet. *Geophys. Res. Lett.*, **41**, 866–872, https://doi.org/10.1002/2013GL059010, https://doi.org/10.1002/2013GL059010.

Erofeeva, S., and G. Egbert, 2020: Arc5km2018: Arctic ocean inverse tide model on a 5 kilometer grid, 2018. *Dataset*, https://doi.org/10.18739/A21R6N14K, https://doi.org/10.18739/A21R6N14K.

Ezhova, E., C. Cenedese, and L. Brandt, 2016: Interaction between a Vertical Turbulent Jet and a Thermocline. *J. Phys. Oceanogr.*, **46**, 3415–3437, https://doi.org/10.1175/JPO-D-16-0035.1, https://doi.org/10.1175/JPO-D-16-0035.1.

Ezhova, E., C. Cenedese, and L. Brandt, 2017: Dynamics of a Turbulent Buoyant Plume in a Stratified Fluid: An Idealized Model of Subglacial Discharge in Greenland Fjords. *J. Phys. Oceanogr.*, **47**, 2611–2630, https://doi.org/10.1175/JPO-D-16-0259.1, https://doi.org/10.1175/JPO-D-16-0259.1.

Farmer, D. M., and H. Freeland, 1983: The physical oceanography of fjords. *Prog. Oceanog.*, **12**, 147–220, **12**, 147–220.

Fettweis, X., J. E. Box, C. Agosta, C. Amory, C. Kittel, C. Lang, D. van As, H. Machguth, and H. Gallée, 2017: Reconstructions of the 1900–2015 Greenland ice sheet surface mass balance using the regional climate MAR model. *Cryosphere*, **11**, 1015–1033, https://doi.org/10.5194/tc-11-1015-2017, https://doi.org/10.5194/tc-11-1015-2017.

FitzMaurice, A., F. Straneo, C. Cenedese, and M. Andres, 2016: Effect of a sheared flow on iceberg motion and melting. *Geophys. Res. Lett.*, **43**, 12,520–12,527, https://doi.org/10.1002/2016GL071602, https://doi.org/10.1002/2016GL071602.

Foukal, N. P., R. Gelderloos, and R. S. Pickart, 2020: A continuous pathway for fresh water along the East Greenland shelf. *Science Advances*, **6 (43)**, eabc4254, https://doi.org/10.1126/sciadv.abc4254, https://doi.org/10.1126/sciadv.abc4254.

Frajka-Williams, E., J. Bamber, and K. Våge, 2016: Greenland melt and the atlantic meridional overturning circulation. *Oceanog.*, **29**, 22–33, https://doi.org/10.5670/oceanog.2016.96, https://doi.org/10.5670/oceanog.2016.96.

Fraser, N. J., and M. E. Inall, 2018: Influence of barrier wind forcing on heat delivery toward the Greenland ice sheet. *J. Geophys. Res. Oceans*, **123**, 2513–2538, https://doi.org/10.1002/2017JC013464, https://doi.org/10.1002/2017JC013464.

Fraser, N. J., M. E. Inall, M. G. Magaldi, T. W. N. Haine, and S. C. Jones, 2018: Wintertime fjord-shelf interaction and ice sheet melting in southeast greenland. *J. Geophys. Res. Oceans*, **123 (12)**, 9156–9177, https://doi.org/10.1029/2018JC014435, https://doi.org/10.1029/2018JC014435.

Gade, H. G., 1979: Melting of ice in sea water: A primitive model with application to the antarctic ice shelf and icebergs. *J. Phys. Oceanogr.*, **9**, 189–198, https://doi.org/10.1175/1520-0485(1979)009⟨0189:MOIISW⟩2.0.CO;2, https://doi.org/10.1175/1520-0485(1979)009⟨0189:MOIISW⟩2.0.CO;2.

Gelderloos, R., T. W. N. Haine, and M. Almansi, 2021: Coastal Trapped Waves and Other Subinertial Variability along the Southeast Greenland Coast in a Realistic Numerical Simulation. *Journal of Physical Oceanography*, **51 (3)**, 861–877, https://doi.org/10.1175/JPO-D-20-0239.1, https://doi.org/10.1175/JPO-D-20-0239.1.

Gelderloos, R., T. W. N. Haine, and M. Almansi, 2022: Subinertial Variability in Four Southeast Greenland Fjords in Realistic Numerical Simulations. *Journal of Geophysical Research: Oceans*, **127 (11)**, e2022JC018 820, https://doi.org/10.1029/2022JC018820, https://doi.org/10.1029/2022JC018820.

Gelderloos, R., T. W. N. Haine, I. M. Koszalka, and M. G. Magaldi, 2017: Seasonal Variability in Warm-Water Inflow toward Kangerdlugssuaq Fjord. *Journal of Physical Oceanography*, **47 (7)**, 1685–1699, https://doi.org/10.1175/JPO-D-16-0202.1, https://doi.org/10.1175/JPO-D-16-0202.1.

Gerland, S., and R. Hall, 2006: Variability of fast-ice thickness in Spitsbergen fjords. *Ann. Glaciol.*, **44**, 231–239, https://doi.org/10.3189/172756406781811367, https://doi.org/10.3189/172756406781811367.

Geyer, W. R., and P. MacCready, 2014: The Estuarine Circulation. *Annu. Rev. Fluid Mech.*, **46**, 175–197, https://doi.org/10.1146/annurev-fluid-010313-141302, https://doi.org/10.1146/annurev-fluid-010313-141302.

Giddings, S. N., and P. MacCready, 2017: Reverse Estuarine Circulation Due to Local and Remote Wind Forcing, Enhanced by the Presence of Along-Coast Estuaries. *J. Geophys. Res. Oceans*, **122**, 10 184–10 205, https://doi.org/10.1002/2016JC012479, https://doi.org/10.1002/2016JC012479.

Giddings, S. N., P. MacCready, B. M. Hickey, N. S. Banas, K. A. Davis, S. A. Siedlecki, V. L. Trainer, R. M. Kudela, N. A. Pelland, and T. P. Connolly, 2014: Hindcasts of potential harmful algal bloom transport pathways on the Pacific Northwest coast. *Journal of Geophysical Research: Oceans*, **119 (4)**, 2439–2461, https://doi.org/10.1002/2013JC009622, https://doi.org/10.1002/2013JC009622.

Gillibrand, P. A., M. E. Inall, E. Portilla, and P. Tett, 2013: A box model of the seasonal exchange and mixing in Regions of Restricted Exchange: Application to two contrasting Scottish inlets. *Environ. Model. Softw.*, **43**, 144–159, https://doi.org/10.1016/j.envsoft.2013.02.008, https://doi.org/10.1016/j.envsoft.2013.02.008.

Gladish, C. V., D. M. Holland, and C. M. Lee, 2014a: Oceanic boundary conditions for jakobshavn glacier. part II: Provenance and sources of variability of disko bay and ilulissat icefjord waters, 1990–2011. *J. Phys. Oceanogr.*, **45 (1)**, 33–63, https://doi.org/10.1175/JPO-D-14-0045.1, https://doi.org/10.1175/JPO-D-14-0045.1.

Gladish, C. V., D. M. Holland, A. Rosing-Asvid, J. W. Behrens, and J. Boje, 2014b: Oceanic boundary conditions for Jakobshavn Glacier. Part I: Variability and renewal of Ilulissat Icefjord Waters, 2001–14. *J. Phys. Oceanogr.*, **45**, 3–32, https://doi.org/10.1175/JPO-D-14-0044.1, https://doi.org/10.1175/JPO-D-14-0044.1.

Goelzer, H., S. Nowicki, A. Payne, E. Larour, H. Seroussi, W. H. Lipscomb, J. Gregory, A. Abe-Ouchi, A. Shepherd, E. Simon, C. Agosta, P. Alexander, A. Aschwanden, A. Barthel, R. Calov, C. Chambers, Y. Choi, J. Cuzzone, C. Dumas, T. Edwards, D. Felikson, X. Fettweis, N. R. Golledge, R. Greve, A. Humbert, P. Huybrechts, S. L. Clec'h, V. Lee, G. Leguy, C. Little, D. P. Lowry, M. Morlighem, I. Nias, A. Quiquet, M. Rückamp, N.-J. Schlegel, D. Slater, R. Smith, F. Straneo, L. Tarasov, R. v. d. Wal, and M. v. d. Broeke, 2020: The future sea-level contribution of the Greenland ice sheet: a multi-model ensemble study of ISMIP6. *Cryosphere Discuss.*, 1–43, https://doi.org/10.5194/tc-2019-319, https://doi.org/10.5194/tc-2019-319.

Hager, A. O., D. A. Sutherland, J. M. Amundson, R. H. Jackson, C. Kienholz, R. J. Motyka, and J. D. Nash, 2022a: Subglacial discharge reflux and buoyancy forcing drive seasonality in a silled glacial fjord. *J. Geophys. Res. Oceans*, **127**, e2021JC018 355, https://doi.org/10.1029/2021JC018355, https://doi.org/10.1029/2021JC018355.

Hager, A. O., D. A. Sutherland, J. M. Amundson, R. H. Jackson, C. Kienholz, R. J. Motyka, and J. D. Nash, 2022b: Subglacial discharge reflux and buoyancy forcing drive seasonality in a silled glacial fjord. *J. Geophys. Res. Oceans*, **127**, https://doi.org/10.1029/2021JC018355, https://doi.org/10.1029/2021JC018355.

Hansen, D., and M. Rattray, 1965: Gravitational circulation in straits and estuaries. *J. Mar. Res.*, **23**, 104–122, **23**, 104–122.

Harden, B. E., I. A. Renfrew, and G. N. Petersen, 2011: A climatology of wintertime barrier

winds off southeast greenland. *J. Climate*, **24 (17)**, 4701–4717, https://doi.org/10.1175/2011JCLI4113.1, https://doi.org/10.1175/2011JCLI4113.1.

Harden, B. E., F. Straneo, and D. A. Sutherland, 2014: Moored observations of synoptic and seasonal variability in the East Greenland Coastal Current. *J. Geophys. Res. Oceans*, **119**, 8838–8857, https://doi.org/10.1002/2014JC010134, https://doi.org/10.1002/2014JC010134.

Hendry, K. R., N. Briggs, S. Henson, J. Opher, J. A. Brearley, M. P. Meredith, M. J. Leng, and L. Meire, 2021: Tracing Glacial Meltwater From the Greenland Ice Sheet to the Ocean Using Gliders. *J. Geophys. Res. Oceans*, **126**, e2021JC017 274, https://doi.org/10.1029/2021JC017274, https://doi.org/10.1029/2021JC017274.

Hersbach, H., B. Bell, P. Berrisford, S. Hirahara, A. Horányi, J. Muñoz-Sabater, J. Nicolas, C. Peubey, R. Radu, D. Schepers, A. Simmons, C. Soci, S. Abdalla, X. Abellan, G. Balsamo, P. Bechtold, G. Biavati, J. Bidlot, M. Bonavita, G. De Chiara, P. Dahlgren, D. Dee, M. Diamantakis, R. Dragani, J. Flemming, R. Forbes, M. Fuentes, A. Geer, L. Haimberger, S. Healy, R. J. Hogan, E. Hólm, M. Janisková, S. Keeley, P. Laloyaux, P. Lopez, C. Lupu, G. Radnoti, P. de Rosnay, I. Rozum, F. Vamborg, S. Villaume, and J.-N. Thépaut, 2020: The ERA5 global reanalysis. *Q. J. R. Meteorol. Soc.*, **146**, 1999–2049, https://doi.org/10.1002/qj.3803, https://doi.org/10.1002/qj.3803.

Hetland, R. D., 2005: Relating River Plume Structure to Vertical Mixing. *J. Phys. Oceanogr.*, **35**, 1667–1688, https://doi.org/10.1175/JPO2774.1, https://doi.org/10.1175/JPO2774.1.

Hines, K. M., and D. H. Bromwich, 2008: Development and testing of Polar Weather Research and Forecasting (WRF) model. Part I: Greenland Ice Sheet meteorology. *Mon. Weather Rev.*, **136**, 1971–1989, https://doi.org/10.1175/2007MWR2112.1, https://doi.org/10.1175/2007MWR2112.1.

Holland, D. M., R. H. Thomas, B. de Young, M. H. Ribergaard, and B. Lyberth, 2008: Acceleration of Jakobshavn Isbræ triggered by warm subsurface ocean waters. *Nat. Geosci.*, **1**, 659–664, https://doi.org/10.1038/ngeo316, https://doi.org/10.1038/ngeo316.

Hopwood, M. J., D. Carroll, T. J. Browning, L. Meire, J. Mortensen, S. Krisch, and E. P. Achterberg, 2018: Non-linear response of summertime marine productivity to increased meltwater discharge around Greenland. *Nat. Commun.*, **9**, 1–9, https://doi.org/10.1038/s41467-018-05488-8, https://doi.org/10.1038/s41467-018-05488-8.

Hopwood, M. J., D. Carroll, T. Dunse, A. Hodson, J. M. Holding, J. L. Iriarte, S. Ribeiro, E. P. Achterberg, C. Cantoni, D. F. Carlson, M. Chierici, J. S. Clarke, S. Cozzi, A. Fransson, T. Juul-Pedersen, M. H. S. Winding, and L. Meire, 2020: Review article: How does glacier discharge affect marine biogeochemistry and primary production in the Arctic? *Cryosphere*, **14**, 1347–1383, https://doi.org/10.5194/tc-14-1347-2020, https://doi.org/10.5194/tc-14-1347-2020.

Horner-Devine, A. R., R. D. Hetland, and D. G. MacDonald, 2015: Mixing and transport in coastal river plumes. *Annu. Rev. Fluid Mech.*, **47**, 569–594, https://doi.org/10.1146/annurev-fluid-010313-141408, https://doi.org/10.1146/annurev-fluid-010313-141408.

Howat, I. M., I. Joughin, S. Tulaczyk, and S. Gogineni, 2005: Rapid retreat and acceleration of Helheim Glacier, east Greenland. *Geophysical Research Letters*, **32 (22)**, https://doi.org/10.1029/2005GL024737, https://doi.org/10.1029/2005GL024737.

Hughes, K. G., 2022: Pathways, Form Drag, and Turbulence in Simulations of an Ocean Flowing Through an Ice Mélange. *Journal of Geophysical Research: Oceans*, **127 (6)**, e2021JC018 228, https://doi.org/10.1029/2021JC018228, https://doi.org/10.1029/2021JC018228.

Hughes, K. G., J. M. Klymak, W. J. Williams, and H. Melling, 2018: Tidally Modulated Internal Hydraulic Flow and Energetics in the Central Canadian Arctic Archipelago. *Journal of Geophysical Research: Oceans*, **123 (8)**, 5210–5229, https://doi.org/https://doi.org/10.1029/2018JC013770, https://doi.org/https://doi.org/10.1029/2018JC013770.

Hunt, G. R., and N. B. Kaye, 2005: Lazy plumes. *Journal of Fluid Mechanics*, **533**, 329–338, https://doi.org/10.1017/S002211200500457X, https://doi.org/10.1017/S002211200500457X.

Inall, M. E., and P. A. Gillibrand, 2010: The physics of mid-latitude fjords: a review. *Geological Society, London, Special Publications*, **344 (1)**, 17–33, https://doi.org/10.1144/SP344.3, URL https://www.lyellcollection.org/doi/10.1144/SP344.3, URL https://www.lyellcollection.org/doi/10.1144/SP344.3.

Inall, M. E., T. Murray, F. R. Cottier, K. Scharrer, T. J. Boyd, K. J. Heywood, and S. L. Bevan, 2014: Oceanic heat delivery via Kangerdlugssuaq Fjord to the south-east Greenland ice sheet. *J. Geophys. Res.: Oceans*, **119**, 631–645, https://doi.org/10.1002/2013JC009295, https://doi.org/10.1002/2013JC009295.

Inall, M. E., F. Nilsen, F. R. Cottier, and R. Daae, 2015: Shelf/fjord exchange driven by coastal-trapped waves in the arctic. *J. Geophys. Res. Oceans*, **120 (12)**, 8283–8303, https://doi.org/10.1002/2015JC011277, https://doi.org/10.1002/2015JC011277.

Jackson, R. H., S. J. Lentz, and F. Straneo, 2018: The Dynamics of Shelf Forcing in Greenlandic Fjords. *J. Phys. Oceanogr.*, **48**, 2799–2827, https://doi.org/10.1175/JPO-D-18-0057.1, https://doi.org/10.1175/JPO-D-18-0057.1.

Jackson, R. H., R. J. Motyka, J. M. Amundson, N. Abib, D. A. Sutherland, J. D. Nash, and C. Kienholz, 2022a: The relationship between submarine melt and subglacial discharge from observations at a tidewater glacier. *J. Geophys. Res. Oceans*, e2021JC018204, https://doi.org/10.1029/2021JC018204, https://doi.org/10.1029/2021JC018204.

Jackson, R. H., R. J. Motyka, J. M. Amundson, N. Abib, D. A. Sutherland, J. D. Nash, and

C. Kienholz, 2022b: The relationship between submarine melt and subglacial discharge from observations at a tidewater glacier. *J. Geophys. Res. Oceans*, **127**, e2021JC018 204, https://doi.org/10.1029/2021JC018204, https://doi.org/10.1029/2021JC018204.

Jackson, R. H., and F. Straneo, 2016: Heat, Salt, and Freshwater Budgets for a Glacial Fjord in Greenland. *J. Phys. Oceanogr.*, **46**, 2735–2768, https://doi.org/10.1175/JPO-D-15-0134.1, https://doi.org/10.1175/JPO-D-15-0134.1.

Jackson, R. H., F. Straneo, and D. A. Sutherland, 2014: Externally forced fluctuations in ocean temperature at Greenland glaciers in non-summer months. *Nat. Geosci.*, **7**, 503–508, https://doi.org/10.1038/ngeo2186, https://doi.org/10.1038/ngeo2186.

Jackson, R. H., E. L. Shroyer, J. D. Nash, D. A. Sutherland, D. Carroll, M. J. Fried, G. A. Catania, T. C. Bartholomaus, and L. A. Stearns, 2017: Near-glacier surveying of a subglacial discharge plume: Implications for plume parameterizations. *Geophys. Res. Lett.*, **44**, 6886–6894, https://doi.org/10.1002/2017GL073602, https://doi.org/10.1002/2017GL073602.

Jackson, R. H., J. D. Nash, C. Kienholz, D. A. Sutherland, J. M. Amundson, R. J. ka, D. Winters, E. Skyllingstad, and E. C. Pettit, 2020: Meltwater intrusions reveal mechanisms for rapid submarine melt at a tidewater glacier. *Geophys. Res. Lett.*, **47**, e2019GL085 335, https://doi.org/10.1029/2019GL085335, https://doi.org/10.1029/2019GL085335.

Jenkins, A., 2011: Convection-Driven Melting near the Grounding Lines of Ice Shelves and Tidewater Glaciers. *J. Phys. Oceanogr.*, **41**, 2279–2294, https://doi.org/10.1175/JPO-D-11-03.1, https://doi.org/10.1175/JPO-D-11-03.1.

Kajanto, K., F. Straneo, and K. Nisancioglu, 2022: Impact of icebergs on the seasonal submarine melt of Sermeq Kujalleq. *The Cryosphere Discuss.*, 1–26, https://doi.org/10.5194/tc-2022-136, https://doi.org/10.5194/tc-2022-136.

Kennelly, M., K. Tracey, and D. R. Watts, 2007: *Inverted Echo Sounder Data Processing Manual*. University of Rhode Island GSO Tech. Rep. 2007-02, 89 pp., https://doi.org/10.21236/ADA477328, https://doi.org/10.21236/ADA477328.

Khazendar, A., I. G. Fenty, D. Carroll, A. Gardner, C. M. Lee, I. Fukumori, O. Wang, H. Zhang, H. Seroussi, D. Moller, B. P. Y. Noël, M. R. van den Broeke, S. Dinardo, and J. Willis, 2019: Interruption of two decades of Jakobshavn Isbrae acceleration and thinning as regional ocean cools. *Nat. Geosci.*, **12**, 277–283, https://doi.org/10.1038/s41561-019-0329-3, https://doi.org/10.1038/s41561-019-0329-3.

Kimura, S., P. R. Holland, A. Jenkins, and M. Piggott, 2014: The Effect of Meltwater Plumes on the Melting of a Vertical Glacier Face. *Journal of Physical Oceanography*, **44 (12)**, 3099–3117, https://doi.org/10.1175/JPO-D-13-0219.1, https://doi.org/10.1175/JPO-D-13-0219.1.

Klinck, J. M., J. J. O'Brien, and H. Svendsen, 1981: A Simple Model of Fjord and Coastal Circulation Interaction. *Journal of Physical Oceanography*, **11 (12)**, 1612–1626, https://doi.org/10.1175/1520-0485(1981)011⟨1612:ASMOFA⟩2.0.CO;2, https://doi.org/10.1175/1520-0485(1981)011⟨1612:ASMOFA⟩2.0.CO;2.

Klymak, J. M., and M. C. Gregg, 2004: Tidally Generated Turbulence over the Knight Inlet Sill. *J.Phys. Oceanogr.*, **34**, 1135–1151, https://doi.org/10.1175/1520-0485(2004)034⟨1135:TGTOTK⟩2.0.CO;2, https://doi.org/10.1175/1520-0485(2004)034⟨1135:TGTOTK⟩2.0.CO;2.

Kärnä, T., A. M. Baptista, J. E. Lopez, P. J. Turner, C. McNeil, and T. B. Sanford, 2015: Numerical modeling of circulation in high-energy estuaries: A Columbia River estuary benchmark. *Ocean Modelling*, **88**, 54–71, https://doi.org/10.1016/j.ocemod.2015.01.001, https://doi.org/10.1016/j.ocemod.2015.01.001.

Large, W. G., J. C. McWilliams, and S. C. Doney, 1994: Oceanic vertical mixing: A review and a model with a nonlocal boundary layer parameterization. *Rev. Geophys.*, **32**, 363–403, https://doi.org/10.1029/94RG01872, https://doi.org/10.1029/94RG01872.

Le Bras, I., F. Straneo, M. Muilwijk, L. H. Smedsrud, F. Li, M. S. Lozier, and N. P. Holliday, 2021: How much arctic fresh water participates in the subpolar overturning circulation? *J. Phys. Oceanogr.*, **51**, 955–973, https://doi.org/10.1175/jpo-d-20-0240.1, https://doi.org/10.1175/jpo-d-20-0240.1.

Le Bras, I. A.-A., F. Straneo, J. Holte, and N. P. Holliday, 2018: Seasonality of Freshwater in the East Greenland Current System From 2014 to 2016. *Journal of Geophysical Research: Oceans*, **123 (12)**, 8828–8848, https://doi.org/10.1029/2018JC014511, https://doi.org/10.1029/2018JC014511.

Li, Q., D. M. Farmer, T. F. Duda, and S. Ramp, 2009: Acoustical measurement of nonlinear internal waves using the inverted echo sounder. *J. Atmos. Oceanic Technol.*, **26**, 2228–2242, https://doi.org/10.1175/2009JTECHO652.1, https://doi.org/10.1175/2009JTECHO652.1.

Lindeman, M. R., F. Straneo, N. J. Wilson, J. M. Toole, R. A. Krishfield, N. L. Beaird, T. Kanzow, and J. Schaffer, 2020: Ocean Circulation and Variability Beneath Nioghalvfjerdsbræ (79 North Glacier) Ice Tongue. *J. Geophys. Res. Oceans*, **125**, e2020JC016 091, https://doi.org/10.1029/2020JC016091, https://doi.org/10.1029/2020JC016091.

Liu, Y., P. MacCready, B. M. Hickey, E. P. Dever, P. M. Kosro, and N. S. Banas, 2009: Evaluation of a coastal ocean circulation model for the Columbia River plume in summer 2004. *Journal of Geophysical Research: Oceans*, **114 (C2)**, https://doi.org/10.1029/2008JC004929, https://doi.org/10.1029/2008JC004929.

Lorenz, M., K. Klingbeil, and H. Burchard, 2020: Numerical Study of the Exchange Flow of the Persian Gulf Using an Extended Total Exchange Flow Analysis Framework. *Journal of Geo-*

physical Research: Oceans, **125 (2)**, e2019JC015 527, https://doi.org/10.1029/2019JC015527, https://doi.org/10.1029/2019JC015527.

Lorenz, M., K. Klingbeil, P. MacCready, and H. Burchard, 2019: Numerical issues of the Total Exchange Flow (TEF) analysis framework for quantifying estuarine circulation. *Ocean Science*, **15 (3)**, 601–614, https://doi.org/10.5194/os-15-601-2019, https://doi.org/10.5194/os-15-601-2019.

Luckman, A., D. I. Benn, F. Cottier, S. Bevan, F. Nilsen, and M. Inall, 2015: Calving rates at tidewater glaciers vary strongly with ocean temperature. *Nat. Commun.*, **6**, https://doi.org/10.1038/ncomms9566, https://doi.org/10.1038/ncomms9566.

Luckman, A., T. Murray, R. de Lange, and E. Hanna, 2006: Rapid and synchronous ice-dynamic changes in East Greenland. *Geophysical Research Letters*, **33 (3)**, https://doi.org/10.1029/2005GL025428, https://doi.org/10.1029/2005GL025428.

MacCready, P., 2011: Calculating Estuarine Exchange Flow Using Isohaline Coordinates. *Journal of Physical Oceanography*, **41 (6)**, 1116–1124, https://doi.org/10.1175/2011JPO4517.1, https://doi.org/10.1175/2011JPO4517.1.

MacCready, P., and W. R. Geyer, 2010: Advances in Estuarine Physics. *Annu. Rev. Mar. Sci.*, **2**, 35–58, https://doi.org/10.1146/annurev-marine-120308-081015, https://doi.org/10.1146/annurev-marine-120308-081015.

MacCready, P., W. R. Geyer, and H. Burchard, 2018: Estuarine Exchange Flow Is Related to Mixing through the Salinity Variance Budget. *Journal of Physical Oceanography*, **48 (6)**, 1375–1384, https://doi.org/10.1175/JPO-D-17-0266.1, https://doi.org/10.1175/JPO-D-17-0266.1.

MacCready, P., R. M. McCabe, S. A. Siedlecki, M. Lorenz, S. N. Giddings, J. Bos, S. Albertson, N. S. Banas, and S. Garnier, 2021: Estuarine Circulation, Mixing, and Residence Times in the Salish Sea. *J. Geophys. Res. Oceans*, **126**, e2020JC016 738, https://doi.org/10.1029/2020JC016738, https://doi.org/10.1029/2020JC016738.

Mankoff, K. D., A. Solgaard, W. Colgan, A. P. Ahlstrøm, S. A. Khan, and R. S. Fausto, 2020: Greenland Ice Sheet solid ice discharge from 1986 through March 2020. *Earth System Science Data*, **12 (2)**, 1367–1383, https://doi.org/10.5194/essd-12-1367-2020, https://doi.org/10.5194/essd-12-1367-2020.

Mankoff, K. D., F. Straneo, C. Cenedese, S. B. Das, C. G. Richards, and H. Singh, 2016: Structure and dynamics of a subglacial discharge plume in a greenlandic fjord. *J. Geophys. Res.: Oceans*, **121**, 8670–8688, https://doi.org/10.1002/2016JC011764, https://doi.org/10.1002/2016JC011764.

Marshall, J., A. Adcroft, C. Hill, L. Perelman, and C. Heisey, 1997: A finite-volume, incompress-

ible Navier Stokes model for studies of the ocean on parallel computers. *J. Geophys. Res.*, **102**, 5753–5766, https://doi.org/10.1029/96JC02775, https://doi.org/10.1029/96JC02775.

McDougall, T. J., and P. M. Barker, 2011: *Getting started with TEOS-10 and the Gibbs Seawater (GSW) Oceanographic Toolbox*. SCOR/IAPSO WG127, 28 pp., 28 pp.

Meinen, C. S., R. C. Perez, S. Dong, A. R. Piola, and E. Campos, 2020: Observed Ocean Bottom Temperature Variability at Four Sites in the Northwestern Argentine Basin: Evidence of Decadal Deep/Abyssal Warming Amidst Hourly to Interannual Variability During 2009–2019. *Geophys. Res. Lett.*, **47**, e2020GL089 093, https://doi.org/https://doi.org/10.1029/2020GL089093, https://doi.org/https://doi.org/10.1029/2020GL089093.

Meire, L., J. Mortensen, S. Rysgaard, J. Bendtsen, W. Boone, P. Meire, and F. J. R. Meysman, 2016a: Spring bloom dynamics in a subarctic fjord influenced by tidewater outlet glaciers (Godthåbsfjord, SW Greenland). *J. Geophys. Res. Biogeosci.*, **121**, 1581–1592, https://doi.org/10.1002/2015JG003240, https://doi.org/10.1002/2015JG003240.

Meire, L., P. Meire, E. Struyf, D. W. Krawczyk, K. E. Arendt, J. C. Yde, T. J. Pedersen, M. J. Hopwood, S. Rysgaard, and F. J. R. Meysman, 2016b: High export of dissolved silica from the Greenland Ice Sheet. *Geophys. Res. Lett.*, **43**, 9173–9182, https://doi.org/10.1002/2016GL070191, https://doi.org/10.1002/2016GL070191.

Meire, L., J. Mortensen, P. Meire, T. Juul-Pedersen, M. K. Sejr, S. Rysgaard, R. Nygaard, P. Huybrechts, and F. J. R. Meysman, 2017: Marine-terminating glaciers sustain high productivity in greenland fjords. *Glob. Change Biol.*, **23**, 5344–5357, https://doi.org/10.1111/gcb.13801, https://doi.org/10.1111/gcb.13801.

Mernild, S. H., D. M. Holland, D. Holland, A. Rosing-Asvid, J. C. Yde, G. E. Liston, and K. Steffen, 2015: Freshwater Flux and Spatiotemporal Simulated Runoff Variability into Ilulissat Icefjord, West Greenland, Linked to Salinity and Temperature Observations near Tidewater Glacier Margins Obtained Using Instrumented Ringed Seals. *J. Phys. Oceanogr.*, **45**, 1426–1445, https://doi.org/10.1175/JPO-D-14-0217.1, https://doi.org/10.1175/JPO-D-14-0217.1.

Moffat, C., 2014: Wind-driven modulation of warm water supply to a proglacial fjord, jorge montt glacier, patagonia. *Geophys. Res. Lett.*, **41 (11)**, 3943–3950, https://doi.org/10.1002/2014GL060071, https://doi.org/10.1002/2014GL060071.

Moon, T., D. A. Sutherland, D. Carroll, D. Felikson, L. Kehrl, and F. Straneo, 2018: Subsurface iceberg melt key to Greenland fjord freshwater budget. *Nat. Geosci.*, **11**, 49–54, https://doi.org/10.1038/s41561-017-0018-z, https://doi.org/10.1038/s41561-017-0018-z.

Morlighem, M., C. N. Williams, E. Rignot, L. An, J. E. Arndt, J. L. Bamber, G. Catania, N. Chauché, J. A. Dowdeswell, B. Dorschel, I. Fenty, K. Hogan, I. Howat, A. Hubbard, M. Jakobsson, T. M. Jordan, K. K. Kjeldsen, R. Millan, L. Mayer, J. Mouginot, B. P. Y. Noël,

C. O'Cofaigh, S. Palmer, S. Rysgaard, H. Seroussi, M. J. Siegert, P. Slabon, F. Straneo, M. R. van den Broeke, W. Weinrebe, M. Wood, and K. B. Zinglersen, 2017a: BedMachine v3: Complete Bed Topography and Ocean Bathymetry Mapping of Greenland From Multibeam Echo Sounding Combined With Mass Conservation. *Geophys. Res. Lett.*, **44**, 11,051–11,061, https://doi.org/10.1002/2017GL074954, https://doi.org/10.1002/2017GL074954.

Morlighem, M., C. N. Williams, E. Rignot, L. An, J. E. Arndt, J. L. Bamber, G. Catania, N. Chauché, J. A. Dowdeswell, B. Dorschel, I. Fenty, K. Hogan, I. Howat, A. Hubbard, M. Jakobsson, T. M. Jordan, K. K. Kjeldsen, R. Millan, L. Mayer, J. Mouginot, B. P. Y. Noël, C. O'Cofaigh, S. Palmer, S. Rysgaard, H. Seroussi, M. J. Siegert, P. Slabon, F. Straneo, M. R. van den Broeke, W. Weinrebe, M. Wood, and K. B. Zinglersen, 2017b: BedMachine v3: Complete bed topography and ocean bathymetry mapping of Greenland from multibeam echo sounding combined with mass conservation. *Geophys. Res. Lett.*, **44**, 11 051–11 061, https://doi.org/10.1002/2017GL074954, https://doi.org/10.1002/2017GL074954.

Mortensen, J., J. Bendtsen, K. Lennert, and S. Rysgaard, 2014: Seasonal variability of the circulation system in a west Greenland tidewater outlet glacier fjord, Godthåbsfjord (64°N). *J. Geophys. Res. Earth Surf.*, **119**, 2591–2603, https://doi.org/10.1002/2014JF003267, https://doi.org/10.1002/2014JF003267.

Mortensen, J., J. Bendtsen, R. J. Motyka, K. Lennert, M. Truffer, M. Fahnestock, and S. Rysgaard, 2013: On the seasonal freshwater stratification in the proximity of fast-flowing tidewater outlet glaciers in a sub-Arctic sill fjord. *J. Geophys. Res. Oceans*, **118**, https://doi.org/10.1002/jgrc.20134, https://doi.org/10.1002/jgrc.20134.

Mortensen, J., K. Lennert, J. Bendtsen, and S. Rysgaard, 2011: Heat sources for glacial melt in a sub-arctic fjord (godthåbsfjord) in contact with the greenland ice sheet. *J. Geophys. Res. Oceans*, **116**, https://doi.org/10.1029/2010JC006528, https://doi.org/10.1029/2010JC006528.

Mortensen, J., S. Rysgaard, K. E. Arendt, T. Juul-Pedersen, D. H. Søgaard, J. Bendtsen, and L. Meire, 2018: Local Coastal Water Masses Control Heat Levels in a West Greenland Tidewater Outlet Glacier Fjord. *J. Geophys. Res. Oceans*, **123**, https://doi.org/10.1029/2018JC014549, https://doi.org/10.1029/2018JC014549.

Mortensen, J., S. Rysgaard, J. Bendtsen, K. Lennert, T. Kanzow, H. Lund, and L. Meire, 2020: Subglacial Discharge and Its Down-Fjord Transformation in West Greenland Fjords With an Ice Mélange. *J. Geophys. Res. Oceans*, **125**, e2020JC016 301, https://doi.org/10.1029/2020JC016301, https://doi.org/10.1029/2020JC016301.

Mortensen, J., S. Rysgaard, M. H. S. Winding, T. Juul-Pedersen, K. E. Arendt, H. Lund, A. E. Stuart-Lee, and L. Meire, 2022: Multidecadal Water Mass Dynamics on the West Greenland Shelf. *J. Geophys. Res. Oceans*, **127**, e2022JC018 724, https://doi.org/10.1029/2022JC018724, https://doi.org/10.1029/2022JC018724.

Morton, B. R., G. I. Taylor, and J. S. Turner, 1956: Turbulent gravitational convection from maintained and instantaneous sources. *Proc. Math. Phys. Eng. Sci.*, **234 (1196)**, 1–23, https://doi.org/10.1098/rspa.1956.0011, https://doi.org/10.1098/rspa.1956.0011.

Motyka, R. J., L. Hunter, K. A. Echelmeyer, and C. Connor, 2003: Submarine melting at the terminus of a temperate tidewater glacier, LeConte Glacier, Alaska, U.S.A. *Ann. Glaciol.*, **36**, 57–65, https://doi.org/10.3189/172756403781816374, https://doi.org/10.3189/172756403781816374.

Motyka, R. J., M. Truffer, M. Fahnestock, J. Mortensen, S. Rysgaard, and I. Howat, 2011: Submarine melting of the 1985 Jakobshavn Isbræ floating tongue and the triggering of the current retreat. *J. Geophys. Res. Earth Surf.*, **116**, https://doi.org/10.1029/2009JF001632, https://doi.org/10.1029/2009JF001632.

Mouginot, J., E. Rignot, A. A. Bjørk, M. van den Broeke, R. Millan, M. Morlighem, B. Noël, B. Scheuchl, and M. Wood, 2019: Forty-six years of Greenland Ice Sheet mass balance from 1972 to 2018. *Proc. Natl. Acad. Sci.*, **116**, 9239–44, https://doi.org/https://doi.org/10.1073/pnas.1904242116, https://doi.org/https://doi.org/10.1073/pnas.1904242116.

Muilwijk, M., F. Straneo, D. A. Slater, L. H. Smedsrud, J. Holte, M. Wood, C. S. Andresen, and B. Harden, 2022: Export of Ice Sheet Meltwater from Upernavik Fjord, West Greenland. *J. Phys. Oceanogr.*, **52**, 363–382, https://doi.org/10.1175/JPO-D-21-0084.1, https://doi.org/10.1175/JPO-D-21-0084.1.

Nghiem, S. V., D. K. Hall, T. L. Mote, M. Tedesco, M. R. Albert, K. Keegan, C. A. Shuman, N. E. DiGirolamo, and G. Neumann, 2012: The extreme melt across the Greenland ice sheet in 2012. *Geophys. Res. Lett.*, **39**, https://doi.org/10.1029/2012GL053611, https://doi.org/10.1029/2012GL053611.

Nguyen, A. T., H. Pillar, V. Ocaña, A. Bigdeli, T. A. Smith, and P. Heimbach, 2021: The Arctic Subpolar Gyre sTate Estimate: Description and assessment of a data-constrained, dynamically consistent ocean-sea ice estimate for 2002–2017. *J. Adv. Model. Earth Syst.*, **13**, e2020MS002 398, https://doi.org/10.1029/2020MS002398, https://doi.org/10.1029/2020MS002398.

Oksman, M., A. B. Kvorning, S. H. Larsen, K. K. Kjeldsen, K. D. Mankoff, W. Colgan, T. J. Andersen, N. Nørgaard-Pedersen, M.-S. Seidenkrantz, N. Mikkelsen, and S. Ribeiro, 2022: Impact of freshwater runoff from the southwest Greenland Ice Sheet on fjord productivity since the late 19th century. *Cryosphere Discuss.*, 1–28, https://doi.org/10.5194/tc-2021-373, https://doi.org/10.5194/tc-2021-373.

Oliver, H., R. M. Castelao, C. Wang, and P. L. Yager, 2020: Meltwater-Enhanced Nutrient Export From Greenland's Glacial Fjords: A Sensitivity Analysis. *J.Geophys. Res. Oceans*, **125**, e2020JC016 185, https://doi.org/10.1029/2020JC016185, https://doi.org/10.1029/2020JC016185.

Oltmanns, M., F. Straneo, H. Seo, and G. W. K. Moore, 2015: The role of wave dynamics and small-scale topography for downslope wind events in southeast Greenland. *J. Atmos. Sci.*, **72**, 2786–2805, https://doi.org/10.1175/JAS-D-14-0257.1, https://doi.org/10.1175/JAS-D-14-0257.1.

Pacini, A., R. S. Pickart, I. A. L. Bras, F. Straneo, N. P. Holliday, and M. A. Spall, 2021: Cyclonic Eddies in the West Greenland Boundary Current System. *Journal of Physical Oceanography*, **51 (7)**, 2087–2102, https://doi.org/10.1175/JPO-D-20-0255.1, https://doi.org/10.1175/JPO-D-20-0255.1.

Padman, L., and S. Erofeeva, 2004: A barotropic inverse tidal model for the Arctic Ocean. *Geophys. Res. Lett.*, **31**, https://doi.org/10.1029/2003GL019003, https://doi.org/10.1029/2003GL019003.

Pawlowicz, R., B. Beardsley, and S. Lentz, 2002: Classical tidal harmonic analysis including error estimates in MATLAB using t_tide. *Comput. Geosci.*, **28**, 929–937, https://doi.org/10.1016/S0098-3004(02)00013-4, https://doi.org/10.1016/S0098-3004(02)00013-4.

Podolskiy, E. A., N. Kanna, and S. Sugiyama, 2021: Co-seismic eruption and intermittent turbulence of a subglacial discharge plume revealed by continuous subsurface observations in Greenland. *Commun. Earth Environ.*, **2**, 1–16, https://doi.org/10.1038/s43247-021-00132-8, https://doi.org/10.1038/s43247-021-00132-8.

Princevac, M., H. J. S. Fernando, and C. D. Whiteman, 2005: Turbulent entrainment into natural gravity-driven flows. *J. Fluid Mech.*, **533**, 259–268, https://doi.org/10.1017/S0022112005004441, https://doi.org/10.1017/S0022112005004441.

Pritchard, D. W., 1956: The dynamic structure of a coastal plain estuary. *J. Mar. Res.*, **15**, 33–42, **15**, 33–42.

Roquet, F., G. Madec, T. J. McDougall, and P. M. Barker, 2015: Accurate polynomial expressions for the density and specific volume of seawater using the TEOS-10 standard. *Ocean Modelling*, **90**, 29–43, https://doi.org/10.1016/j.ocemod.2015.04.002, https://doi.org/10.1016/j.ocemod.2015.04.002.

Rysgaard, S., T. Vang, M. Stjernholm, B. Rasmussen, A. Windelin, and S. Kiilsholm, 2003: Physical Conditions, Carbon Transport, and Climate Change Impacts in a Northeast Greenland Fjord. *Arctic, Antarctic, and Alpine Research*, **35 (3)**, 301–312, https://doi.org/10.1657/1523-0430(2003)035[0301:PCCTAC]2.0.CO;2, https://doi.org/10.1657/1523-0430(2003)035[0301:PCCTAC]2.0.CO;2.

Rysgaard, S., W. Boone, D. Carlson, M. K. Sejr, J. Bendtsen, T. Juul-Pedersen, H. Lund, L. Meire, and J. Mortensen, 2020: An Updated View on Water Masses on the pan-West Greenland Continental Shelf and Their Link to Proglacial Fjords. *Journal of Geophysical Research: Oceans*, **125 (2)**, e2019JC015 564, https://doi.org/10.1029/2019JC015564, URL https://onlinelibrary.wiley.com/doi/abs/10.1029/2019JC015564, URL https://onlinelibrary.

wiley.com/doi/abs/10.1029/2019JC015564.

Sanchez, R., F. Straneo, and M. Andres, 2021: Using Acoustic Travel Time to Monitor the Heat Variability of Glacial Fjords. *Journal of Atmospheric and Oceanic Technology*, **38 (9)**, 1535–1550, https://doi.org/10.1175/JTECH-D-20-0176.1, URL https://journals.ametsoc.org/view/journals/atot/38/9/JTECH-D-20-0176.1.xml, URL https://journals.ametsoc.org/view/journals/atot/38/9/JTECH-D-20-0176.1.xml.

Schaffer, J., T. Kanzow, W.-J. von Appen, L. von Albedyll, J. E. Arndt, and D. H. Roberts, 2020: Bathymetry constrains ocean heat supply to greenland's largest glacier tongue. *Nat. Geosci.*, **13 (3)**, 227–231, https://doi.org/10.1038/s41561-019-0529-x, https://doi.org/10.1038/s41561-019-0529-x.

Sciascia, R., F. Straneo, C. Cenedese, and P. Heimbach, 2013a: Seasonal variability of submarine melt rate and circulation in an east Greenland fjord. *J. Geophys. Res. Oceans*, **118**, 2492–2506, https://doi.org/10.1002/jgrc.20142, https://doi.org/10.1002/jgrc.20142.

Sciascia, R., F. Straneo, C. Cenedese, and P. Heimbach, 2013b: Seasonal variability of submarine melt rate and circulation in an East Greenland fjord. *J. Geophys. Res. Oceans*, **118**, 2492–2506, https://doi.org/10.1002/jgrc.20142, https://doi.org/10.1002/jgrc.20142.

Shepherd, A., and Coauthors, 2020: Mass balance of the Greenland Ice Sheet from 1992 to 2018. *Nature*, **579 (7798)**, 233–239, https://doi.org/10.1038/s41586-019-1855-2, https://doi.org/10.1038/s41586-019-1855-2.

Shroyer, E. L., L. Padman, R. M. Samelson, A. Münchow, and L. A. Stearns, 2017: Seasonal control of Petermann Gletscher ice-shelf melt by the ocean's response to sea-ice cover in Nares Strait. *Journal of Glaciology*, **63 (238)**, 324–330, https://doi.org/10.1017/jog.2016.140, https://doi.org/10.1017/jog.2016.140.

Slater, D. A., D. Carroll, H. Oliver, M. J. Hopwood, F. Straneo, M. Wood, J. K. Willis, and M. Morlighem, 2022: Characteristic depths, fluxes, and timescales for Greenland's tidewater glacier fjords from subglacial discharge-driven upwelling during summer. *Geophys. Res. Lett.*, **49**, e2021GL097 081, https://doi.org/10.1029/2021GL097081, https://doi.org/10.1029/2021GL097081.

Slater, D. A., D. Felikson, F. Straneo, H. Goelzer, C. M. Little, M. Morlighem, X. Fettweis, and S. Nowicki, 2020: Twenty-first century ocean forcing of the Greenland ice sheet for modelling of sea level contribution. *The Cryosphere*, **14**, 985–1008, https://doi.org/10.5194/tc-14-985-2020, https://doi.org/10.5194/tc-14-985-2020.

Slater, D. A., D. N. Goldberg, P. W. Nienow, and T. R. Cowton, 2016: Scalings for submarine melting at tidewater glaciers from buoyant plume theory. *J. Phys. Oceanogr.*, **46**, 1839–1855, https://doi.org/10.1175/JPO-D-15-0132.1, https://doi.org/10.1175/JPO-D-15-0132.1.

Slater, D. A., and F. Straneo, 2022: Submarine melting of glaciers in Greenland amplified by atmospheric warming. *Nature Geoscience*, 1–6, https://doi.org/10.1038/s41561-022-01035-9, https://doi.org/10.1038/s41561-022-01035-9.

Slater, D. A., F. Straneo, S. B. Das, C. G. Richards, T. J. W. Wagner, and P. W. Nienow, 2018: Localized plumes drive front-wide ocean melting of a greenlandic tidewater glacier. *Geophys. Res. Lett.*, **45**, 12,350–12,358, https://doi.org/10.1029/2018GL080763, https://doi.org/10.1029/2018GL080763.

Slater, D. A., F. Straneo, D. Felikson, C. M. Little, H. Goelzer, X. Fettweis, and J. Holte, 2019: Estimating Greenland tidewater glacier retreat driven by submarine melting. *Cryosphere*, **13**, 2489–2509, https://doi.org/10.5194/tc-13-2489-2019, https://doi.org/10.5194/tc-13-2489-2019.

Smith, B., H. A. Fricker, A. S. Gardner, B. Medley, J. Nilsson, F. S. Paolo, N. Holschuh, S. Adusumilli, K. Brunt, B. Csatho, K. Harbeck, T. Markus, T. Neumann, M. R. Siegfried, and H. J. Zwally, 2020: Pervasive ice sheet mass loss reflects competing ocean and atmosphere processes. *Science*, **368 (6496)**, 1239–1242, https://doi.org/10.1126/science.aaz5845, https://doi.org/10.1126/science.aaz5845.

Snow, T., F. Straneo, J. Holte, S. Grigsby, W. Abdalati, and T. Scambos, 2021: More than Skin Deep: Sea Surface Temperature as a Means of Inferring Atlantic Water Variability on the Southeast Greenland Continental Shelf Near Helheim Glacier. *Journal of Geophysical Research: Oceans*, **126 (4)**, e2020JC016 509, https://doi.org/https://doi.org/10.1029/2020JC016509, https://doi.org/https://doi.org/10.1029/2020JC016509.

Spall, M., R. H. Jackson, and F. Straneo, 2017: Katabatic wind-driven exchange in fjords. *J. Geophys. Res. Oceans*, **122**, 8246–8262, https://doi.org/10.1002/2017JC013026, https://doi.org/10.1002/2017JC013026.

Staalstrøm, A., L. Arneborg, B. Liljebladh, and G. Broström, 2015: Observations of Turbulence Caused by a Combination of Tides and Mean Baroclinic Flow over a Fjord Sill. *J. Phys. Oceanogr.*, **45**, 355–368, https://doi.org/10.1175/JPO-D-13-0200.1, https://doi.org/10.1175/JPO-D-13-0200.1.

Stevens, L. A., F. Straneo, S. B. Das, A. J. Plueddemann, A. L. Kukulya, and M. Morlighem, 2016: Linking glacially modified waters to catchment-scale subglacial discharge using autonomous underwater vehicle observations. *Cryosphere*, **10**, 417–432, https://doi.org/https://doi.org/10.5194/tc-10-417-2016, https://doi.org/https://doi.org/10.5194/tc-10-417-2016.

Stigebrandt, A., 1999: Resistance to Barotropic Tidal Flow in Straits by Baroclinic Wave Drag. *J. Phys. Oceanogr.*, **29**, 191–197, https://doi.org/10.1175/1520-0485(1999)029⟨0191:RTBTFI⟩2.0.CO;2, https://doi.org/10.1175/1520-0485(1999)029⟨0191:RTBTFI⟩2.0.CO;2.

Stigebrandt, A., and J. Aure, 1989: Vertical Mixing in Basin Waters of Fjords. *J. Phys.*

Oceanogr., **19**, 917–926, https://doi.org/10.1175/1520-0485(1989)019⟨0917:VMIBWO⟩2.0.CO;2, https://doi.org/10.1175/1520-0485(1989)019⟨0917:VMIBWO⟩2.0.CO;2.

Straneo, F., and C. Cenedese, 2015: The dynamics of greenland's glacial fjords and their role in climate. *Annu. Rev. Mar. Sci.*, **7**, 89–112, https://doi.org/10.1146/annurev-marine-010213-135133, https://doi.org/10.1146/annurev-marine-010213-135133.

Straneo, F., R. G. Curry, D. A. Sutherland, G. S. Hamilton, C. Cenedese, K. Våge, and L. A. Stearns, 2011: Impact of fjord dynamics and glacial runoff on the circulation near Helheim Glacier. *Nat. Geosci.*, **4**, 322–327, https://doi.org/10.1038/ngeo1109, https://doi.org/10.1038/ngeo1109.

Straneo, F., G. Hamilton, L. Stearns, and D. Sutherland, 2016: Connecting the Greenland Ice Sheet and the ocean: A case study of Helheim Glacier and Sermilik Fjord. *Oceanog.*, **29**, 34–45, https://doi.org/10.5670/oceanog.2016.97, https://doi.org/10.5670/oceanog.2016.97.

Straneo, F., G. S. Hamilton, D. A. Sutherland, L. A. Stearns, F. Davidson, M. O. Hammill, G. B. Stenson, and A. Rosing-Asvid, 2010: Rapid circulation of warm subtropical waters in a major glacial fjord in east Greenland. *Nat. Geosci.*, **3**, 182–186, https://doi.org/10.1038/ngeo764, https://doi.org/10.1038/ngeo764.

Straneo, F., and P. Heimbach, 2013: North Atlantic warming and the retreat of Greenland's outlet glaciers. *Nature*, **504**, 36–43, https://doi.org/10.1038/nature12854, https://doi.org/10.1038/nature12854.

Straneo, F., D. A. Sutherland, D. Holland, C. Gladish, G. S. Hamilton, H. L. Johnson, E. Rignot, Y. Xu, and M. Koppes, 2012: Characteristics of ocean waters reaching Greenland's glaciers. *Ann. Glaciol.*, **53**, 202–210, https://doi.org/10.3189/2012AoG60A059, https://doi.org/10.3189/2012AoG60A059.

Straneo, F., D. A. Sutherland, L. Stearns, G. Catania, P. Heimbach, T. Moon, M. R. Cape, K. L. Laidre, D. Barber, S. Rysgaard, R. Mottram, S. Olsen, M. J. Hopwood, and L. Meire, 2019: The case for a sustained Greenland Ice Sheet-Ocean observing system (GrIOOS). *Front. Mar. Sci.*, **6**, https://doi.org/10.3389/fmars.2019.00138, https://doi.org/10.3389/fmars.2019.00138.

Straneo, F., D. Slater, C. Bouchard, M. Cape, M. Carey, L. Ciannelli, J. Holte, P. Matrai, K. Laidre, C. Little, L. Meire, H. Seroussi, and M. Vernet, 2022: An Interdisciplinary Perspective on Greenland's Changing Coastal Margins. *Oceanography*, https://doi.org/10.5670/oceanog.2022.128, https://doi.org/10.5670/oceanog.2022.128.

Stuart-Lee, A. E., J. Mortensen, A.-S. v. d. Kaaden, and L. Meire, 2021: Seasonal Hydrography of Ameralik: A Southwest Greenland Fjord Impacted by a Land-Terminating Glacier. *J.Geophys. Res. Oceans*, **126**, e2021JC017 552, https://doi.org/10.1029/2021JC017552, https://doi.org/10.1029/2021JC017552.

Sutherland, D. A., and R. S. Pickart, 2008: The east greenland coastal current: Structure, variability, and forcing. *Prog. Oceanogr.*, **78 (1)**, 58–77, https://doi.org/10.1016/j.pocean.2007.09.006, https://doi.org/10.1016/j.pocean.2007.09.006.

Sutherland, D. A., G. E. Roth, G. S. Hamilton, S. H. Mernild, L. A. Stearns, and F. Straneo, 2014a: Quantifying flow regimes in a Greenland glacial fjord using iceberg drifters. *Geophysical Research Letters*, **41 (23)**, 8411–8420, https://doi.org/10.1002/2014GL062256, https://doi.org/10.1002/2014GL062256.

Sutherland, D. A., F. Straneo, and R. S. Pickart, 2014b: Characteristics and dynamics of two major Greenland glacial fjords. *J. Geophys. Res. Oceans*, **119**, 3767–3791, https://doi.org/10.1002/2013JC009786, https://doi.org/10.1002/2013JC009786.

Sutherland, D. A., F. Straneo, G. B. Stenson, F. J. M. Davidson, M. O. Hammill, and A. Rosing-Asvid, 2013: Atlantic water variability on the SE greenland continental shelf and its relationship to SST and bathymetry. *J. Geophys. Res. Oceans*, **118 (2)**, 847–855, https://doi.org/10.1029/2012JC008354, https://doi.org/10.1029/2012JC008354.

Sutherland, D. A., R. H. Jackson, C. Kienholz, J. M. Amundson, W. P. Dryer, D. Duncan, E. F. Eidam, R. J. ka, and J. D. Nash, 2019: Direct observations of submarine melt and subsurface geometry at a tidewater glacier. *Science*, **365**, 369–374, https://doi.org/10.1126/science.aax3528, https://doi.org/10.1126/science.aax3528.

Taylor, K. E., 2001: Summarizing multiple aspects of model performance in a single diagram. *Journal of Geophysical Research: Atmospheres*, **106 (D7)**, 7183–7192, https://doi.org/10.1029/2000JD900719, https://doi.org/10.1029/2000JD900719.

Tedesco, M., X. Fettweis, T. Mote, J. Wahr, P. Alexander, J. E. Box, and B. Wouters, 2013: Evidence and analysis of 2012 greenland records from spaceborne observations, a regional climate model and reanalysis data. *TC*, **7**, 615–630, https://doi.org/https://doi.org/10.5194/tc-7-615-2013, https://doi.org/https://doi.org/10.5194/tc-7-615-2013.

Thornalley, D. J., D. W. Oppo, P. Ortega, J. I. Robson, C. M. Brierley, R. Davis, I. R. Hall, P. Moffa-Sanchez, N. L. Rose, P. T. Spooner, I. Yashayaev, and L. D. Keigwin, 2018: Anomalously weak Labrador Sea convection and Atlantic overturning during the past 150 years. *Nature*, **556**, 227–230, https://doi.org/10.1038/s41586-018-0007-4, https://doi.org/10.1038/s41586-018-0007-4.

Turner, J. S., 1973: *Buoyancy effects in fluids*. Cambridge University Press, 368pp pp., 368pp pp.

Valle-Levinson, A., 2008: Density-driven exchange flow in terms of the kelvin and ekman numbers. *J.Geophys. Res. Oceans*, **113**, https://doi.org/10.1029/2007JC004144, https://doi.org/10.1029/2007JC004144.

Wagner, T. J. W., F. Straneo, C. G. Richards, D. A. Slater, L. A. Stevens, S. B. Das, and H. Singh,

2019: Large spatial variations in the flux balance along the front of a Greenland tidewater glacier. *Cryosphere*, **13**, 911–925, https://doi.org/https://doi.org/10.5194/tc-13-911-2019, https://doi.org/https://doi.org/10.5194/tc-13-911-2019.

Wain, D. J., M. C. Gregg, M. H. Alford, R.-C. Lien, R. A. Hall, and G. S. Carter, 2013: Propagation and dissipation of the internal tide in upper Monterey Canyon. *J. Geophys. Res. Oceans*, **118**, https://doi.org/10.1002/jgrc.20368, https://doi.org/10.1002/jgrc.20368.

Washam, P., K. W. Nicholls, A. Münchow, and L. Padman, 2020: Tidal Modulation of Buoyant Flow and Basal Melt Beneath Petermann Gletscher Ice Shelf, Greenland. *Journal of Geophysical Research: Oceans*, **125 (10)**, e2020JC016 427, https://doi.org/10.1029/2020JC016427, URL https://agupubs.onlinelibrary.wiley.com/doi/abs/10.1029/2020JC016427, URL https://agupubs.onlinelibrary.wiley.com/doi/abs/10.1029/2020JC016427.

Watts, D. R., and H. T. Rossby, 1977: Measuring dynamic heights with inverted echo sounders: Results from MODE. *J. Phys. Oceanogr.*, **7**, 345–358, https://doi.org/10.1175/1520-0485(1977)007⟨0345:MDHWIE⟩2.0.CO;2, https://doi.org/10.1175/1520-0485(1977)007⟨0345:MDHWIE⟩2.0.CO;2.

Watts, D. R., M. Wimbush, K. Tracey, W. Teague, J.-H. Park, D. Mitchell, J.-H. Yoon, M.-S. Suk, and K.-I. Chang, 2006: Currents, eddies, and a "fish story" in the southwestern japan/east sea. *Oceanog.*, **19**, 64–75, https://doi.org/10.5670/oceanog.2006.44, https://doi.org/10.5670/oceanog.2006.44.

Williams, J. J., N. Gourmelen, P. Nienow, C. Bunce, and D. Slater, 2021: Helheim Glacier Poised for Dramatic Retreat. *Geophysical Research Letters*, **48 (23)**, e2021GL094 546, https://doi.org/10.1029/2021GL094546, https://doi.org/10.1029/2021GL094546.

Willmott, C. J., 1982: Some Comments on the Evaluation of Model Performance. *Bulletin of the American Meteorological Society*, **63 (11)**, 1309–1313, https://doi.org/10.1175/1520-0477(1982)063⟨1309:SCOTEO⟩2.0.CO;2, https://doi.org/10.1175/1520-0477(1982)063⟨1309:SCOTEO⟩2.0.CO;2.

Wood, M., E. Rignot, I. Fenty, D. Menemenlis, R. Millan, M. Morlighem, J. Mouginot, and H. Seroussi, 2018: Ocean-Induced Melt Triggers Glacier Retreat in Northwest Greenland. *Geophysical Research Letters*, **45 (16)**, 8334–8342, https://doi.org/10.1029/2018GL078024, https://doi.org/10.1029/2018GL078024.

Wood, M., E. Rignot, I. Fenty, L. An, A. Bjørk, M. van den Broeke, C. Cai, E. Kane, D. Menemenlis, R. Millan, M. Morlighem, J. Mouginot, B. Noël, B. Scheuchl, I. Velicogna, J. K. Willis, and H. Zhang, 2021: Ocean forcing drives glacier retreat in Greenland. *Sci. Adv.*, **7**, eaba7282, https://doi.org/10.1126/sciadv.aba7282, https://doi.org/10.1126/sciadv.aba7282.

Xu, Y., E. Rignot, D. Menemenlis, and M. Koppes, 2012: Numerical experiments on subaque-

ous melting of Greenland tidewater glaciers in response to ocean warming and enhanced subglacial discharge. *Ann. Glaciol.*, **53**, 229–234, https://doi.org/10.3189/2012AoG60A139, https://doi.org/10.3189/2012AoG60A139.

Zhao, K. X., A. L. Stewart, and J. C. McWilliams, 2018: Sill-influenced exchange flows in ice shelf cavities. *J.Phys. Oceanogr.*, **49**, 163–191, https://doi.org/10.1175/JPO-D-18-0076.1, https://doi.org/10.1175/JPO-D-18-0076.1.

Zhao, K. X., A. L. Stewart, and J. C. McWilliams, 2021: Geometric Constraints on Glacial Fjord–Shelf Exchange. *J. Phys. Oceanogr.*, **51**, 1223–1246, https://doi.org/10.1175/JPO-D-20-0091.1, https://doi.org/10.1175/JPO-D-20-0091.1.

Zhao, K. X., A. L. Stewart, and J. C. McWilliams, 2022a: Linking Overturning, Recirculation, and Melt in Glacial Fjords. *Geophys. Res. Lett.*, **49**, https://doi.org/10.1029/2021GL095706, https://doi.org/10.1029/2021GL095706.

Zhao, K. X., A. L. Stewart, J. C. McWilliams, I. G. Fenty, and E. J. Rignot, 2022b: Standing Eddies in Glacial Fjords and their Role in Fjord Circulation and Melt. *Journal of Physical Oceanography*, **-1 (aop)**, https://doi.org/10.1175/JPO-D-22-0085.1, https://doi.org/10.1175/JPO-D-22-0085.1.